

Measurements of the Energy Spectrum and
the Mass Composition of Ultra-High
Energy Cosmic Rays with Telescope Array
Fluorescence Detectors in Monocular Mode

Toshihiro Fujii

Mail: fujii@alpha.sci.osaka-cu.ac.jp

Supervisor: Shoichi Ogio

Graduate School of Science,
Osaka City University,
Sumiyoshi, Osaka 558-8585, Japan

September 2012

Abstract

In 1912, just one century ago, V.F.Hess discovered energetic elementary particles came from the universe, so called “Cosmic Rays”. However, currently their origins are still unknown. Among them, ultra-high energy cosmic rays (UHECRs) with $E > 10^{19}$ eV are the most energetic particles in the universe, and their origins might be related with energetic astronomical phenomena or exotic physics. Thus, in order to conclude origins of cosmic rays, we steadily observe UHECRs by the Telescope Array (TA) experiment in Utah of USA from 2008. The TA is the largest detector in the northern hemisphere, and it consists of 38 fluorescence detectors and 507 surface detectors covering with 700 km² ground area. In this thesis, the author analyzed data collected by the newly constructed fluorescence detectors of TA during 3.7 years in monocular mode, and measured a mass composition and an energy spectrum with broad energies from $10^{17.5}$ eV to $10^{20.0}$ eV. The obtained mass composition indicated a transition of dominated components from heavy to light nuclei from $10^{17.5}$ eV to $10^{18.5}$ eV and proton dominant above $10^{18.5}$ eV. The observed energy spectrum was in good agreement with results of TA surface detectors and Middle Drum fluorescence detectors which are transported from the HiRes experiment.

Keyword: ultra-high energy cosmic rays, energy spectrum, mass composition, extensive air showers, Telescope Array experiment, fluorescence light, active galactic nuclei, gamma-ray bursts, large scale structure

Acknowledgments

I am deeply thankful to my supervisor *Shoichi Ogio* for the much I have learned from him and the full support given during the development of my thesis. And to *Yoshio Hayashi*, *Koji Kojima* and *Nobuyuki Sakurai*, that accompanied at close distance the whole work and given their valuable advice.

I would like to thank all of the Telescope Array collaborators for great help about the science work and pleasant days. At first, I am grateful to *Masaki Fukushima* and *Hiroyuki Sagawa* for the great management and giving me the opportunity to participate in the Telescope Array experiment.

Next, as the same analysis group of the Telescope Array fluorescence detectors, I would like to thank to *Yuichiro Tameda*, *Daisuke Ikeda* and *Takayuki Tomida*. I'm very happy to work with you, enjoy many tourist spots and get precious memories all over the world. I would also like to express my gratitude to *Sean Stratton* and *Elliott Barcikowski* for the helpful discussion and cross checkings of my analysis. I would like to thank to *Yoshiki Tsunesada* for their advice and guidance for my work as an organizer of our analysis group. And to *Hisao Tokuno* and *Shigeharu Udo*, *Masahiro Takeda* and *Tatsunobu Shibata* for their valuable support and helpful comments. I am also very grateful to *Pierre Sokolsky*, *Gordon Thomson*, *Charlie Jui*, *John Matthews* and *Douglas Bergman* for precious discussions and their kindly support at Utah. I would like to thank to *Toshiyuki Nonaka*, *Takeshi Okuda*, *Eiji Kido* and *Akimichi Taketa* for their important advice and leaning the experimental technique at the Telescope Array site, Utah of U.S.A.

As the members of our laboratory including graduated students, I would like to thank to *Akitoshi Oshima*, *Mayuko Minamino*, *Hitoshi Miyachi*, *Yu Yamashita*, *Eri Usui*, *Katsuya Yamazaki*, *Kazuyuki Kuramoto*, *Daisuke Matsumiya*, *Yasuhisa Yoneda*, *Ryo Yamane*, *Takashi Goto* and *Shogo Kobayashi* for their pleasant communications and encouragements. As the collaborators of other institutes including graduated students, I'm grateful to *Takanori Fukuda*, *Kentaro Hayashi*, *Yusaku Kobayashi*, *Rie Ishimori*, *Yoshiaki Takahashi*, *Daisuke Oku*, *Fumiya Shibata*, *Kanetsugu Kitamoto*, *Kazuki Tsutsumi*, *Takanori Matsumura*, *Seiji Kitamura* and *Yuki Kitamura* for their discussions and delightful drinking sessions.

I gratefully acknowledge the valuable financial support by the Japan Society for the Promotion of Science (JSPS). I also gratefully thank the contributions of computing system at Institute for Cosmic Ray Research (ICRR) of University

of Tokyo and the University of Utah Center for High Performance Computing (CHPC).

Finally, I am very grateful to my family, especially *Nobuyuki Fujii* and *Akemi Fujii*, for putting up with me and supporting my research life. I would also like to thank to my dear friends for their encouragements.

皆さんに出会え、成長できたことに深く感謝しています。

2012年9月

藤井 俊博



Contents

1	Introduction	1
2	Ultra-High Energy Cosmic Rays	5
2.1	Overview of UHECR Physics	5
2.2	Cosmic Rays	5
2.2.1	Energy Spectrum	6
2.2.2	Acceleration Mechanism	6
2.3	Ultra-High Energy Cosmic Rays	10
2.3.1	GZK Cutoff	10
2.3.2	Candidates of CR Origins	13
2.4	Extensive Air Shower	16
2.4.1	Air Shower Cascades	16
2.4.2	Characteristic Parameters of EAS	18
2.5	Techniques for EAS Measurement	20
2.5.1	Air Shower Array	20
2.5.2	Fluorescence Technique	21
2.6	Recent Results and Mysteries of UHECRs	27
2.6.1	Energy Spectrum	28
2.6.2	Mass Composition	30
2.6.3	Arrival Direction Distribution	35
3	Telescope Array Experiment	41
3.1	Aims of the Telescope Array Project	41
3.2	Overview of TA Hybrid Detector	42
3.3	Fluorescence Detector	42
3.3.1	Telescope and Optics	44
3.3.2	Photomultiplier Tube (PMT) and Camera	45
3.3.3	Calibration of PMT Gain	50
3.3.4	Trigger Electronics	53
3.4	Atmospheric Monitoring	60
3.4.1	Radiosonde	61
3.4.2	LIDAR	61
3.4.3	CLF	63
3.4.4	Cloud Monitoring	65

3.4.5	Star Analysis	67
3.4.6	The End-to-End Absolute Energy Calibration	68
3.5	Surface Detector	68
4	TA FD Detector Simulation Software	75
4.1	Extensive Air Shower Generation	75
4.1.1	CORSIKA shower simulation	75
4.1.2	Fluorescence Light Emission	78
4.1.3	Direct Čerenkov Light	79
4.1.4	Scattered Čerenkov Light	79
4.2	TA FD Detector Simulation	82
4.2.1	Ray-tracing technique	82
4.2.2	Night Sky background	83
4.3	Cross Checking of Simulation Software	83
4.3.1	Photon Emission Processes and Atmospheric Models	84
4.3.2	Comparison of Ray-Tracing	84
5	TA FD Reconstruction Software	87
5.1	PMT Selection	88
5.1.1	1st Selection : Signal Search	88
5.1.2	2nd Selection : Line Structure Search	89
5.1.3	3rd Selection : Timing Sequence Search	91
5.1.4	4th Selection : Small Signal Research	92
5.2	Geometry Reconstruction	93
5.2.1	Estimation of the Line of Sight for Each PMT	94
5.2.2	Shower-Detector Plane	94
5.2.3	Monocular Geometry Reconstruction	96
5.3	Shower Profile Reconstruction – Inverse Monte Carlo –	97
5.3.1	X_{\max} Determination	97
5.3.2	N_{\max} Determination	98
5.3.3	Energy Determination	98
6	Performance Estimation of TA FD	101
6.1	Resolution and Aperture of the Monocular Mode	101
6.1.1	Simulation Conditions	101
6.1.2	Resolutions in the Monocular Mode	102
6.1.3	Estimations of Apertures	108
6.2	Mass Composition Study	110
6.2.1	Mass Composition Measurement by X_{\max} Technique	110
6.2.2	Acceptance Biases on X_{\max} Limited Fields of View of FDs	111
6.2.3	Fiducial Volume Cuts	112

7	Data Analysis	117
7.1	Data Set	117
7.1.1	Calculation of Live Time	117
7.1.2	Number Spectrum	119
7.2	Data/MC Comparison	121
7.3	Check of Resolution in Monocular Mode	121
7.4	Mass Composition Analysis	123
7.4.1	Mass Composition Results in BRM or LR Station	123
7.4.2	Mass Composition Results in Combined Mode	124
7.4.3	Compatibility of X_{\max} Distribution on Kolmogorov-Smirnov Test	127
7.5	Energy Spectrum	137
7.5.1	Combined Exposure	137
7.6	Study of Systematic Uncertainty	139
7.6.1	Fluorescence Yields	140
7.6.2	Atmospheric parameters	141
7.6.3	Calibrations	141
7.6.4	Geometry of Fluorescence Telescopes	142
7.6.5	Reconstruction Methods	142
7.6.6	Total Systematic Uncertainty	143
8	Discussion	145
8.1	Mass Composition Measurement	145
8.1.1	Transition of Mass Composition from $10^{17.5}$ eV to $10^{18.5}$ eV	146
8.1.2	Proton Dominant above $10^{18.5}$ eV	148
8.2	Energy Spectrum Measurement	150
8.3	Combined Interpretation	153
8.4	Future Plans	154
9	Conclusions	159
	Appendix	161
A.1	Observed EAS Events	161
A.2	Data/MC comparison	162
	Bibliography	178

List of Figures

1.1	A schematic views of an extensive air shower (EAS) and its X_{\max} .	2
2.1	Overview of the cosmic ray spectrum. Approximate energies of the two breaks commonly referred to as knee and the ankle are indicated by arrows. Data are from LEAP [7], Proton [8], AKENO [9], KASCADE [10], Auger surface array [11], Auger hybrid [12], AGASA [44], HiRes-I Monocular [50], HiRes-II Monocular [50].	7
2.2	Attenuation lengths of UHECR particles. The thick solid lines shows attenuation lengths for UHE protons, the thin solid lines are for UHE photons and the dotted line is for UHE iron nuclei.	11
2.3	Expected energy spectra of UHE protons [13] [14]. The left figure shows the expected spectra from a single source of several different red shift ($z = 0.004 \sim 1.0$). The right figure shows expected energy spectra assuming uniform source distribution with with different source evolution models.	12
2.4	UHECR spectrum to be expected from a two component model, where UHECRs consist of protons and iron nuclei and they are accelerated with a statistical process, with assumptions that, the injection power law index is $\gamma_g = 2.0$ and the maximum energy is $E_{\max} = 4Z \times 10^{18}$ eV. The data plot of energy spectrum is measured by Auger [15].	13
2.5	The Hillas plot, a relation between magnetic field strengths and scales of astronomical objects. The solid and dashed lines show the maximum energies by statistical accelerations estimated by (2.17) [59].	14
2.6	Schematic views of an extensive air shower.	18
2.7	Longitudinal developments of protons and irons for a EAS simulation.	20
2.8	The lateral density distribution of electron number density in air shower whose primary is proton with energy 10^{19} eV at the shower maximum.	21
2.9	The schematic view of stereoscopic observations.	23
2.10	The relative line spectrum of air fluorescence light measured by FLASH [92]. The sum of the line strengths is set to unity.	25

2.11	The parameters for (2.43).	27
2.12	UHECR spectra measured by Yakutsk, AGASA, HiRes and Auger [35] [44] [50] [51].	28
2.13	The averaged X_{\max} for Stereo Fly's Eyes (left) and HiRes/MIA and HiRes (right) compared with predictions for primary protons and irons with several hadron interaction models after full Monte Carlo detector simulations [38] [37].	31
2.14	Preliminary results of the averaged X_{\max} measured by the Telescope Array experiment compared with the prediction rails for protons and irons using three types of hadron interaction models: QGSJet-I (a solid line) QGSJet-II (a dash-dotted line) and SIBYLL (a dotted line) [39].	32
2.15	Auger measured $\langle X_{\max} \rangle$ compared with air shower simulations using different hadronic interaction models[40].	32
2.16	Distribution of X_{\max} observed by the Pierre Auger Observatory [41]. The values of the energy limits and the number of events selected are indicated for each panel.	33
2.17	Averaged X_{\max}^{μ} values as a function of the energy measured by Auger surface detectors [42]. The number of real data events in each energy bin is indicated. The predictions for primary protons and irons following different hadronic models are shown as well.	34
2.18	Arrival directions of cosmic rays with energies above 4×10^{19} eV observed by AGASA. Red squares and green circles represent cosmic rays with energy of $> 10^{20}$ eV, and $(4 - 10) \times 10^{19}$ eV, respectively. Shaded circles indicate event cluster within 2.5° . At $(10^h 29^m, 57^{\circ})$, three 4×10^{19} cosmic rays are observed against expected 0.06 events. [46]	36
2.19	Aitoff projection of the celestial sphere in galactic coordinates with circles of radius 3.1° centered at the arrival directions of the 27 cosmic rays with highest energy detected by the Pierre Auger Observatory [29]. The position of the 472 AGN(318 in the field of view of the Observatory) with the redshift $z \leq 0.018$ ($D < 75$ Mpc) from the 12th edition of the catalog of quasars and active galactic nuclei by Véron-Cetty and Véron (VCV catalog) [62] are indicated by red asterisks. The solid line represents the border of the field of view (zenith angle smaller than 60°). Darker color indicates larger relative exposure. Each colored band has equal integrated exposure. The dashed line is the super-galactic plane. Centaurus A, one of our closet AGN, is marked in white.	36

2.20	The 69 arrival directions with energy $E \leq 55$ EeV detected by the Pierre Auger Observatory up to 31 December 2009 are plotted as black dot in an Aitoff-Hammer projection of the sky in galactic coordinates [30]. The solid line represents the field of view of the Southern Observatory for zenith angles smaller than 60° . Blue circles of radius 3.1° are centered at the positions of the 318 AGNs in the VCV catalog [62] that lie within 75 Mpc and that are within the field of view of the Observatory. Darker blue indicates larger relative exposure. The exposure-weighted fraction of the sky covered by the blue circles is 21%.	37
2.21	The ratio between total number of UHECRs and UHECRs direction correlated with AGN observed by Auger. $P_{\text{data}} = N^{\text{correlated}}/N^{\text{total}}$ [30].	37
2.22	Hammer projection of the UHECRs with $E > 57$ EeV observed by TA and nearby AGNs in the Galactic coordinates. Correlating and non-correlating events are shown by filled red and empty blue circles, respectively. AGNs are represented by black dots. The dashed line shows the boundary of the TA exposure [31]. .	38
2.23	The number of the UHECRs with $E > 57$ EeV observed by TA correlating with AGNs from VCV catalog as a function of the total number of events. The expectation according to the original Auger claim is represented by the blue line together with the 1- and 2-sigma significance bands. The black dashed line shows the expected number of random coincidences [31].	38
3.1	The detector configuration of TA. The red square plots: surface detector, the yellow pentagon-shaped plots: station of fluorescence detectors, the blue cross shape: the Central Laser Facility.	43
3.2	The BRM station (top-left), the fluorescence detectors of BRM station (top-right) and the MD station and MD fluorescence detectors transported from HiRes-I and HiRes II experiment (down).	44
3.3	The newly developed telescopes and their designs at BRM and LR site.	45
3.4	The variation of the reflectance of the LR mirror in June 2008. Colors on the left figures correspond to the colors on the right figure. The vertical axis is the variation from installing. It depends on the height of mirrors.	46
3.5	The spectral reflectance of the camera 06 of BRM station (left) and a picture in mirror washing (right). Open circles are the reflectance before washing and filled circles are after washing .	47
3.6	Variation in the mirror reflectance at 360 nm of a typical lower FD (FOV: 17.5-33 in elevation) of camera 04 at LR. The mirror was washed after these measurements in July 2007, August 2009 and May 2010 [53].	47
3.7	TA camera (left) and PMT of R9508 attached the UV filter (right).	48

3.8	The typical transmittance of the KURARAY paraglas on the front of camera.	48
3.9	The typical transmittance of the UV filter in the front of photo-tubes. Data points are the medians for all the sampled filters with the bars corresponding the on standard deviation.	49
3.10	The typical quantum efficiency of photo-tubes. The data plot shows the median with one standard deviation error of all PMTs measured by HAMAMATSU PHOTONICS.	49
3.11	Multiplication values of the typical values of mirror reflectance, paraglas transmittance, UV filter transmittance and quantum efficiency of PMT.	50
3.12	The typical non-uniformity map with 1 mm \times 1 mm resolution of the photo-cathode of our photo-tube. It is normalized with the bins inside a circle with 36 mm diameter. The obtained map show an asymmetry long the x axis caused by the dynode structure of the PMT.	51
3.13	The comparison of results between the HAMAMATSU data and the data measured by XY-scanner. The left and right figure show the result along X axis and Y axis, respectively. The definition of the coordinate of x and y axis is the same as Fig. 3.12. Filled circle are the HAMAMATSU data and open circles are XY's scanners.	51
3.14	The schematic view and photograph of XY-scanner. The covering area of each LED is 2.5 PMTs vertically and 16 PMTs horizontally.	52
3.15	Measurement set up of CRAYS [75].	53
3.16	The UV pulsed light source located in front and center of the standard PMT, named YAP.	53
3.17	The image of Xe flasher.	54
3.18	Block diagram of electronics and trigger system of the TA FD .	54
3.19	Photos of the trigger modules of TA fluorescence detector . . .	55
3.20	Block diagram of TA Track Finder module.	56
3.21	Schematic diagram of the track finding process.	56
3.22	Schematic diagram of the partial track search near the boundary of a camera.	57
3.23	Block diagram of TA Central Trigger Distributor module. . . .	58
3.24	The procedures of a single trigger.	59
3.25	The histogram of typical dead time durations in log scale for some observation terms on Apr/2008, Oct/2008, Apr/2009, Oct/2009.	60
3.26	The overview of LIDAR system. A left picture is LIDAR's optical system (telescope, laser, etc), a right picture is a connection block diagram of device of LIDAR.	62
3.27	The histogram of the extinction coefficient for Mie scattering on the ground. The median value 0.034 km^{-1} is equivalent to the attenuation length of 29.411 km.	63

3.28	The CLF system located at the center of TA (left) and the inside picture of CLF (right).	64
3.29	The image of LIDAR system installed at the CLF location (left) and VAOD relationship measured by CLF and LIDAR (right).	64
3.30	The overview of IR camera (left). The right figure is the 12 photographs taken by each telescope directions of FD. The number shows the analyzed cloud score on 4 horizontally categorized regions.	65
3.31	The photo of CCD fish-eye at LR station and picture taken at CLF, BRM and LR location. The yellow region shows the FOV of each FD, the green region shows the cover of CLF-LIDAR for online monitoring.	66
3.32	Simulation results of time variance of BG level with the different SSPs. Red square: SSP = 0.0 degree, Blue circle: SSP = 0.1 degree, Black triangle: SSP = 0.2 degree.	67
3.33	Fitting sample of BG level time variance (BRM00). Error bars of observed data show their statistical errors. Circle: observed, Square: simulated.	68
3.34	The photos of ELS installed at BRM site.	69
3.35	The schematic view of ELS system.	69
3.36	The event display of the first ELS beams observed by FD.	69
3.37	The surface detector deployed TA site.	70
3.38	Inside of a scintillator box with scintillator plates, WLS fibers and PMTs. A total 104 WLS fibers are laid on each layer to collect and transmit scintillation light.	70
3.39	The electronics of TA SD.	71
3.40	The Black Rock Mesa communication tower, one of three in the array. There are three stands each with solar panels. Those stands contain batteries, data acquisition PC and network instruments for long distance link.	72
3.41	The long-distance links for all the facilities and three FD stations in the entire TA site. The open triangles represent the communication towers where the trigger decision electronics for sub-arrays are installed. The lines that connect the towers and facilities represent the links between antennas. The red lines are used for trigger decision. The dotted line shows the border of the entire surface detector array [82].	72
3.42	Trigger pattern taken at the TA surface array. If any three adjacent SDs have timing difference within 8 μ sec the trigger will be generated.	73
3.43	Typical air shower event and recorded waveforms triggered across the border of sub-array. The event display of observed air shower (left) and observed waveforms (right).	74

4.1	The ratio between calorimetric energies and primary energies as a function of primary energies for primary protons and irons using the QGSJet-II hadron interaction model. The calorimetric energies are estimated from an integration of energy deposits fitted by the Gaisser-Hillas function.	77
4.2	The photon emission processes from extensive air showers. Not only fluorescence light, but also direct Čerenkov light and scattered Čerenkov light.	78
4.3	The phase function of Mie scattering observed at the HiRes site, Dugway [83].	80
4.4	The number of fluorescence, direct Čerenkov, Rayleigh scattered Čerenkov and Mie scattered Čerenkov photons injected into telescope. The top figure is the shower geometry across the FOV, the bottom figure is the geometry going toward FD.	81
4.5	The structure of FD implemented in TA FD simulation software with the ray-tracing trajectory emitted from line assumed shower axis.	82
4.6	The response function of SDF. The time constant is 50 ns. . . .	84
4.7	The example of the database for the background observed by BRM camera 06. The upper figure shows the mean for 2^{14} “bundles”. The bundle consists of the sum of 16 bins of FADC count and is continuously recorded by SDF. The lower figure represents the dispersion for the same telescope. The black line is the averaged value of the pedestal. The horizontal axis shows the measured data (year/month).	85
4.8	the photon density of fluorescence, direct Čerenkov, Rayleigh and Mie scattered Čerenkov photons as a function of slant depth. The black line represents another result with perfectly agreement.	86
4.9	The two-dimensional histogram at the PMT camera by 10000 photons ray-tracing using our software(left) and another independently developed software (right). Our results is reasonable agreement with another result.	86
5.1	The typical waveforms recorded by FD.	87
5.2	The schematic diagram of the weighted triangle filter.	88
5.3	The distribution of significance calculated the weighted triangle filter. The left figure is the distribution without air shower signal, the right figure is one with air shower signal.	90
5.4	The shower track (left) and the distribution of separate angle β (right). While the data from air shower are concentrated at the smaller separate angle, the noise data are not located around zero.	90
5.5	Shower track (left) and timing fitting to search for noise (right). In the right figure, isolated PMT (-2.5° , $19 \mu s$) is judged to noise signal.	91

5.6	The event display observed by FD comparing before(left) and after(right) PMT selections. The noise PMTs are removed by the PMT selection.	93
5.7	The total directional characteristic of all PMTs in camera00 at BRM (top) and of each PMTs located center, edge and corner. The direction is the relative angle from the line of sight of the telescope. The color map indicates the sensitivity calculated by Ray-Trace simulation.	95
5.8	Stereo geometry reconstruction. The shower axis is determined by intersecting two SDPs.	96
5.9	Geometry reconstruction in monocular mode	96
5.10	The shower signals injected from longitudinal development curves of IMC fitting result and an observed air shower signal. The plot is the observed data, the red show the contribution of fluorescence light, the blue indicates of the direct Čerenkov light, the purple and green shows the scattered Čerenkov light of Rayleigh and Mie process, respectively.	99
6.1	Core location distribution of Monte Carlo showers. (0, 0) shows the center of the distribution corresponding to the location of CLF. The vertical axis, Y-axis, is the direction from south to north, the horizontal axis, X-axis, is from east to west. The yellow triangles indicate the FD station locations.	102
6.2	Averaged X_{\max} of protons and irons generated by CORSIKA QGSJet-II and SIBYLL model without detector simulation. The solid line shows the QGSJet-II, the dashed line shows the SIBYLL, the red line is the result of protons, the blue line is the result of irons.	103
6.3	The open angle distribution comparing between thrown arrival directions and reconstructed ones.	104
6.4	The resolutions of the impact parameter estimation. It is a comparison between simulated and reconstructed values.	105
6.5	The angle resolution on SDP compared between simulated and reconstructed.	105
6.6	The resolution of X_{\max} including protons of different energies under the simulation condition of section 6.1.1(left). The energy dependence for the X_{\max} resolutions (right).	106
6.7	The energy resolution including protons of different energies under the simulation condition of section 6.1.1(left). The energy dependence for the energy resolutions (right).	106
6.8	The energy systematics are fitted by a linear function. Plots indicate the means and error bars indicate the errors of the mean.	107
6.9	The corrected energy resolution reconstructed by the monocular mode as a function of energy. The systematic bias was removed.	107

6.10	The weighted histogram of simulated and reconstructed energy estimated from protons of QGSJET-II model.	109
6.11	The left figure is an aperture in BRM and LR only monocular mode. The iron and proton simulated results are shown. The right plot shows the BRM and LR combined aperture comparing with BRM and LR monocular aperture assumed pure proton primary. The bottom plot shows the comparison of combined apertures estimated by protons and irons.	110
6.12	Longitudinal development curves simulated for primary protons and irons with the energy of 10^{18} eV. The red curves show longitudinal developments of protons, the blue curves are of irons.	111
6.13	Showers which can not be observed by FD caused by limited a field of view.	112
6.14	Averaged values of simulated and reconstructed X_{\max} under only standard cuts. Reconstructed averaged X_{\max} has large biases caused by limited fields of view. The red line and blue dashed line indicate averaged X_{\max} with acceptance biases for primary protons and irons, respectively. The pink dash-dotted line and sky-blue two-dotted line indicates thrown averaged X_{\max} for primary protons and irons, respectively.	112
6.15	Averaged X_{\max} as a function of X_{start} and X_{end} in order to determine the optimum range for X_{start} and X_{end} . The red and blue plots indicate results for primary protons and irons, respectively. The pink plots indicate results for a mixed composition which consists of 50% protons and 50% irons.	113
6.16	Simulated and reconstructed of averaged X_{\max} under FVC. Reconstructed averaged X_{\max} is much close to thrown one. These lines are the same definitions shown in Fig. 6.14.	114
6.17	Averaged X_{\max} with acceptance biases for primary protons and irons with QGSJet-II and SIBYLL model under FVC. The solid lines indicate results using QGSJet-II model. The dashed lines indicate results using SIBYLL models. The red and blue color indicate primary protons and irons, respectively.	115
7.1	The schematic view of calculation of BRM and LR live time. There are 3 types of live time: stereo (blue), BRM monocular (orange), LR monocular (green).	118
7.2	The three types of live times with the WEAT code cut. These broken lines indicate the total live time durations in the stereo (blue), the BRM station (orange) and the LR station (green). The growth rates of live times vary with the seasons.	118
7.3	Number spectra under the standard cuts (a) and under the FVC (b). There are three types of reconstructed energy histograms for the BRM station (red), the LR station (blue) and combined them (green).	120

7.4	Pull plots of energies (a) and X_{\max} (b). The peak energy of reconstructed EASs including pull plots is $10^{18.6}$ eV.	122
7.5	Scatter plot of reconstructed energy and X_{\max} applied the fiducial volume cut in BRM and LR monocular analysis.	123
7.6	The measured and expected of averaged X_{\max} in the monocular analyses at the BRM station (a) and the LR stations (b) under the fiducial volume cuts. The pink and sky blue lines indicates the averaged X_{\max} of thrown MC which are estimated only to use CORSIKA simulations. The red and blue lines indicates the averaged X_{\max} which are calculated in our MC simulations with acceptance biases of limited FOV of FDs. The MC lines are estimated using the QGSJet-II model as a hadron interaction model.	124
7.7	Scatter plots of energies and X_{\max} reconstructed at both the BRM and LR stations under the fiducial volume cuts.	125
7.8	The averaged X_{\max} as a combination of both BRM and LR reconstructed events under the fiducial volume cuts. The pink and sky blue lines indicates the averaged X_{\max} of thrown MC estimated by only CORSIKA shower generations. The red and blue lines indicates the averaged X_{\max} with the acceptance bias of each FD station. The MC lines are estimated using the QGSJet-II model as a hadron interaction model.	126
7.9	The comparison with data and MC line estimated from QGSJet-II model and SIBYLL model under the fiducial volume cuts. The number symbols indicates the number of EASs in each bin. . .	127
7.10	X_{\max} distribution in $10^{17.5}$ eV $\leq E < 10^{17.8}$ eV and $10^{17.8}$ eV $\leq E < 10^{18.0}$ eV compared with the expected distribution estimated from MC simulation for primary protons (red), irons (blue) or mixed compositions (pink) under the fiducial volume cuts. Three types of the vertical axis indicate the linear scale, the logarithmic scale and its ratio between data and MC simulations.	128
7.11	X_{\max} distribution in $10^{18.0}$ eV $\leq E < 10^{18.2}$ eV and $10^{18.2}$ eV $\leq E < 10^{18.4}$ eV compared with the expected distribution estimated from MC simulation for primary protons (red), irons (blue) or mixed compositions (pink) under the fiducial volume cuts. Three types of the vertical axis indicate the linear scale, the logarithmic scale and its ratio between data and MC simulations.	129
7.12	X_{\max} distribution in $10^{18.4}$ eV $\leq E < 10^{18.6}$ eV and $10^{18.6}$ eV $\leq E < 10^{18.8}$ eV compared with the expected distribution estimated from MC simulation for primary protons (red), irons (blue) or mixed compositions (pink) under the fiducial volume cuts. Three types of the vertical axis indicate the linear scale, the logarithmic scale and its ratio between data and MC simulations.	130

7.13	X_{\max} distribution in $10^{18.8} \text{ eV} \leq E < 10^{19.0} \text{ eV}$ and $10^{19.0} \text{ eV} \leq E < 10^{19.3} \text{ eV}$ compared with the expected distribution estimated from MC simulation for primary protons (red), irons (blue) or mixed compositions (pink) under the fiducial volume cuts. Three types of the vertical axis indicate the linear scale, the logarithmic scale and its ratio between data and MC simulations.	131
7.14	X_{\max} distribution in $10^{19.3} \text{ eV} \leq E$ compared with the expected distribution estimated from MC simulation for primary protons (red), irons (blue) or mixed compositions (pink) under the fiducial volume cuts. Three types of the vertical axis indicate the linear scale, the logarithmic scale and its ratio between data and MC simulations.	132
7.15	The X_{\max} distribution of the observed data and MC simulated by protons and irons with $10^{18.4} \text{ eV} \leq E < 10^{18.6} \text{ eV}$ under the fiducial volume cuts, which is the same data shown in Fig. 7.10(e).	133
7.16	The probabilities estimated by KS test using several compositions of QGSJet-II and SIBYLL. Red: proton, Blue: iron, Pink: mixed composition assuming 50% proton and 50% iron primaries.	134
7.17	The proton fraction and the averaged $\langle \ln A \rangle$ measured by the BRM and the LR stations under the fiducial volume cuts. . . .	135
7.18	The measured and expected of averaged X_{\max} with <i>only the standard cuts</i> . The pink and sky blue lines indicates the averaged X_{\max} of thrown MC estimated by only CORSIKA shower generations. The red and blue lines indicates the averaged X_{\max} with the acceptance bias of each FD station. The MC lines are estimated using the QGSJet-II model as the hadron interaction model.	136
7.19	Energy Spectra. In the right figure, the size of binning is changed from $d \log E = 0.1$ step to $d \log E = 0.2$	138
7.20	The proton fraction measured by HiRes/MIA experiment [84].	138
7.21	TA combined spectra assuming several compositions: pure proton, HiRes/MIA composition and measurement result in TA monocular mode.	139
7.22	Energy spectra in the TA measurement. The blue plots show the spectrum analyzing data collected at the BRM and the LR stations, the open squares show the spectrum measured at the Middle Drum station [71], the pink triangles indicate the spectrum measured by TA SD with 27% scaled as the same energies with TA FD energies [72]	140
7.23	The fluorescence yield comparisons between several measurements with US standard atmosphere [60] [61] [92] [93] [94]. . . .	141
8.1	The measured averaged X_{\max} fitted by two types of line functions using the least square method.	146

8.2	The averaged X_{\max} for Stereo Fly's Eyes (a) and HiRes/MIA and HiRes (b) [38] [37]. Auger measured $\langle X_{\max} \rangle$ compared with air shower simulations using different hadronic interaction models [40]. They are the same figures shown in Fig. 2.13 and Fig. 2.15.	147
8.3	Energy spectra of several composition observed by several experiments around the knee region. The dotted lines indicate the expected flux assuming a rigidity dependent acceleration model using the results of the Tibet group [97].	148
8.4	The P-values of KS test with the systematic shift on X_{\max} , $\pm 19 \text{ g/cm}^2$ under the fiducial volume cut. The solid and dotted lines show results of the systematic shift of $+19 \text{ g/cm}^2$ and -19 g/cm^2 , respectively. The red, blue, and pink lines show the result of primary protons, irons and mixed composition, respectively.	149
8.5	The measured energy spectrum fitted by three types of power-law function using the method of least squares.	150
8.6	The energy spectra compared with several measurements [9] [11] [12] [44] [50] [71] [72].	151
8.7	The comparison of fitted values measured by AGASA, Yakutsk, HiRes and TA(SD) reported at UHECR2012 Symposium and by BRM and LR monocular mode [98].	152
8.8	Propagated spectra, $f(E) \cdot E^3$, for pure proton extra-galactic cosmic ray sources (left). The injection spectral index is $E^{-2.6}$ for the HiRes data. Two different propagated spectra and the corresponding inferred galactic cosmic ray component are shown, for an injection spectrum either with or without a low energy cut [99]. UHECR spectra to be expected from a two component model (right) [15], which is the same figure shown in Fig. 2.4. .	152
8.9	The scaled energy spectra measured by AGASA, Yakutsk, HiRes and TA(SD) reported at UHECR2012 Symposium [98]. The TA SD, HiRes and Auger are in agreement well within the systematic uncertainties.	153
8.10	The schematic view of the TALE experiment. The yellow circle shows newly constructed dense SDs, the red circle shows the SDs of TA. The green hexagon indicates the TALE FD at the same location of TA MD.	155
8.11	The comparison of effective area of UHECR observations: AGASA, Auger, TA SD and TA-2.	155
8.12	Overview of JEM-EUSO project [101].	156
A.1	The observed UHECRs : $E = 10^{19.77} \text{ eV}$, $X_{\max} = 796 \text{ g/cm}^2$.	161
A.2	The observed UHECRs : $E = 10^{19.75} \text{ eV}$, $X_{\max} = 758 \text{ g/cm}^2$.	161
A.3	The observed UHECRs : $E = 10^{19.67} \text{ eV}$, $X_{\max} = 743 \text{ g/cm}^2$.	162
A.4	The distribution of Energy between data and MC simulation under the standard cut. At the highest region, there is slightly difference caused by the assumption of spectrum index, $E^{-3.1}$. .	163

A.5	The distribution of the track length between data and MC simulation under the standard cut.	163
A.6	The distribution of the number of selected PMTs between data and MC simulation under standard cut. The result indicates the difference of physics model of the lateral density distribution of EAS. The observed lateral density distribution is wider than one expected from NKG function used in our software.	164
A.7	The distribution of the number of photo-electrons divided by track length between data and MC simulation under the standard cut.	164
A.8	The distribution of the number of selected PMTs divided by time extent between data and MC simulation under the standard cut.	165
A.9	The distribution of the impact parameter between data and MC simulation applied under the standard cut. At the highest region, there is slightly difference caused by the assumption of spectrum index, $E^{-3.1}$	165
A.10	The distribution of the angle on SDP between data and MC simulation applied under the standard cut.	166
A.11	The distribution of core location of West-East direction between data and MC under the standard cut.	166
A.12	The distribution of core location of South-North direction between data and MC simulation under the standard cut.	167
A.13	The distribution of zenith angle between data and MC simulation under the standard cut.	167
A.14	The distribution of azimuth angle between data and MC simulation under the standard cut.	168
A.15	The distribution of X_{start} between data and MC simulation under the standard cut.	168
A.16	The distribution of X_{end} between data and MC simulation under the standard cut.	169
A.17	The distribution of X_{max} between data and MC simulation under the standard cut. Since the discrepancy of difference between protons and irons is large, X_{max} is the most sensitive parameter to evaluate the mass composition of EASs.	169
A.18	The distribution of energy between data and MC simulation under the <i>fiducial volume cut</i> . At the highest region, there is slightly difference caused by the assumption of spectrum index, $E^{-3.1}$	170
A.19	The distribution of the track length between data and MC simulation under the <i>fiducial volume cut</i>	170
A.20	The distribution of the number of selected PMTs between data and MC simulation under the <i>fiducial volume cut</i> . The result indicates the difference of physics model of the lateral density distribution of EAS. The observed lateral density distribution is wider than one expected from NKG function used in our software.	171

A.21	The distribution of the number of photo-electrons divided by track length between data and MC simulation under the <i>fiducial volume cut</i>	171
A.22	The distribution of the number of selected PMTs divided by time extent between data and MC simulation under the <i>fiducial volume cut</i>	172
A.23	The distribution of the impact parameters between data and MC simulation under the <i>fiducial volume cut</i> . At the highest region, there is slightly difference caused by the assumption of spectrum index, $E^{-3.1}$	172
A.24	The distribution of the angle on SDP between data and MC simulation under the <i>fiducial volume cut</i> . The angle of $\Psi > 120$ are excluded because of Čerenkov contaminations.	173
A.25	The distribution of the core location of West-East direction between data and MC simulation under the <i>fiducial volume cut</i>	173
A.26	The distribution of the core location of South-North direction between data and MC simulation under the <i>fiducial volume cut</i>	174
A.27	The distribution of the zenith angle between data and MC simulation under the <i>fiducial volume cut</i> . The inclined shower is disappeared under the fiducial volume cut to avoid the acceptance bias of X_{\max}	174
A.28	The distribution of the azimuth angle between data and MC simulation under the <i>fiducial volume cut</i>	175
A.29	The distribution of X_{start} between data and MC simulation under the <i>fiducial volume cut</i> . We applied the selection rule as $150 \text{ g/cm}^2 < X_{\text{start}} < 700 \text{ g/cm}^2$	175
A.30	The distribution of X_{end} between data and MC simulation under the <i>fiducial volume cut</i> . We applied the selection rule as $900 \text{ g/cm}^2 < X_{\text{end}}$	176
A.31	The distribution of X_{\max} between data and MC simulation under the <i>fiducial volume cut</i> . Since the discrepancy of difference between protons and irons is large, X_{\max} is the most sensitive parameter to evaluate the mass composition of EASs.	176
A.32	X_{\max} distribution in several energy ranges compared with the expected distribution estimated from MC simulation for primary protons (red), irons (blue) or mixed compositions (pink) under the fiducial volume cuts. These figures are identical with the figures from Fig. 7.10to Fig. 7.14.	177

List of Tables

2.1	Efficiencies of fluorescence emissions relative intensity with wavelengths of 300 ~ 400 nm under a collisionless condition [60]. . .	24
4.1	Parameters of the U.S. standard atmosphere	76
4.2	Parameters of air shower simulation using CORSIKA.	76
5.1	The criteria for selecting the candidate PMTs in the 4th selection.	92
5.2	The criteria for judgment by the linear fitting in the 4th PMT selection.	93
7.1	The number of reconstructed EASs under both selection rules.	121
7.2	The total systematic uncertainty of energy and X_{\max}	143

Abbreviation

AGASA	Akeno Giant Air Shower Array
Auger	Pierre Auger Observatory
BRM	Black Rock Mesa (name of FD station)
CCD	Charge Coupled Device
C.L.	Confidence Level
CLF	Central Laser Facility (a center of TA site)
CMBR	Cosmic Microwave Background Radiation
CORSIKA	COsmic Ray SIMulations for KAscade
CRAYS	Calibration using RAYleigh Scattering
CTD	Central Trigger Distributor
EAS	Extensive Air Shower
ELS	Electron Light Source
FD	Fluorescence Detector
FVC	Fiducial Volume Cut
GH function	Gaisser-Hillas function
GPS	Global Positioning System
GZK cutoff	Greisen, Zatsepin and Kuzmin
HiRes	High Resolution Fly's Eye
IMC	Inverse Monte Carlo (reconstruction method)
ICRC	International Cosmic Ray Conference
ISS	International Space Station

- JEM-EUSO** Extreme Universe Space Observatory on board Japanese Experiment Module
- KS test** Kolmogorov-Smirnov test
- LIDAR** Light Detection And Ranging
- LR** Long Ridge (name of FD station)
- MC** Monte Carlo
- MD** Middle Drum (name of FD station)
- MPD** Muon Production Depth
- NKG function** Nakamura-Kamata-Greisen function
- NS** Neutron Star
- PMT** Photo-Multiplier Tube
- PPS** Pulse Per Second
- SD** Surface Detector
- SDP** Shower Detector Plane
- SDF** Signal Digitizer and Finder
- SN** SuperNova
- SSP** Spot Size Parameter
- TA** Telescope Array
- TALE** Telescope Array Low energy Extension
- TF** Track Finder
- UHE** Ultra-High Energy
- UHECR** Ultra-High Energy Cosmic Ray
- VAOD** Vertical Aerosol Optical Depth
- VCV catalog** The 12th edition of the catalog of quasars and active galactic nuclei by Véron-Cetty and Véron
- VEM** Vertical Equivalent Muon

Chapter 1

Introduction

In 1912, V.F.Hess discovered cosmic rays which are elementary particles or nuclei with relativistic kinetic energies in the universe. The energy spectrum of cosmic rays are measured in energies from 10^8 eV to beyond 10^{20} eV in this recent one hundred. Since a power-law index of the energy spectrum is about -3, ultra-high energy cosmic rays (UHECRs) exceeding $10^{19.5}$ eV on the ground are very rare events, and the event rate is about once per century within an ground area of 1 km^2 . Because UHECRs are the most energetic elementary particles on record, we believe that their origins are related with energetic astronomical phenomena or other exotic phenomena, for example decays or annihilations of super heavy relic particles created at early phase of the development of the universe. Therefore, search for origins of UHECRs and revealing their acceleration mechanisms are one of the most exciting and important subjects in the research field covering astrophysics, cosmology and elementary particle physics.

Moreover, if assumed UHECRs are pure protons, the cosmic microwave background radiation (CMBR) interacts with UHE protons via pion productions, and the mean free path for the UHE protons becomes short. As a result, the energy spectrum above $10^{19.5}$ eV leads to be suppressed, and the phenomenon is called as GZK cutoff. Additionally, scientists suggest cosmic rays with energies of $10^{18.7}$ eV are expected to interact with CMBR through pair creations of electrons and positrons, or to be the transition from galactic to extra-galactic sources. To conclude these models, measurements of the mass composition and the energy spectrum with broad energies are essential.

In order to observe UHECRs, Telescope Array (TA) experiment has been constructed in the desert in the Utah State of USA, with the collaboration of scientists from Japan, USA, Korea, Russia and Belgium and it has been started with full operations in 2008. The TA consists of an array of 507 surface detectors (SDs) deployed 1.2 km separation covering with 700 km^2 ground area and of three stations of fluorescence detectors (FDs) looking inward over the array. The one station located north is transported from HiRes-I and II experiment, and the other two stations located south-east and south-west

are newly constructed for the TA experiment. In total, we have 38 fluorescence telescopes for FDs. The TA experiment observes UHECRs using two air shower detection techniques independently and simultaneously.

When a cosmic ray enters Earth’s atmosphere, a huge number of secondary particles are generated via hadronic and electromagnetic interactions with atmospheric nuclei, and this swarm of secondary particles is called extensive air shower (EAS) shown in Fig. 1.1.

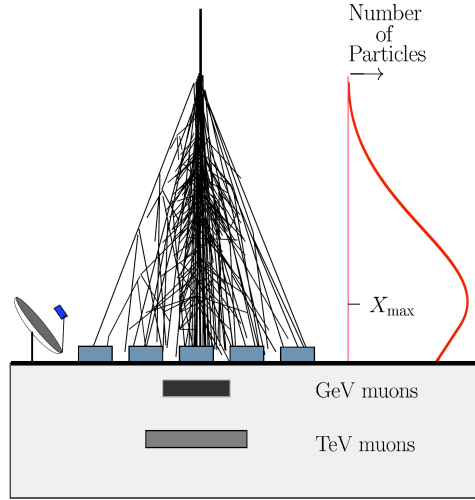


Figure 1.1: A schematic views of an extensive air shower (EAS) and its X_{\max} .

The SD array detects EAS’s particle densities and arrival times on SDs. On the other hand the FD telescopes detect air fluorescence photons emitted by atmospheric molecules excited by EAS particles. A simulation-independent determination of primary energies provided by FD observations gives an advantage on this technique, because FDs measure the energy deposit to the atmosphere through energy losses by electro-magnetic particles which are dominant in EAS and less dependent of hadron interaction models.

In this thesis, the author reports a development of a set of data analysis code for FDs which means an observation by only single FD station, and a new method for the shower profile determination, called “Inverse Monte Carlo (IMC)”, and evaluate a performance of this monocular analysis procedure and an aperture of FDs through analyzing Monte Carlo (MC) simulated events. In order to measure the mass composition of UHECRs, the maximum depth of EAS’s longitudinal development (X_{\max}) is an important parameter, because it depends on the primary mass composition of UHECRs. Since the TA FDs have a limited field of view in elevation ranging from about 3° to 33° , the limitation makes on observational bias in the distribution of X_{\max} from the observed showers. However, we can establish un-biased X_{\max} distribution applying a

sophisticated event selection, called fiducial volume cuts [67], and the resulted un-biased X_{\max} distribution is useful for comparing with MC simulated ones. To apply this selection in our analysis, the author determined selection conditions and confirmed the efficiency with MC. Moreover, our analysis procedure was confirmed through cross-checking with the other independently developed software.

The data collected by newly constructed two station of TA FD from January 2008 to September 2011 are analyzed in monocular mode by our developed software, and we finally obtain more than twenty thousand EASs. As further enhancement of our reliability in our analysis, the author confirmed that distributions of several parameters, such as an impact parameter and core position distribution, are reasonable agreement between data and MC simulation. After that, the author evaluated the mass composition through a comparison between observed average X_{\max} values and those of MC predictions for primary protons and irons. Moreover the author calculated the averaged X_{\max} measurement applied *without* the fiducial volume cuts in both data and MC to study the dependence of the fiducial volume cuts in the X_{\max} technique.

As a result, the observed X_{\max} indicates there is a transition of the dominated components from heavy to light nuclei from $10^{17.5}$ eV to $10^{18.5}$ eV, and protons are dominant above $10^{18.5}$ eV. The mass composition results without the fiducial volume cuts are consistent with those with the fiducial volume cuts, because the MC predicted lines without the fiducial volume cuts are shifted as same as measured data. Thus, we conclude that the estimated mass composition result and its energy dependence are independent of the fiducial volume cuts.

Moreover, the author measured an energy spectrum with broad energies above $10^{17.5}$ eV from observed number spectra, apertures and observation times of newly constructed two stations. The obtained energy spectrum is good agreement with the result of the TA surface detectors and Middle Drum fluorescence detectors which are transported from the HiRes experiment.

In this thesis, Chapter 2 is an review of UHECR physics, detection techniques and latest results. In Chapter 3, details of the TA experiment are explained. The detailed MC simulations and reconstruction method used here are described in Chapter 4 and 5, respectively. Systematic errors, apertures and expected X_{\max} distributions are evaluated with reconstructing and analyzing MC events, and the results are shown in Chapter 6. The result for the data of 3.7 year observations is shown in Chapter 7. Chapter 8 and 9 are discussion and conclusions.

Chapter 2

Ultra-High Energy Cosmic Rays

2.1 Overview of UHECR Physics

In a research field of ultra-high energy cosmic rays (UHECRs) physics, there are three important measurements : the energy spectrum, the mass composition and the anisotropy of UHECRs. In this chapter, we discuss not only recent results of their observations, but also a history of cosmic ray measurements, theoretic models of acceleration mechanism and detection techniques of UHECRs.

In Sec. 2.2 we discuss a history of cosmic ray physics and acceleration mechanism with energies less than 10^{15} eV. The possible origin models of UHECRs are shown in Sec. 2.3. We induct methods and techniques to observe UHECRs by extensive air showers in Sec. 2.4. In Sec. 2.6, we discuss the latest results and mysteries of UHECRs.

2.2 Cosmic Rays

Cosmic rays are high energy particles traveling in the universe and large amount of cosmic rays are continuously entering the Earth's atmosphere. In 1912 V.F.Hess carried out balloon flight measurements as high as 5 km above the ground to measure levels of ionizing radiation [1]. This was a clear evidence of the fact that sources of the ionizing radiations must be located above the atmosphere. Before this discovery, people believed that all the high energy particles are emitted from radioactive isotopes in the air, on and under the ground. Ionizing radiations from the universe are called "Cosmic Rays", due to the achievement, V.F.Hess were award the Nobel Prize in 1936.

In 1930, the East-West effect, flux asymmetry, because of the terrestrial magnetic field was found so then it was clear that the major component of cosmic rays are not neutral particles, but charged particles. In 1932, the electron and positron pair creation was discovered in the cloud chamber. Strong

penetrating particles called muon meson were discovered in 1937. In 1941, with a balloon measurement, cosmic rays consist of several nuclei groups, such as proton, boron, carbon, nitrogen and iron. Recent measurements show cosmic ray consists of 90% of proton, 9% of α particles and heavy nuclei.

2.2.1 Energy Spectrum

Around 1945, scientists have started to measure the energy spectrum of cosmic rays. The observed energy spectrum in the range from 10^8 eV to 10^{21} eV is shown in Fig. 2.1. In the energy range above 10^{11} eV, cosmic rays flux is not affected by the solar activity, the spectrum follows the power-law structure of $dN/dE \propto E^{-\gamma}$. The index value is $\gamma \sim 2.7$ up to 10^{15} eV, and it changed $\gamma \sim 3.0$ above 10^{15} eV. Again the spectrum becomes hardened $\gamma \sim 2.7$ above 10^{19} eV. The two broken on the spectrum are, in order of increasing energy, called “knee” and “ankle”. At the highest energy around 10^{20} eV, cosmic ray flux reaches quite low, once per year on 100 km^2 area, then a huge effective area and a large exposure are essential to measure cosmic rays with such energies.

One idea to explain the spectral break at the knee is based on the difference of acceleration mechanisms below and above the knee energy. There is another theory for the knee to be explained by the cosmic ray’s leakage from the galaxy. For cosmic ray protons of 10^{15} eV the Larmor radius is 0.3 pc in the galactic magnetic field of $3 \mu\text{G}$. This is smaller than the galactic disk thickness, but above this energy the confinement in the galaxy by the diffusion dynamics becomes less efficient to confine cosmic rays.

There are two models for cosmic rays at the ankle energy. In one model the ankle structure reflects the transition from galactic to extragalactic origins with increasing energy. Since the Larmor radius is larger than the radius of the galaxy above the ankle energy, the confinement with magnetic field is not efficient. If this model is correct, we expect to observe that anisotropy of arrival directions and the chemical composition change at ankle energy.

On the other hand, in the other model the ankle is due to cosmic ray flux decreasing by energy loss. The interaction of pair creations $p\gamma \rightarrow pe^+e^-$ between cosmic rays protons and 3 K Cosmic Microwave Background Radiation (CMBR) is opened at around the ankle energy. The origin should have already changed the outer-galaxy before the ankle region. Thus, the mass composition remains the proton across the ankle energy. In this case, this would give an increasingly light composition associated with $10^{17.5}$ eV, called “2nd knee”. Therefore, to conclude the ankle model, it is important to observe the mass composition measurement at these energy.

2.2.2 Acceleration Mechanism

The studies of cosmic-ray acceleration mechanisms are not understood very well. In general, the acceleration mechanism should produce cosmic ray flux following the power-law spectrum, described before.

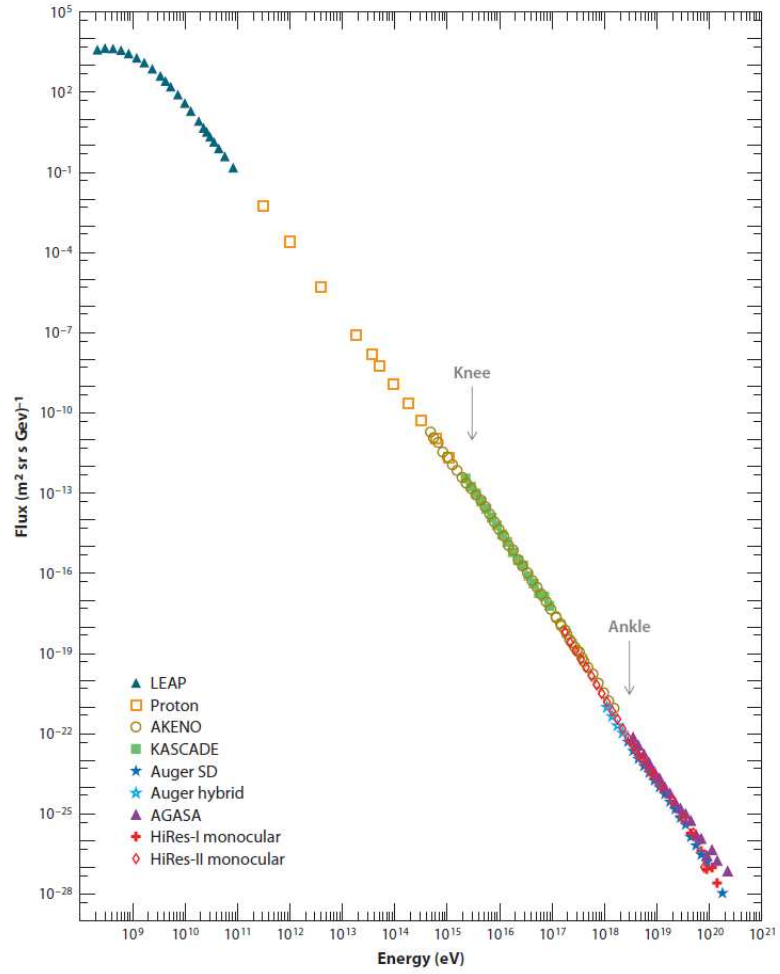


Figure 2.1: Overview of the cosmic ray spectrum. Approximate energies of the two breaks commonly referred to as knee and the ankle are indicated by arrows. Data are from LEAP [7], Proton [8], AKENO [9], KASCADE [10], Auger surface array [11], Auger hybrid [12], AGASA [44], HiRes-I Monocular [50], HiRes-II Monocular [50].

Fermi Acceleration

The Fermi acceleration mechanism was proposed by E.Fermi in 1949, which is a model of the statistical acceleration of charged particles which gain large kinetic energies repeatedly interacting with molecular clouds. In this model, although directions of the interaction is statistical random, the averaged energy gain per encounter is positive. This value is proportional to its energy, $\Delta E = \alpha E$. Since α is proportional to square of the velocity of the cloud, this acceleration are called "2nd Fermi acceleration".

Cosmic rays are also accelerated by a plasma termination shock. Based on a geometry of the shock, the plasma acceleration is superior to 2nd Fermi acceleration. In this case, α is proportional to a velocity of the shock wave considering a structure of the acceleration region, called 1st Fermi acceleration. Then, if $\Delta E = \alpha E$ per encounter, after n encounters,

$$E_n = E_0 (1 + \alpha)^n \quad (2.1)$$

where E_0 is the energy at injection of the acceleration. The number of encounters n needed to reach an energy E ,

$$n = \frac{\ln(E/E_0)}{\ln(1 + \alpha)}. \quad (2.2)$$

If the probability of escape from the acceleration region is P_{esc} per encounter, then the probability of remaining in the acceleration region after n is $(1 - P_{\text{esc}})^n$. Thus, the proportion of particles accelerated to energies greater than E is

$$N(\geq E) \propto \sum_{m=n}^{\infty} (1 - P_{\text{esc}})^m = \frac{(1 - P_{\text{esc}})^n}{P_{\text{esc}}}, \quad (2.3)$$

with n given by (2.2). Substitution of (2.2) into (2.3) gives,

$$N(\geq E) \propto \frac{1}{P_{\text{esc}}} \frac{E^{-\gamma}}{E_0^{-\gamma}}, \quad (2.4)$$

with

$$\gamma = \frac{\ln[(1 - P_{\text{esc}})^{-1}]}{\ln(1 + \alpha)} \approx \frac{P_{\text{esc}}}{\alpha}. \quad (2.5)$$

Thus, the Fermi mechanism naturally leads to a desired power law spectrum.

Supernova blast wave

Ejected materials from a supernova (SN) explosion spread out through the interstellar medium driving a shock wave at which acceleration can occur. Here we express the diffusion coefficient and its velocity in D and u , respectively, as long as the characteristic length for diffusion in the plasma, D/u , is much less than the radius of curvature of the shock, the plane shock approximation can be used. The life time of the SN blast wave is estimated as the time for

taking the expanding shell to sweep out interstellar medium of its own mass. For shell of $10 M_{\odot}$, expanding at mean velocity of 5×10^8 cm/sec into the interstellar medium with average density of 1 proton/cm³, and then the life time is $T_A \sim 1000$ yrs and the shell size reaches 5 pc.

The finite lifetime of SN blast wave as a strong shock also limits the maximum energy per particle that can be achieved with 1st order Fermi acceleration mechanism. The acceleration rate is written as

$$\frac{dE}{dt} = \frac{\alpha E}{T_{\text{cycle}}}, \quad (2.6)$$

with the characteristic time for a single back and forth acceleration cycle, T_{cycle} . For the estimation of E_{max} with integrating (2.6), we need to know T_{cycle} .

Firstly, let's consider the upstream region. The particle current with the convection is given by

$$\mathbf{J} = -D\Delta N + \mathbf{u}N. \quad (2.7)$$

In the upstream region the fluid velocity \mathbf{u}_1 is negative relative to the shock front, and there is no net current in equilibrium,

$$D_1 \frac{dN}{dz} = -u_1 N. \quad (2.8)$$

Then in the upstream region

$$N(z) = \rho_{\text{cr}} \exp(-zu_1/D_1), \quad (2.9)$$

where ρ_{cr} is the number density of cosmic rays at the shock. The total number of particles per unit area in the upstream region is $\rho_{\text{cr}} D_1/u_1$. The particle crossing rate per unit area on the shock plane is $\rho_{\text{cr}} c/4$. Thus the mean residence time of a particle in the upstream region is

$$(\rho_{\text{cr}} D_1/u_1) (\rho_{\text{cr}} c/4)^{-1} = 4D_1/(u_1 c). \quad (2.10)$$

The downstream region is somewhat more complicated to analyze because it is necessary to average the residence time only over those particles that do not escape. The analysis is straightforward and is shown explicitly by Drury [16]. The mean residence time in downstream region is identical with that in the upstream region, $4D_2/(c u_2)$, where u_2 is the fluid velocity in the downstream region. Thus,

$$T_{\text{cycle}} = \frac{4}{c} \left(\frac{D_1}{u_1} + \frac{D_2}{u_2} \right). \quad (2.11)$$

Next, we need to estimate the diffusion coefficient. Lagage and Cesarsky argue the the diffusion length of charged particles, λ_D , cannot be smaller than its Larmor radius, r_L [17]. The Larmor radius is given by

$$r_L = \frac{p}{ZeB} \quad (2.12)$$

where e is the elementary charge, Z is the charge of the particle, p is its total momentum and B is the magnetic field strength. Then the minimum diffusion coefficient D_{\min} is calculated from r_L as

$$D_{\min} = \frac{r_L c}{3} \sim \frac{1}{3} \frac{E c}{Z e B}. \quad (2.13)$$

Here, $T_{\text{cycle}} \geq 20E/(3u_1 Z e B)$ for a strong shock with $u_2 = u_1/4$. Substituted to $D_1 = D_2 = D_{\min}$, the maximum energy of the nucleus being accelerated, E_{\max} ,

$$E_{\max} \leq \frac{3}{20} \frac{u_1}{c} Z e B (u_1 T_A). \quad (2.14)$$

For SN which ejects $10M_{\odot}$ at 5×10^8 cm/sec during $T_A \sim 1000$ years, into a interstellar medium with the density of one proton per cubic centimeter, and with the galactic magnetic field of $3 \mu\text{G}$, the maximum energy reaches

$$E_{\max} \leq Z \times 3 \times 10^{13} \text{eV}. \quad (2.15)$$

Therefore, cosmic rays can be accelerated by the SN blast shock up to only 10^{15} eV.

2.3 Ultra-High Energy Cosmic Rays

In the field of cosmic ray physics, one of the most interesting topics is ultra-high energy cosmic rays (UHECRs). UHECRs are the most energetic particles, above 10^{19} eV, in the universe. Here, I briefly describe and discuss theoretical predictions about propagations and origins of UHECRs, and also introduce related unsolved problems about UHECR physics.

2.3.1 GZK Cutoff

In 1963, as soon as Cosmic Microwave Background Radiation (CMBR) was discovered, Greisen, Zatsepin and Kuzmin pointed out that this relic photons make the universe opaque for cosmic rays with sufficiently high energies [13] [14]. Since UHECRs have large Lorentz factors, energies of CMBR photons ($\sim 10^{-3}$ eV) are converted very high energies, 100 MeV, in the rest frame of the cosmic rays. The interaction of proton at rest with CMBR of such high energy usually excites the protons to nucleon resonance condition. Since the resonance decays with emitting pion through the following process, the proton energy decreased.

$$\gamma(\sim 300\text{MeV}) + p \rightarrow \Delta(1232) \rightarrow p + \pi^0, n + \pi^+ \quad (2.16)$$

The pair creation with CMBR photons ($\gamma p \rightarrow p e^+ e^-$) can also occur for protons above $10^{18.5}$ eV

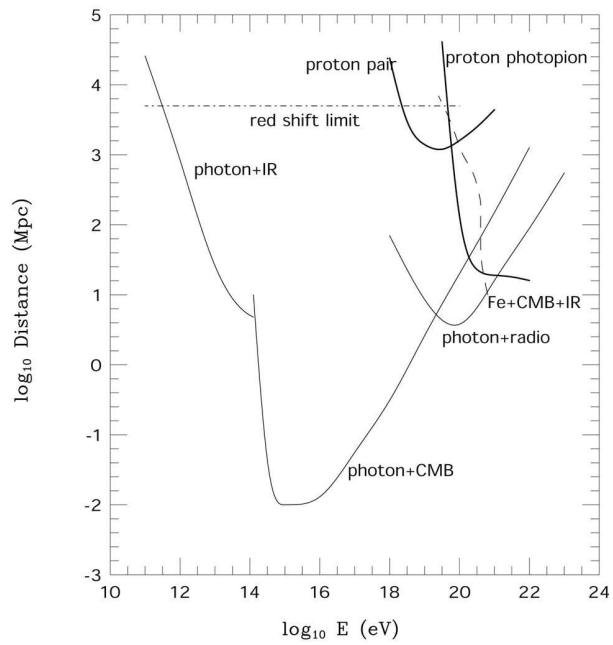


Figure 2.2: Attenuation lengths of UHECR particles. The thick solid lines shows attenuation lengths for UHE protons, the thin solid lines are for UHE photons and the dotted line is for UHE iron nuclei.

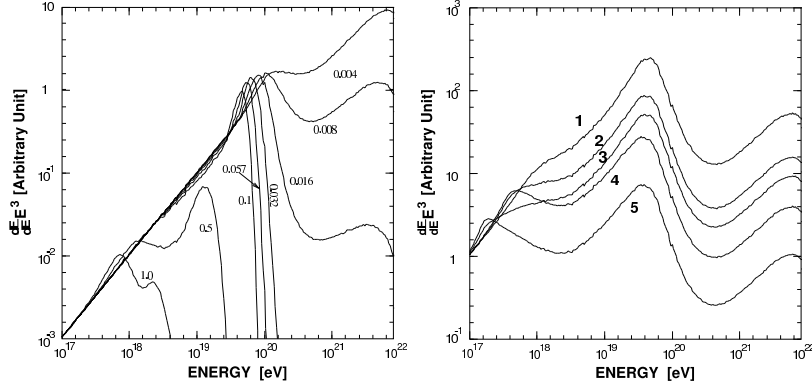


Figure 2.3: Expected energy spectra of UHE protons [13] [14]. The left figure shows the expected spectra from a single source of several different red shift ($z = 0.004 \sim 1.0$). The right figure shows expected energy spectra assuming uniform source distribution with with different source evolution models.

Fig. 2.2 shows attenuation lengths of UHECRs simulated by propagations of several types of charged particles in CMBR. In this Figure, attenuation length of protons above 10^{20} eV is less than 50 Mpc. Thus, protons above 10^{20} eV observed on the Earth must have their origin within 50 Mpc from the Earth. UHE protons which are ejected at origins more than about 50 Mpc from the Earth with primary energies of more than 10^{20} eV reduce their own energies through the interactions with CMBR. So then, at the Earth these protons are detected as more lower energy protons.

However, if there is a violation of relativity at ultra-high energies, the GZK mechanism is absent [27]. That's why anyone could not confirm the validity of the relativity at the energy range with Lorentz factor above $\gamma \geq 10^{11}$.

Fig. 2.3 shows expected energy spectra using a several type of the source model of cosmic rays. For example, if it is assumed that UHECR sources are uniformly distributed on the universe, the energy spectrum must have the cutoff structure at about 4×10^{19} eV, called GZK cutoff. Therefore, detailed measurements of energy spectrum to reveal its structure give us the most important hint for identifying origins of UHECRs.

If cosmic rays are not protons rather than heavier nuclei, another interaction, photo-disintegration process, should be considered during their propagations in CMBR field [15]. Heavy nuclei with energies more than 2×10^{19} eV lose 3-4 nucleons per 1 Mpc travel. Thus, if UHECRs consisted of heavy nuclei, the origins for nuclei at high energy end is within 20 Mpc from the Earth. With the same reason, if the origins of UHE nuclei existed uniformly in the universe, the observed energy spectrum would have a sharp cutoff at a certain energy. Fig. 2.4 shows the propagated spectrum with the assumption of the two component model, which has the suppression structure above $10^{19.5}$

eV [15].

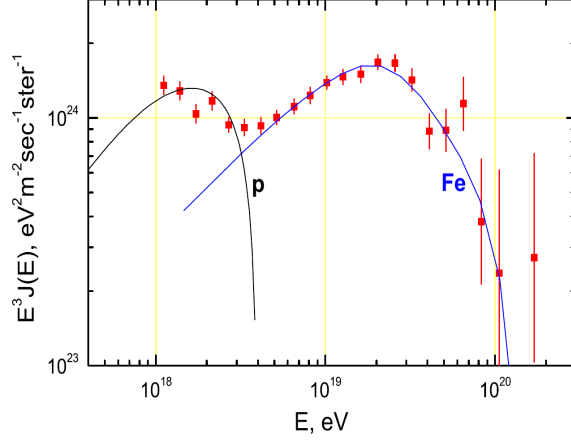


Figure 2.4: UHECR spectrum to be expected from a two component model, where UHECRs consist of protons and iron nuclei and they are accelerated with a statistical process, with assumptions that, the injection power law index is $\gamma_g = 2.0$ and the maximum energy is $E_{max} = 4Z \times 10^{18}$ eV. The data plot of energy spectrum is measured by Auger [15].

2.3.2 Candidates of CR Origins

Origins of UHECRs are still unknown. There are two different types of proposed models for explanation of the existence of UHECRs. One type is called the “bottom-up model”, and the other is called “top-down model”.

Bottom-up Model

The bottom-up model describes that UHECRs originate from lower energy, and they gain their energies with repeating acceleration processes, such as Fermi accelerations. Then, finally their energies reach ultra-high energies of larger than 10^{20} eV when they escape from the acceleration regions. The upper limit of accelerated energy E_{max} is expressed as,

$$E_{max} \leq \gamma e Z B R, \quad (2.17)$$

where γ is the Lorentz factor of a shock wave, Z is the atomic number of a cosmic ray, B is the magnetic field on the acceleration region and R is the size of the region. Fig. 2.5 is the Hillas plot, which shows the relations between strength of the magnetic field strength and the scale of astronomical objects which have each maximum acceleration energy [59]. From Fig. 2.5, it is clearly shown that most objects in our galaxy are not candidates of UHECR sources

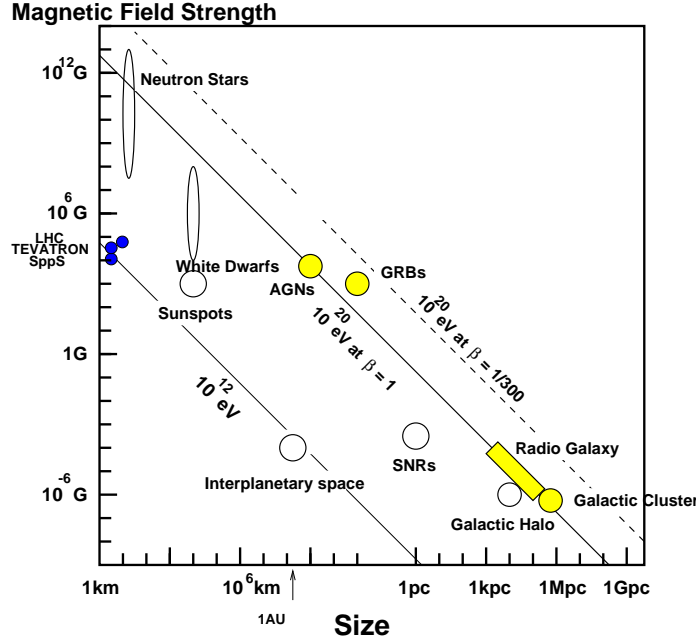


Figure 2.5: The Hillas plot, a relation between magnetic field strengths and scales of astronomical objects. The solid and dashed lines show the maximum energies by statistical accelerations estimated by (2.17) [59].

expect for gamma-ray bursts and neutron stars. Source candidates located outside of our galaxy are active galactic nuclei, gamma-ray bursts, radio galaxies and galactic clusters.

Here, I summarize discussions about possibilities as UHECR sources for several types of astronomical objects.

- Neutron stars : Since a typical neutron star has strong magnetic fields with strength of more than 10^{13} G, iron nuclei could be accelerated up to 10^{20} eV if they did not suffer any efficient energy loss processes [18]. However, If in the magnetic fields 10^{13} G, the energy loss via synchrotron radiations is not negligible. In fact, cosmic rays cannot be accelerated to ultra-high energy. The energy loss rate via synchrotron radiations depends on magnetic field strength, so then depends on the distance from the neutron star surface. If acceleration regions are apart more than 10^9 cm from the surface, any nuclei can escape without suffering large energy losses [19].

This model predicts most UHECR origins exist inside our galaxy. Moreover it also predicts particles accelerated by neutron stars consist largely of heavy nuclei, so then the mass composition and anisotropy measurements are very important for confirmation of the model.

- Active galactic nuclei (AGN) : AGN is an astronomical system which consists of a super heavy rotating black hole and accretion disk, and in the system gravitational potential energies are converted to kinetic energies of matters, heat of the disk and magnetic field energies, and then finally they are emitted as radiations and outflows of magnetized plasma particles [20]. Charged particles are accelerated by the electric fields induced by rotating magnetic fields. The maximum acceleration energy of AGN is limited at 10^{19} eV, because charged particles suffer energy losses through the interactions with radiation fields [21].
- Radio lobes : Radio lobes are normally accompanied by AGN, and they are emission regions of charged particles accelerated and excited by termination shocks of jets with intergalactic matter. The typical size of radio lobes is 100 kpc [20]. In a radio lobe, the radio hot spot, which is emitting radiations with higher radio intensity than other lobe region, is usually seen, and this hot spot region is expected to have a strong magnetic fields enough to confine charged particles accelerated to ultra-high energies [22].
However, AGN with the hot spots are very rare and usually exist far from the earth. Moreover, it is found that the positions of hot spot AGN do not agree with the observed UHECR arrival direction distribution. If we assumed that M87, which is 18.4 Mpc away, is a UHECR source, the arrival direction of UHECRs would have a clearly anisotropy concentrating toward the object. The next nearest candidate NGC315, which is 100 Mpc away, is too far from the earth beyond GZK horizon for UHECRs to reach us.
- Gamma-ray bursts (GRB) : The GRB are also promising candidates of UHECR accelerators. The average rate of energy release rate as gamma-rays by GRBs is comparable to that by sources UHECRs with energies above 10^{19} eV, 10^{44} ergs $\text{Mpc}^{-3} \text{yr}^{-1}$ [23]. Since for highest energy UHECRs sources are required to exist within GZK horizon of about 50 Mpc, and the rate of GRBs is 1 per 100 years in such volume, the arrival direction distribution would have a strong anisotropy for highest energy UHECRs.
- Galactic clusters : The spatial size of the typical cluster is about 500 kpc, and the typical magnetic field strength is estimated to be $0.1 \mu\text{G}$. So then the maximum acceleration energy can reach 10^{20} eV from the relation of (2.17) [24]. However, propagating to the earth for a long distance, accelerated UHECRs suffers effective energy losses via GZK mechanism because the distance from the earth is longer than any other candidates.

Top-down Model

In contract to the bottom-up models, top-down models are associated with the new physics beyond the standard model, for instance, the existence of super

heavy relic particles or topological defects.

- Topological defects and annihilations of super heavy particles : In these models, UHECR sources are hypothetical particles of topological defects which are expected to be generated at beginning of the universe. Decays or annihilations of super heavy particles or high density topological defects can induce cascades of UHE particles [25].

Topological defects are expected to decay to super heavy gauge bosons or Higgs bosons. Succeeding hadron jet induced by these particles decay to gamma-rays, electrons and neutrinos with only a few percent of nucleons. When these contribution effects the spectrum beyond the GZK cutoff, a transition of mass composition is expected at GZK energy, 4×10^{19} eV because the UHE protons with this energies suffer effective ionization losses. Thus, the topological defect scenario suggests that proton is the dominate component in energy region less than GZK energy and gamma-rays are dominant above this energy.

When the super heavy relic particles are rich abundance at galactic halo, the mass composition is not changed as a function of energy, because of enough short distance to avoid the GZK mechanism.

- Z-burst model : In Z-burst model, UHECRs are generated via interactions between UHE neutrinos and cosmic background relic neutrinos [26]. In general, these interactions via the decay of Z^0 products UHE photons.

2.4 Extensive Air Shower

As discussed in Sec. 2.2, since the flux of cosmic rays follows E^{-3} , there are the thirty orders of magnitude difference for fluxes between 10^9 eV and 10^{20} eV. In less than 10^{14} eV, the relative low energy cosmic rays are observed by direct measurements with balloons and satellite measurements. However, the higher energy cosmic rays is very rare, so that we need the enough large effective area and exposure to measure UHECRs. Thus, it is difficult to observed UHECRs by direct measurements. Then, we measure extensive air showers in which the huge numbers of secondary particles are generated via interactions between primary cosmic rays and the atmospheric nuclei.

2.4.1 Air Shower Cascades

When a primary cosmic ray proton or a nucleus enters the earth's atmosphere, it interacts with a nucleus in the air (nitrogen, oxygen, etc) and generates secondary particles. The each generated particles also interacts with a nucleus and generated the huge numbers of secondary particles. Repeating this interactions, the phenomena in which many secondary particles are generated by primary cosmic rays is called extensive air showers (EAS). In general, an extensive air shower consists of the electromagnetic cascades and hadron cascades.

Electromagnetic Cascades

The electromagnetic cascades are the result of a series of electromagnetic interactions of electrons and photons with atmosphere. Electrons and positrons are created from high energy gamma-rays. Gamma-rays are emitted via bremsstrahlung from electrons and positrons. Bremsstrahlung is a process by which a high energy electron emits a photon when a photon interacts with the electromagnetic field of the nucleus in the medium. The cross section of bremsstrahlung for a electron, $\sigma_{\text{brems.}}$, with E provides

$$\sigma_{\text{brems.}}(E, v)dv = \frac{4Z^2 r_e^2}{137} \frac{dv}{v} \left[\left(1 + (1-v)^2 - \frac{2}{3}(1-v) \right) \ln \left(184Z^{-\frac{1}{3}} \right) + \frac{1}{9}(1-v) \right] \quad (2.18)$$

where $v = h\nu/E$, Z is the atomic number of the target, r_e is the classical electron radius. Thus, the energy loss $(dE/dX)_{\text{brems.}}$ per a atmospheric depth is

$$\left(\frac{dE}{dX} \right)_{\text{brems.}} \simeq -\frac{E}{X_0}, \quad (2.19)$$

where X_0 is the radiation length, it defined as

$$\frac{1}{X_0} = \frac{4Z^2 r_e^2}{137} \frac{N}{A} \ln \left(184Z^{-\frac{1}{3}} \right) \quad (2.20)$$

where N is Avogadro's number, A is the atomic mass number of the target. In the air, X_0 is approximately 38 g/cm².

Then, the cross section of electron-positron pair creation, σ_{pp} , is

$$\sigma_{\text{pp}}(h\nu, u)du = \frac{4Z^2 r_e^2}{137} du \left[\left(u^2 + (1-u)^2 - \frac{2}{3}(1-u) \right) \ln \left(184Z^{-\frac{1}{3}} \right) + \frac{1}{9}(1-u) \right], \quad (2.21)$$

where, $u = E/h\nu$ and E are energies of a generated electron. The interaction length of pair creation is calculated from σ_{pp} ,

$$\left(\frac{dE}{dX} \right)_{\text{pair}} \simeq -\frac{7}{9} \frac{E}{X_0}. \quad (2.22)$$

Therefore, the interaction lengths of a pair creation and a bremsstrahlung are almost similar. Thus, primary cosmic rays create more and more electrons, positrons and photons propagating down in the atmosphere. Through interactions, their numbers increase while their energies decrease. The resulting avalanche of electrons and photons are called electromagnetic cascades or electromagnetic showers. While secondary particles decreases their own energies, ionization losses are dominant. Since low energy charged particles are captured by the atmosphere, the total number of particles decreases. The critical energy of electrons is 84 MeV in the air.

When hadrons, which major component of cosmic rays are interacted with atmospheric nuclei, the multiple productions of hadrons, pions and Kaons are

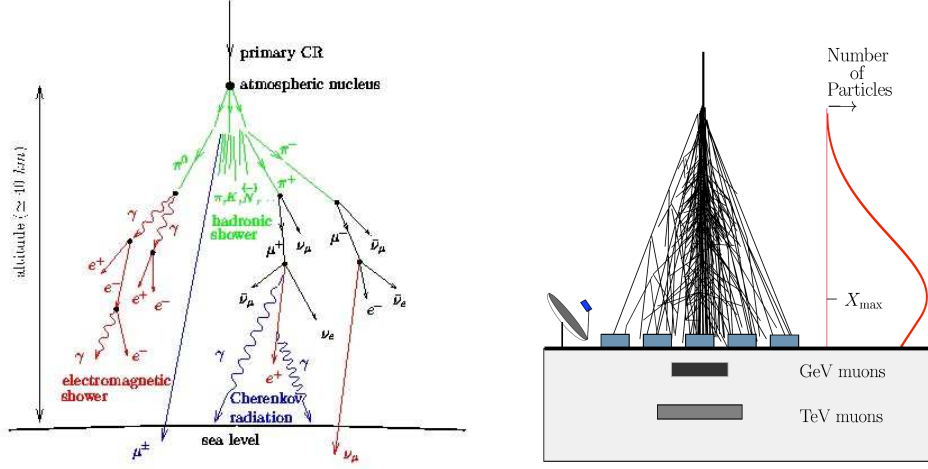


Figure 2.6: Schematic views of an extensive air shower.

happened. Most of secondary particles are pions. π^0 is shortly decay with the life time of 8.4×10^{-17} sec into two gamma-rays which generate electromagnetic cascades. The decay mode of π^\pm is

$$\pi^+ \rightarrow \mu^+ + \nu_\mu \quad (2.23)$$

$$\pi^- \rightarrow \mu^- + \bar{\nu}_\mu \quad (2.24)$$

$$(2.25)$$

with the life time of $\tau = 2.60 \times 10^{-8}$ sec, μ^\pm is also decay with the life time of $\tau = 2.20 \times 10^{-6}$ sec, with modes of

$$\mu^+ \rightarrow e^+ + \bar{\nu}_\mu + \nu_e \quad (2.26)$$

$$\mu^- \rightarrow e^- + \nu_\mu + \bar{\nu}_e. \quad (2.27)$$

Hadrons induce nuclear cascades. Since the atmospheric depth is 10 times larger than the mean free path of hadron multiple productions or 25 times larger than the radiation length of electrons. As the result, the huge number of particles are generated through the hadronic interactions and electromagnetic interactions. Fig. 2.6 shows a schematic vies of extensive air showers.

2.4.2 Characteristic Parameters of EAS

Longitudinal Development of EAS

While the huge number of secondary particles are created, energies per particles are smaller. When EAS particles have less than critical energies E_{cri} , $E_{\text{cri}} = 84$ MeV in the air, their energies are lost and absorbed through energy losses without generating secondary particles. As the result, the total number of

particles in EAS are decreased. The increase and decrease of the number of particles as a function of slant depth is called longitudinal development.

When a gamma-ray with an energy of E_0 enters the atmosphere, a longitudinal development is described as,

$$N_e(t) \sim \frac{0.31}{\sqrt{y}} \exp \left[t \left(1 - \frac{3}{2} \ln s \right) \right] \quad (2.28)$$

$$y = \ln \left(\frac{E_0}{E_{\text{cri}}} \right) \quad (2.29)$$

$$s = \frac{3t}{t + 2y} \quad (2.30)$$

where t is a unit of radiation length in the air 38 g/cm^2 , s is the shower age parameter represented a level of shower longitudinal development. The shower age parameter indicates $s = 1$ at the maximum development.

Longitudinal developments of EAS are described by Gaisser and Hillas as

$$N_e(X) = N_{\text{max}} \left(\frac{X - X_0}{X_{\text{max}} - X_0} \right)^{\frac{X_{\text{max}} - X_0}{\lambda}} \exp \left(\frac{X_{\text{max}} - X}{\lambda} \right) \quad (2.31)$$

where N_{max} is the number of particles at the maximum development, X_{max} g/cm^2 is the slant depth at the maximum development, X_0 is the first interaction point and λ is the attenuation length, typically $\lambda = 70 \text{ g/cm}^2$.

N_{max} approximately corresponds to the primary energy, $N_{\text{max}} \sim 2 \times E_0 \times 10^{-9}$, where E_0 is the primary energy. At an identical energy, the difference of mass composition appears a first interaction point, X_0 , and a slant depth at the maximum of a longitudinal development, X_{max} . X_0 of heavier nuclei are smaller than those of protons, because they have bigger cross sections and start interactions at higher altitude. Since iron nuclei consists of 56 nuclei, the energy per nucleon of heavier nuclei is smaller than the same energy of proton. Since X_{max} is roughly proportional to an energy, averaged X_{max} values of heavier nuclei are also smaller than those of protons with an identical energy.

In a toy model, $X_{\text{max}} \propto \ln(E_0/A)$, where A is atomic mass number. Fig. 2.7 shows the longitudinal development simulated protons and irons EAS.

Lateral Density Distribution of EAS

A particle distribution spread on a plane perpendicular to an arrival direction of EAS is called a lateral density distribution. The lateral density distribution of electromagnetic cascades are analytically-calculated and approximated by Nishimura-Kamata-Greisen(NKG) function, as follows,

$$f(r, s) = C(s) \left(\frac{r}{r_M} \right)^{s-2} \left(\frac{r}{r_M} + 1 \right)^{s-4.5}, \quad (2.32)$$

$$\rho(r, s) = \frac{N_e f(r, s)}{r_M^2}, \quad (2.33)$$

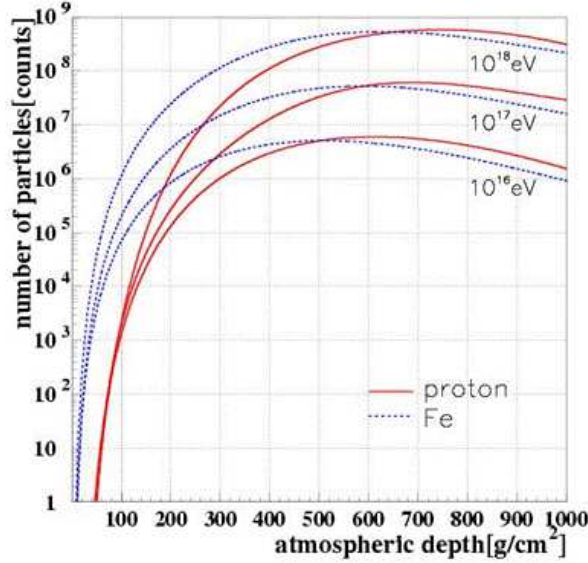


Figure 2.7: Longitudinal developments of protons and irons for a EAS simulation.

where r is a distance from a shower core of EASs, $C(s)$ is a normalization factor, N_e is the total number of secondary particles, r_M is a Molière unit, which is the characteristic unit of length in a high energy electron scattering. r_M is defined as

$$r_M = X_0 \frac{E_{\text{scatt}}}{E_c} \text{ [g/cm}^2\text{]} \quad (2.34)$$

where E_{scatt} is a constant called the scattering energy (21.2 MeV) and X_0 is the radiation length of the medium. It is approximately 1/4 radiation unit or 9.5 g/cm² and $r_M \simeq 79$ m at sea level. Fig. 2.8 shows the lateral density distribution of an EAS induced by a cosmic ray proton with $E = 10^{19}$ eV at its shower maximum.

2.5 Techniques for EAS Measurement

There are two types of EAS measurement techniques, which is called air shower array and fluorescence technique.

2.5.1 Air Shower Array

The technique, called air shower array, traditionally measures the cosmic ray using a lot of surface detectors (SDs) spread on the ground. A best merit of an air shower array is to observe UHECRs with the duty 100%. 90% of EAS particles are electromagnetic particles, 10% of them are muons and a few

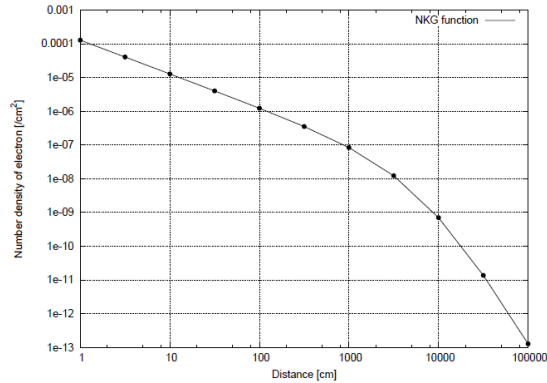


Figure 2.8: The lateral density distribution of electron number density in air shower whose primary is proton with energy 10^{19} eV at the shower maximum.

percent of them are hadron components. A typical detector is a scintillation counter sensitive to charged particles and muons. To measure muons, we can use special scintillation counters shielded by lead, soils, rocks or other dense materials. Moreover, to measure a hadron flux in the vicinity of shower axis, hadron calorimeters had been used in several experiments.

In air shower array, an arrival direction of EASs is reconstructed from a timing distribution of each surface detector because a front of EAS has a thin plane like *pan cakes*. The energy of a primary particle is estimated from the air shower size which is estimated by the shower lateral density distribution of the shower. However, it is difficult to avoid an uncertainty of from hadron interaction models, because a particle distribution of EASs is relatively large dependent on hadron interaction models.

2.5.2 Fluorescence Technique

In fluorescence technique, we measure the fluorescence photons emitted by atmospheric molecules excited by air shower particles. After high energy particles penetrate the atmosphere, atmospheric molecules, for example nitrogens or oxygens, are excited and emit ultra-violet fluorescence photons. In other words, the atmosphere plays a role of scintillators. When a single electron with the kinetic energy of 80 MeV passes through 1 m in the unit atmosphere of 1 atm, 4 fluorescence photons are emitted. From a detailed Monte Carlo calculation, 2×10^{15} photons integrated over the all slant depth are emitted from an EAS with the energy 10^{20} eV, and the time duration is about $30 \mu\text{s}$.

Since the fluorescence photon emission is isotropic, we observe the fluorescence photons from all directions of UHECRs within effective area.

In general, there are two steps of data analysis in the fluorescence technique to obtain the information of primary cosmic rays, as follows,

1. geometrical reconstruction
2. longitudinal development reconstruction

In the geometrical reconstruction, the arrival direction of a primary cosmic ray is calculated from recorded signals at the camera installed at the focal plane of a fluorescence telescope. In particular, when a EAS is observed by two separated telescopes stereoscopically, the shower axis is determined as the intersection of the two planes including the position of fluorescence telescopes and the shower axis, called shower detector plane (SDP), shown in Fig. 2.9. If fluorescence telescopes of a station detect fluorescence photons enough to reconstruct the information of a primary cosmic ray, after determined a SDP, arrival timing differences injected photons on each photomultiplier tubes are used for reconstruction of the shower geometry. To determine shower geometries using fluorescence telescopes of a single station is called a monocular mode. However, the monocular mode is slightly hard to reconstruct a geometry of EASs, because arrival timing differences are relatively small.

After the determination of the shower geometry, the longitudinal development are reconstructed with a following procedure.

- i. Expected number of the photons on camera planes are calculated considering the reconstructed geometry of Ethe AS and atmospheric scattering attenuations. The expected photons include not only fluorescence photons but also Čerenkov photons.
- ii. Comparing between the real observed signals on the cameras and expected signals, the optimum shower parameters of Gaisser-Hillas function (2.31) fitted to the event are reconstructed.

Since 90% of a primary energy is converted into electromagnetic particles, the primary energy E_0 is provided from integration of the longitudinal development of $N_e(X)$ shown in (2.31),

$$E_0 = \frac{E_{\text{cri}}}{X_0} \int N_e(X) dX \quad (2.35)$$

where X_0 is the radiation length in the atmosphere 38.0 g/cm^2 and E_{cri} is the critical energy, $E_{\text{cri}} = 84 \text{ MeV}$.

Therefore, the fluorescence technique provides a rich information of primary cosmic rays compared with the air shower array technique. However, in order to measure the primary energy and X_{max} , we estimate fluorescence yields, scattering of ultra-violet photons, reflectivities of mirror, the transmittance of filters and quantum efficiencies of photomultiplier tubes.

Photon Emissions, Scattering and Attenuation

Air Fluorescence Photon Yield

When high energy particles pass through the atmosphere, the atmospheric molecule are excited and fluorescence photons are emitted. After passing the

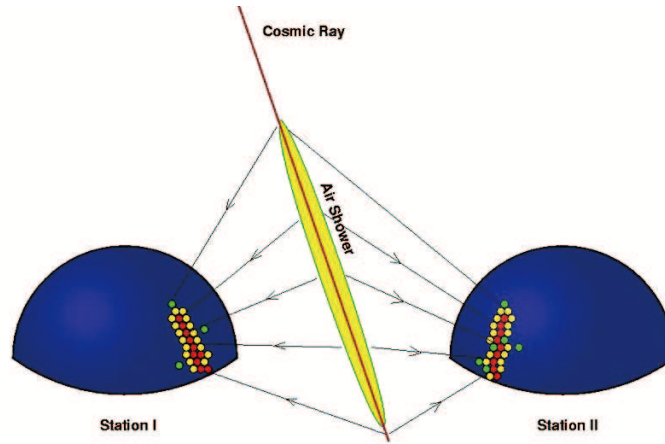


Figure 2.9: The schematic view of stereoscopic observations.

particles, rapidly emitted photons within 10^{-3} s are called fluorescence light. Slowly emitted photons are called phosphorescence. Here, we discuss the physics processes for emissions of fluorescence photons with wavelengths, $300 \sim 400$, which are our nm for our target wavelength.

For near violet region, the excited states are mainly N_2^+ first negative (1N) band system ($B^2\Pi_u^+ \rightarrow X^2\Pi_g^+$) and N_2 second positive (2P) band system ($C^3\Pi_u^+ \rightarrow B^3\Pi_g^+$).

The deactivation processes of excited molecules have following three processes.

1. nonradiative process (internal conversion)
2. radiative process (fluorescence, phosphorescence)
3. intermolecular energy transfer

In nonradiative processes, energies of excited molecules are lost by vibration relaxations or internal conversions without emitting fluorescence and phosphorescence photons. In radiative process, molecules move from excited to stable conditions via photon emissions. In fluorescence emissions, the spin multiplicity is invariant, but in phosphorescence, it is changed. In intermolecular energy transfers, molecules lose their energies to collide with other molecules. In fact, a deactivation process includes all three processes. Fig. 2.1 and Fig. 2.10 shows the efficiencies of fluorescence photon emissions and the relative intensity [60] [92]. The relative intensity spectrum has some emission lines between 300 nm and 400 nm.

Čerenkov Light

When a fast charged particle moves through a medium at a constant velocity v greater than the speed of light in that medium, c/n where c is the light speed

wavelength (nm)	band system	initial state(v')	final state(v'')	$E_0(\times 10^{-2})$
297.7	2P	2	0	0.016
311.7	2P	3	2	0.005
313.6	2P	2	1	0.029
315.9	2P	1	0	0.050
328.5	2P	3	3	0.015
330.9	2P	2	2	0.002
333.9	2P	1	1	0.004
337.1	2P	0	0	0.082
346.9	2P	3	4	0.006
350.0	2P	2	3	0.004
353.7	2P	1	2	0.029
357.7	2P	0	1	0.062
367.2	2P	3	5	0.005
371.1	2P	2	4	0.010
375.6	2P	1	3	0.027
380.5	2P	0	2	0.021
389.4	2P	3	6	0.003
391.4	1N	0	0	0.330
394.3	2P	2	5	0.006
399.8	2P	1	4	0.016
405.9	2P	0	3	0.007

Table 2.1: Efficiencies of fluorescence emissions relative intensity with wavelengths of 300 ~ 400 nm under a collisionless condition [60].

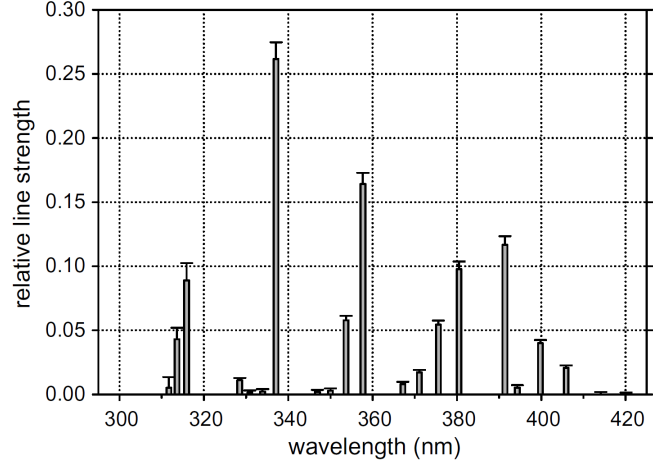


Figure 2.10: The relative line spectrum of air fluorescence light measured by FLASH [92]. The sum of the line strengths is set to unity.

in the vacuum and n is the refractive index of the medium, the particle emits Čerenkov radiation. The process is used as *threshold detectors*, because the Čerenkov radiation is only emitted if the particle has velocity greater than c/n . The Čerenkov radiation is only observed at a particular angle θ with respect to the track of a particle. The angle is described by

$$\theta = \cos^{-1} \left(\frac{c}{nv} \right) \quad (2.36)$$

which is known as the Čerenkov relation. Since the refractive index of the air with a pressure of one atm is $n \sim 1.00029$, θ is 1.4° , and for electrons the threshold energy for the Čerenkov light is 21 MeV.

The number of photons with wavelength λ nm,

$$\frac{d^2 N}{dx d\lambda} = \frac{2\pi\alpha z^2}{\lambda^2} \left(1 - \frac{c^2}{n^2 v^2} \right) \quad (2.37)$$

$$= \frac{2\pi\alpha z^2}{\lambda^2} \sin^2 \theta. \quad (2.38)$$

where $\alpha = e^2/4\pi\epsilon_0\hbar c = 1/137$ is the fine structure constant, z is the atomic number of the medium. When an electron above 21 MeV passes through the atmosphere 1 m, 30 photons are radiated.

Though θ is small in real showers, Čerenkov photons spread over following angular distributions of shower particles. Moreover, the photons are scattered by the atmosphere. In fluorescence techniques, the Čerenkov photons and their scatted photons are noise, because it causes a large systematic uncertainty for energy determinations. Therefore, we need to estimate a contamination of Čerenkov photons.

Night Sky Background

Photons from the sky at night are called night sky background. There are three types of emitted sources.

1. airglow : photons emitted from molecules and nucleons at the upper area of atmosphere, which are excited by low energy cosmic rays or are chemiluminescence process.
2. zodiacal light : the solar photons scattered by dusts in the interplanetary space.
3. stellar light : photons from stars and other astronomical objects.

These photons are measured in every photomultiplier tube as DC currents. From a science catalog, the brightness of the night sky background is $320 S_{10}(vis)$ $\left(1S_{10}(vis) = 1.20 \times 10^{-9} \text{ erg cm}^{-2} \text{ sec}^{-1} \text{ sr}^{-1} \text{ \AA}^{-1} \right)$.

There is a peak at wavelength 557.7 nm emitted by oxygen nucleon. The continuous spectrum is a large contribution in long wavelengths. Thus, since there are many night sky background photons in wavelengths longer than 400 nm and fluorescence process emits photons with a wavelength of 300 ~ 400 nm, the solution to measure fluorescence photons is observations in 300 ~ 400 nm.

Rayleigh and Mie Scattering

Scattering by atmospheric molecules are called "Rayleigh scattering", the probability of scattering are provided

$$\frac{\text{Intensity of scattered wave}}{\text{Intensity of incident wave}} = \frac{8\pi^4 N \alpha (1 + \cos^2 \theta)}{\lambda^4 r^2} \quad (2.39)$$

where N is the number of molecules, α is a polarizability and θ is a scattered angle, λ is a wavelength, r is a distance between a observed point and a scattered place.

For the Rayleigh process, photons are scattered by small dielectric spheres. In contrast to the Rayleigh process, for a Mie process, photons are scattered by dielectric spheres larger than wavelengths of photons, called the Mie scattering. The Mie scattering occurs by aerosols which are fogs, dusts or smokes.

For each process, transmittances are approximately calculated by the following formula.

For Rayleigh scattering,

$$T_{\text{Rayleigh}} = \exp \left[-\frac{X_{\text{trans}}}{X_{\text{Rayleigh}}} \left(\frac{400}{\lambda} \right)^4 \right] \quad (2.40)$$

where, X_{trans} is the slant depth through the atmosphere in the unit of g/m^2 , X_{Rayleigh} is the radiation length of the Rayleigh scattering, which is 2974 g/cm^2 , λ is the wavelength of light.

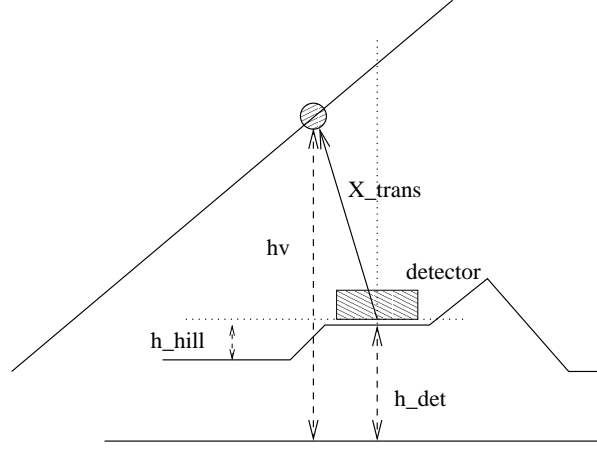


Figure 2.11: The parameters for (2.43).

For Mie scattering,

$$T_{\text{Mie}} = \exp \left[\left(e^{-\frac{h_v^{\text{eff}}}{h_m}} - e^{-\frac{h_d^{\text{eff}}}{h_m}} \right) \frac{h_m}{l_m \cos \theta} \left(1 - \frac{h_m \tan \theta}{R} \right) \right] \quad (2.41)$$

$$- \frac{h_m \tan \theta}{R l_m \cos \theta} \left(h_v^{\text{eff}} e^{-\frac{h_v^{\text{eff}}}{h_m}} - h_d^{\text{eff}} e^{-\frac{h_d^{\text{eff}}}{h_m}} \right) \quad (2.42)$$

where h_m is a scale height of an aerosol distribution and l_m is a mean free path of the Mie scattering, R is the radius of the earth and h_v^{eff} and h_d^{eff} are

$$h_v^{\text{eff}} = h_v (h_{\text{det}} - h_{\text{hill}}), \quad h_d^{\text{eff}} = h_d (h_{\text{det}} - h_{\text{hill}}). \quad (2.43)$$

Fig. 2.11 shows the explanation of other variables.

The transmittance of the Rayleigh scattering can be estimated with a straightforward calculation from a known of a density of the atmosphere. However, since there are large time variations in a transmittance of the Mie scattering, we need to measure conditions of aerosols by atmospheric monitoring systems.

2.6 Recent Results and Mysteries of UHECRs

We consider origins of UHECRs to be associated with explosive phenomena and/or new unknown physics, such as super heavy relic particles or topological defects, which are products at early universe. However, origins are still unknown attributed to difficulties to measure EASs because of extraordinary low fluxes and their extremely high energies of UHECRs. Here, we discuss recent results and outstanding mystery in the research field of UHECRs.

2.6.1 Energy Spectrum

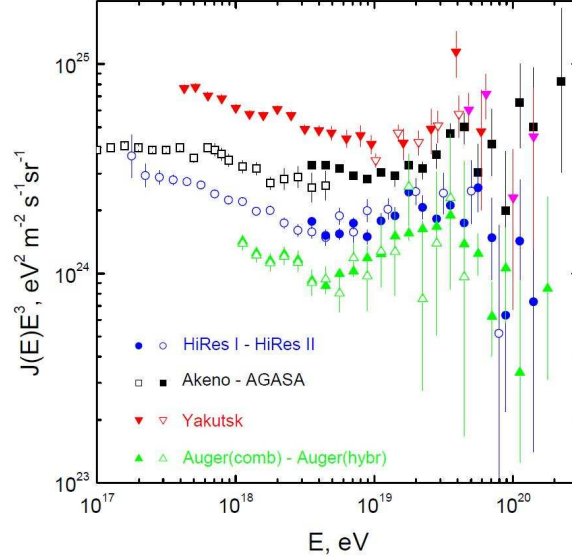


Figure 2.12: UHECR spectra measured by Yakutsk, AGASA, HiRes and Auger [35] [44] [50] [51].

Firstly, energy spectra reported by akeno - AGASA (Akeno Giant Air Shower Array), HiRes (High Resolution Fly's Eye) I - HiRes-II, Auger (Pierre Auger Observatory) and Yakutsk are displayed in Fig. 2.12 [35] [44] [50] [51]. The vertical axis indicates cosmic ray fluxes of Fig.=2.1 multiplied by E^3 in order to see detail of structures on the energy spectra, such as variations of the index, break points, etc. We can clearly see that there are large systematic differences among experiments about 20% on energy. Here, we briefly review methods and characteristics to measure UHECRs for several experiments.

AGASA (Akeno Giant Air Shower Array)

The AGASA experiment is an air shower array consisting of 111 scintillation detectors with the effective area of 100 km^2 located in Yamanashi, Japan with the altitude of 900 m. The air shower array technique was adopted in the AGASA experiment. In the air shower array technique, although we can observe UHECRs with 100% duty cycle, there are two large systematic uncertainties attributed to primary species and shower ages of EASs depending on zenith angles of EASs. Because of the zenith angle dependence of the column density of the atmosphere with respect to a given observation level, EASs are subject to increasing absorption with increasing zenith angle.

In the AGASA experiment, particle density detectors consisting of plastic

scintillators of 2.2 m^2 area are spread over 100 km^2 with inter detector separations of about 1 km. The plastic scintillator is sensitive to detect all charged particles, electromagnetic components and muons. In order to estimate cosmic ray energies above 10^{19} eV , the particle density observed at a distance of 600 m from the shower axis, S600, has been widely used as a good energy estimator, because the S600 value is almost independent of primary species. The observed particle densities are fitted to an empirical formula for the lateral density distribution function for determining S600. In the AGASA, a conversion factor from S600 values to primary energies is estimated from MC simulations. Further, the estimated $S_{\theta}600$ for a shower arriving at zenith angle θ is transformed to the equivalent value in the vertical direction, S_0600 , using the attenuation curve for S600 which is estimated from observed EASs with an energy at $2 \times 10^{19} \text{ eV}$ and $9 \times 10^{18} \text{ eV}$ [45]. The method is called “equi-intensity cuts” and the systematic uncertainty on energy determination is estimated to be 18% for the AGASA experiment [47]. The AGASA spectrum indicates an evidence for a continuation of the spectrum beyond the GZK cutoff.

HiRes (High Resolution Fly’s Eye)

The HiRes experiment observe UHECRs by the fluorescence technique at two sites (HiRes I and II) 12.6 km apart, located at Dugway providing ground in Utah [50]. Each site consists of fluorescence telescope units (22 at HiRes I and 42 at HiRes II) The fluorescence detectors (FDs) observe the full 360° in azimuth but cover from 3° to 16.5° (HiRes I) and from 3° to 30° (HiRes II) in elevation. The FDs observe longitudinal developments of EASs and determine the calorimetric energies of primary particles. However, we need to measure a lot of calibration factors such as fluorescence yields, atmospheric parameters, gains of PMTs, reflectivities of mirrors and so on. The total systematic uncertainty of the HiRes experiment is estimated to be 17% on energies [50]. The HiRes spectrum clearly shows the existence of a termination in the cosmic ray flux consistent with the GZK cutoff prediction.

Auger (Pierre Auger Observatory)

The Pierre Auger Observatory is the largest detector located in Argentina to measure cosmic rays by combinations of the air shower array and the air fluorescence technique, so called “hybrid technique” [3]. The air shower array of Auger consists of 1600 water Čerenkov detectors, each of which consists of 10 m^2 water tank and three 9-inch PMTs, and detects Čerenkov photons emitted by mainly muons into the water. The number of muons is more sensitive on hadron interaction models than electromagnetic components. Thus, impacts of uncertainties attributed to uncertainties on hadron interaction models for Auger are larger than those for TA [109].

The magnitude of the signal in each tank is measured in “vertical equivalent muons” (VEM), a quantity easily inferred by the abundant single muons

passing through each tank. The values of VEM measured at 1000 m from a reconstructed core of EAS are used as an energy scaler. Since this quantity varies with zenith angles of EASs, an effective attenuation is determined from the data assuming that intensity of cosmic rays for a fixed energy must be independent of the zenith angle, which is the same with the equi-intensity cuts method adopted in the AGASA experiment. Using the equi-intensity cut, the signal that each shower produces at 1000 m is adjusted to the signal that would have been produced at z zenith angle of 38° which is the median angle for cosmic rays with zenith angle $\leq 60^\circ$. The hybrid showers which are triggered by both the surface array and the fluorescence detectors of Auger are used for absolute energy determinations. The absolute energies measured by the surface array of Auger are calibrated by those measured by FDs. The systematic error in the energy determination is estimated to be 22%. There is also a suppression structure in the Auger spectrum as same as the HiRes spectrum.

A possible interpretation of 20% discrepancy on energies among AGASA, HiRes and Auger measurements might be attributed to the difference of detection methods between the air shower array technique and the fluorescence technique. Additionally, all energy systematic uncertainties are large, 18% for the AGASA, 17% for the HiRes, 22% for the Auger, and these uncertainties are comparable with the systematic discrepancy on energies among them. Therefore, in order to understand a reason of the discrepancy, we need to measure UHECR flux with a smaller systematic uncertainty and more statistics than current measurements, and then conclude whether the GZK mechanism occurs or not at high energies above $10^{19.5}$ eV.

2.6.2 Mass Composition

Secondly, recent results on mass composition studies for UHECRs with X_{\max} technique by fluorescence detectors are reported in this section. The maximum depth of longitudinal developments of EAS, X_{\max} is an important parameter to measure mass composition of UHECRs, because X_{\max} depends on primary species as shown in Fig. 6.2. The difference of averaged X_{\max} is about 100 g/cm² between primary protons and irons, and more than 300 g/cm² between primary protons and gamma rays or neutrinos, and these values are larger than resolutions of fluorescence detectors. Thus, we distinguish primary species by the X_{\max} technique of fluorescence detectors.

Fig. 2.13 shows the averaged X_{\max} measured by the Stereo Fly's Eye (left) and the HiRes/MIA and the HiRes experiments (right), which are compared with the prediction rails estimated from Monte Carlo simulations for primary protons and those for irons [38] [37]. There are transitions of dominant components from heavy to light nuclei with energies from $10^{17.5}$ eV and $10^{18.5}$ eV in Fly's Eye experiments. The transit energy measured by the Fly's Eye experi-

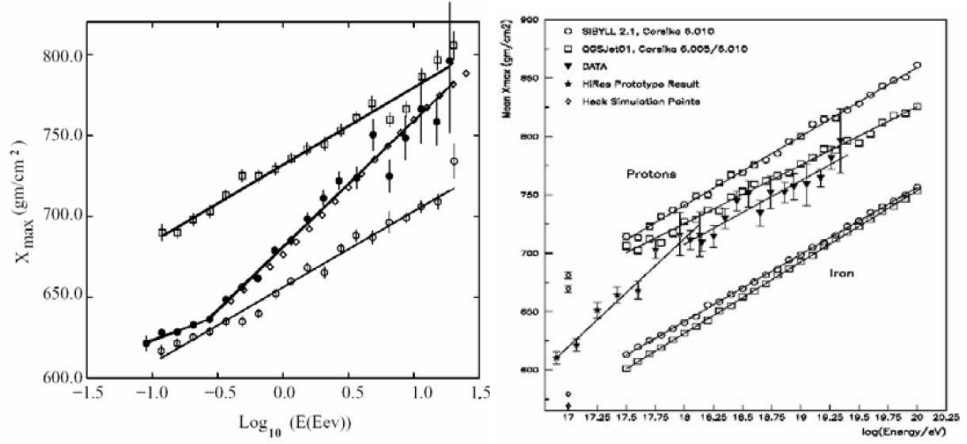


Figure 2.13: The averaged X_{\max} for Stereo Fly's Eyes (left) and HiRes/MIA and HiRes (right) compared with predictions for primary protons and irons with several hadron interaction models after full Monte Carlo detector simulations [38] [37].

ment indicates a half order of magnitude large compared with that measured by the HiRes/MIA experiment. However, HiRes collaborators reported averaged X_{\max} values measured by the HiRes/MIA experiment are in reasonable agreement with those measured by the Fly's Eye experiment with $13 \text{ g}/\text{cm}^2$ systematic shift on X_{\max} within systematic uncertainties [38]. In energy ranges above $10^{18.0} \text{ eV}$, the averaged X_{\max} values measured by the HiRes experiment are consistent with the expectation line estimated from MC simulations for proton primaries using the QGSJet model as hadron interaction models.

The latest preliminary results on the mass composition observed by Telescope Array (TA) are shown in Fig. 2.14 [39]. The averaged X_{\max} is consistent with the red line calculated with assuming purely primary protons, which is same with the result of light components above 10^{18} eV measured by the HiRes experiment. The rails are also averaged X_{\max} from full Monte Carlo simulations for primary protons and irons using QGSJet-I, QGSJet-II and SIBYLL models.

Fig. 2.15 shows the averaged X_{\max} measured by Auger in the southern hemisphere [40]. The total systematic uncertainty in X_{\max} measured by Auger goes from $10 \text{ g}/\text{cm}^2$ at low energies to $13 \text{ g}/\text{cm}^2$ at high energies [41]. The results by Auger indicate the mass composition of UHECRs shows a transition from protons to heavier nuclei in energies above $10^{18.5} \text{ eV}$. Fig. 2.16 shows distributions of X_{\max} in several energy ranges measured by Auger [41]. The reduction in the width of X_{\max} distributions as the energy increases can be clearly observed from the figures. The distributions are also compatible with the transition from light components to significant fraction of nuclei (CNO or heavier).

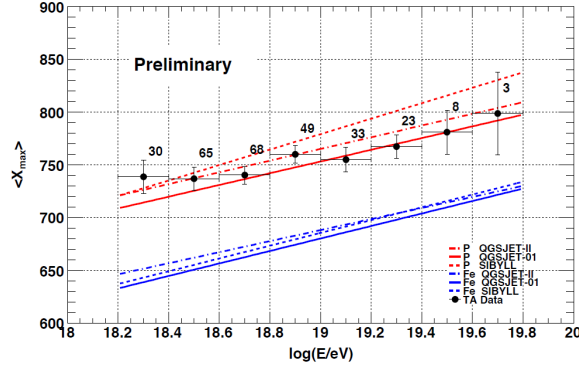


Figure 2.14: Preliminary results of the averaged X_{\max} measured by the Telescope Array experiment compared with the prediction rails for protons and irons using three types of hadron interaction models: QGSJet-I (a solid line), QGSJet-II (a dash-dotted line) and SIBYLL (a dotted line) [39].

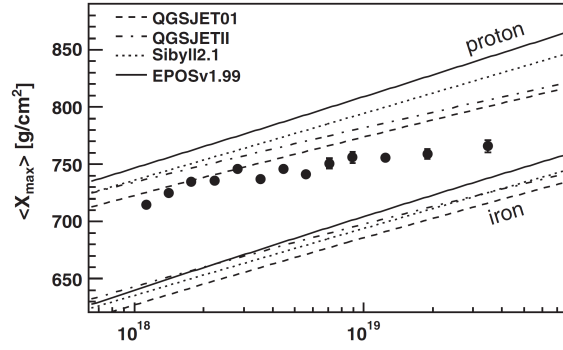


Figure 2.15: Auger measured $\langle X_{\max} \rangle$ compared with air shower simulations using different hadronic interaction models[40].

Moreover, Auger reports mass composition results estimated from surface detectors to achieve more statistics than FD measurements at high energies above $10^{19.3}$ eV. In Auger, muon production depth (MPD) distributions for inclined showers are reconstructed from FADC traces of the surface detectors far from the core. Since the MPD distributions depend on longitudinal developments of EASs, Auger group defined a new observable X_{\max}^{μ} to estimate the mass composition of UHECRs. Auger group selects showers with zenith angles between 55° to 65° and with reconstructed energies above 2×10^{19} eV consists of 427 events. Fig. 2.17 shows observed X_{\max}^{μ} values and expected rails of X_{\max}^{μ} estimated from MC simulations for primary protons and irons using several hadron interaction models [42]. The uncertainties on the MPD reconstruction

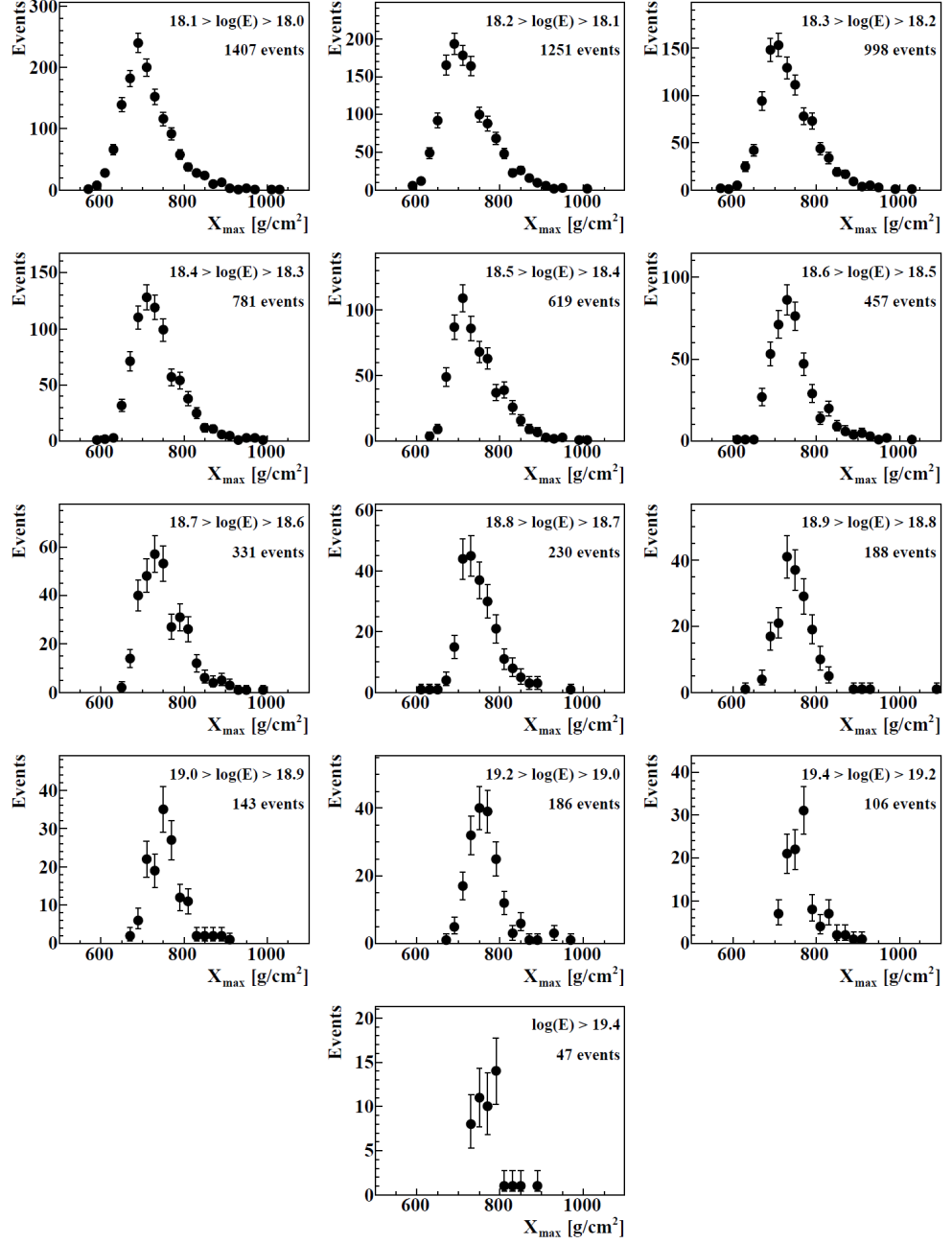


Figure 2.16: Distribution of X_{\max} observed by the Pierre Auger Observatory [41]. The values of the energy limits and the number of events selected are indicated for each panel.

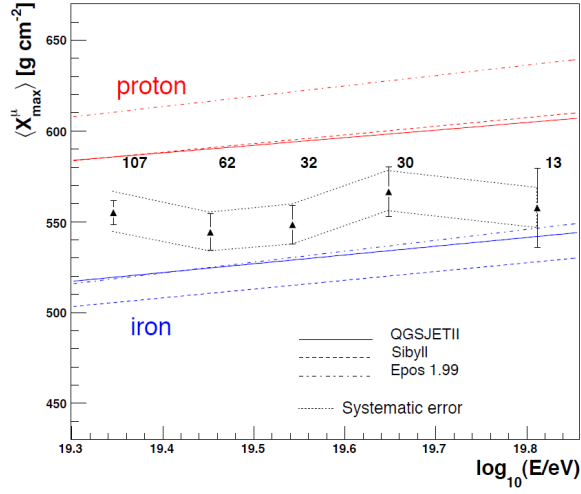


Figure 2.17: Averaged X_{\max}^{μ} values as a function of the energy measured by Auger surface detectors [42]. The number of real data events in each energy bin is indicated. The predictions for primary protons and irons following different hadronic models are shown as well.

and event selection translate into a systematic uncertainty on averaged X_{\max}^{μ} of 11 g/cm² [42]. The result of observed X_{\max}^{μ} is in good agreement with the Auger results obtained with other completely independent methods.

Note that strong quality cuts were applied in the Auger analysis of fluorescence detectors in order to avoid acceptance biases caused by FDs limited fields of views. In contrast, such the strong quality cuts were not adopted in TA and HiRes analyses. Thus, although detectors and methods of data acquisition are similar, details of analyses are different each other. In general, shower events the X_{\max} is observed outside of fields of view of FDs are removed with quality cuts to obtain reasonable resolutions. Since fluorescence detectors have the limited field of view, a distribution of observed X_{\max} is changed from an original distribution. The prediction lines of averaged X_{\max} for primary protons and that of irons corresponding to HiRes and TA results are obtained by MC data calculated with full Monte Carlo simulations of air showers and the HiRes and TA experiments and analyzed with the identical analyses procedures applied on real observed data, and then these prediction lines include the acceptance biases due to the detector and the analysis process of each experiment. Therefore, even though the principle of the detections and the analysis is identical between HiRes and TA FD, the predictions are different between the two experiments, because they are *different* experiments. Thus, it is difficult to make graphical comparisons of the prediction lines, and also of the averaged X_{\max} of two experiments by plotting these values on a chart.

On the other hand, in order to avoid the acceptance bias of FDs, Auger

group applied strong quality cuts on the observed data and Monte Carlo simulations, called the “fiducial volume cuts”. With the fiducial volume cuts only well contained events in the field of view of the FDs were selected and remained for analyses, and then, for example, many nearly vertical showers are removed from the analyses. Thus, the event statistics becomes much lower than without it. As a result, X_{\max} distributions are obtained without acceptance biases.

Thus, since each experiment reported their result analyzed with their own rules and methods, and each results has their own bias caused by detectors, analysis methods and event selections, then these biases are different each other. So then it is not possible to compare these results by simply plotting data points on one chart. For comparisons, we need special care about their observation and analysis biases. To check the discrepancy between the results by TA and those by Auger, and also in order to compare results by two experiments, here I apply the fiducial volume cut to FD data detected by the TA FDs and corresponding MC data to avoid acceptance biases.

2.6.3 Arrival Direction Distribution

Thirdly, we report recent results for point source searches and anisotropy studies. Fig. 2.18 shows arrival direction plots of UHECRs with energies above 4×10^{19} eV observed by the AGASA experiment [46]. The red squares and the green circles represent arrival directions of UHECRs with energies above 10^{20} eV, and $(4 - 10) \times 10^{19}$ eV, respectively. The red and blue lines indicate the galactic plane and the super galactic plane. AGASA group reported that this arrival direction distribution is compatible with an isotropic random distribution [46]. Moreover, they reported that there is no clear correlation with already known astronomical objects [46]. However, they report that they found six “event clusters” which the shaded circles indicate the event clustering within 2.5° . Specially, at $(10^h 29^m, 57^\circ)$, three 4×10^{19} eV cosmic rays are observed against expected 0.06 events. The chance probability of observing such triplet under an isotropic distribution is only 0.9%.

On the other hand, correlations between arrival directions of UHECRs and nearby AGN are published by the Auger group in 2007 [29]. Fig. 2.19 shows Aitoff projections of the celestial sphere in galactic coordinates with circles of 3.1° radius centered at the arrival directions of 27 events with energies above 57 EeV detected by the Pierre Auger SD array. The positions of 472 AGN (318 in the field of view of the Observatory) with the redshift $z \leq 0.018$ ($D < 75$ Mpc) from the 12th edition of the catalog of quasars and active galactic nuclei by Véron-Cetty and Véron (VCV catalog) [62][62] are indicated by red asterisks. The solid line represents the border of the field of view (zenith angle smaller than 60°). Darker blue indicates larger relative exposure. Each colored band has an equal integrated exposure.

However, after that, up to December in 2009, the significance of the correlations between arrival directions of UHECRs and positions of nearby AGN decreased [62]. The sky map observed 69 cosmic rays with energies above 55

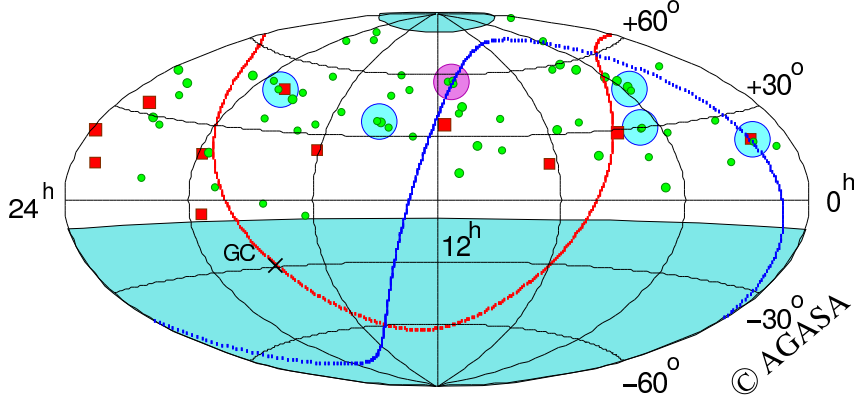


Figure 2.18: Arrival directions of cosmic rays with energies above 4×10^{19} eV observed by AGASA. Red squares and green circles represent cosmic rays with energy of $> 10^{20}$ eV, and $(4 - 10) \times 10^{19}$ eV, respectively. Shaded circles indicate event cluster within 2.5° . At $(10^h 29^m, 57^\circ)$, three 4×10^{19} cosmic rays are observed against expected 0.06 events. [46]

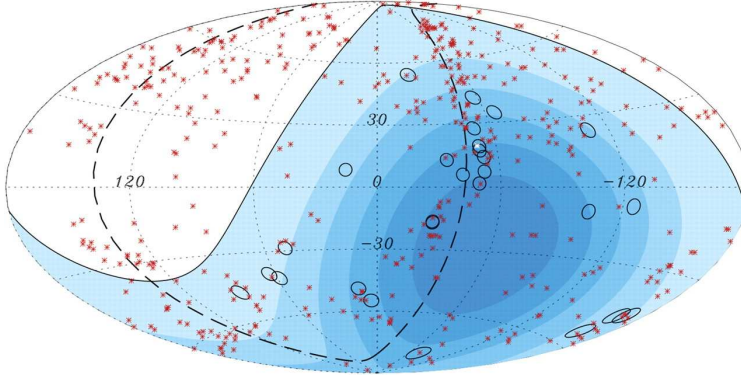


Figure 2.19: Aitoff projection of the celestial sphere in galactic coordinates with circles of radius 3.1° centered at the arrival directions of the 27 cosmic rays with highest energy detected by the Pierre Auger Observatory [29]. The position of the 472 AGN (318 in the field of view of the Observatory) with the redshift $z \leq 0.018$ ($D < 75$ Mpc) from the 12th edition of the catalog of quasars and active galactic nuclei by Véron-Cetty and Véron (VCV catalog) [62] are indicated by red asterisks. The solid line represents the border of the field of view (zenith angle smaller than 60°). Darker color indicates larger relative exposure. Each colored band has equal integrated exposure. The dashed line is the super-galactic plane. Centaurus A, one of our closet AGN, is marked in white.

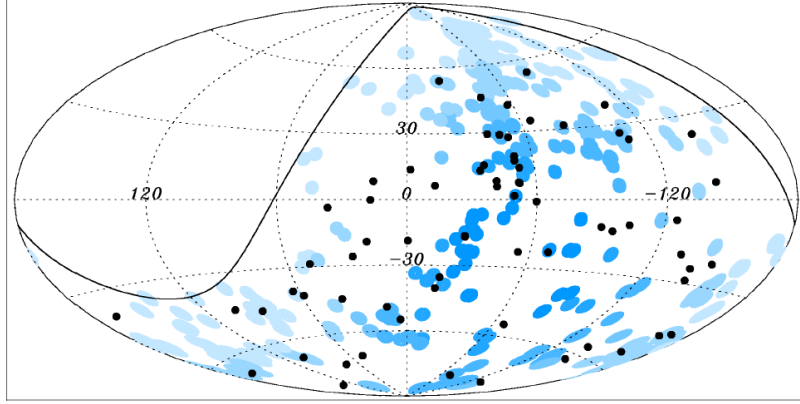


Figure 2.20: The 69 arrival directions with energy $E \leq 55$ EeV detected by the Pierre Auger Observatory up to 31 December 2009 are plotted as black dot in an Aitoff-Hammer projection of the sky in galactic coordinates [30]. The solid line represents the field of view of the Southern Observatory for zenith angles smaller than 60° . Blue circles of radius 3.1° are centered at the positions of the 318 AGNs in the VCV catalog [62] that lie within 75 Mpc and that are within the field of view of the Observatory. Darker blue indicates larger relative exposure. The exposure-weighted fraction of the sky covered by the blue circles is 21%.

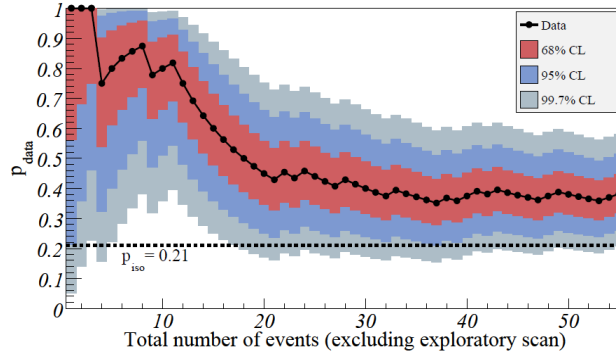


Figure 2.21: The ratio between total number of UHECRs and UHECRs direction correlated with AGN observed by Auger. $P_{\text{data}} = N^{\text{correlated}}/N^{\text{total}}$ [30].

EeV is shown in Fig. 2.20. As shown in Fig. 2.21, the amount of correlation observed has decreased $(69^{+11}_{-13})\%$, from 9 out of 13 correlations, to its current estimate of $(38^{+7}_{-6})\%$, based on 21 correlations out of a total of 55 events. The

degree of observed correlation (38_{-6}^{+7})% is compatible with 21% expected to occur by chance if flux were isotropic.

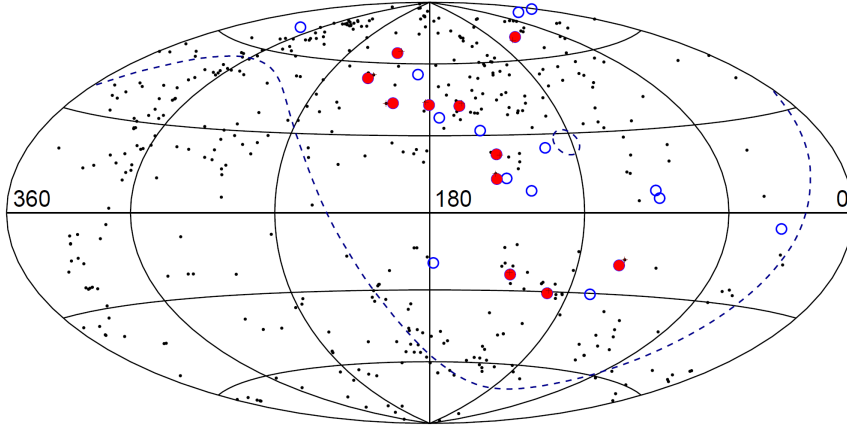


Figure 2.22: Hammer projection of the UHECRs with $E > 57$ EeV observed by TA and nearby AGNs in the Galactic coordinates. Correlating and non-correlating events are shown by filled red and empty blue circles, respectively. AGNs are represented by black dots. The dashed line shows the boundary of the TA exposure [31].

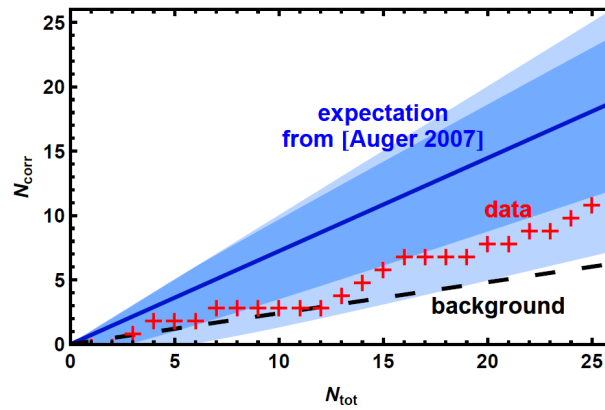


Figure 2.23: The number of the UHECRs with $E > 57$ EeV observed by TA correlating with AGNs from VCV catalog as a function of the total number of events. The expectation according to the original Auger claim is represented by the blue line together with the 1- and 2-sigma significance bands. The black dashed line shows the expected number of random coincidences [31].

Recently, TA reported the anisotropy of UHECRs collected by the TA SD in the first 40 months of operation [31]. The sky map of UHECRs with $E > 57$ EeV observed by TA and nearby AGNs from the VCV catalog is represented in Fig. 2.22 in Galactic coordinates. The UHECRs are shown by filled red (correlating events) and empty blue circles (non-correlating events). AGN are shown by black dots.

Fig. 2.23 shows the number of UHECRs observed by TA correlating with AGNs as a function of the total number of events with $E > 57$ EeV ordered according to arrival time. The black dashed line represents the expected number of random coincidences in case of a uniform distribution calculated via Monte Carlo simulation. The blue line shows the expected number of correlating events as derived from the original Auger claim [29]. Shaded regions represent 68% and 95% C.L. deviations from this expectation calculated by the maximum likelihood method of Ref. [32]. As is seen from Fig. 2.23, present TA data are compatible with both isotropic distribution and the AGN hypothesis.

In the full TA data set, there are 11 correlating events out of 25 total, while the expected number of random coincidence for this total number of events is 5.9. Making use of the binomial distribution with the probability of a single event to correlate 24%, one finds that such an excess has probability of $\sim 2\%$ to occur by chance with isotropic distribution of arrival directions.

Here, I briefly summarize recent results of UHECR measurements.

- The mass composition measurement is the proton dominant above $10^{18.5}$ eV at north hemisphere, against the transition from light to heavy nuclei above $10^{18.5}$ eV at south hemisphere.
- In the energy spectrum measurement, there are large systematic difference among measurements. The presence or absence of the GZK cutoff is still unknown considering the mass composition measurements.
- In the anisotropy, there is not still clear significant correlation between arrival direction of UHECRs and already known astronomical objects.

Everyone hopes enough statistics of UHECRs to understand the physics of UHECRs and to conclude their origins.

Chapter 3

Telescope Array Experiment

In order to conclude origins of cosmic rays, the Telescope Array(TA) experiment has been started in 2003. TA experiment has the largest detector in the northern hemisphere to observe UHECRs, consisting of two types of detectors: 507 surface detectors (SDs) arrayed with a spacing of 1.2 km between each SD in a area of approximately 700 km², and 38 air fluorescence detectors (FDs) located around the SDs facing inward and looking over the array. The TA experiment has been constructed at Utah desert in United States (at latitude 39.3° north and longitude -112.91° west and at 1382 m above sea level) with an international collaboration of AGASA, HiRes and more scientists in Japan, US, Korea, Russia and Belgium.

3.1 Aims of the Telescope Array Project

Principle purposes of the TA experiment are listed as follows.

- In order to detect a clue to the mystery of origins of UHECRs, we measure the energy spectrum of UHECRs with the world's best accuracy and with the highest statistics in the north hemisphere.
- We measure the UHECR flux precisely in the super GZK energy region and settle the contradiction between AGASA's super-GZK continuation and HiRes's cutoff, with the "hybrid" detector which consists of AGASA type, *i.e.*, a plastic scintillation detector array and HiRes type, *i.e.*, fluorescence telescopes.
- To confirm whether the GZK mechanism occurs at the cutoff region or not, we observe the mass composition of UHECRs to measure a maximum depth, X_{max} , of extensive air showers, because the X_{max} depends on the mass composition of the primary cosmic rays. If the mass composition is proton dominant above 10^{19.0} eV, it indicates an evidence of the GZK mechanism via interaction with UHE protons and CMBR. On the other hand, if the mass composition is iron dominant above 10^{19.0} eV, it

shows a photo-disintegration mechanism for iron nuclei occurs above this energy. Moreover, the composition in the ankle region around $10^{18.8}$ eV is important to determine a reason of the ankle structure. For a point source search, the mass composition is also essential because the bending attributed to galactic magnetic fields is proportional to a charge of the primary species.

- In order to search for the clusterings of UHECRs observed by AGASA and a correlation between arrival directions of UHECRs and known astronomical objects, we observe enough statistics of UHECRs using the largest effective area in the north hemisphere. Moreover, we search for an anisotropy as a function of energies or the transition of cosmic ray origins. As a result, we establish a charged particle astronomy as a next-generation astronomy.

3.2 Overview of TA Hybrid Detector

The construction of the TA detectors started at the end of 2003. Fig. 3.1 shows layouts of the detectors for the TA experiment. The 507 SDs with 1.2 km separation are spread in the area of about 700 km². The total 38 FDs are installed in the three stations, called the Black Rock Mesa (BRM) station, the Long Ridge (LR) station and the Middle Drum station (MD), and these locations are east, west and north from the array, respectively. The field of view of three FD stations are also shown in Fig. 3.1 covering with the effective area of the SD array.

In March 2008, we have finished the constructions of the full TA detectors, and we started the full operations. Moreover, the observation at the LR station was improved to operate and monitor from the BRM station, and we have started unmanned operation in May 2010.

3.3 Fluorescence Detector

Fluorescence technique is to collect fluorescence photons emitted from atmosphere excited by air shower particles using spherical mirrors, and to detect by cameras consisting of 256 photomultiplier tubes (PMTs) located at the focal plane. At the north of the TA site, 14 fluorescence detectors of the MD station are transported from HiRes-I and HiRes-II experiments. The effective mirror area transported from HiRes-II is 3.75 m² and the curvature radius is 4.74 m. The field of view is 15.5° in azimuth and 16° in elevation. The sample and hold system of the HiRes-I electronics is applied [74].

On the other hand, the BRM station and LR station contained 12 fluorescence detectors, respectively, are newly designed and constructed for the TA experiment. The total field of view of each station is 108° in azimuth and 3-33° in elevation overlapping the effective area of SD array. The fluorescence

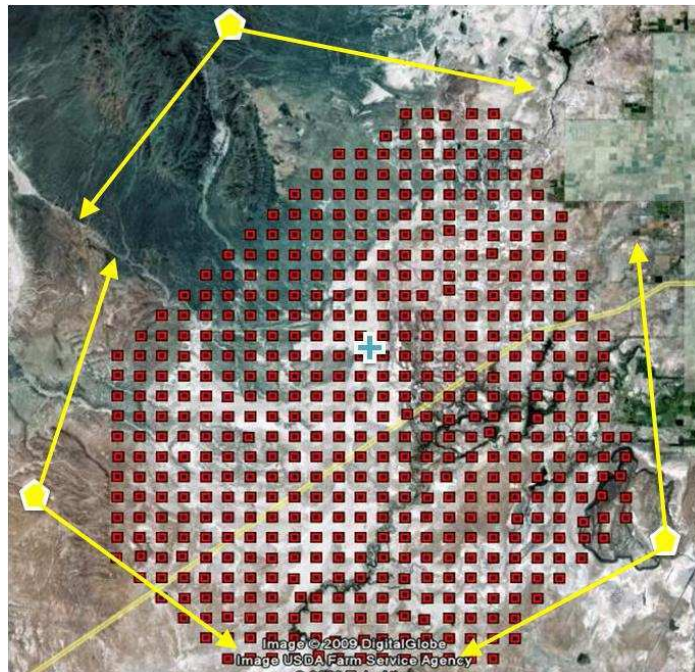


Figure 3.1: The detector configuration of TA. The red square plots: surface detector, the yellow pentagon-shaped plots: station of fluorescence detectors, the blue cross shape: the Central Laser Facility.



Figure 3.2: The BRM station (top-left), the fluorescence detectors of BRM station (top-right) and the MD station and MD fluorescence detectors transported from HiRes-I and HiRes II experiment (down).

detector consists of 18 segments of spherical mirrors with diameter of 3.3 m and a camera assembled by 256 PMTs as shown in Fig. 3.7. More details are described in following sections.

3.3.1 Telescope and Optics

The field of view of each TA fluorescence telescope is 18° in azimuth, 15.5° in elevation with two lines consisting of upper 6 telescopes and lower 6 telescopes. The field of view of upper layer is $3^\circ \sim 15.5^\circ$ and the lower is $18.5^\circ \sim 33^\circ$ with total $3^\circ \sim 33^\circ$. The locations of each telescopes are fanned out covering total 108° in azimuth.

We use spherical mirror optics to obtain a wide field of view with reasonable focusing power. The support and adjustment mechanism for the segmented mirrors is also simple for the spherical mirror compared with the parabolic system. According to ray-tracing simulations, the spot size of 30 mm at the

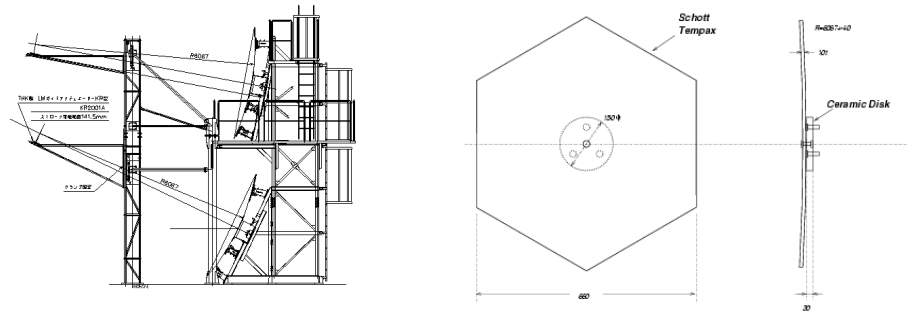


Figure 3.3: The newly developed telescopes and their designs at BRM and LR site.

focal plane is obtained in the field of view when the spot size of each mirror at the curvature center is within 20 mm. For all of the segment mirrors, we measured the curvature radius and the spot size at the curvature center before installing.

The BRM and LR telescopes have a spherical mirror with a diameter of 3.3 m which is composed of 18 hexagonal segment mirrors. The design of the segment mirror is shown in Fig. 3.3. The mirrors are made 10.5 mm thick Tempax glass coated with 200 nm thick aluminum produced by the vacuum deposition. A hard protection surface of Al_2O_3 crystal with thickness of 5 nm is produced in the solution containing ammonium hydroxide, tartaric acid and ethylene glycol. Reflectivities of greater than 90% of the mirrors are obtained between 300 ~ 400 nm wavelength. The spectral reflectivities can be adjusted to a peak around 350 nm by tuning the thickness of anodization. The anodized surface is stable and the degradation of the reflectivity is $\sim 1\%$ / year from the experience of the Fly's Eye experiment and Utah Seven Telescope groups. However, dusts on the mirror surface leads to make less reflectivities due to the expose to the outer air directly. In order to monitor time tendencies of reflectivities, we measures the reflectivities by a portable reflectance spectrophotometer at regular intervals. The measured reflectivities of each layers are shown in Fig. 3.4 are divided by the height. Results indicate the decreasing tendency proportional to exposed time and the localization in which the reflectivities become worse as lower layers. The mirrors can be washed by pure water for regular maintenances. After washing the mirrors, reflectivities of the mirrors were completely recovered as shown in Fig. 3.6.

3.3.2 Photomultiplier Tube (PMT) and Camera

TA cameras are installed on a focal plane of the spherical mirrors, and the size of camera is 1 m by 1 m a shown in Fig. 3.7. The camera of FDs consists of 256

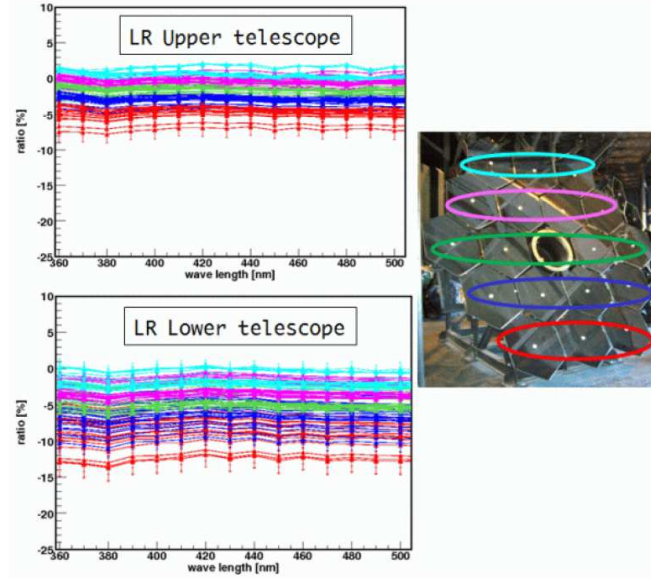


Figure 3.4: The variation of the reflectance of the LR mirror in June 2008. Colors on the left figures correspond to the colors on the right figure. The vertical axis is the variation from installing. It depends on the height of mirrors.

hexagonal PMTs arranged in 16×16 array to form an imaging plane which are protected by the acrylic filter, KURARAY paraglas. Typical transparencies of the acrylic filter are $>90\%$ above 300 nm shown in Fig. 3.8. Each camera covers with the FOV of 18° in azimuth, 15.5° in elevation with a pixel acceptance of 1.1° corresponding to directional resolutions for PMTs. A Ultra-Violet transparent filter (BG3) with a thickness of 6 mm is attached in front of the PMT to reduce the number of night sky background photons with an extra wavelength of our interest. The night sky background is about ~ 30 photoelectrons within 100 ns.

HAMAMATSU R9508 is adopted for the photon sensor of the FD camera in TA, which has a hexagonal bialkali photo-cathode and borosilicate glass window. The dimensions of the PMT and a typical quantum efficiency are 25% shown in Fig. 3.10. The PMT has 8 dynodes of a box-line focus and they are set to have an equal gain of 8×10^4 . The PMT adopts a DC-coupling to measured the variation of night sky background directly.

Fig. 3.11 shows multiplication values of the typical values of mirror reflectance, paraglas transmittance, UV filter transmittance and quantum efficiency of PMT. TA FD telescopes and optics are sensitive to wavelengths from 300 nm to 400 nm corresponding to fluorescence photon wavelengths.

In the PMT camera, PMTs are arranged in zigzag with 1 mm spacing. The sensitive area of PMTs is not uniform and the spot size on the focal

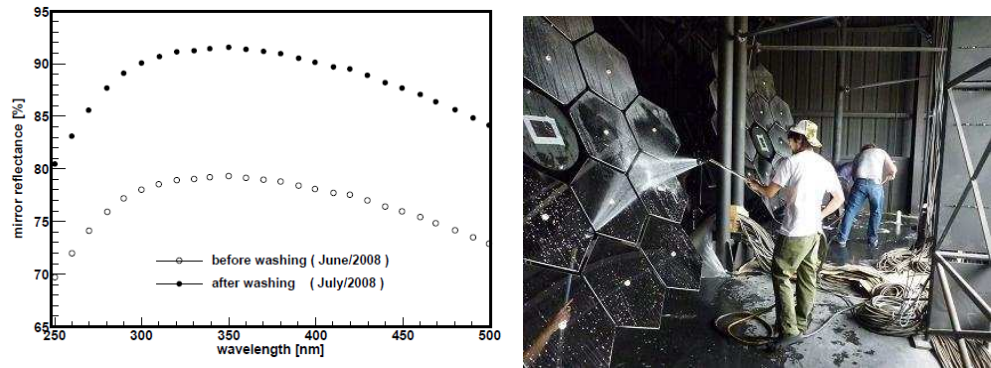


Figure 3.5: The spectral reflectance of the camera 06 of BRM station (left) and a picture in mirror washing (right). Open circles are the reflectance before washing and filled circles are after washing

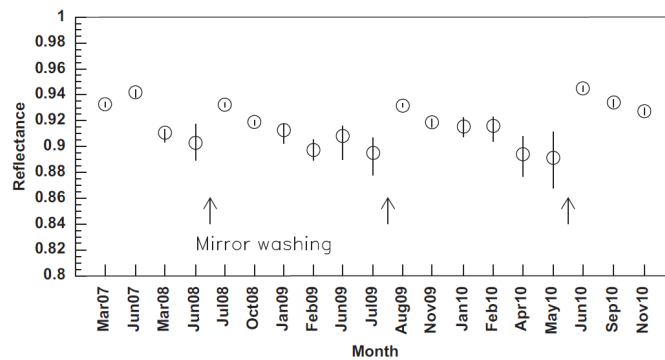


Figure 3.6: Variation in the mirror reflectance at 360 nm of a typical lower FD (FOV: 17.5-33 in elevation) of camera 04 at LR. The mirror was washed after these measurements in July 2007, August 2009 and May 2010 [53].



Figure 3.7: TA camera (left) and PMT of R9508 attached the UV filter (right).

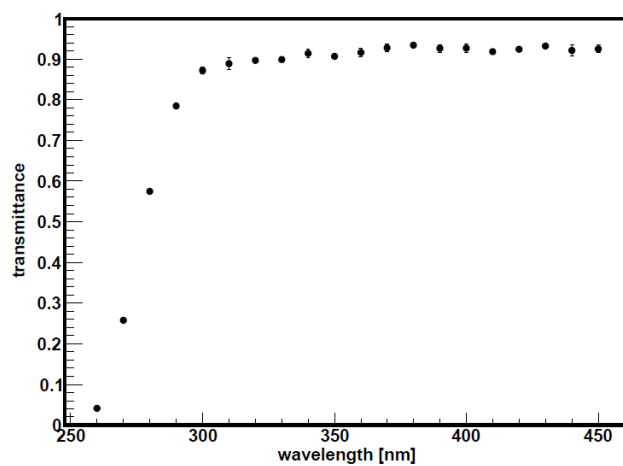


Figure 3.8: The typical transmittance of the KURARAY paraglas on the front of camera.

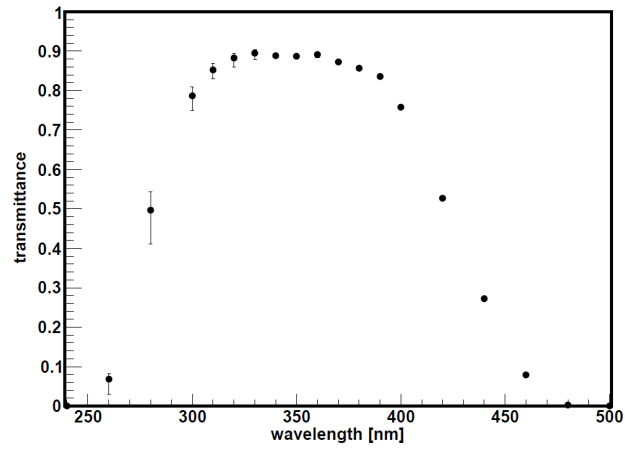


Figure 3.9: The typical transmittance of the UV filter in the front of photo-tubes. Data points are the medians for all the sampled filters with the bars corresponding the on standard deviation.

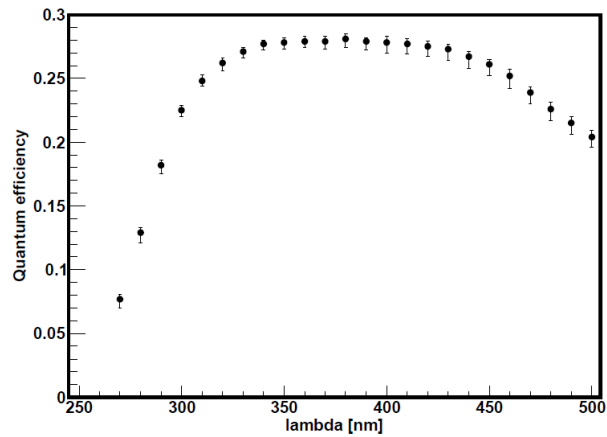


Figure 3.10: The typical quantum efficiency of photo-tubes. The data plot shows the median with one standard deviation error of all PMTs measured by HAMAMATSU PHOTONICS.

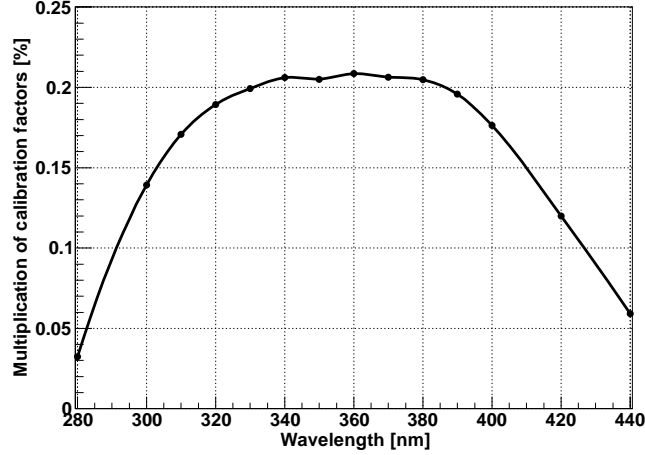


Figure 3.11: Multiplication values of the typical values of mirror reflectance, paraglas transmittance, UV filter transmittance and quantum efficiency of PMT.

plane is less than 30 mm. Therefore, output signals of PMT suffer from the non-uniformity effect. Fig. 3.12 shows the averaged non-uniformity map over 253 PMTs measured by the XY-scanner which consists of the eight UV LEDs (NSHU590B, NICHIA). The wavelength of UV LEDs is 365 ± 10 nm with 400 ns pulse width and 1000 photoelectrons per pulse. The result is consistent with the HAMAMATSU data shown in Fig. 3.13, and the non-uniformity is considered in detector Monte Carlo simulation discussed in the next chapter.

3.3.3 Calibration of PMT Gain

The calibration and monitoring of the PMT gains are achieved in three steps: the absolute measurement of standard PMT, the relative gain monitoring for each camera and the correction by the PMT temperature [52].

The absolute gain of standard PMTs are measured by CRAYS (calibration using Rayleigh scattering) in a laboratory [75]. The standard light source of CRAYS is Rayleigh scattered photons emitted from a pulsed laser ($N_2 = 337.1$ nm) in nitrogen molecule gas (see Fig. 3.15). The absolute gain is acquired to measure scattered photons with the 10 MHz FADC readout system as the same with TA FD. The total systematic uncertainty of the CRAYS calibration is estimated to be 7.2% and an additional uncertainty of 3.7% is introduced by the transport of the calibrated PMTs from the laboratory to the TA experimental site [75]. Two or three “standard” PMTs whose gain was measured by CRAYS are installed in each camera.

In order to monitor the gain of standard PMTs, a small light pulser of

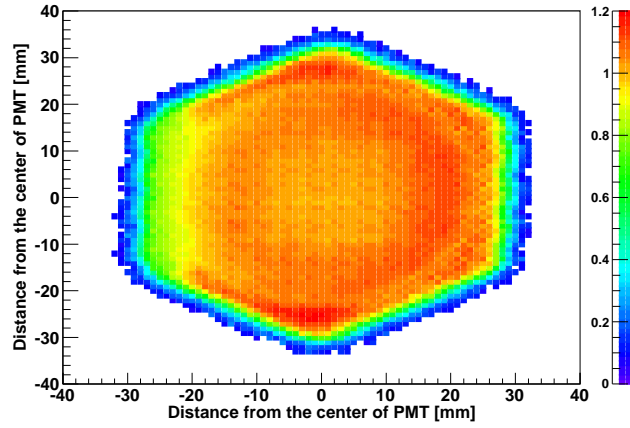


Figure 3.12: The typical non-uniformity map with $1 \text{ mm} \times 1 \text{ mm}$ resolution of the photo-cathode of our photo-tube. It is normalized with the bins inside a circle with 36 mm diameter. The obtained map show an asymmetry long the x axis caused by the dynode structure of the PMT.

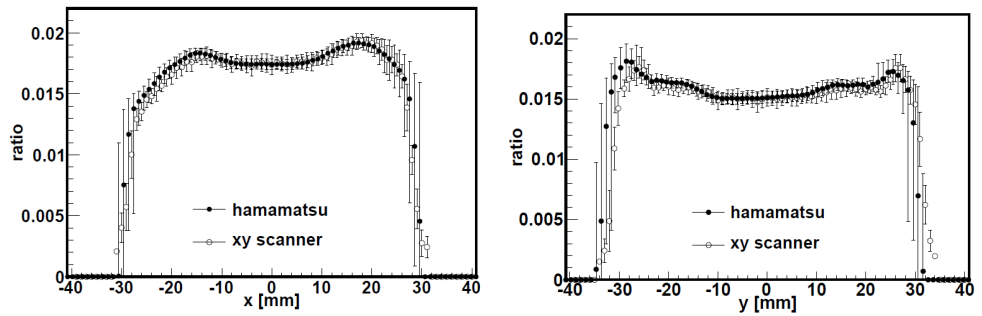


Figure 3.13: The comparison of results between the HAMAMATSU data and the data measured by XY-scanner. The left and right figure show the result along X axis and Y axis, respectively. The definition of the coordinate of x and y axis is the same as Fig. 3.12. Filled circle are the HAMAMATSU data and open circles are XY's scanners.

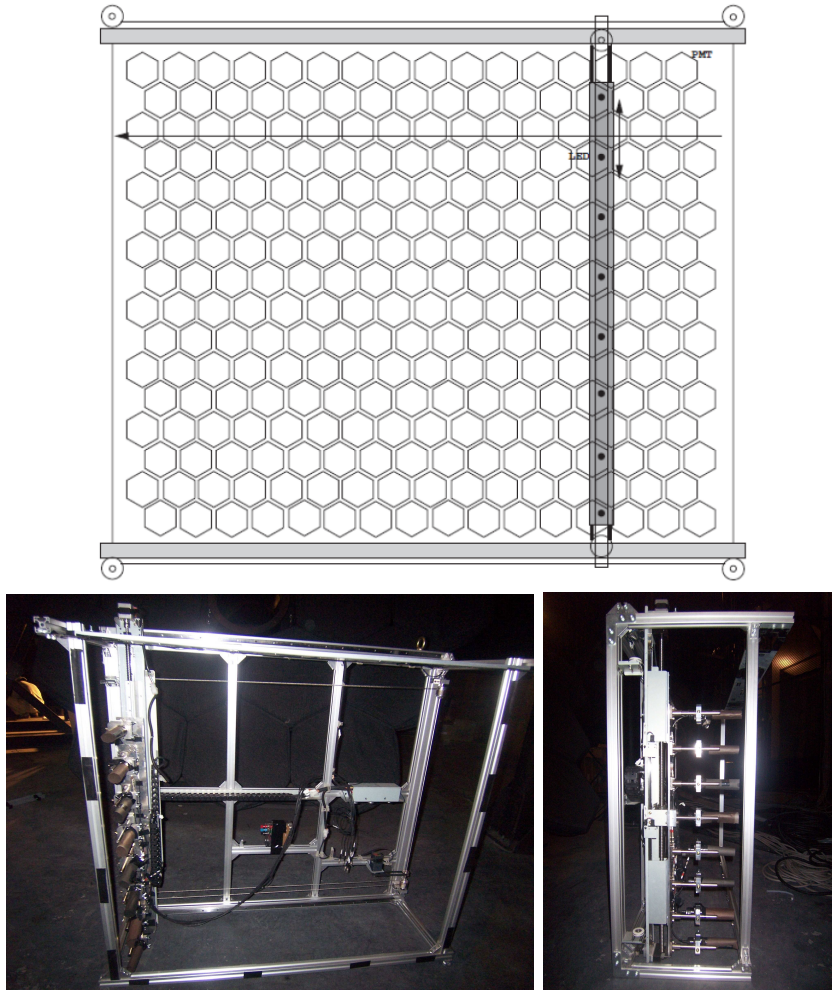


Figure 3.14: The schematic view and photograph of XY-scanner. The covering area of each LED is 2.5 PMTs vertically and 16 PMTs horizontally.

YAP(YAlO₃: Ce) scintillator with ²⁴¹Am [79] is mounted in a BG3 filter of them. The temperature dependence of an intensity is measured about -0.2% / degree from -10 to 40 °C. The typical intensity is equivalent to 450 p.e. with a fluctuation of 10% and an individual difference of less than 5%.

The gain of other PMTs can be monitored relatively to compare with intensities of Xe flash lamps which are installed in the center of each mirror [52]. Fig. 3.17 shows the relative light intensities of Xe flashers which consist of the Xe lamp (L4646), socket (E2418) and the electric circuit (C3484) made by HAMAMATSU and a teflon diffuser. The Xe flasher emits pulsed photons with an intensity equivalent to 2×10^4 p.e. with time width 2 μ s and frequency 25 Hz. We monitor once per hour during observations with the Xe flasher. As the

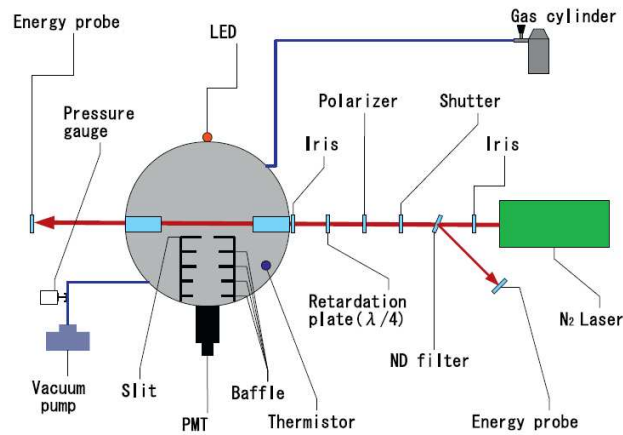


Figure 3.15: Measurement set up of CRAYS [75]

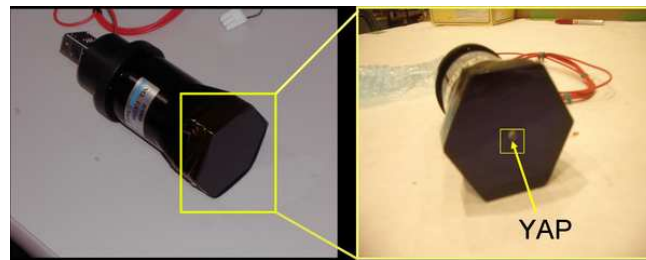


Figure 3.16: The UV pulsed light source located in front and center of the standard PMT, named YAP.

result, the standard deviation of the adjusted relative gains for each camera is about 1% [52].

3.3.4 Trigger Electronics

Fig. 3.18 shows the block diagram of the TA fluorescence detector electronics and trigger systems in the FD station. The system consists of three type modules: 1) signal digitizer and finder (SDF), 2) track finder (TF) and 3) central trigger distributor (CTD) [54] shown in Fig. 3.19. The SDF module digitizes and records the signal from PMT and calculate S/N to find fluorescence signals from EAS. The FD modules recognize the air shower track based on the result of SDF. The CTD module unifies all of the modules and controls the DAQ process.



Figure 3.17: The image of Xe flasher.

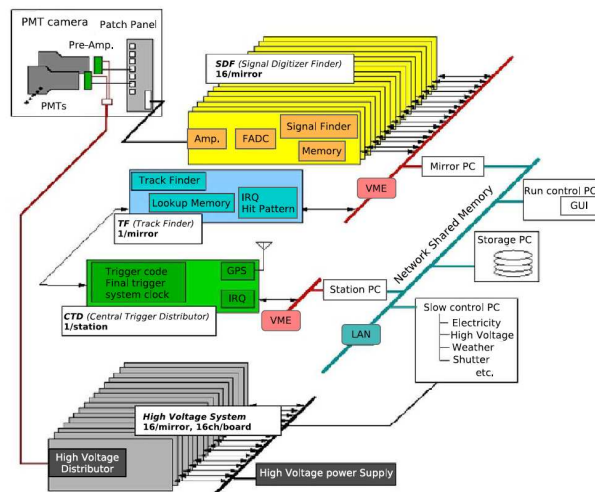


Figure 3.18: Block diagram of electronics and trigger system of the TA FD

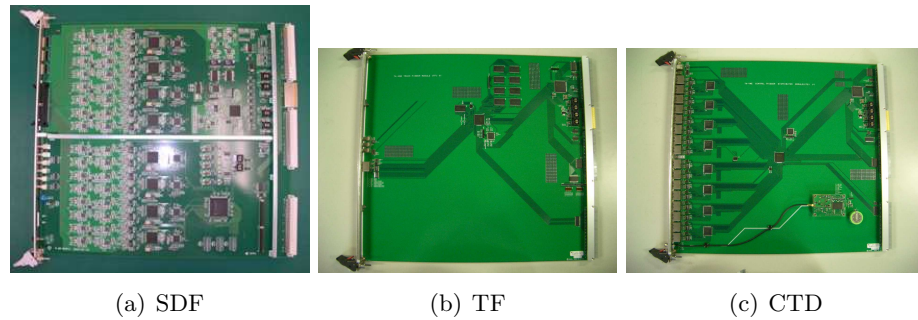


Figure 3.19: Photos of the trigger modules of TA fluorescence detector

Signal Digitizer and Finder

The SDF module digitizes the signal from PMT by 12 bit 40 MHz FADC and records the output of FADC added up with 4 bins as a waveform. Each SDF has 16 input channel from PMTs and 16 SDFs are assigned for each telescope for each channel,

In order to find large excess signals over the night sky background, SDF calculates moving average in several time windows of 1.6, 3.2, 6.4 and 12.8 μs . The average and the standard deviation are also calculated from past 1.6 ms, to normalize moving average counts. The SDF module examines the moving average counts to find fluorescence signals by comparing with a pre-set threshold level. The results of SDF on each PMT are sent to the TF.

Track Finder

The TF module processes the hit patterns of one camera in every frame. The hit patterns are the map of results of the first level trigger of each channels. When it recognizes the hit patterns as an air shower track, it sends the second level trigger to the CTD. The major components of the TF are one CPLD (XC95288XL), one FPGA (XC3S400E), one configuration ROM (XC18V04) and nine SPAMs (CY7C1041). These devices are assembled onto 9U VME printed circuit board. The block diagram of the TF module is shown in Fig. 3.20.

At each camera, one TF module communicates with the 16 SDFs via the VME bus lines. To form the second level trigger, the TF searches through the PMT hits, determined by the SDFs, looking for patterns in space and time. It recognizes shower tracks on the camera or rejects accidental coincidences caused by night sky backgrounds or other artificial sources such as light from airplanes. The TF scans over hits in the camera, as identified by the SDFs, in sub arrays of 5 by 5 PMTs. The sub array window scans over all camera at a given observatory site for 25.6 μs search window every 12.8 μs . Those observed patterns are compared with the lookup table for possible track recognition.

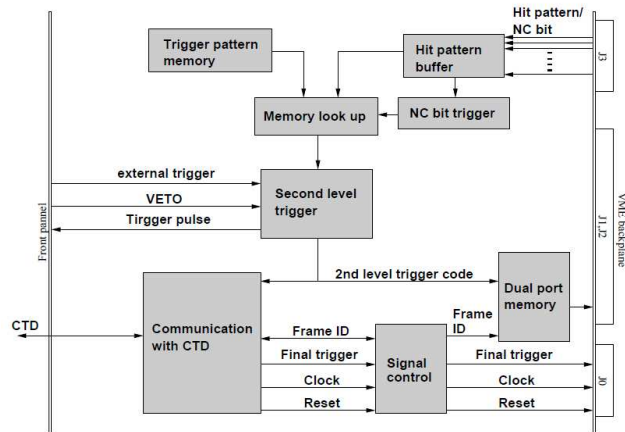


Figure 3.20: Block diagram of TA Track Finder module.

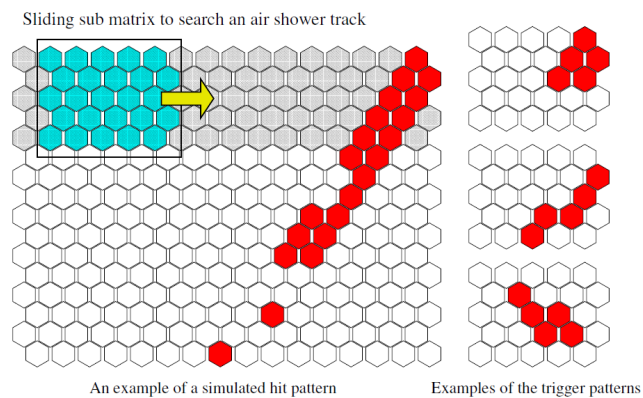


Figure 3.21: Schematic diagram of the track finding process.

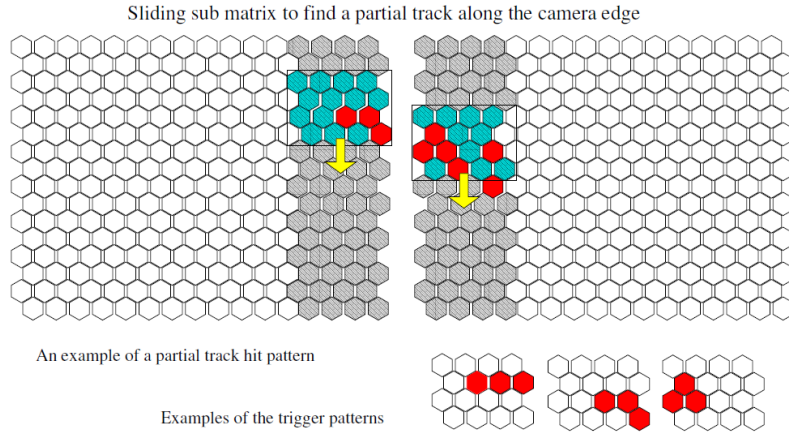


Figure 3.22: Schematic diagram of the partial track search near the boundary of a camera.

At the same time, the TF module receives “Non-Conditional” (NC) trigger information from the SDFs, which are set when significantly large signals are found in the PMTs. The TF module can also generate trigger signals by using the NC information without track identifications for calibration runs. The trigger signals generated by the TF (“second level” triggers) are sent to the CTD module. Each TF has two inputs on its front panel for veto and external triggers, and also has an output pulse indicating a second level trigger.

The track recognition criterion for a “complete track” condition is that five adjacent PMTs in the camera are above threshold within a coincidence window of $25.6 \mu\text{s}$, as shown in Fig. 3.21. The TF crops a hit pattern into a 5×5 sub-matrix and searches for complete tracks in the sub-matrix. The sub-matrix is shifted column by column, row by row across the face of the camera repeating the search for a track. The number of hit patterns of 5×5 pixels is 2^{25} , the lookup table is programmed in the 8 static RAMs (CY7C1041, $256\text{k} \times 16$). The processing time is $3.5 \mu\text{s}$, corresponding to $25 \text{ ns} \times 155$, for the pattern matching of 155 sub-matrices in a camera.

An additional trigger condition implemented in the TF helps it to recognize showers which straddle two cameras leaving short tracks in each. These “partial tracks” are identified if there are three adjoining PMTs above threshold in a 4×4 sub-matrix at the boundaries of two adjacent cameras, (see Fig. 3.22). This is equivalent to the complete track condition, because there is an overlap with a width of one PMT ($\text{FOV} \simeq 1^\circ$) between the field of view of two neighboring cameras.

The TF can generate the second level trigger in other two cases: first when the NC trigger initiated by a large signal in the SDF and second when an external trigger is induced by a pulse input to the TF front-panel. When one of the trigger criteria is fulfilled, the TF sends the second level trigger information

to CTD with a frame ID.

Central Trigger Distributer

The CTD module generates the final trigger judgment for the FD DAQ system to record air shower candidates. It also serves as the controller of the FD station system distributing the system clock to keep all of SDFs and TFs synchronized. It also sends the “reset” signals to initialize the frame counters.

The CTD module is a VME-9U single width board. Its major components are nine CPLD (one XC95288XL and eight XC95144), one FPGA (XC2S200E) and a configuration ROM (XC18V02). A GPS module (Motorola M12 + Timing Oncore (P283T12T1X)) is also installed on the CTD to provide precise timing of the shower events. The block diagram of CTD is shown in Fig. 3.23. The CTD module receives and examines the second level trigger codes from

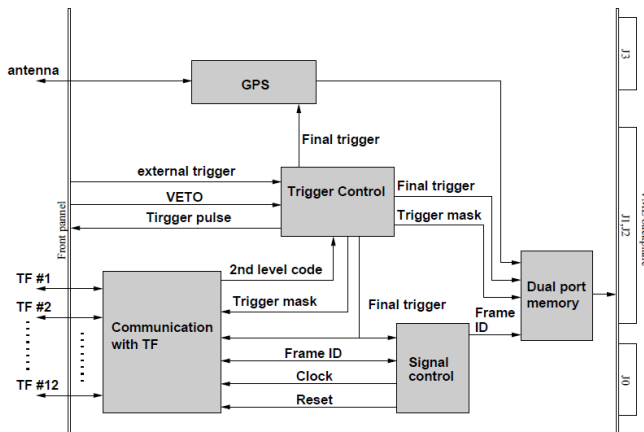


Figure 3.23: Block diagram of TA Central Trigger Distributer module.

all TFs at an observatory station. When the CTD receives the second level trigger with the code of a complete track from one or more TFs, it generates and distributes a “final trigger” to all TFs to record the waveform data of all the PMTs in the station. Aside from this condition, the CTD also triggers the DAQ system when two neighboring TFs send second level triggers with the code of a partial track. The CTD can generate the final trigger if TFs sent trigger codes of NC triggers or external trigger for calibration runs, for example to acquire a reference light source to monitor the PMT gain [52]. A final trigger signal consists of a trigger pulse with a readout mask which is a 12-digit binary number indicating a second level trigger in the telescopes as well as a trigger ID. At the moment of the generation of final trigger signals, the CTD and TFs supply DAQ signals for each VME control PC to start a DAQ cycle.

Event times are calculated from the difference between the rise time of the

latest 1 pulse per second (PPS) signal from GPS module and the beginning of the frame. The time difference is counted with 40 MHz system clock, the resolution of absolute time is 25 ns. The accuracy of absolute times depends on the stability of 1 PPS signals, which is 20 ns from our measurement.

The time table of a signal DAQ cycle, from the beginning of the signal finding process to the end of data transmissions into readout buffers, is shown in Fig. 3.24. It is dominated by the time required for the track finding process and

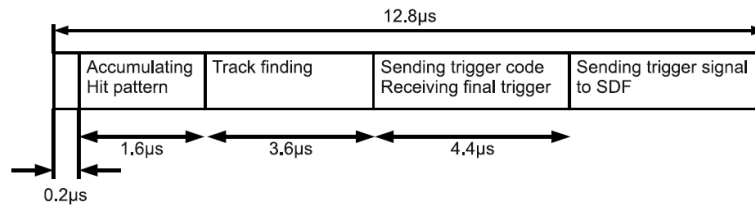


Figure 3.24: The procedures of a single trigger.

data transmissions of trigger information between modules. The total process time is smaller than the frame interval of 12.8 μ s. If the readout buffers of SDFs and TFs are full, CTD suspends trigger distributions. In order to measure the dead time in operations, the CTD recored the IDs and the absolute times of the first and last frame in each suspended period, and also it calculates the sum (length) of those periods. This information is transferred to the VME control PC for the CTD.

The CTD module supplies 40 MHz system clock pulse to all the trigger electronics modules and sends the reset pulse to synchronize all of them. If TF misses to receive the system clock, TF switches to the TF inner clock and stands the error bit.

The absolute time information can be known for each triggered data by GPS time and the number of clock pulse from the latest 1 PPS. This time is important in analysis other FD station's and the SD array's triggered events and accuracy of less than μ sec order is essential.

By track finding algorithm, aircraft exterior light is also triggered. In a stable run, trigger rate is about 2 \sim 3 Hz. However, once airplane flights into the FOV of telescope, trigger rate become higher to the maximum of DAQ rate \sim 30 Hz. The CTD module can distinguish airplane trigger from others. If there are a continuous trigger whose duration is over 100 μ s, the CTD regard them as airplane's light. After than in \sim 10 μ s trigger is vetoed. Before installation of airplane veto, the ratio of airplane was about 1/3. Currently, most of the signal from air plane are vetoed by the CTD.

Because of the read out and airplane veto, dead time is included in a observation time. Dead time is essential to be accounted for to estimate an accurate

exposure. The CTD module can calculate the accurate dead time. The buffer is prepared, which is less than 0.1 Hz. If the trigger rate becomes more than 30 Hz temporally, the data are left in the buffer not to be acquired. At this time the buffer becomes full (8 or predetermined limit more event data are stored) and we can not acquire the air shower data, even though there is a triggered air shower. This interval should be added up as a dead time. The TF modules send the buffer status which means that the buffer is full or not to CTD. The CTD module counts the number of dead time frames and records the start and end frame ID of the dead time interval. By this information we can know the accurate dead time Fig. 3.25. The first group is caused by the airplane veto, and the

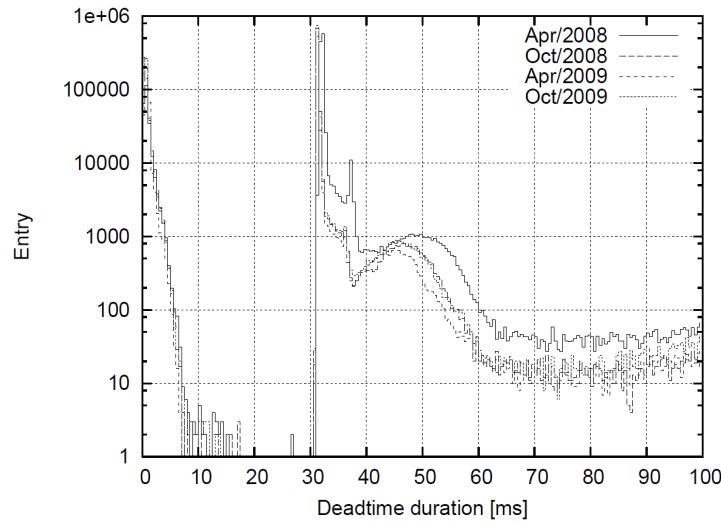


Figure 3.25: The histogram of typical dead time durations in log scale for some observation terms on Apr/2008, Oct/2008, Apr/2009, Oct/2009.

second group is caused by the read out, 30 ms is the minimum time to read out the data.

3.4 Atmospheric Monitoring

TA has several methods to monitor an atmospheric condition. Air shower measurement by FD is achieved to detect fluorescence photons emitted along the air shower axis apart from several kilometers. Then, the intensity of fluorescence photons is attenuated by atmospheric scattering in propagating through the atmosphere. In order to estimate the primary energy of air showers from detected fluorescence photons, it is quite important to study the atmospheric profile.

The TA FD analysis uses the following three parameters.

- Atmospheric parameters (temperature, pressure and humidity)
- Transmittance (horizontal attenuation length)
- Cloud

The atmospheric parameters such as temperature, pressure and humidity are used for estimation of a yield of the fluorescence light and transmittance by the Rayleigh scattering. Those parameters are measured by the radiosonde.

Since the transmittance of the atmospheric affects the reconstructed energy directly, this is one of the most important calibration factors. The main uncertainty of the transmittance is caused by the Mie scattering. Since it depends on the time, the transmittance has to be measured frequently. In FD analysis, the transmittance is measured by Light Detection And Ranging (LIDAR) system at the start and the end of daily operation of FD.

The aperture of FD is affected by the cloud, because the cloud shields the fluorescence photons emitted from EAS. In TA, there are three methods to measure the amount of the cloud: the weather code (WEAT code) visually recorded by the operator in the MD station, the picture taken by the IR camera at the BRM station, and CCD-fisheye camera installed at BRM, LR and CLF locations. The WEAT code is adopted in FD analysis because almost all dataset of FD observations are recorded.

3.4.1 Radiosonde

The atmospheric parameters such as pressure, temperature and humidity are important for the FD analysis. These parameters are used for the calculation of the fluorescence yield, atmospheric depth, transparency of the atmosphere and so on. Since the atmosphere is changed by time, these parameters should be measured periodically. For each altitude, the measurement is done by a balloon up to 30 km above sea level. There are six launching the site for the radiosonde around the TA site by meteorological instrument. At each site, the characteristics of the atmosphere are measured every 12 hours and they are opened to the public on the web site [96]. The atmospheric parameters measured by ELKO site (40.87 North, 115.73 West) are adopted in FD analysis because the climate of ELKO is similar to the experimental site of TA. All of the data are prepared as a database to use for the analysis. The detailed study for the radiosonde is written in [76] [108].

3.4.2 LIDAR

For measurements of the attenuation in atmosphere, TA has a laser system called light detection and ranging (LIDAR) [77] which is located 100 m far from the BRM station. The overview of LIDAR system is shown in Fig. 3.26. It consists of the YAG laser with 355 nm wavelength, 4 mJ power and 1 Hz frequency (ORION made by ESI), the energy prob with a UV sensitive (J50LP-1A made by Coherent) and a 30 cm diameter telescope (LX200GPS-30 made

by MEADE) on the steerable mounting and a PMT (R3479, HAMAMATSU) with a UV filter. The remote operation can be done from the FD station.

The atmospheric attenuation is measured using the photons scattered backward in the laser shooting. The photons are detected by the PMTs with the telescope and digitized by the oscillo scope (WaveRunner6039 made by Lecroy). The LIDAR system operated before and after observation with 4 types of measurement: 500 vertical shots and 500 horizontal shots with two types of energy, respectively. The details of the operation and analysis are written in [77]

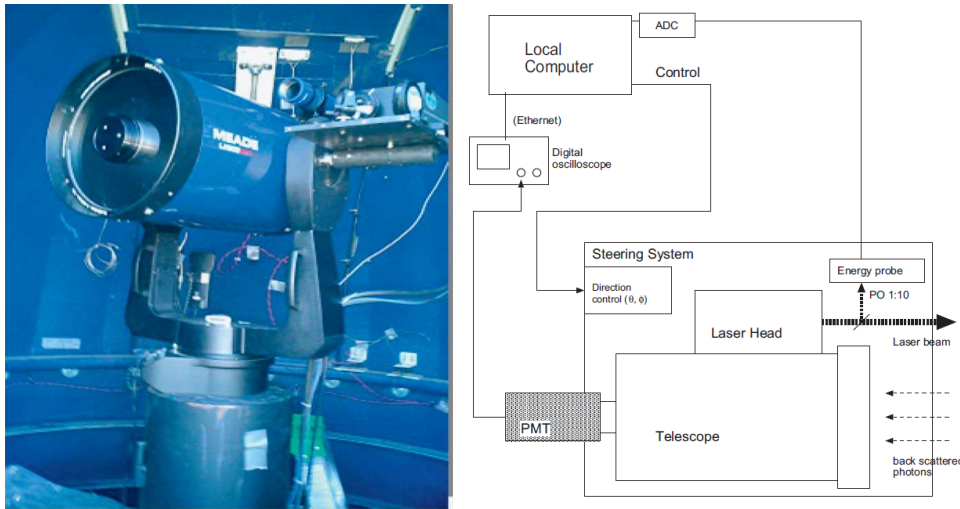


Figure 3.26: The overview of LIDAR system. A left picture is LIDAR's optical system (telescope, laser, etc), a right picture is a connection block diagram of device of LIDAR.

The atmosphere has two main components for the attenuation. One is molecules in the atmosphere, another is aerosols. The scattering phenomenon caused by molecules is called Rayleigh scattering. It is well known by atmospheric parameters corresponding to temperature and pressure. Thus, the important things for measurement of the atmospheric attenuation is the scattering caused by aerosols, called Mie scattering. The factor of Mie scattering for the aerosol scattering can be measured by LIDAR system through detecting back-scattered photon. Additionally, the component of the Rayleigh scattering can be calculated by the atmospheric parameters measured by Radiosonde. Therefore, the component of the Mie scattering can be obtained by the measured total attenuation subtracted by the calculated attenuation for the Rayleigh scattering.

The LIDAR system measures the extinction coefficient which is the inverse of the horizontal attenuation length for each height for every observation day. The data obtained by the horizontal shots can measure the extinction coefficient on the ground. The distribution of the attenuation for the component of the

Mie scattering is shown in Fig. 3.27. The typical attenuation length on the ground is 29.4 km. For the index of the attenuation, we define the vertical aerosol optical depth (VAOD)

$$T_{\text{Mie}} = \exp(-\text{VAOD}), \quad (3.1)$$

where T_{Mie} is the transparency by the Mie scattering. The typical VAOD of the measured data is about 0.034 shown in Fig. 3.27, and then T_{Mie} is 0.967.

The amount of the aerosol is reduced as the altitude increases. So the extinction coefficient $\text{Mie}(h)$ at the several heights h is expressed as

$$\text{Mie}(h) = \exp(-h/H) \quad (3.2)$$

where H is the scale height for the aerosol distribution. This parameter can be obtained by fitting for the attenuation length on the ground and VAOD at each height. The fitted scale height is obtained for 1.0 km, the VAOD at the 3.5 km or 5.0 km is 0.033, 0.034 respectively. It shows in good agreement with the measured VAOD. The obtained value is also in reasonable agreement with those of HiRes [78]. In the FD analysis, the typical value shown in Fig 3.27 are used for the attenuation of the Mie scattering.

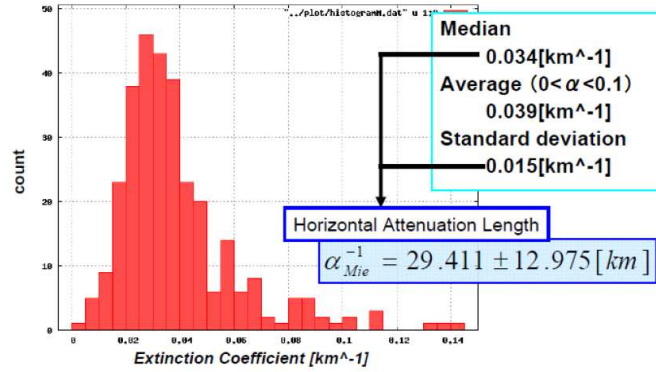


Figure 3.27: The histogram of the extinction coefficient for Mie scattering on the ground. The median value 0.034 km^{-1} is equivalent to the attenuation length of 29.411 km.

3.4.3 CLF

The central laser facility (CLF) was installed at the center of TA site with the same distance 20.85 km far from all three stations and shooting the vertical UV laser same as LIDAR (355 nm, 5 mJ). Side scattered photons can be measured by three stations to monitor the relative gain and atmospheric condition every 30 minute. Fig. shows the CLF system and inside picture of CLF.



Figure 3.28: The CLF system located at the center of TA (left) and the inside picture of CLF (right).

Additionally, the LIDAR system has been installed at CLF location in September 2010. When shooting the laser, the back-scattered photons are detected at the ground. Thus, the telescope system same as LIDAR was set up to measure back scattered photons from CLF laser. Fig. 3.29 shows the image of LIDAR system and the typical result of VAOD measured by both LIDAR systems located at BRM and CLF. While the LIDAR at BRM operates in the time to start and finish every observation, CLF is shooting the laser every 30 minutes. Since these results are consistent and complementary, we can use the atmospheric parameter with better time resolution in near future.

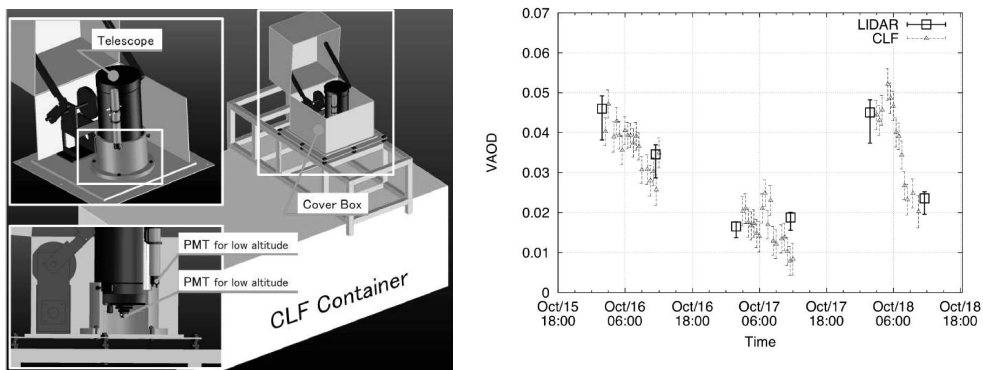


Figure 3.29: The image of LIDAR system installed at the CLF location (left) and VAOD relationship measured by CLF and LIDAR (right).

3.4.4 Cloud Monitoring

When the sky is covered with the cloud, the fluorescence light cannot be measured by fluorescence detector caused by cloud shielding. Thus we need to know whether there is cloud or not in the FOV.

WEAT Code

In order to know the cloud existence in the sky, an operator of the MD station is monitoring the mount of cloud by own eyes every one hour. The recorded code is called as the “WEAT code”. The code consists of whether there is the cloud or not in the North, East, South, West and Overhead recorded 0 or 1, the ratio of area covered by cloud recorded from 0 to 4, 4 is full sky, and haze recorded by 0 or 1. The monitoring method is the same as that of HiRes experiment [50]. Since the measurement have been started at the beginning of MD observation, the code is available in all observation term. Thus the information of WEAT code of the cloud South and East is used in BRM and LR FD analysis. We analyze the data with which the total score of south and east direction is less than 2.

IR Camera

The TA has been installed the infrared camera (Avio TV S-600) which is sensitive in a infrared wavelength of $8 \sim 14 \mu\text{m}$ to monitor a temperature of the atmosphere inside FOV. The camera and taken pictures are shown in Fig. 3.30. If there is the cloud in the sky, the cloud region is relative higher temperature than the sky area. The camera measured the temperature in a field of view $25.8^\circ \times 19.5^\circ$ moving to 14 direction every 1 hour. The 12 directions are the almost same direction with the FOV of FD, and the others are horizontal and vertical pictures.

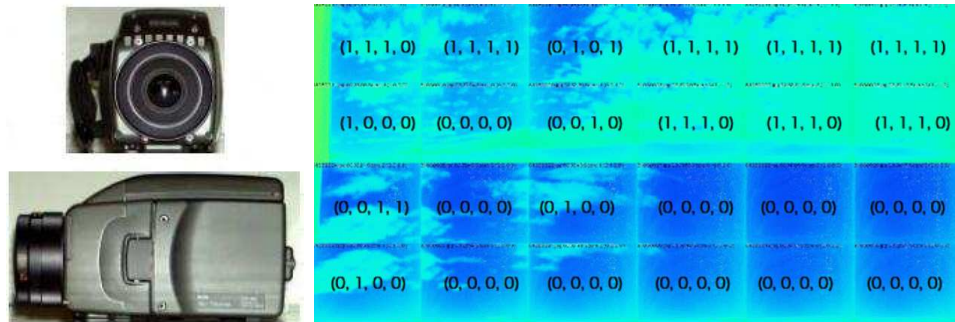


Figure 3.30: The overview of IR camera (left). The right figure is the 12 photographs taken by each telescope directions of FD. The number shows the analyzed cloud score on 4 horizontally categorized regions.

The IR camera and photograph taken by IR camera are shown in Fig. 3.30. In the data analysis each IR picture is divided into 4 regions in the horizontal direction. Using temperature information, the each picture is scored from 0 to 4. The score of 4 means full cloud while 0 is clear night. Although the IR camera is not always operating all observation because of a trouble and a repair of device, we confirmed the score of WEAT code is consistent with IR camera score [80].

CCD Fish-eye

In Jan 2012, the charge coupled device fish-eye has been installed at CLF, BRM and LR station. The CCD fish-eye consists of the CCD (1/2" WAT-120N+, Watec Vedeo output), fish-eye lens (FE185C057HA-1, Fujinon). During the moonless night, the camera takes pictures with the full sky FOV. Fig. 3.31 shows the overview of CCD fish-eye and photographs taken at CLF, BRM and LR with the star name and the FOV of FD. If the sky is covered with some clouds, we cannot see the star so that we recognized whether there is cloud in the sky or not. Moreover the "stereo" observation which is used more than two CCD fish-eye data can be reconstructed the altitude of cloud. Since recently started full operations, we are steadily collecting the data enough to analyze.

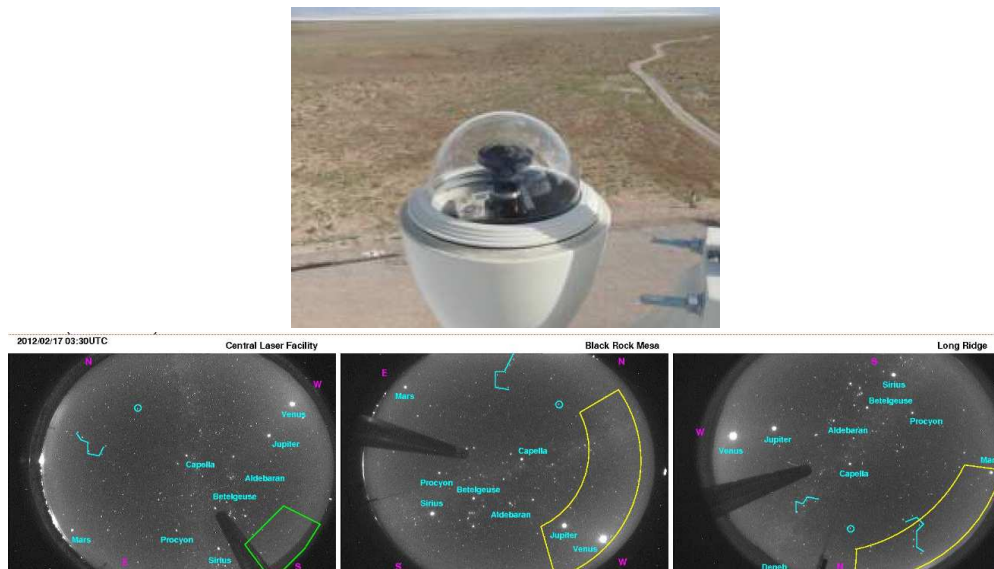


Figure 3.31: The photo of CCD fish-eye at LR station and picture taken at CLF, BRM and LR location. The yellow region shows the FOV of each FD, the green region shows the cover of CLF-LIDAR for online monitoring.

3.4.5 Star Analysis

Stars are a useful light source to calibrate the line of sight direction of each telescope and PMT. When FD station is triggered with 2-4 Hz, all PMT waveforms of 12 camera are collected at short intervals. Thus, a variation of BG level from star light are steadily observed by FD. In general, since each PMT has the FOV about 1° , the BG level of FADC are increased during 5 minute. Since we can evaluate star directions from star catalogs at given time, geometries of FD are calibrated from these directions. Many types of star catalogs from various star observations were already released. In this analysis, we used a planet position catalog [89], a visible star catalog [90] and stellar flux catalog in ultra-violet catalog [91].

Parallel rays from a star inside FD FOV make a spot on the camera. From ray-tracing simulation discussed in section 4.2.1, the spot radius is estimated of 21 mm (68% C.L.) on the camera center with the ideal alignment accuracy. The actual spot radius might be larger than the ideal value owing to the alignment accuracies of FD. To evaluate these accuracies by ray-tracing simulation, mirror reflected photons are a 2-dimensional Gaussian distribution with a standard deviation. This standard deviation is called as Spot Size Parameter (SSP). Fig 3.32 shows the simulation of star transition by of the ray-tracing of parallel photons with several SSP. The red square, blue circle and black triangle indicate the simulation result with $SSP = 0.0$, 0.1 and 0.2 , respectively.

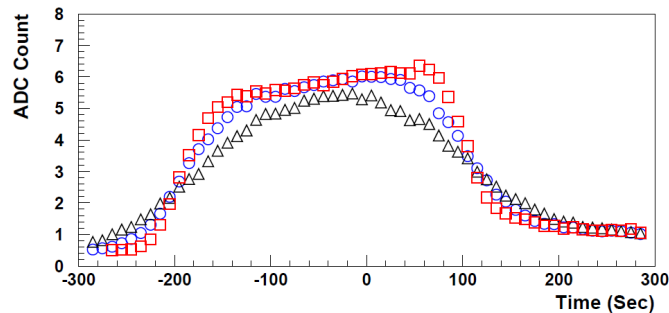


Figure 3.32: Simulation results of time variance of BG level with the different SSPs. Red square: $SSP = 0.0$ degree, Blue circle: $SSP = 0.1$ degree, Black triangle: $SSP = 0.2$ degree.

To obtain SSPs for each FD, we compare observed time variance of BG level with these simulated ones. Fig. 3.33 shows an example of fit result, and this fitting provides the best fit SSP value of 0.200 degree. From the fitting, we obtained SSP value for each FD. As result of the star analysis, the accuracy of FD telescope direction is 0.01 degree, and the accuracy of each PMT direction is within 0.1 degree.

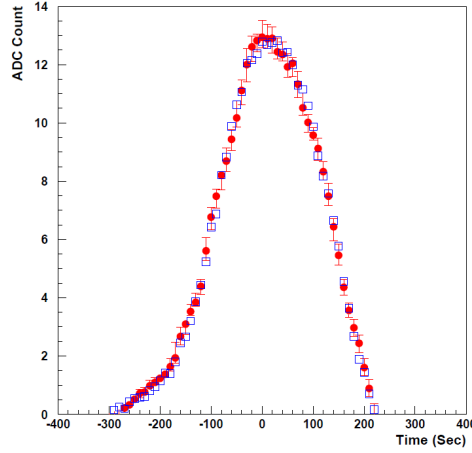


Figure 3.33: Fitting sample of BG level time variance (BRM00). Error bars of observed data show their statistical errors. Circle: observed, Square: simulated.

3.4.6 The End-to-End Absolute Energy Calibration

The electron light source (ELS) is a unique and first of its kind apparatus that can be used for end-to-end absolute energy calibration at BRM [36].

Fig. 3.34 shows the ELS located 100 m far from BRM station, and can fire an upward going electron beam through the FOV of the telescopes. The typical output beam consists of about $40 \text{ MeV} \times 10^9$ electrons per pulse with 0.5 Hz and its water cooling system in 40-ft and 20-ft container, respectively (see Fig. 3.35). The fluorescence light from ELS corresponds to photons emitted from 10^{20} eV shower injected 20 km far from BRM. Since the fluorescence photons from electron beams are the identical phenomena emitted from EAS, the FDs can be calibrated all detector components, for example, fluorescence yield, mirror reflectance, filter transmittance, PMT gain. When the ELS calibration can be achieved at BRM site, a systematic uncertainty of FD is dramatically smaller than before. We have started the ELS beam operation in September, 2010. The event display observed by FD from the first shot of ELS is shown in Fig. 3.36

3.5 Surface Detector

The 507 surface detector (SD) have been deployed 1.2 km separations in Utah desert with covering 700 km^2 . Fig. 3.37 shows the deployed SD which consists of a scintillator box, a communication antenna and solar panels [82]. The schematic view of inside the scintillator box is shown in Fig. . Each surface detector consists of two layer of plastic scintillator which has 3 m^2 effective area and a thickness of 1.2 cm. A 1 mm stainless-steel plate is inserted in between

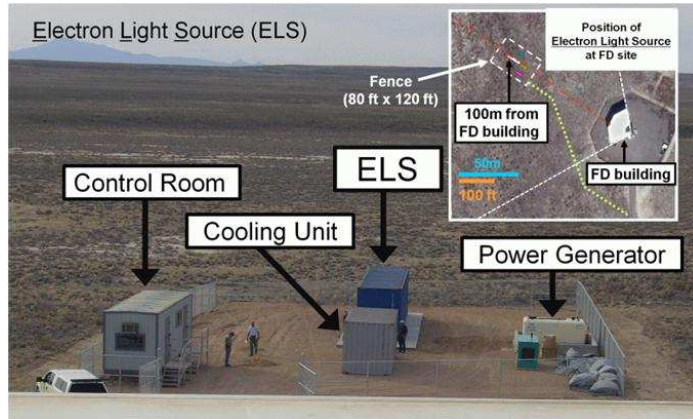


Figure 3.34: The photos of ELS installed at BRM site.

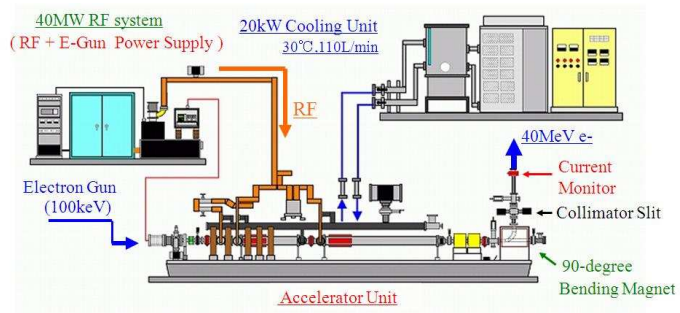


Figure 3.35: The schematic view of ELS system.

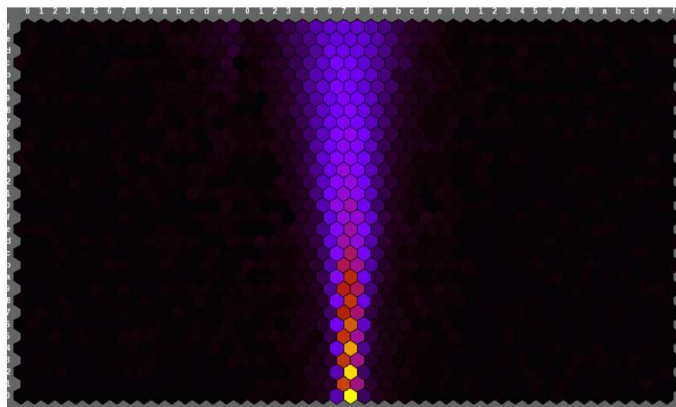


Figure 3.36: The event display of the first ELS beams observed by FD.

layers. A scintillation light is collected through 104 wavelength shifting (WLS) fibers that are 5 m distance (Y-11, KURARAY Co. Ltd.) and laid on each layer. The fibers along the grooves connect to a PMT (9124SA, Electron Tubes Ltd.) and convert the photons to signal.



Figure 3.37: The surface detector deployed TA site.

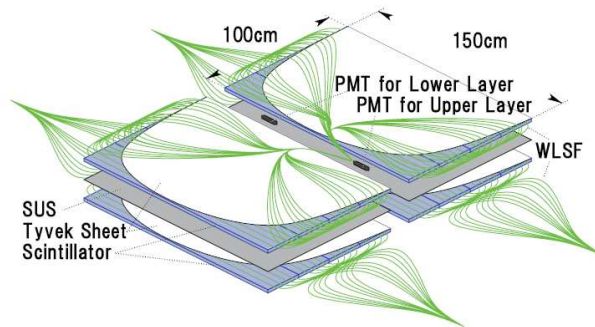


Figure 3.38: Inside of a scintillator box with scintillator plates, WLS fibers and PMTs. A total 104 WLS fibers are laid on each layer to collect and transmit scintillation light.

Fig. shows the detector electronics for the scintillator counter installed in a stainless-steel box under the solar panel. The output signals from PMTs are digitized by a 12 bit FADC (AD9235RU-65, Analog Devices Co.) with a 50 MHz sampling rate on the CPU board (SH4, Renesas Electronics Co.). Signals greater than approximately 0.3 minimum ionizing particles (MIP) are stored in a memory buffer on CPU board as LEVEL-0 trigger data. The stored waveform

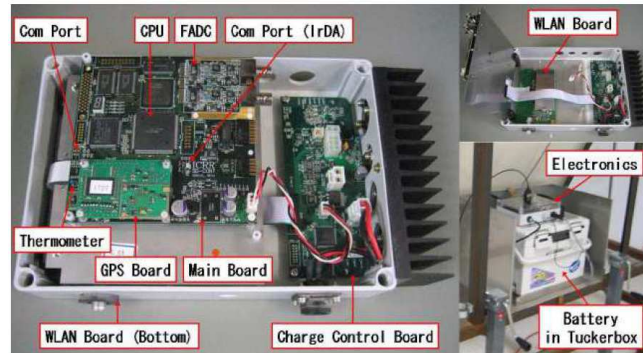


Figure 3.39: The electronics of TA SD.

is $2.56 \mu\text{sec}$ long (128 FADC bins). Signals greater than 3.0 MIP are recorded as Level-1 trigger events which are sent to the trigger decision electronics at the communication tower via a wireless LAN modem (ADLINK540F, ADTEC. Co) using a custom made communication protocol [81]. The local trigger rate of single SD is $\sim 750 \text{ Hz}$ for Level-0 trigger and $\sim 30 \text{ Hz}$ for Level-1 trigger.

The synchronization of electronics of the surface detectors is done by 1 PPS signal received by GPS units (Motorola M12+ oncore module) like FD. A time stamp with a precision of about 20 nsec is created by the 50 MHz sub-clock on the main board. Each SD is powered from one solar panel (KC125J, KYOCERA corp.) and one deep cycle battery (DCS100, C&D Technologies, Inc). The charging battery is controlled by home made charge control board that works with main CPU board. The solar panel system provides a sufficient power required from the electronics ($\sim 5 \text{ W}$).

One of the three communication towers of TA is shown in Fig. 3.40, which is located at near BRM FD station. The schematic view of three tower locations and connections is shown in Fig. 3.41. They play a role of the collection of trigger informations from the SDs and providing communications for the FD stations and CLF site. The data communication between the trigger decision electronics at communication towers and SDs is done by 2.4 GHz wireless LAN. The trigger decision electronics at each communication tower requests the SD to send its Level-1 trigger list and the total counts of the sub-clock between PPS signals. From the lists, an air shower trigger is generated when three adjacent SDs are coincident within $8 \mu\text{sec}$.

Fig. 3.42 shows a current trigger pattern of three adjacent SDs with Level-1 trigger, called Level-2 trigger. With this trigger, the data of waveform of SDs will be collected to the communication towers. The trigger electronics collects waveforms coincident within $\pm 32 \mu\text{sec}$ from the trigger timing. When the Level-2 trigger is generated within one sub-array, the trigger time information is transmitted to the central trigger decision process running at the data acquisition PC (TS7800, Technologic System Co. Ltd.) in the tower. From



Figure 3.40: The Black Rock Mesa communication tower, one of three in the array. There are three stands each with solar panels. Those stands contain batteries, data acquisition PC and network instruments for long distance link.

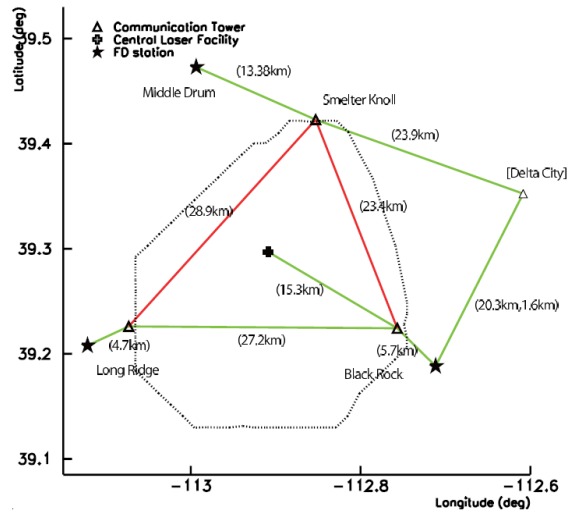


Figure 3.41: The long-distance links for all the facilities and three FD stations in the entire TA site. The open triangles represent the communication towers where the trigger decision electronics for sub-arrays are installed. The lines that connect the towers and facilities represent the links between antennas. The red lines are used for trigger decision. The dotted line shows the border of the entire surface detector array [82].

the one tower triggered, the trigger signal is distributed to the other towers. Thus, when the air shower impacts at the border of sub-array, data of the other

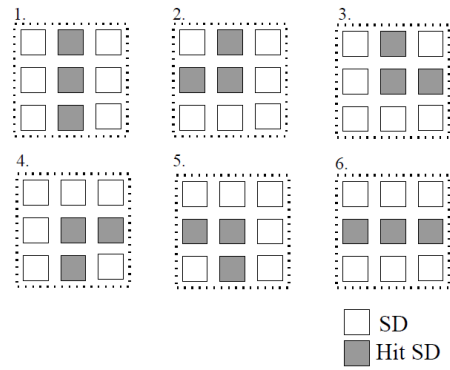


Figure 3.42: Trigger pattern taken at the TA surface array. If any three adjacent SDs have timing difference within $8 \mu\text{sec}$ the trigger will be generated.

sub-array were collected by the board-casting of trigger. Fig. 3.43 is an event display and measured waveforms of a typical air shower triggered across the border of sub-array.

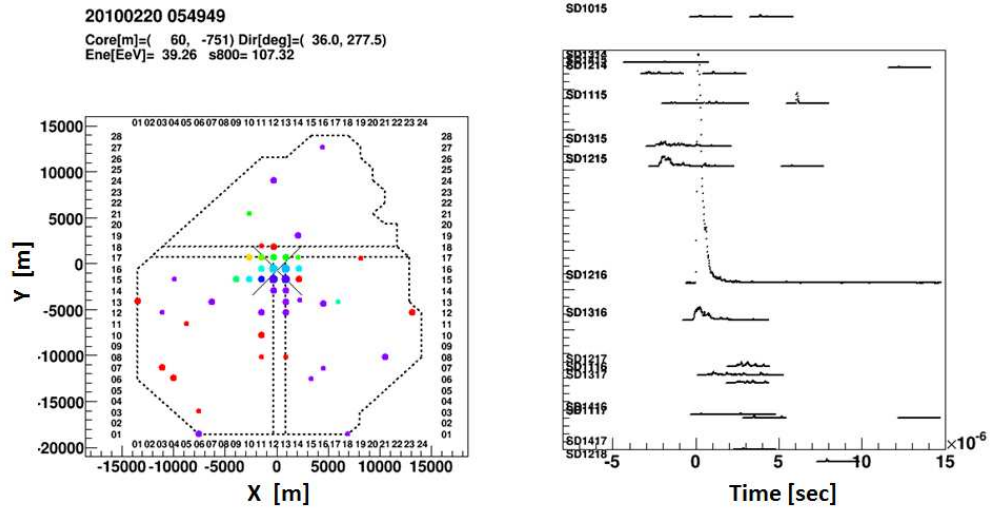


Figure 3.43: Typical air shower event and recorded waveforms triggered across the border of sub-array. The event display of observed air shower (left) and observed waveforms (right).

Chapter 4

TA FD Detector Simulation Software

In order to estimate performance and aperture in monocular mode, we developed a detector Monte Carlo software. In this chapter, we explain how to simulate the signal detected on PMT camera. The simulation software consists of the shower generation, photon emission processes and each waveform calculation on the PMT considering the details of detector structure.

4.1 Extensive Air Shower Generation

4.1.1 CORSIKA shower simulation

At first, we simulate air shower developments. Air shower developments in the atmosphere are given by the CORSIKA air shower simulation [33]. CORSIKA (cosmic ray simulations for KASCADE) is the most popular to simulate the EASs initiated by high energy cosmic ray particles originally made for KASCADE experiment. CORSIKA can treat many kind of primary particles as protons, light nuclei up to iron and photons, take various model of particle interaction. For hadron interaction models, GHEISHA and FLUKA are available at low energy region and VENUS, QGSJET, DPMJET, SIBYLL, neXus and EPOS are adopted at high energy region. For electromagnetic interactions, EGS4 or the analytical NKG formula can be used. Options for the generation of Čerenkov radiation and neutrinos are also available in CORSIKA.

In the FD shower library, the primary particles are considered as only protons or irons because the resolution of composition is not enough clear to separate in the nuclei level. Thus, the composition model is assumed as pure protons or pure irons. Moreover QGSJET-II and SIBYLL models are adopt as the hadron interaction model. The QGSJET model is based on the Gribov-Regge theory [85] [86], while SIBYLL is a mini-jet model [87]. The most influence factor of shower developments are an inelastic cross-section and the energy spectrum of forward emitted particles. However, those cannot be measured by

the present accelerator and are just extrapolated. In near future, it is expected to measure the cross-section and the energy spectrum of forward particles in the energy region up to 10^{17} eV by the LHCf experiments [88].

In general, U.S. standard atmosphere are adopted, in which atmospheric density is given by

$$T(h) = \begin{cases} a_i + b_i \exp(\frac{-b}{c_i}), & i = 1, 2, 3, 4 \\ a_i - b_i \frac{h}{c_i}, & i = 5 \end{cases} \quad (4.1)$$

where h is the height and parameters are shown in Tab. 4.1.

Layer i	altitude h km	a_i g/cm ²	b_i g/cm ²	c_i cm
1	0 - 4	-186.5562	1222.6562	994186.38
2	4 - 10	-94.919	1144.9069	878153.55
3	10 - 40	0.61289	1305.5948	636143.04
4	40 - 100	0	540.1778	772170.16
5	100 <	0.01128292	1	10^9

Table 4.1: Parameters of the U.S. standard atmosphere

To reduce a computing time, the thinning option is applied in which particles with energy below the thinning factor of primary energy are grouped as the weighted particle. Moreover, particles with energy below the E_{cut} are not traced. In the case of FD shower library, thinning factor of 10^{-4} is enough to simulate the shower developments because the distribution of shower parameters such as X_{max} almost the same as the case of 10^{-5} , 10^{-6} . The parameters of air shower simulation are shown in Table 4.2.

Model	QGSJET-II, SIBYLL
Energy range	$10^{17} \sim 10^{20}$ eV
Zenith angle	0 \sim 65 degree, uniformly
Azimuth angle	0 \sim 360 degree, uniformly
Thinning factor	10^{-4}
E_{cut}	100 keV for electromagnetic component 100 MeV for hadronic component
Number of showers	500 events per $d \log E = 0.1$

Table 4.2: Parameters of air shower simulation using CORSIKA.

CORSIKA gives particle distributions at the ground and longitudinal profiles. Longitudinal profiles at each atmospheric depth are mainly divided in two parts, the number of particles and energy depositions. For the number of particles, γ , e^+ , e^- , μ^+ , μ^- , hadrons and nuclei are taken into account. In the energy depositions, γ energy cut, ionization and energy cut of e^\pm , μ^\pm , hadrons

and nuclei are given, where energy cut is the total energy of particles with energy below the given threshold level. For the fluorescence technique, the energy deposits can be applied because they are proportional to the number of fluorescence photons in principle. Thus, the information for each slant depth is defined as “segment” and stored energy deposit, position, shower age and slant depth which use in the calculation of photon emission. Some characteristic parameters of longitudinal profile, X_{\max} , N_{\max} , X_{int} , are also given as fitting parameters of Gaisser-Hillas function.

Missing Energy

Neutral particles, mainly neutrinos and neutrons, do not emit fluorescence photons. Thus, FD can not measure energies of these neutral particles and the total calorimetric energies, E_{cal} , are smaller than primary energies E_0 . The discrepancy of energy is defined as “Missing Energy” E_{miss} which is given by

$$E_{\text{cal}} = E_0 - E_{\text{miss}}. \quad (4.2)$$

The missing energies are estimated from the CORSIKA simulation and correct

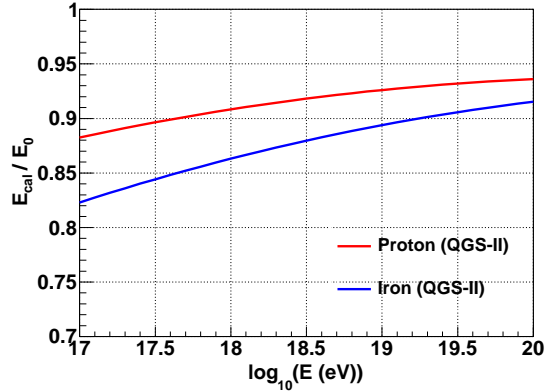


Figure 4.1: The ratio between calorimetric energies and primary energies as a function of primary energies for primary protons and irons using the QGSJet-II hadron interaction model. The calorimetric energies are estimated from an integration of energy deposits fitted by the Gaisser-Hillas function.

to calorimetric energies observed by FD. In the CORSIKA simulation discussed as section 4.1.1, missing energies for primary protons and irons are shown in Fig. 4.1. Fig. 4.1 also indicates the ratio between an integration of energy deposits fitted by the Gaisser-Hillas function and primary energies for primary protons (red) and irons (blue) using the QGSJet-II hadron interaction model. In FD analysis, the missing energies for primary protons are adopted to estimate the primary energies. Thus, the discrepancy of missing energies between

primary protons and irons is 5%, which is considered as systematic uncertainty of the primary energy.

In next step, the number of photons emitted from fluorescence and Čerenkov physical processes is calculated from each segment information. There are three processes for photon emission from EAS: fluorescence light, direct Čerenkov light and scattered Čerenkov light Fig. shown in 4.2).

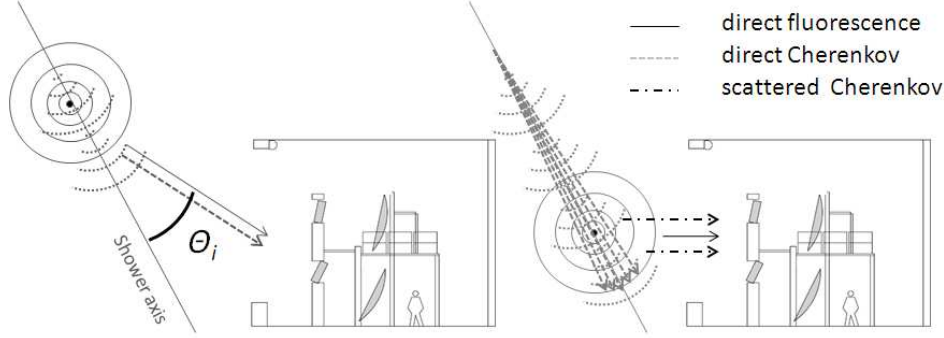


Figure 4.2: The photon emission processes from extensive air showers. Not only fluorescence light, but also direct Čerenkov light and scattered Čerenkov light.

4.1.2 Fluorescence Light Emission

The number of fluorescence photons $N_{i\lambda}^{\text{Fl}}$ for each wavelength λ are calculated from the energy deposit $\frac{dE_{\text{dep.}}}{dX}$ stored in each segment.

$$N_{i\lambda}^{\text{Fl}} = \frac{dE_{\text{dep.}}}{dX} Y_{i\lambda}^{\text{Fl}}(H_i) S_{\lambda}^{\text{Fl}}(H_i) dl_i \quad (4.3)$$

where i is the ID of segments, $Y_{i\lambda}^{\text{Fl}}(H_i)$ and $S_{\lambda}^{\text{Fl}}(H_i)$ are the fluorescence yield and emitted spectrum on its height H_i , dl_i is the length of segment. Since the fluorescence photons are emitted isotropy, the number of photon $N_{i\lambda}^{\text{Fl,tel}}$ injected to telescope is calculated by

$$N_{i\lambda}^{\text{Fl,tel}} = N_{i\lambda}^{\text{Fl}} T_{i\lambda}^{\text{Rayleigh}}(r_i) T_{i\lambda}^{\text{Mie}}(r_i) \frac{A_i}{4\pi r_i^2}, \quad (4.4)$$

where r_i is the distance from the segment to the telescope, $T_{i\lambda}^{\text{Rayleigh}}(r_i)$ and $T_{i\lambda}^{\text{Mie}}(r_i)$ are a transmittance for the wavelength λ propagating the distance r_i of Rayleigh scattering and Mie scattering, respectively. A_i is an effective area of the telescope. The effective area discussed here is defined as an area assumed the combined mirror as a single spherical mirror.

4.1.3 Direct Čerenkov Light

The number of Čerenkov photons is also estimated from energy deposit stored segment same as fluorescence. The calculation of Čerenkov needs the number of electrons, and then the energy deposit should be divided the mean ionization loss rate $\alpha_{\text{eff}}(s)$ simulated by CORSIKA.

$$\alpha_{\text{eff}}(s) = \frac{c_1}{(c_2 + s)^{c_3}} + c_4 + c_5 \cdot s, \quad (4.5)$$

where $c_1 = 3.90883$, $c_2 = 1.05301$, $c_3 = 9.91717$, $c_4 = 2.41715$ and $c_5 = 0.13180$ [63].

In contract to fluorescence photon, the emitted spectrum depends on the shower age parameter in Čerenkov. Moreover only electrons with energies above their threshold radiates Čerenkov photons. Thus, the energy spectrum $f_e(E, s)$ of an individual shower with shower age s and energy E is parameterized as

$$f_e(E, s) = a_0 \cdot \frac{E}{(E + a_1)(E + a_2)^s} \quad (4.6)$$

where a_0 , a_1 , a_2 are the same parameter described in [63]. Then, the number of photon is calculated by

$$N_{i\lambda}^{\text{C}} = \frac{1}{\alpha_{\text{eff}}(s)} \frac{dE_{\text{dep}}(x)}{dX} \int_{\ln E_{\text{thr}}} Y_{i\lambda}^{\text{C}}(H_i, s_i, E) S_{i\lambda}^{\text{C}}(H_i, s_i, E) \Delta l_i f_e(E, s) d \ln E. \quad (4.7)$$

where $Y_{i\lambda}^{\text{C}}(H_i, s_i)$ and $S_{i\lambda}^{\text{C}}(H_i, s_i)$ is Čerenkov yield and emitted spectrum with shower age s_i and energy E , H_i is the altitude of the segment. Moreover the Čerenkov light depends on the angular distribution. Therefore the good approximation are applied in the Čerenkov angular distribution D_i^{C} ,

$$D_i^{\text{C}}(\theta_i) = \frac{1}{\theta_0} \exp\left(-\frac{\theta_i}{\theta_0}\right) \quad (4.8)$$

where θ_i is the angle between shower axis and emitted direction, θ_0 is a parameter determined from an threshold energy of Čerenkov light, $\theta_0 = a E_{\text{thr}}^{\text{C}-b}$, $(a, b) = (0.83, 0.67)$ [63]. Additionally considering the atmospheric scattering, the number of Čerenkov photons $N_{i\lambda}^{\text{C,tel}}$ is estimated as

$$N_{i\lambda}^{\text{C,tel}} = N_{i\lambda}^{\text{C}} T_{i\lambda}^{\text{Rayleigh}}(r_i) T_{i\lambda}^{\text{Mie}}(r_i) \frac{2}{\sin \theta_i} \frac{A_i}{4\pi r_i^2} D_i^{\text{C}}(\theta_i). \quad (4.9)$$

4.1.4 Scattered Čerenkov Light

The observed Čerenkov photons at PMT camera include not only the direct injected photons but also scattered photons by atmospheric molecule and aerosol, called scattered Čerenkov photons. Since Čerenkov photons are accumulated by each segments, the scattered photons number is proportional to an integration of Čerenkov photons along the shower axis from the top of atmosphere.

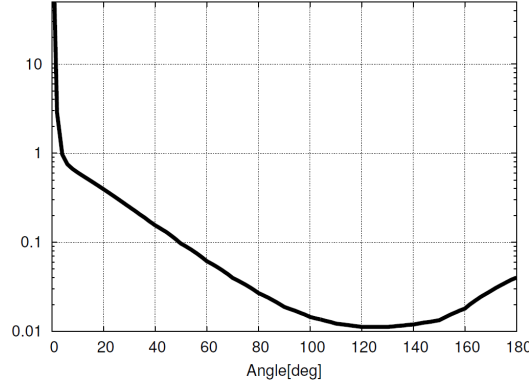


Figure 4.3: The phase function of Mie scattering observed at the HiRes site, Dugway [83].

The total number of Čerenkov photons $N_{i\lambda}^{\text{C Total}}$ with i segment is calculated the sum of emitted Čerenkov photons in this segment and the integrated Čerenkov photons before this segments,

$$N_{i\lambda}^{\text{C Total}} = N_{i\lambda}^{\text{C}} + N_{i-1}^{\text{C pass}}, \quad (4.10)$$

From total integrated photons $N_{i\lambda}^{\text{C Total}}$, scattered photons by Rayleigh process $N_{i\lambda}^{\text{RayC}}$, Mie process $N_{i\lambda}^{\text{MieC}}$ and photons transmissive photons to next segment $N_{i\lambda}^{\text{C pass}}$ are calculated.

$$N_{i\lambda}^{\text{C pass}} = N_{i\lambda}^{\text{C Total}} T_{i\lambda}^{\text{Rayleigh}}(dl_i) T_{i\lambda}^{\text{Mie}}(dl_i) \quad (4.11)$$

$$N_{i\lambda}^{\text{RayC}} = N_{i\lambda}^{\text{C Total}} \left[1 - T_{i\lambda}^{\text{Rayleigh}}(dl_i) \right] T_{i\lambda}^{\text{Mie}}(dl_i) \quad (4.12)$$

$$N_{i\lambda}^{\text{MieC}} = N_{i\lambda}^{\text{C Total}} T_{i\lambda}^{\text{Rayleigh}}(dl_i) \left[1 - T_{i\lambda}^{\text{Mie}}(dl_i) \right] \quad (4.13)$$

and, considering difference of angular distribution, called phase function, of Rayleigh and Mie processes, we calculate the number of photons injected from the segment to telescopes.

$$N_{i\lambda}^{\text{RayC, tel}} = N_{i\lambda}^{\text{RayC}} T_{i\lambda}^{\text{Rayleigh}}(r_i) T_{i\lambda}^{\text{Mie}}(r_i) \frac{A_i}{4\pi r_i^2} D_i^{\text{Ray}}(\theta_i) \quad (4.14)$$

$$N_{i\lambda}^{\text{MieC, tel}} = N_{i\lambda}^{\text{MieC}} T_{i\lambda}^{\text{Rayleigh}}(r_i) T_{i\lambda}^{\text{Mie}}(r_i) \frac{A_i}{4\pi r_i^2} D_i^{\text{Mie}}(\theta_i) \quad (4.15)$$

Here, the phase function of Rayleigh scattering, D^{Ray} , is theoretically given by

$$D^{\text{Ray}} = \frac{3}{16\pi} (1 + \cos^2 \theta), \quad (4.16)$$

and, the phase function of Mie scattering measured at near the TA site, Dugway where HiRes located, is adopted in MC simulations. Fig.4.3 shows the phase function observed at the HiRes site, Dugway [83].

As discussed before, we estimate the number of fluorescence photons, direct Čerenkov and scattered Čerenkov photons from a longitudinal development simulated by CORSIKA. In next step, waveforms detected at PMT camera is simulated using the detector simulation considering the lateral density distribution of EAS.

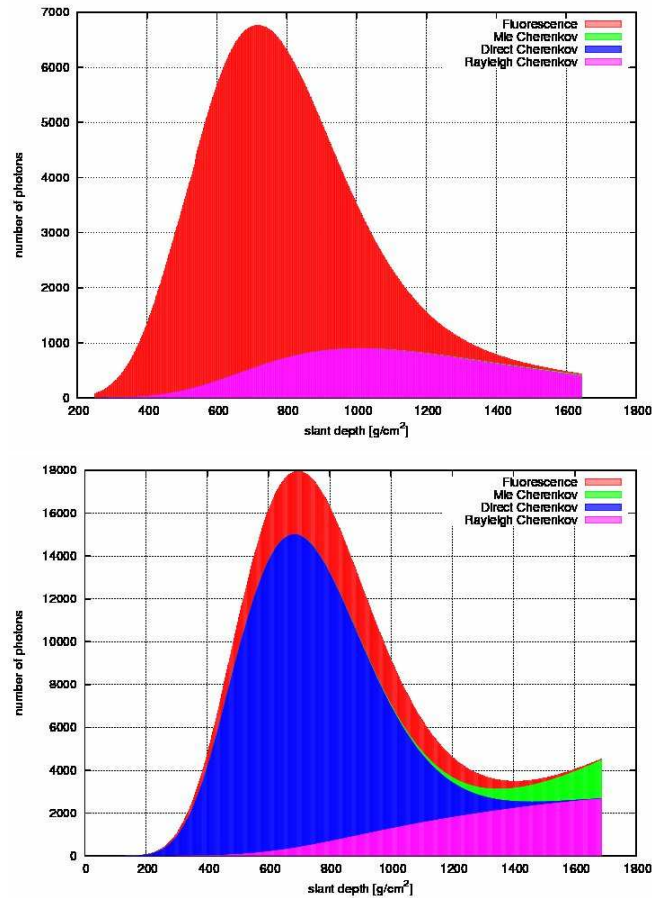


Figure 4.4: The number of fluorescence, direct Čerenkov, Rayleigh scattered Čerenkov and Mie scattered Čerenkov photons injected into telescope. The top figure is the shower geometry across the FOV, the bottom figure is the geometry going toward FD.

Fig. 4.4 represents the contributions of fluorescence, direct Čerenkov, Rayleigh scattered Čerenkov and Mie scattered Čerenkov photons injected to the telescope. The red area shows the number of fluorescence photons, the blue area shows the direct Čerenkov photons, the purple area shows Rayleigh scattered

photons and the green area shows the Mie scattered Čerenkov photons. The top figure shows the result with the geometry across the FOV of FD which is almost fluorescence light and slightly Rayleigh scattered photons at the large slant depth. The bottom figure shows the result with the geometry coming toward FD which has large direct Čerenkov contamination and scattered Čerenkov photons. Thus, the Čerenkov photon is systematic background photons in fluorescence technique.

4.2 TA FD Detector Simulation

4.2.1 Ray-tracing technique

“Ray-tracing” technique is used in TA FD detector simulation in order to estimate the signal detected at PMT camera. In the ray-tracing simulation, a trajectory for each photon is simulated on the reflected point on the mirror and injected point on the PMT camera. Owing to reproduce the real response, the detail structure should be implemented in the software. Fig. 4.5 shows a

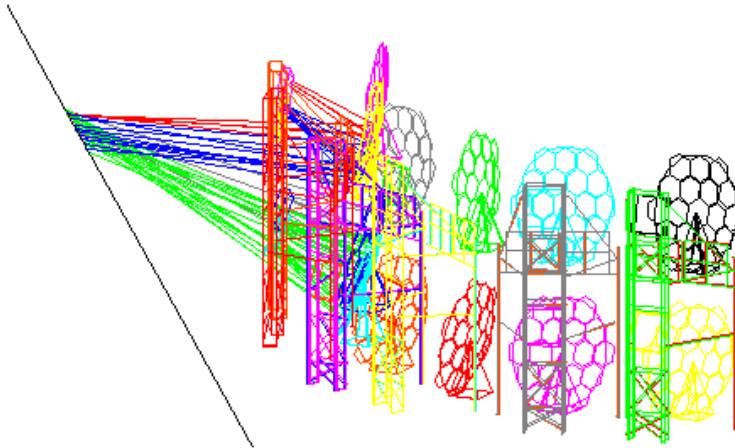


Figure 4.5: The structure of FD implemented in TA FD simulation software with the ray-tracing trajectory emitted from line assumed shower axis.

detail structure of the FD station developed in the simulation software. The combined spherical mirror, supporting columns are implemented in the same as the actual FD station.

The ray-tracing calculation should need the computing power, because all of enormous photons should simulate their trajectory. For the purpose of a shorter calculation time, the number of photons for ray-tracing is multiplied by the factor of the mirror reflectance and the paraglas transmittance for each telescope which depend on the observation time. In concrete terms, the number

of photons injected to PMT camera N_i^{RayTrace} is given by

$$N_i^{\text{RayTrace}} = \int N_{i\lambda}^{\text{p, tel}} R_{i\lambda}^{\text{mirror}} \tau_{i\lambda}^{\text{para}} \tau_{i\lambda}^{\text{BG3}} Q_{i\lambda} d\lambda \quad (4.17)$$

where $N_{i\lambda}^{\text{p, tel}}$ is already derived from (4.4), (4.9) and (4.15), $R_{i\lambda}^{\text{mirror}}$ is the reflectance of the mirror, $\tau_{i\lambda}^{\text{para}}$ and $\tau_{i\lambda}^{\text{BG3}}$ are the transmittance of the paraglas and the BG3 filter, $Q_{i\lambda}$ is the quantum efficiency of PMT. Since a non-uniformity of the PMT cathode is dependent on the injected position, the factor is considered after ray-tracing.

In the beginning of ray-tracing, the position emitted photon is determined by NKG function shown in (2.32). Next, the reflect point is determined a random point inside the mirror effective area. The line is calculated by the emitted point and reflect point and it corresponding to “ray” of the photon. The ray reflects at the mirror and enters PMT camera by tracing. Since the mirror is the combined mirror, when the reflect point is selected the dip of segment mirror or the obscuration structure like the supporting column, the ray-tracing of the photon is finished. Effects of the detector shielding and combined mirror are considered by repeating N_i^{RayTrace} ray-tracing, and the injection point at the PMT cathode is fixed.

After that, to calculate the non-uniformity of the PMT, we multiplied the non-uniformity factor depending on the position of PMT, which is measured by XY-scanner and shown in Fig. 3.12 section 3.3.1.

The injected photons are converted to the photo-electrons, amplified by each PMT gain and digitized by the SDF through the response function. The response function of SDF is shown in Fig. 4.6), the time constant is 50 ns. After injected time is determined by the trajectory of ray, considered the response function, the waveform of PMT is generated by the sum of these signals. Repeating the procedure, all PMT signal from the air shower is calculated and stored in each PMTs.

4.2.2 Night Sky background

The background light is important to calculate the resolution and the performance in fluorescence technique. Thus, the value of mean and dispersion of the background recorded SDF are stored in the database of every 10 minutes. The 10 minutes corresponds to the time during which a star goes through the FOV of a PMT. We use the database to obtain the actual background in our detector simulation. The example of the data in the database is shown in Fig. 4.7.

4.3 Cross Checking of Simulation Software

In the TA collaborator, there are two developed softwares in official. We have compared the results with another independently developed software in order to confirm more confident in our analysis.

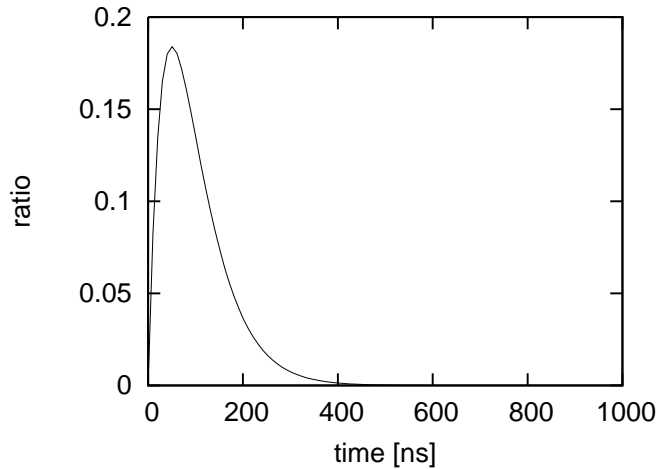


Figure 4.6: The response function of SDF. The time constant is 50 ns.

4.3.1 Photon Emission Processes and Atmospheric Models

First of all, an identical air shower cascade are generated by identical Gaisser-Hillas function with the same parameters. When we implemented the exactly same function, our result should be in perfectly agreement within the computing error. The common parameters are

- Gaisser-Hillas function,
- geometry of shower axis,
- fluorescence yield and spectrum,
- Čerenkov yield and spectrum and
- U.S. atmosphere and the transmittance of aerosol.

By the same method to integrate, we generate the identical “standard” shower using own software. Calculated the factor of attenuation by atmosphere and the contribution from scattered Čerenkov light, the comparison figure of photon density arrived at the mirror is shown in Fig. 4.8. The figure represent the photon density of fluorescence, direct Čerenkov, Rayleigh and Mie scattered Čerenkov photons as a function of slant depth. The another software result is overwriting as the black line with the perfectly agreement. As the result, we confirmed that the exactly same physics model and parameters are implemented in our software.

4.3.2 Comparison of Ray-Tracing

After confirmed perfectly agreement in the photon densities at the mirror, we move to the comparison of ray-tracing. Note that, the ray-tracing is randomly

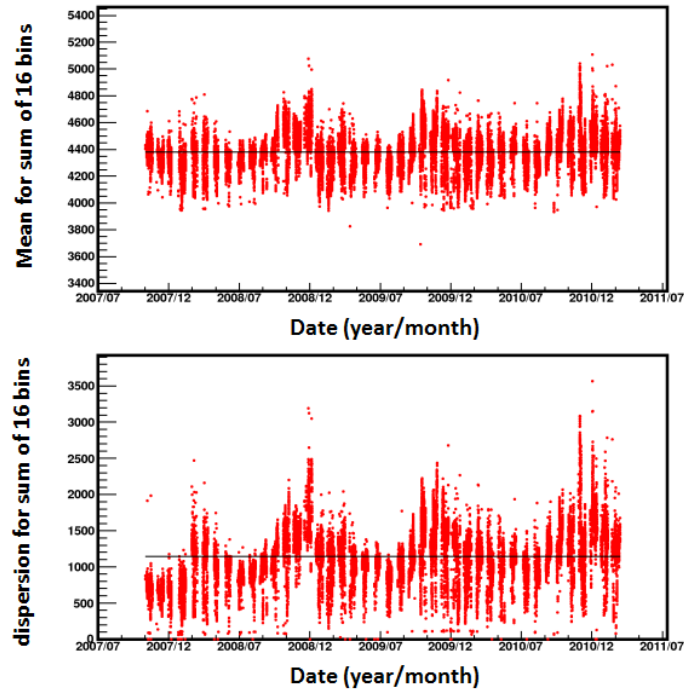


Figure 4.7: The example of the database for the background observed by BRM camera 06. The upper figure shows the mean for 2^{14} “bundles”. The bundle consists of the sum of 16 bins of FADC count and is continuously recorded by SDF. The lower figure represents the dispersion for the same telescope. The black line is the averaged value of the pedestal. The horizontal axis shows the measured data (year/month).

selected the injected point and reflected point to consider the effects of shielding and the dip of segment mirrors. Thus, the standard light source is defined in our software independently, and we compared the injected photon distribution at the camera. Fig. 4.9 show the two-dimensional histogram at the PMT camera by 10000 photons ray-tracing each other. The point of standard light is located at CLF with altitude 4 km (0 km, 0 km, 4 km). Since the telescope direction and structure is compared in this step, the calibration factor, for example reflectance and transmittance, is 100%. While the left figure of Fig. 4.9 is our result, the right figure is another result. We checked the result from the other two point light sources located at (10 km, 0 km, 4 km) and (0 km, -10 km, 4 km). The number of photons injected to camera is in reasonable agreement within 2 % and the distribution of photons is also very similar. Therefore we have confirmed that the telescope directions and the PMT camera alignments are in agreement each other.

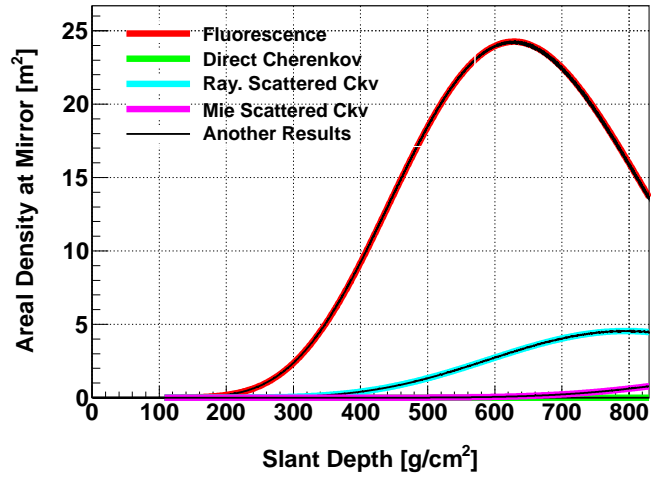


Figure 4.8: the photon density of fluorescence, direct Čerenkov, Rayleigh and Mie scattered Čerenkov photons as a function of slant depth. The black line represents another result with perfectly agreement.

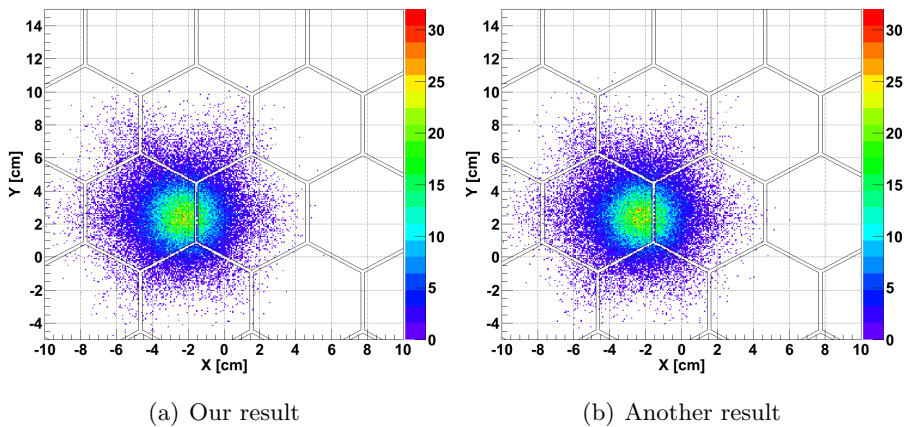


Figure 4.9: The two-dimensional histogram at the PMT camera by 10000 photons ray-tracing using our software(left) and another independently developed software (right). Our results is reasonable agreement with another result.

Chapter 5

TA FD Reconstruction Software

The data measured and recorded by FD consists of digitized waveforms of $51.2 \mu\text{s}$ length from the PMT for each image pixel shown in Fig. 5.1. There are

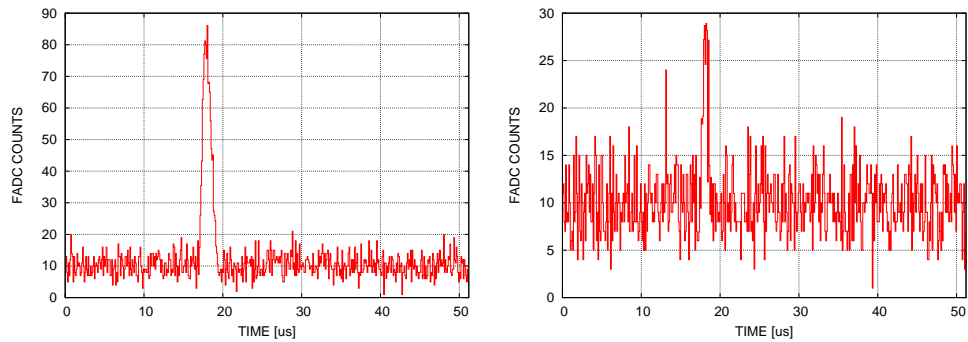


Figure 5.1: The typical waveforms recorded by FD.

three processes to reconstruct an information of primary cosmic rays as follows:

1. PMT Selection,
2. Geometry Reconstruction, and
3. Shower Profile Reconstruction (Inverse Monte Carlo).

For each shower image we distinguish and select air shower signals for further analysis and separate them from noise signals, for example night sky background and artificial light. In the geometry reconstruction, we determine the arrival direction and the core position of air showers. In shower profile reconstruction, we evaluate the energy and the depth of maximum development of air showers. Here, we describe an “Inverse Monte Carlo” method in which we

search for an optimum solution via repeating Monte Carlo (MC) simulations and comparing observed data with MC simulation.

When the FD station is triggered and stored the data, all PMT waveforms are recorded for 12 files of each telescope separately. Since the recorded data are too large (~ 1 TB / month), only waveforms of PMT with a significant signal are picked up, and combined 12 files to a single file. The threshold level of significant is 3σ , and by this procedure, the data size is reduced to about 10%.

5.1 PMT Selection

When a fluorescence light is incident on a PMT, the output current of the PMT is increased during $1 \sim 10 \mu\text{s}$. At first, we selected the PMT which injects fluorescence photons emitted from EAS, and judged to use in the next reconstruction. Moreover, the signal timing and the number of photo-electrons are estimated in this step, which are important in the geometrical reconstruction and the shower profile reconstruction.

5.1.1 1st Selection : Signal Search

The waveform with air shower signal has the triangle shape as shown in Fig. 5.1, called “triangle filter”. Fig. 5.2 shows the schematic diagram of weighted

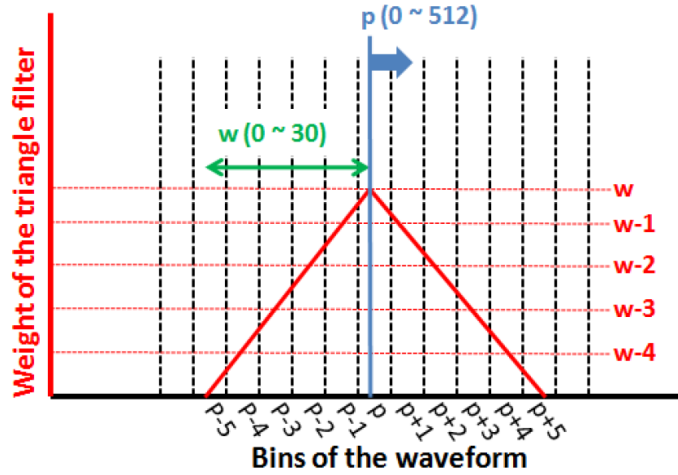


Figure 5.2: The schematic diagram of the weighted triangle filter.

triangle filter in order to search for an maximum significance $\sigma(w, p)$ with peak

p and width w in the waveform,

$$\sigma(w, p) = \frac{\sum_{i=p-w}^{p+w} F_{sub}(i)W(i)}{\sum_{i=p-w}^{p+w} P_{rms}(i)W(i)} \quad (5.1)$$

$$W(i) = w - |p - i| \quad (5.2)$$

where F_{sub} is the i -th bin of waveform subtracted by a pedestal mean, $W(i)$ is the weight, P_{rms} is the pedestal fluctuation. The mean and fluctuation of each pedestal are recorded by SDF. The filter searches for the width w from 0 to 30-th bin and the peak bin p in all of the bins. When the pair of p and w with maximum significance are found, the timing T and its error σ_T are calculated by

$$T = \frac{\sum_{i=p-w}^{p+w} i \times F_{sub}(i)}{\sum_{i=p-w}^{p+w} F_{sub}} \times 100 \text{ ns} \quad (5.3)$$

$$\sigma_T^2 = \frac{\sum_{i=p-w}^{p+w} (T-i)^2 \times F_{sub}(i)}{\sum_{i=p-w}^{p+w} F_{sub}} \times 100 \text{ ns}. \quad (5.4)$$

Here, 100 ns is the bin width corresponding to the 10 MHz sampling. The timing T indicates the center of gravity in the assigned width. If the selected width of a PMT is 30 bins, the PMT is treated as failed fitting for noise PMT and is not used for the analysis. The number of photo-electrons N_{pe} is given by

$$N_{pe} = \text{Gain} \times \sum_{i=p-3w}^{p+3w} F_{sub}(i) \quad (5.5)$$

where $Gain$ is the conversion factor from the FADC count to the number of photo-electrons which is obtained by calibration as discussed in section 3.3.3. The integration area between $p \pm w$ is enough larger than the width of the detected pulse.

The distribution of significance of weighted triangle filter is shown in 5.3 comparing without and with shower signals. The significance distribution without air shower signal is almost less than 6σ , but one with shower signals has a tail at the region of more than 6σ . Thus, we pick up the PMTs with significance more than 6σ as the initial parameters for next step. The PMTs with a slightly significance less than 6σ are used in the 4-th selection as discussed later.

5.1.2 2nd Selection : Line Structure Search

Although the 1st selection can remove almost all noise PMTs, the larger signal noise caused by night sky background is selected by only 1st selection. When air shower signals inject on the PMT camera, the PMTs with shower signals are spatially continued distribution along a line. The line structure can be used in the 2nd selection. In general, a line in X-Y plane is represented by a parameter pair (ρ, ω) as

$$\rho = x \cos \omega + y \sin \omega \quad (5.6)$$

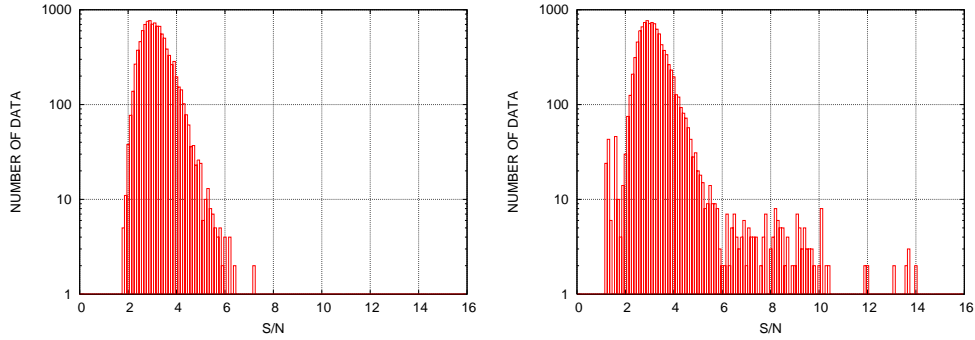


Figure 5.3: The distribution of significance calculated the weighted triangle filter. The left figure is the distribution without air shower signal, the right figure is one with air shower signal.

The $\rho - \omega$ space is called Hough space and this parameterization is called Hough transform. A line group which goes through the same point (x_i, y_i) is shown as the curve line in the Hough space. Therefore the cross point of all curved lines which corresponds to all positions of PMTs is shown as the track line on the PMT direction plane.

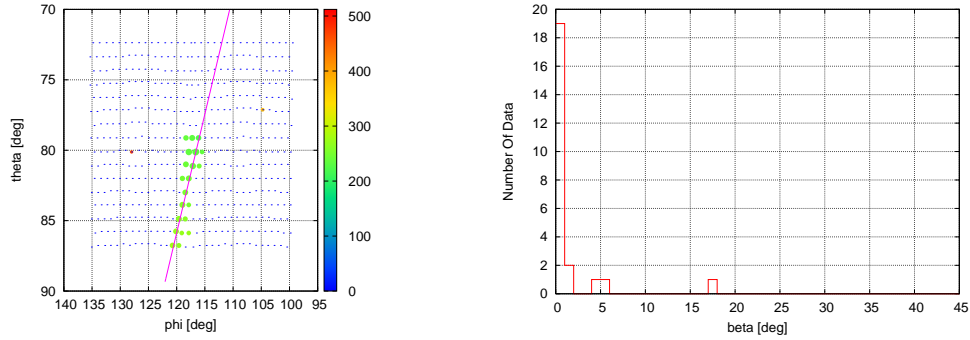


Figure 5.4: The shower track (left) and the distribution of separate angle β (right). While the data from air shower are concentrated at the smaller separate angle, the noise data are not located around zero.

The number of electron is the most around a shower axis, and the number decreases the location far from the axis. Since fluorescence lights emit isotropic photons, the PMT far from shower axis can not inject the fluorescence photons. Therefore the shower track approximately considers the shower line, and the separate angle between line and PMT direction are calculated. The larger separate angle of PMT is defined as the noise PMT, and removed in next step. However, the distribution of separate angle is dependent on a primary energy

and geometry. Thus, the isolated PMT is removed using calculated distribution of separate angle as shown in Fig. 5.4.

5.1.3 3rd Selection : Timing Sequence Search

Although the isolated PMTs far from shower axis were excluded in 2nd selection, the noise PMTs beside shower axis are passed through 2nd selection. Since timings of all selected PMTs are fitted in geometry reconstruction, a geometrical resolution is worse when we select the noise PMT. In the 3rd selection, we use the timing information T_i estimated in 1st selection.

The injected timing of each PMT depends on arrival directions and core locations of air showers. The expected arrival time t_i is represented as

$$t_i = t^* + \frac{1}{c} \frac{\sin \psi - \sin \alpha_i}{\sin(\psi + \alpha_i)} r^* \quad (5.7)$$

where ψ is the angle between the FOV direction of PMT and shower core direction, α_i is elevation angle of PMT direction, t^* is timing when the shower core hits on the ground, r_0 is the distance from FD station to shower core.

In the case of $\phi - \theta$ of the Cartesian coordinates, (5.7) is not exactly approved. However, when α is enough small, it is approximately approved. The separate angle α_i , between the direction vector toward the center of shower track, \mathbf{n}_c and the PMT viewing direction vector $\mathbf{n}_i^{\text{proj}}$ is given by

$$\alpha_i = \cos^{-1} \left(\mathbf{n}_i^{\text{proj}} \cdot \mathbf{n}_c \right) \quad (5.8)$$

The α_i of each PMTs and T_i estimated by (5.7) are fitted, and the isolated PMTs are removed.

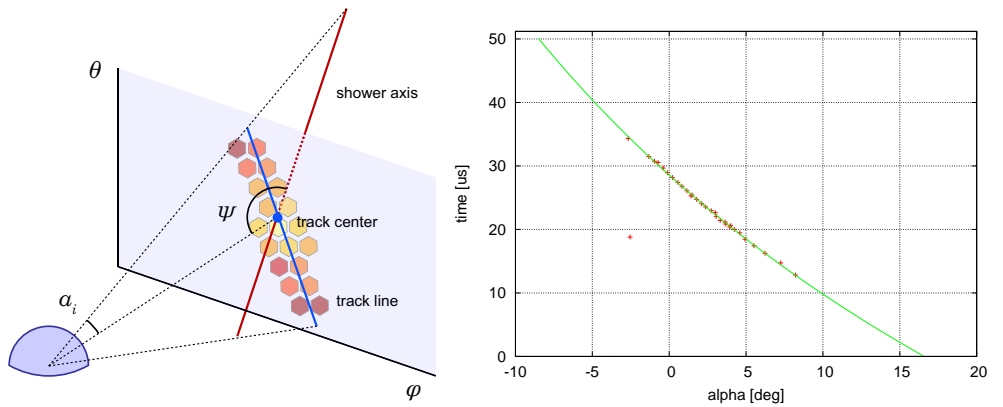


Figure 5.5: Shower track (left) and timing fitting to search for noise (right). In the right figure, isolated PMT (-2.5° , $19 \mu\text{s}$) is judged to noise signal.

5.1.4 4th Selection : Small Signal Research

In this step, we select PMTs by timing information almost same as monocular geometrical reconstruction. By 1st, 2nd, 3rd selection, only PMTs with $> 6\sigma$ significance are selected. Here, we include the PMT with small signals like less than $< 6\sigma$. Moreover the 4th selection works not only for the rejection but also for the addition of the rejected PMTs in the previous selections.

First of all, the elevation angles of the PMT directions on the obtained Shower Detector Plane (SDP) and timing of all selected PMTs are fitted by timing fitting in monocular mode. The details for the timing fit and how to obtain the SDP are described in section 5.2.3.

Next, the timing difference R_i from fitted function, pseudo χ^2 and separate angle with SDP β_i are calculated for all PMTs, including all rejected PMTs in the previous steps.

$$R_i = |f(\alpha_i) - T_i| \quad (5.9)$$

$$\chi^2 = \left(\frac{R_i}{\sigma_{T_i}} \right)^2 \quad (5.10)$$

$$\beta_i = \vec{P}_i \cdot \vec{V}_{SDP} \quad (5.11)$$

where α_i is projected elevation angle to the SDP of i -th PMT, $f(\alpha_i)$ is the obtained timing from the fitted function at α_i , σ_{T_i} is the error of the peak timing obtained by the 1st selection, \vec{P}_i is the pointing vector, \vec{V}_{SDP} is the perpendicular direction on the SDP. These parameters are used for the judgment for addition/rejection of PMTs. These PMTs are categorized by the criteria, which is shown in Tab. 5.1. There are two types of criteria: SOFT and HARD.

item	SOFT	HARD
R_i	$< 1.2 \mu s$	$< 0.8 \mu s$
χ^2	< 20	< 15
β_i	$< 4^\circ$	$< 2^\circ$

Table 5.1: The criteria for selecting the candidate PMTs in the 4th selection.

Firstly, the SOFT criterion is applied in 4th selection. After finished SOFT selection, the same routine is applied again with HARD criterion for the precise selection.

Each categorized PMT is judged by the ‘‘linear’’ fitting of α_i and T_i with the neighboring PMTs, which are selected by the separate angle with the judged PMT $< 5^\circ$ and timing difference $< 5 \mu s$. The time difference from fitted function R_{linear} , pseudo χ_{linear}^2 and the number of used PMTs N_{linear} are used for this judgment. The criteria are shown in Tab. 5.2 The judgment works for rejections for PMTs which have isolated position and timing. When the PMT which is fulfilled in these criteria, this PMT is picked up and the 4th selection starts again. If a PMT which is not in these two criteria, the PMT is rejected,

item	THRESHOLD
N_{linear}	> 3
R_{linear}	$1.2 \mu s$
χ_{linear}^2	20

Table 5.2: The criteria for judgment by the linear fitting in the 4th PMT selection.

and then the 4th selection is also restarted. This iteration is continued until there is no candidate for the addition or rejection of PMT.

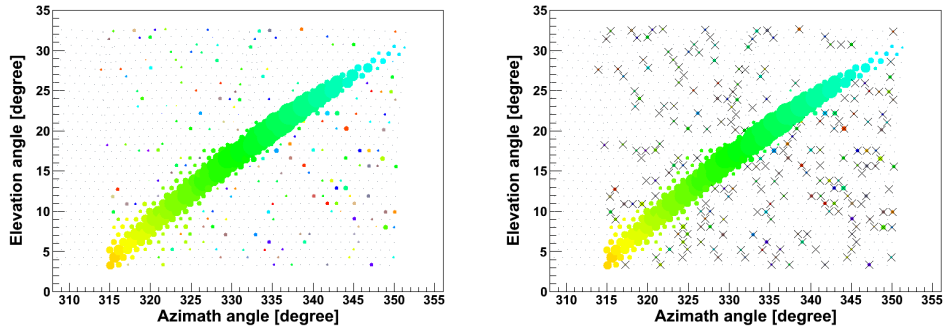


Figure 5.6: The event display observed by FD comparing before(left) and after(right) PMT selections. The noise PMTs are removed by the PMT selection.

Fig. 5.6 shows the event display of actually observed shower candidate at BRM. The data plot represents the PMT viewing direction, the color indicates the injected timing, the size shows the number of photo-electrons. The left figure is the data with $> 3\sigma$ before all selections, and there are many noise PMTs caused by night sky background. In the right figure after applied with 1th to 4th selections, the removed PMTs shows \times mark. Therefore these selection are valid for noise reductions.

5.2 Geometry Reconstruction

In the geometry reconstruction, we determine a shower geometry which is a core position and an arrival direction of air showers. The methods reconstructed by data of two FD stations, called “Stereo mode”, and by data of only 1 station, called “Monocular mode”, are described here. In the both cases, first of all, the station should be determined the Shower-Detector Plane (SDP) which consists of the shower axis and the detector location. In general, the stereo mode is better resolution than the monocular mode, because the two SDPs are estimated

by each station separately.

5.2.1 Estimation of the Line of Sight for Each PMT

In order to estimate the SDP, we must know the line of sight for each PMT. These the line of sight is dependent on not only the location of PMT and the combined mirror, but also the supporting column, the whole structure, its shielding and non-uniformity of PMT. Therefore it is estimated from ray-tracing using the detector simulation.

The simulation is simple, in which the parallel photons inject on the mirror, and hence we estimate the directional characteristic of each PMT. The obtained the directional characteristics are shown in Fig. 5.7. Although the each PMT FOV of the camera is 1° , a distribution of sensitive direction is difference for each PMT caused by a spherical aberration. We calculate a center of gravity of the distribution and use the direction as the line of sight for each PMT. The directional characteristic is also important to calculate faster in Inverse Monte Carlo as discussed later.

5.2.2 Shower-Detector Plane

Shower-Detector Plane (SDP) is the plane consisting of the FD station and a shower axis. The location of FD station is assumed as the single point because the distance between the shower axis and FD station is enough large compared with the distance among telescopes. When the i -th PMT injects photons emitted from EAS, a normal vector of the SDP is perpendicular to all PMT of line of a sight \mathbf{k}^i . Since the air shower photons are detected by several PMTs, the optimal normal vector of SDP is estimated from the minimum value of

$$\chi^2 = \sum_i \frac{w_i (\mathbf{n} \cdot \mathbf{k}^i)^2}{\sigma_i^2} \quad (5.12)$$

where σ_i is the normalize factor of the PMT FOV, $\sigma_i = \sin 0.8^\circ$, w_i is the wight of PMT. The PMTs with larger photons near the shower axis are weighted by

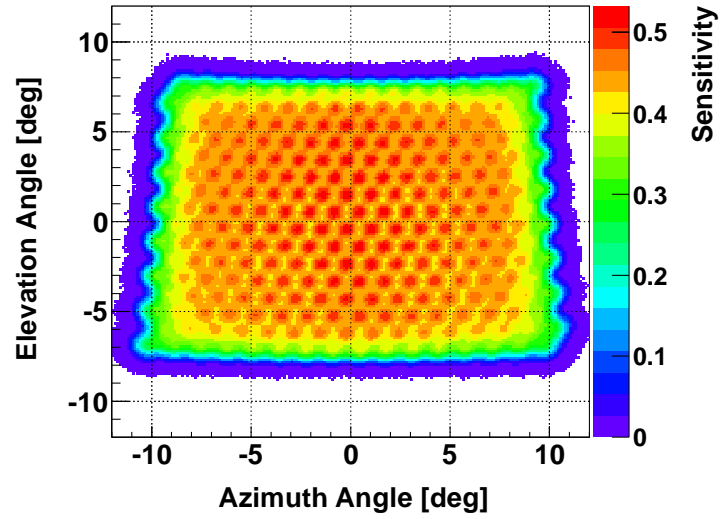
$$w_i = \frac{N_i^{\text{pe}}}{\bar{N}^{\text{pe}}}. \quad (5.13)$$

where N_i^{pe} is the number of photo-electrons of i -th PMT, \bar{N}^{pe} is the averaged value of all selected PMTs.

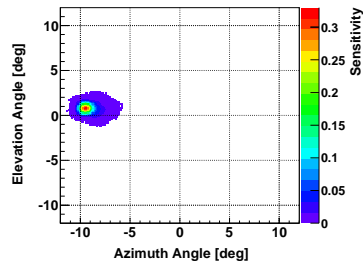
The geometry of stereo event is calculated from an intersection line of two SDPs. Once the shower planes are determined, finding the stereo geometry reconstruction is a very simple matter by simply intersecting the two SDPs as shown in Figure 5.8. Thus, the shower axis \mathbf{s} is given by

$$\mathbf{s} = \mathbf{n}_1 \times \mathbf{n}_2 \quad (5.14)$$

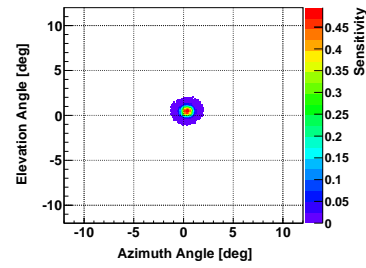
where \mathbf{n}_1 and \mathbf{n}_2 are the two SDP normal vectors.



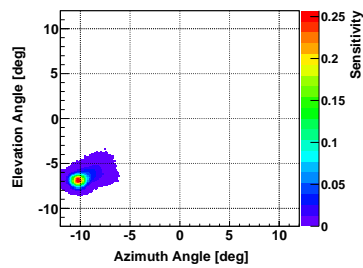
(a) Total



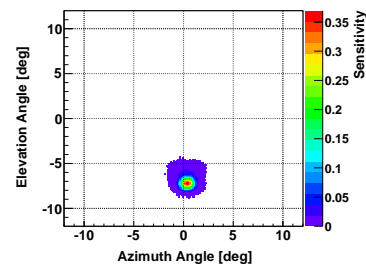
(b) PMT 247



(c) PMT 119



(d) PMT 255



(e) PMT 127

Figure 5.7: The total directional characteristic of all PMTs in camera00 at BRM (top) and of each PMTs located center, edge and corner. The direction is the relative angle from the line of sight of the telescope. The color map indicates the sensitivity calculated by Ray-Trace simulation.

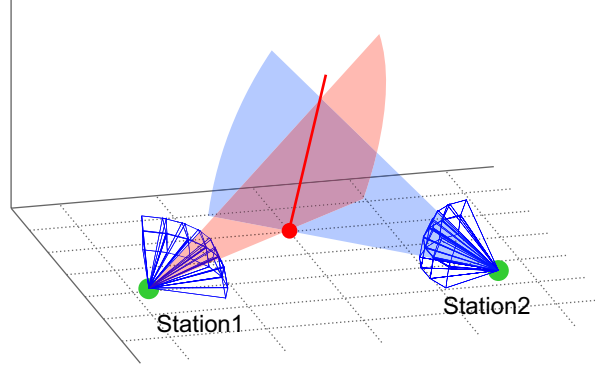


Figure 5.8: Stereo geometry reconstruction. The shower axis is determined by intersecting two SDPs.

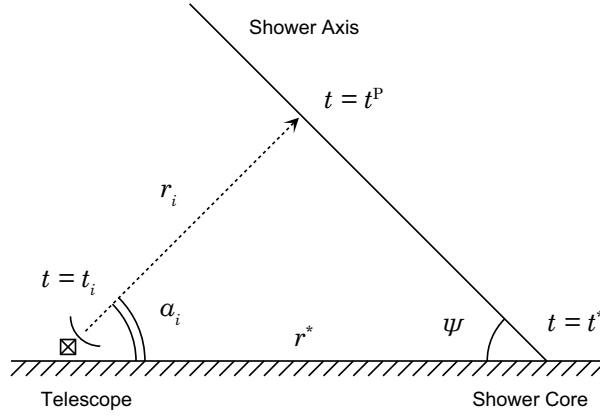


Figure 5.9: Geometry reconstruction in monocular mode

5.2.3 Monocular Geometry Reconstruction

On the other hand, a shower geometry by mono reconstruction in which we use data from a single station is estimated by taking account of signal timings of each PMTs, as shown in Figure 5.9. where \mathbf{r}^* is a vector of the core position and t^* is the timing which the air shower injects on the ground. When timing t^P emitted photon at the location \mathbf{r}_i is measured on i -th PMT at the timing t_i , the relation of these parameters is

$$t_i = t^P + \frac{1}{c}|\mathbf{r}_i| \quad (5.15)$$

$$t^* = t^P + \frac{1}{c}|\mathbf{r}^* - \mathbf{r}_i|, \quad (5.16)$$

removing t^P value,

$$t_i - t^* = \frac{1}{c} (|\mathbf{r}_i| - |\mathbf{r}^* - \mathbf{r}_i|). \quad (5.17)$$

Since the line of the sight of each PMT is already calculated, the elevation angle \mathbf{r}_i toward the emitted location of photon is also known. The (5.17) is transformed to

$$t_i = t^* + \frac{1}{c} \frac{\sin \psi - \sin \alpha_i}{\sin(\psi + \alpha_i)} r^* \quad (5.18)$$

where ψ is the elevation angle on SDP toward the shower axis. The formula is same as 3th selection one. In the reconstruction routine, the optimal solutions of t^* , r^* and ψ are determined by the minimized χ^2 considering the error of injection time σ_i .

$$\chi^2 = \sum_i \left[\left\{ t_i - t^* - \frac{1}{c} s_i(\psi) r^* \right\}^2 / \sigma_i^2 \right] \quad (5.19)$$

where $s_i(\psi)$ is

$$s_i(\psi) = \frac{\sin \psi - \sin \alpha_i}{\sin(\psi + \alpha_i)}. \quad (5.20)$$

The \mathbf{r}^* and ψ are estimated in (5.20) so that the shower axis and the core location are determined.

5.3 Shower Profile Reconstruction – Inverse Monte Carlo –

As discussed in chapter 4, the fluorescence technique detects not only fluorescence light but also the Čerenkov light and its scattered. In TA, the reconstruction of shower profile is estimated by an “Inverse Monte Carlo” (IMC) method. The IMC method is newly developed in TA and searched for an optimum solution via repeating Monte Carlo (MC) simulations and comparing observed data with MC simulation including all photon emission and scattered processes.

In this IMC procedure, we use the Gaisser-Hillas function as the longitudinal development curve. The first interaction point, X_0 , and the interaction length, λ , are fixed at 0 g/cm² and 70 g/cm², respectively. The scanned values are the optimum X_{\max} , the slant depth of maximum development and N_{\max} , the shower size at X_{\max} .

5.3.1 X_{\max} Determination

Initially, we obtain a optimum solution of X_{\max} . We calculate energy deposited along the shower axis from Gaisser-Hillas function with X_{\max} , X_0 , λ and $N_{\max} = 1.0$ and the mean ionization loss rate, α_{eff} [63].

We adopt the fluorescence yield measured by Kakimoto et al. [61] as the absolute value, the emitted fluorescence spectra measured by FLASH [92] and Čerenkov yield estimated in [63]. Using atmospheric parameters measured by the radiosonde and the LIDAR system, we evaluate the number of fluorescence

photons, Čerenkov photons and scattered Čerenkov photons along the shower axis.

Next, we simulate signals on all the FDs by ray-trace taking into the calibration constants, an atmosphere transmittance, a mirror reflectivity and QE \times CE [52]. Moreover in order to increase the speed of the calculations, we use a database of the directional characteristic shown in Figure 5.7. The number of photo-electrons n_i^{sim} on i -th PMT is simulated by

$$n_i^{\text{sim}} = \int_x \int_\lambda N(x, \lambda) \times f_i(\vec{r}_x) d\lambda dx \quad (5.21)$$

where $N(x, \lambda)$ is the number of photons incident upon a telescope from a each slant depth x , $f_i(\vec{r}_x)$ is the sensitivity of i -th PMT. Then, we calculate the following likelihood using the observed photo-electrons n_i^{obs} and simulated ones n_i^{sim} from (5.21),

$$L = \sum_i \{n_i^{\text{obs}} \log \frac{n_i^{\text{sim}}}{n^{\text{sim, st}}}\} \quad (5.22)$$

$$n^{\text{sim, st}} = \sum_i n_i^{\text{sim}} \quad (5.23)$$

where $n^{\text{sim, st}}$ is the total number of photo-electrons on a station from MC calculations, and $n_i/n^{\text{sim, st}}$ is a probability for one photo-electron to enter the i -th PMT. While changing X_{max} , we search for the optimum X_{max} with the maximum likelihood value.

5.3.2 N_{max} Determination

After X_{max} is determined, we estimate N_{max} which is the scale of shower developments. Since the number of simulated photo-electrons, n_i^{sim} , is calculated under a condition of $N_{\text{max}} = 1$, we determine N_{max} from the ratio of the total number of detected photo-electrons to the simulated one,

$$N_{\text{max}} = \frac{\sum_i n_i^{\text{pe, data}}}{\sum_i n_i^{\text{pe}}}. \quad (5.24)$$

Fig. 5.10 shows an observed longitudinal development curve superimposed on the corresponding IMC fitting result. The contributions of the different emission and scattering mechanisms are shown by different colors.

5.3.3 Energy Determination

The primary energy of an UHECR can be estimated from the sum of energy deposited along the shower axis. In our analysis, we first calculate the calorimetric energy, E_{cal} , from the integration of the Gaisser-Hillas function with the optimum X_{max} and N_{max} and minimum ionization loss rate α_{eff} ,

$$E_{\text{cal}} = \int_{X_0}^{\infty} N_e(x, N_{\text{max}}, X_{\text{max}}, X_0) \alpha_{\text{eff}}(x) dx. \quad (5.25)$$

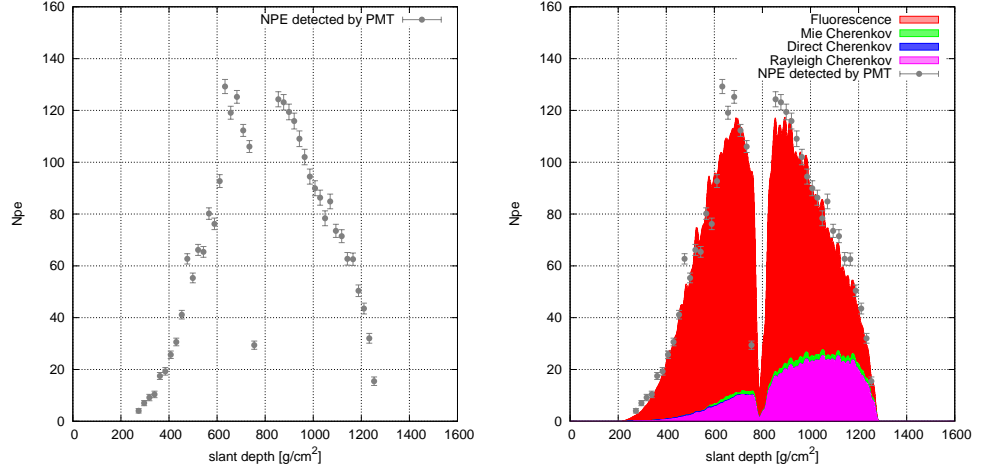


Figure 5.10: The shower signals injected from longitudinal development curves of IMC fitting result and an observed air shower signal. The plot is the observed data, the red show the contribution of fluorescence light, the blue indicates of the direct Čerenkov light, the purple and green shows the scattered Čerenkov light of Rayleigh and Mie process, respectively.

By the way, Gaisser-Hillas function is transformed by

$$t = \frac{X - X_0}{\lambda} \quad (5.26)$$

$$\xi = \frac{X_{\max} - X_0}{\lambda}, \quad (5.27)$$

and we obtain

$$N_e(t) = N_{\max} \left(\frac{e}{\xi} \right)^\xi e^{-t\xi}. \quad (5.28)$$

As the result, the primary energy E_{cal} is estimated by the integration with Γ function,

$$E_{\text{cal}} = \lambda N_{\max} \overline{\frac{dE}{dX}} \left(\frac{e}{\xi} \right)^\xi \Gamma(\xi + 1) \quad (5.29)$$

Next, as discussed in section 4.1.1, we correct missing energy which does not deposit in the atmosphere, such as neutral particles and their kinetic energies and then we obtain estimate the primary energy E_0 .

Chapter 6

Performance Estimation of TA FD

In this chapter, we evaluate a performance of the monocular mode of TA FD with the simulation and reconstruction software developed by our collaboration. In order to measure the energy spectrum and the mass composition of UHECRs, we estimate the aperture of the monocular mode of TA FD and the resolution is also estimated using the same way. In the mass composition analysis of UHECRs, we simulate expectation lines of a averaged X_{\max} and its energy dependence for primaries of protons and irons. After analyzed observed data, an observed X_{\max} is compared with their expectation lines.

6.1 Resolution and Aperture of the Monocular Mode

6.1.1 Simulation Conditions

First of all, simulation conditions were defined for the MC simulation software. EASs were simulated under the following conditions for both BRM and LR trigger modes.

- Energy, E_0 : $10^{17.5} \sim 10^{20.0}$ eV random.
- Spectral index : $\gamma = -1$.
- Zenith angle : $0^\circ \sim 65^\circ$ with isotropic distributions.
- Azimuth angle : $0^\circ \sim 360^\circ$ with isotropic distributions.
- Core position : uniformly distribution within the circle of 35 km radius from the CLF location.
- Hadron interaction models : two types of models, QGSJet-II or SIBYLL.
- Mass composition : two types of nuclei, protons or irons.

- Background photon : database of observed background photons generated from means and standard deviations of FADC counts.
- Calibration : calibration factors dependent on times as same as those used for data analysis.

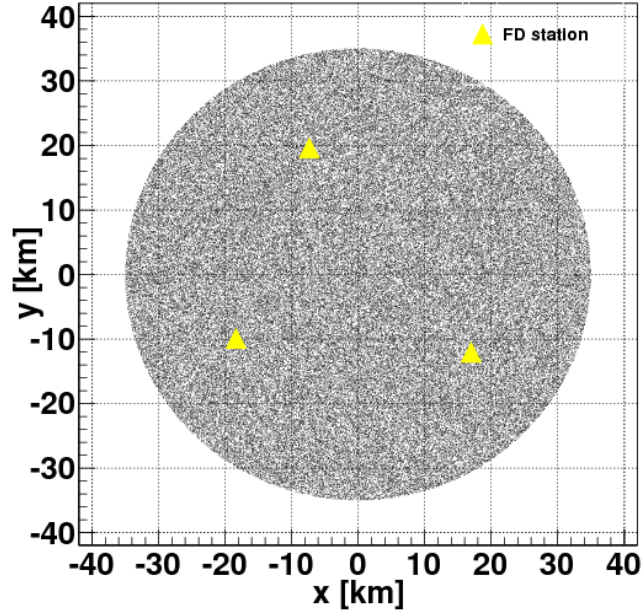


Figure 6.1: Core location distribution of Monte Carlo showers. (0, 0) shows the center of the distribution corresponding to the location of CLF. The vertical axis, Y-axis, is the direction from south to north, the horizontal axis, X-axis, is from east to west. The yellow triangles indicate the FD station locations.

Fig. 6.1 shows locations of the FD stations and core positions of the simulated EASs. The area of the core locations for MC was defined having enough size of area compared with an effective area of FDs.

Fig. shows the averaged X_{\max} of MC air showers induced by primary protons or irons generated by CORSIKA QGSJet-II and SIBYLL. The solid lines indicate averaged X_{\max} values for the QGSJet-II interaction model, the dashed lines indicate those for the SIBYLL, the red lines are averaged X_{\max} values for primary protons, the blue lines are those for irons. The difference of averaged X_{\max} between protons and irons is about 100 g/cm^2

6.1.2 Resolutions in the Monocular Mode

Resolutions in the monocular mode are estimated with analysis and studies of MC events by comparing the MC thrown information with reconstructed

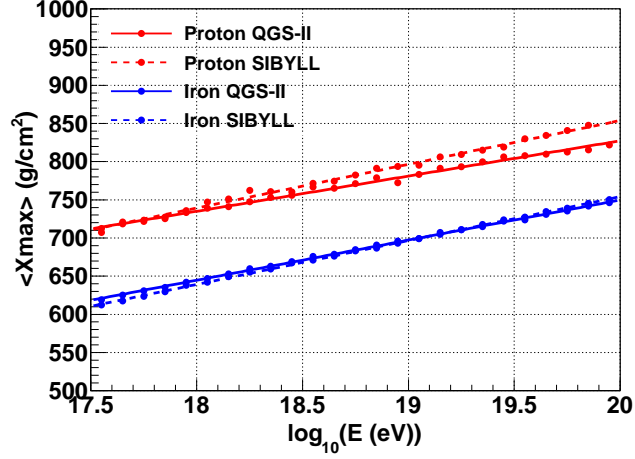


Figure 6.2: Averaged X_{\max} of protons and irons generated by CORSIKA QGSJet-II and SIBYLL model without detector simulation. The solid line shows the QGSJet-II, the dashed line shows the SIBYLL, the red line is the result of protons, the blue line is the result of irons.

ones in event by event manner. Before comparisons, the following quality cuts are applied in the monocular analysis, because faint shower signals with short tracks are difficult to reconstruct to determine their geometries. Thus, short tracks and small time extent events were removed with the following quality cut.

- The geometrical and the longitudinal fittings are converged.
- The number of selected PMTs is larger than 10.
- The track length is larger than 10° .
- The time extent is larger than $2 \mu s$.
- The reduced χ^2 for the geometrical fitting is less than 20.
- The maximum depth of EAS is observed inside the field of view of FD, $X_{\text{start}} < X_{\max} < X_{\text{end}}$ where X_{start} is the start of slant depth detected photons inside FOV, X_{end} is the end of slant depth detected photons inside FOV.

When we reconstruct data triggered by *head* or *edge* of air showers without X_{\max} inside the FOV FD, their showers are difficult to fit by shower profile reconstructions, introducing large uncertainties of energies. The energy are overestimated from reconstructed shower events which don't observed X_{\max}

inside of FOV. In traditionally, we select air showers which X_{\max} positions are inside of FOV.

We defined the simulation conditions of zenith angles and core locations, which are less than 55° , within 35 km, respectively. In order to avoid a contamination caused by geometrical resolutions in monocular mode, we applied two addition cuts for consistencies with observed data and MC simulations.

- The reconstructed zenith angle is less than 55° .
- The reconstructed core location is within a circle with 25 km radius from the location of CLF.

Here, we define the set of eight quality cuts is a “standard cut”.

As discussed in simulation conditions, simulated showers are independently triggered by both BRM and LR stations. When cosmic rays with energies above 10^{19} eV inject within FD effective area, air showers induced by them are triggered by both stations and hence are reconstructed from data recorded by both stations. When EASs are reconstructed by both stations, we adopt a result of the station with the larger number of photo-electrons than that of the other station, because bright shower signals are easy to reconstruct geometries.

Here, resolutions in the monocular mode are estimated by comparing MC thrown information with reconstructed one. At first, an open angle distribution, comparing arrival directions between thrown values and reconstructed ones, is shown in Fig. 6.3. The one sigma region which includes 68% of data is from 0° to 7.4° . So then, the geometrical resolution is determined as 7.4° in the monocular mode and it is worse than stereo reconstructions which is about 1° .

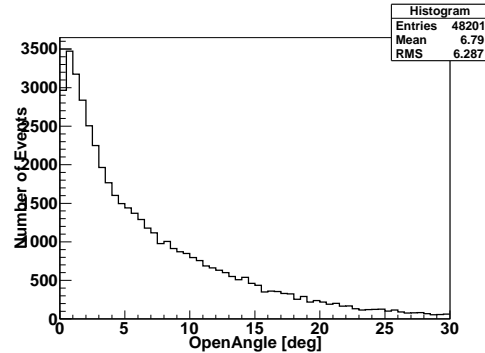


Figure 6.3: The open angle distribution comparing between thrown arrival directions and reconstructed ones.

Fig. 6.4 and Fig. 6.5 show resolutions of the impact parameter and the Ψ angle which is the angle in SDP shown in Fig. 5.9. The mean of the reconstructed impact parameter is -130 m and the averaged difference of the Ψ angle is -2.9° . As a result, the monocular analysis has a tendency to reconstruct inclined geometries at a shorter distance than actual ones.

6.1. RESOLUTION AND APERTURE OF THE MONOCULAR MODE 105

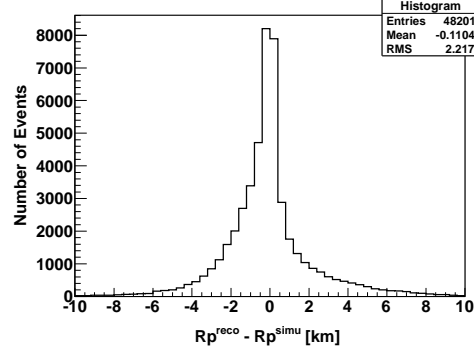


Figure 6.4: The resolutions of the impact parameter estimation. It is a comparison between simulated and reconstructed values.

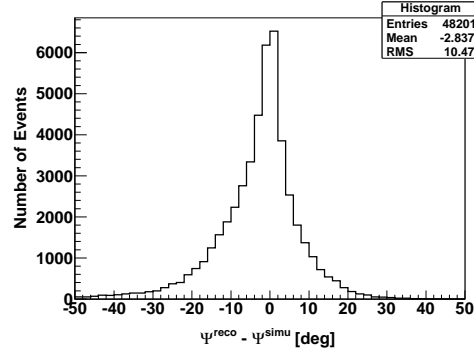


Figure 6.5: The angle resolution on SDP compared between simulated and reconstructed.

The resolutions of other parameters in shower profile reconstructions are evaluated by the same way. The left figure of Fig. 6.6 shows comparisons between thrown values of X_{\max} and reconstructed ones. The average is almost zero and the RMS is 104 g/cm^2 . The Gaussian fitted mean and the standard deviation for the histogram from -150 g/cm^2 to $+150 \text{ g/cm}^2$ is 9 g/cm^2 and 66 g/cm^2 , respectively. The right figure of Fig. 6.6 shows the energy dependence of X_{\max} resolutions. The plot shows the mean and the error-bar shows the standard deviation. The standard deviation is small at low energies, because FD triggers low energy showers at only short distances so that these showers are better geometrical resolutions than showers with a large distance. While the mean of low energies is almost zero, those of high energies above $10^{19.0} \text{ eV}$ is slightly systematic smaller than zero. Since EASs with high energies have deep X_{\max} , these X_{\max} are usually located at an edge of FOV. Moreover, a reconstructed X_{\max} fluctuates within X_{\max} resolutions in monocular mode

and must be observed within a FOV of FD. Showers with X_{\max} reconstructed out of the FOV are removed under standard cuts. As a result, air showers reconstructed smaller X_{\max} compared with the thrown X_{\max} are selected, and then it causes the systematic small averaged X_{\max} in high energy region.

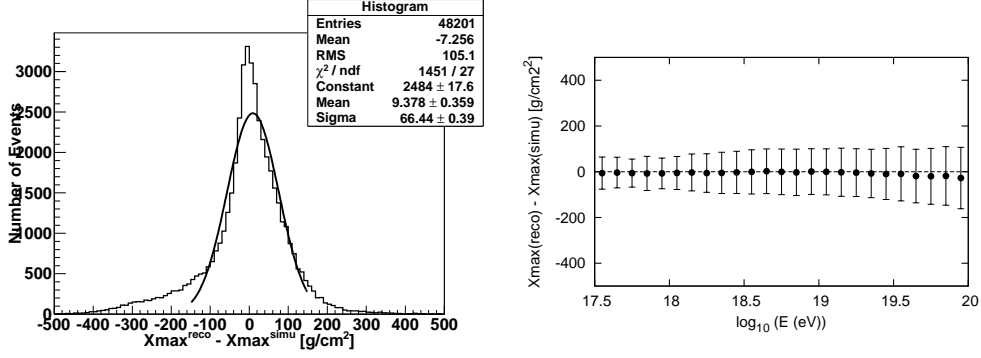


Figure 6.6: The resolution of X_{\max} including protons of different energies under the simulation condition of section 6.1.1 (left). The energy dependence for the X_{\max} resolutions (right).

Fig. 6.7 shows the energy resolutions and its energy dependence. The average of reconstructed energies are smaller than corresponding thrown energies at the higher energy region. It is consistent with the tendency of the geometrical reconstruction which estimate inclined shower geometries at a shorter distances. At high energies, the effect is large caused by the geometrical resolution in the monocular mode. RMS of residual energy distributions are almost same at all energy ranges. Since the systematic difference on the energy reconstructions are

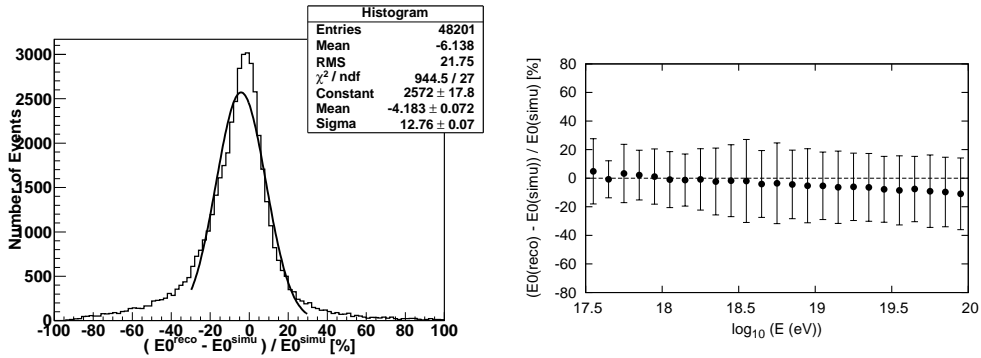


Figure 6.7: The energy resolution including protons of different energies under the simulation condition of section 6.1.1 (left). The energy dependence for the energy resolutions (right).

caused by the systematics on the geometrical reconstruction, observed shower

6.1. RESOLUTION AND APERTURE OF THE MONOCULAR MODE 107

energies are also underestimated. Therefore, we correct the systematic difference. Fig. 6.1.2 shows a linear fitting result of energy systematics. The error bar shows the error of the mean, σ/\sqrt{N} , where σ is the standard deviation and N is the number of events for each bins. Reconstructed energies are additionally corrected by the fitted results to avoid geometrical reconstruction biases in monocular mode.

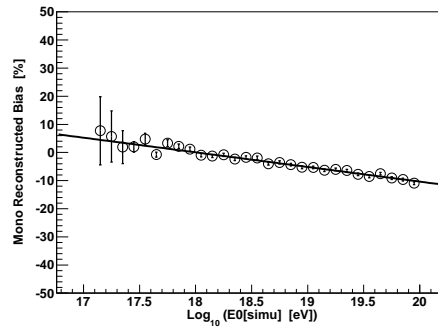


Figure 6.8: The energy systematics are fitted by a linear function. Plots indicate the means and error bars indicate the errors of the mean.

After the correction for the geometrical bias on energies, the energy resolutions were calculated and shown in Fig. again. We can see that the systematic bias was corrected. Of course, the energy correction is applied in both MC simulation and data in the same way.

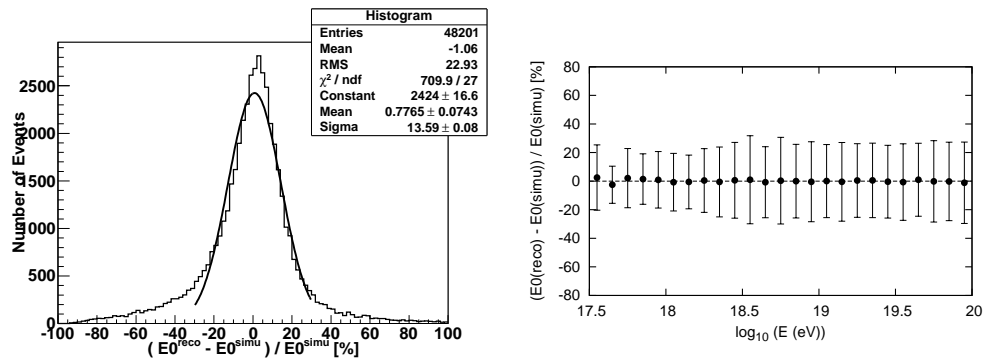


Figure 6.9: The corrected energy resolution reconstructed by the monocular mode as a function of energy. The systematic bias was removed.

6.1.3 Estimations of Apertures

Here, we estimate a geometrical factor, called aperture, of FD stations which is an important factor for calculation of energy spectra. The aperture of FDs can not be estimated by analytical calculations, and it must be estimated by the Monte Carlo simulation. The geometrical aperture $A\Omega^G$ simulated under the MC condition discussed in section 6.1.1 is analytically calculated by,

$$A\Omega^G = \pi R^2 \times \int_0^{\theta_{\max}} 2\pi \sin \theta \cos \theta d\theta \quad (6.1)$$

$$= (\pi R \sin \theta_{\max})^2 \quad (6.2)$$

where R is the radius of a thrown circle area of MC simulations on the ground and θ_{\max} is the maximum of a thrown zenith angle of MC simulations. Here, substituting from $R = 35$ km and $\theta_{\max} = 65^\circ$ in section 6.1.1, therefore $A\Omega^G = 9930.87$ km²·sr.

In order to obtain the correct aperture, detection efficiencies which are the ratios between the simulated number of events and the corresponding reconstructed number of events with the standard cuts are needed. Then, the aperture, $A\Omega(E)$, is given by

$$A\Omega(E) = A\Omega^G \times \frac{N_{\text{reco}}(E_{\text{reco}}^{\text{MC}})}{N_{\text{thrown}}(E_{\text{thrown}}^{\text{MC}})} \quad (6.3)$$

where N_{thrown} is the thrown number of events within an energy bin calculated from MC *thrown* (true) energies, $E_{\text{thrown}}^{\text{MC}}$. N_{reco} is the reconstructed number of events within the same energy bin calculated from *reconstructed* energies, $E_{\text{reco}}^{\text{MC}}$.

To estimate the aperture by Monte Carlo simulation, the aperture depends on the primary cosmic rays. Here, we used protons and irons for the QGSJet-II, and estimated the systematic difference of apertures for primary nuclei.

$N_{\text{reco}}/N_{\text{thrown}}$ is calculated from our MC simulation which is generated by a spectral index, $\gamma = -1.0$ under simulation conditions. Reconstructed energies fluctuate within the energy resolution shown in Fig 6.9. Thus, if the spectral index assumed in MC simulations differs from an observed one, effects of bin-to-bin movements also make a discrepancy. Since observed UHECR spectrum almost follows spectral index about -3.1, the simulated showers are also weighted with $\gamma = -3.1$ shown in Fig. 6.10.

Finally, FD aperture, $A\Omega(E)$, is obtained from $A\Omega^G$ multiplied by the ratio, $N_{\text{reco}}/N_{\text{thrown}}$, shown in Fig. 6.10. The aperture is fitted by an empirical function shown in (6.4) in order to avoid irregular variations on the aperture caused by fluctuations in the MC simulations.

$$\log_{10} A\Omega(E) = A \left(1 - \exp \left(\frac{B - \log_{10}(E)}{C} \right) \right) \quad (6.4)$$

The left plot of Fig. 6.11(a) shows the apertures for BRM and LR FD stations in the monocular mode. The solid red and blue lines show the apertures

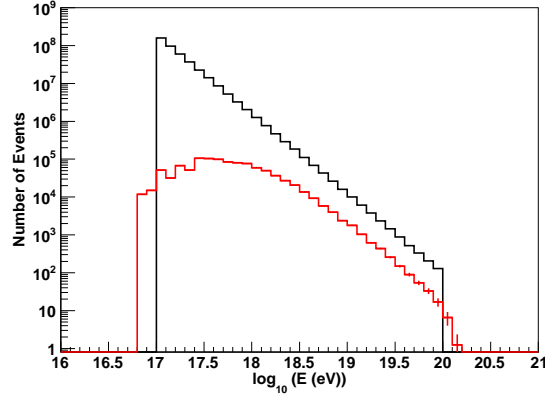


Figure 6.10: The weighted histogram of simulated and reconstructed energy estimated from protons of QGSJET-II model.

assuming proton primaries of BRM and LR, respectively, the dotted yellow and green lines show the aperture assuming iron primaries observed by the BRM and LR stations, respectively. The difference of apertures indicate the difference between detection efficiencies for protons and irons.

The difference between the aperture for primary protons and that for irons is large in the low energy region, because an averaged X_{\max} of irons is 100 g/cm^2 smaller than that of protons. Although the detectors in the BRM station is identical as the detectors in the LR station, the discrepancies in the aperture come from the difference of the site altitudes. The altitude of the LR station is 150 m higher than that of the BRM station. Thus, the BRM station favors detectors of deeper X_{\max} showers than the LR station.

The right plot of Fig. 6.11(b) shows the combined aperture of the monocular mode analysis for the BRM and LR data. This curve was carefully calculated for avoiding double counting with two stations for high energy EASs. The green curve shows the combined aperture comparing the monocular apertures by BRM and LR, respectively. Since both the BRM and the LR aperture have a common sensitive area near the center of the array, the growth rate of the combined aperture is smaller than the single station apertures in higher energies. Fig. 6.11(c) indicates a comparison of combined aperture calculated for primary protons or irons. The aperture for protons is systematic larger than that for irons in less than $10^{18.0} \text{ eV}$. Since averaged X_{\max} values of iron primaries are 100 g/cm^2 smaller than those of proton primaries with the same energy, more iron showers with low energies are removed under the standard cut of X_{\max} , $X_{\text{start}} < X_{\max} < X_{\text{end}}$, than proton showers.

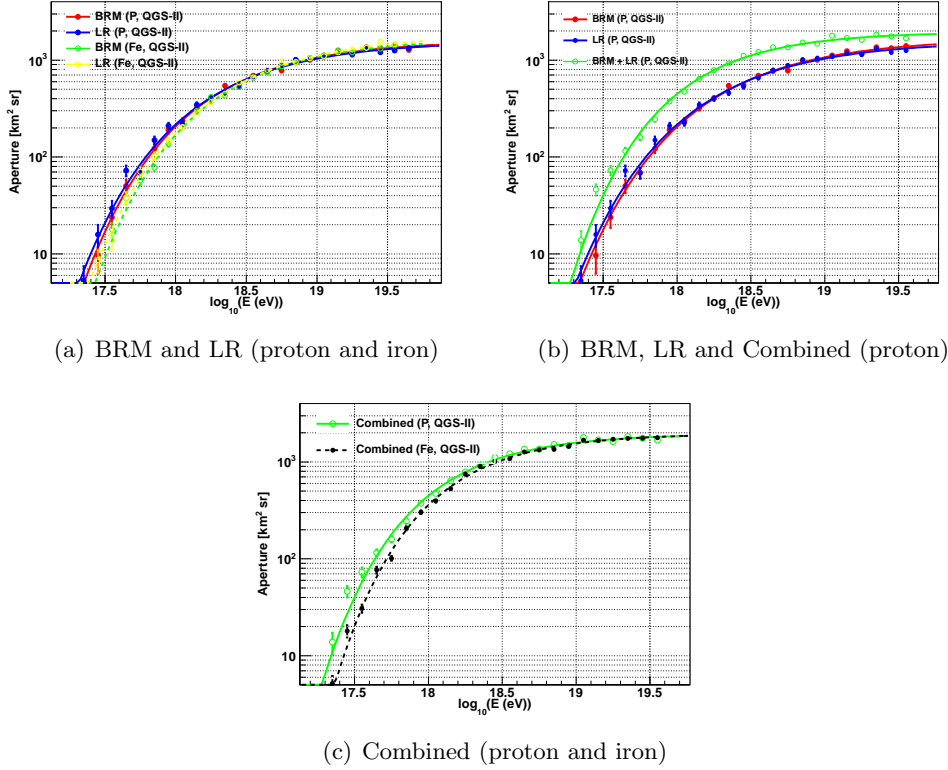


Figure 6.11: The left figure is an aperture in BRM and LR only monocular mode. The iron and proton simulated results are shown. The right plot shows the BRM and LR combined aperture comparing with BRM and LR monocular aperture assumed pure proton primary. The bottom plot shows the comparison of combined apertures estimated by protons and irons.

6.2 Mass Composition Study

6.2.1 Mass Composition Measurement by X_{\max} Technique

Depth of the maximum developments, X_{\max} , is an important parameter to distinguish primary species of UHECRs.

As shown in Fig. 6.2, an averaged X_{\max} is proportional to a primary energies. Since an iron consists of 56 nucleons, an iron with an energy, E , assumes 56 proton with an energy of $E/56$. Therefore, X_{\max} of irons are smaller than that of protons with the same primary energies of irons. Fig. 6.12 shows longitudinal development curves of protons and irons at $E = 10^{18}$ eV. The red curves show longitudinal developments of protons, the blue curves are those of irons. X_{\max} of irons are tend to be smaller than that of protons. The averaged X_{\max} as a function of energy from $10^{17.5}$ eV to 10^{20} eV is already shown in Fig. 6.2.

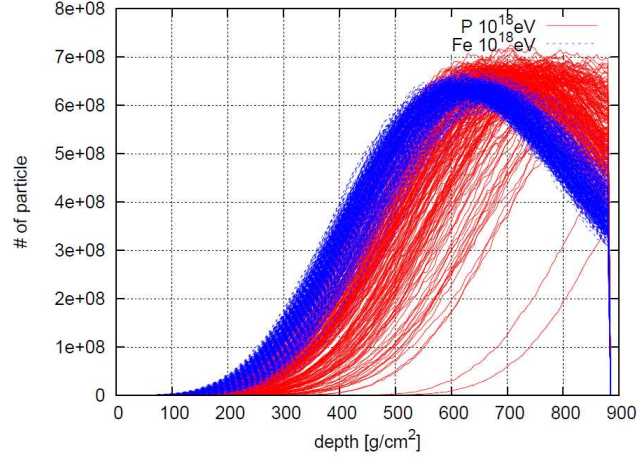


Figure 6.12: Longitudinal development curves simulated for primary protons and irons with the energy of 10^{18} eV. The red curves show longitudinal developments of protons, the blue curves are of irons.

6.2.2 Acceptance Biases on X_{\max} Limited Fields of View of FDs

Since the FOV of the FD's is limited in an elevation from about 3° to 33° , observed X_{\max} distribution is an irregular distribution which is difference from an actual X_{\max} distribution, unless acceptance bias-free selections are applied. This bias is amplified under the standard cut of X_{\max} within an observed FD FOV, $X_{\text{start}} < X_{\max} < X_{\text{end}}$. The reason for this bias in the X_{\max} distribution is that most showers landing close to the FD have their X_{\max} at upper side of the FOV and X_{\max} of observed developments is not located inside FOV or deeper developed showers simply are not detected, as shown in Fig. 6.13. As a result, the averaged X_{\max} appears to be larger i.e., deeper, than the average of thrown or the unbiased values. A similar bias happens for high energy showers. High energy showers develop as their X_{\max} deeper in the atmosphere than showers by lower primary energies, then for some near vertical showers X_{\max} are below the station's FOV, as shown in Fig. 6.13, and then, those deep showers are removed and not used for further analysis. Therefore, the averaged X_{\max} appears to be smaller.

In the monocular mode, the biases are evaluated from Monte Carlo simulations. Fig. 6.14 shows the averaged values of the simulated and reconstructed X_{\max} with lines obtained by linear fittings of the plotted points. At the high energy of $10^{19.5}$ eV, there is the acceptance bias of -60 g/cm 2 and at the low energy of $10^{17.5}$ eV, there is that of $+10$ g/cm 2 .

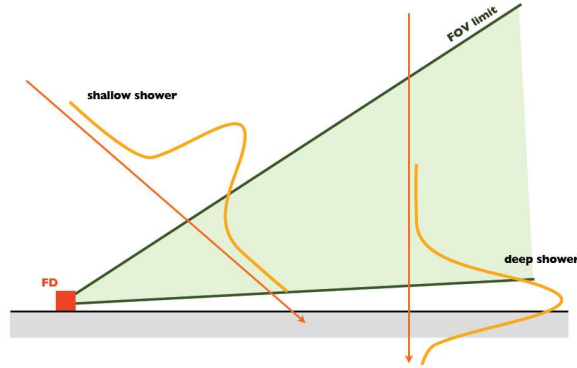


Figure 6.13: Showers which can not be observed by FD caused by limited a field of view.

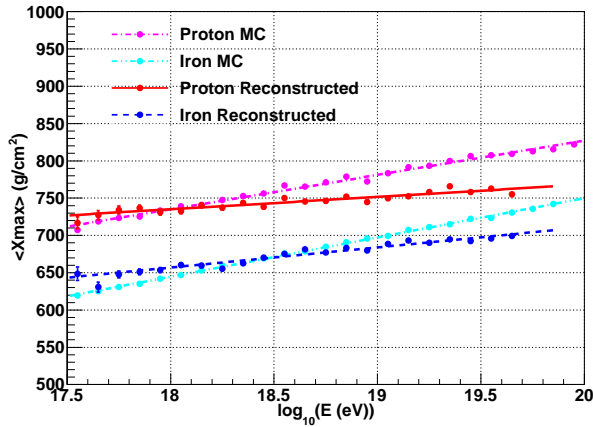


Figure 6.14: Averaged values of simulated and reconstructed X_{\max} under only standard cuts. Reconstructed averaged X_{\max} has large biases caused by limited fields of view. The red line and blue dashed line indicate averaged X_{\max} with acceptance biases for primary protons and irons, respectively. The pink dash-dotted line and sky-blue two-dotted line indicates thrown averaged X_{\max} for primary protons and irons, respectively.

6.2.3 Fiducial Volume Cuts

Under the standard cuts, there are large biases in reconstructed averaged X_{\max} caused by acceptance of FDs. Since averaged X_{\max} of data observed by FD already includes these biases, we can compare the observed averaged X_{\max} with the expected lines calculated from MC simulations for primary protons and irons.

However, we can determine selection rules to remove biased geometries of showers using MC simulations and apply bias-free cuts in a FD monocular analysis with a similar way developed by Pierre Auger group [67], called fiducial volume cut (FVC). In FVC, important parameters are not only X_{\max} , but also X_{start} and X_{end} . X_{start} and X_{end} are upper and lower limits of the slant depth along a shower axis that is inside the FD field of view. These limits are defined at where a shower axis intercepts the FD field of view limit or where a shower axis intercepts the maximum distance which a shower with an energy is still detectable. Note that values for X_{start} and X_{end} depend only on geometries of showers and not on a particular depth of shower profiles. In order to determine optimum ranges for X_{start} and X_{end} , we use a averaged X_{\max} as a function of X_{start} and X_{end} in Fig. 6.15. The pink plots indicates results of mixed composition which consists of 50% protons and 50% irons.

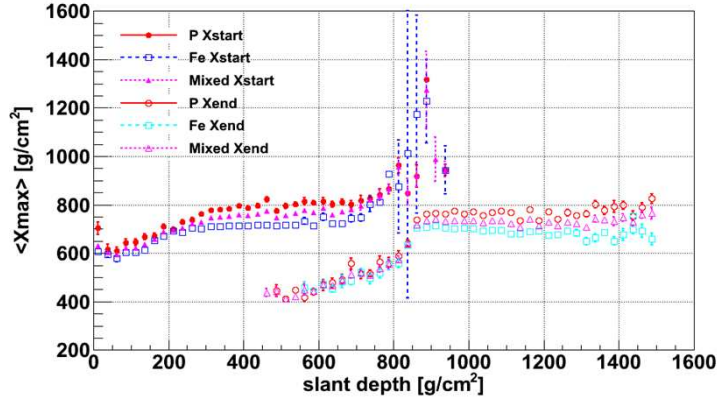


Figure 6.15: Averaged X_{\max} as a function of X_{start} and X_{end} in order to determine the optimum range for X_{start} and X_{end} . The red and blue plots indicate results for primary protons and irons, respectively. The pink plots indicate results for a mixed composition which consists of 50% protons and 50% irons.

For $700 \text{ g}/\text{cm}^2 < X_{\text{start}}$ and $X_{\text{end}} < 900 \text{ g}/\text{cm}^2$, the averaged X_{\max} has large biases compared with the other averaged X_{\max} . Moreover averaged X_{\max} at a small X_{start} is systematic smaller than thrown one caused by a Čerenkov contamination. Biased ranges of X_{start} and X_{end} should be excluded for bias-free measurements of X_{\max} .

Therefore, we determined selection rules on addition to standard cuts discussed in section 6.1.2.

- The minimum viewing angle is larger than 20° .
- The Ψ angle within SDP is smaller than 120.
- The X_{start} is larger than $150 \text{ g}/\text{cm}^2$.

- The value of $X_{\text{end}} - X_{\text{start}}$ is larger than 150 g/cm^2 .
- The X_{start} is smaller than 700 g/cm^2 and X_{end} is larger than 900 g/cm^2 .

A set of cuts with the criteria listed above is defined as “fiducial volume cut (FVC)”. These criteria are determined to fulfill small acceptance biases within 10 g/cm^2 for all energy ranges and to leave as many EASs as possible. The first three cuts are effective to remove EASs with geometries of a large Čerenkov contamination. The last two cuts are impacts to avoid biased geometries of EASs.

After applied with FVC, the same plot of Fig. 6.14 is shown in Fig. 6.16 using showers survived in FVC. The red and blue lines of averaged X_{max} with the acceptance bias for primary protons and irons are close to the pink and sky-blue lines of thrown averaged X_{max} for them. To compare at $10^{19.5} \text{ eV}$, the acceptance bias under FVC, 10 g/cm^2 , is much smaller than that under standard cuts, 60 g/cm^2 .

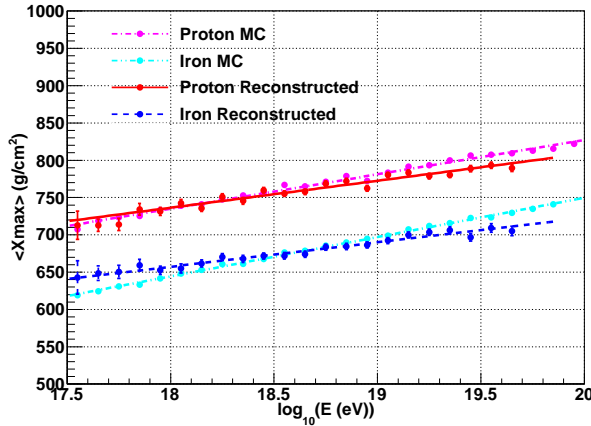


Figure 6.16: Simulated and reconstructed of averaged X_{max} under FVC. Reconstructed averaged X_{max} is much close to thrown one. These lines are the same definitions shown in Fig. 6.14.

We estimated the averaged X_{max} with acceptance biases under FVC using not only QGSJet-II, but also SIBYLL model as shown in Fig. 6.17.

However, although we have successfully developed and applied the bias-free analyses of averaged X_{max} , large percentages, about 50%, of observed EASs are removed under FVC. Although the acceptance bias is larger in measurements applied with only the standard cuts, more statistic is achieved than one applied with FVC. Therefore, we also compare the results FVC with the results only with the standard cuts to check whether both results are consistent or not. It is also essential important to understand the discrepancy between mass

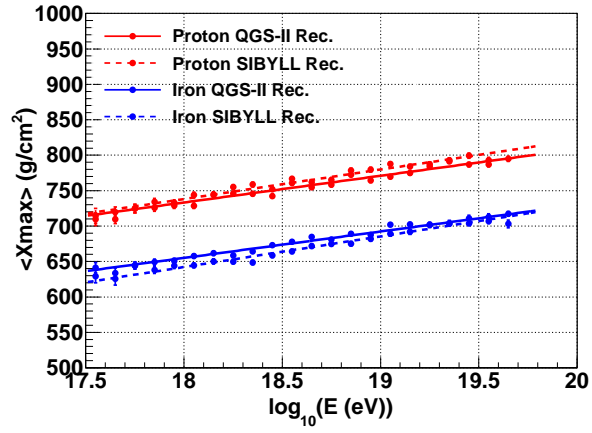


Figure 6.17: Averaged X_{\max} with acceptance biases for primary protons and irons with QGSJet-II and SIBYLL model under FVC. The solid lines indicate results using QGSJet-II model. The dashed lines indicate results using SIBYLL models. The red and blue color indicate primary protons and irons, respectively.

composition analyses and results by the TA and those by the Pierre Auger group.

Chapter 7

Data Analysis

In this chapter, we report analyzed results for data collected by BRM and LR from January 2008 to September 2011. Firstly, we confirm that the several distribution of the shower parameters obtained data reconstructions are in good agreement with MC expectations not only with the standard cut, but also with the fiducial volume cut. Secondly, the observed averaged X_{\max} are compared with the expectations simulated by the primary protons and irons, and thirdly we discuss about mass composition. Moreover, we evaluate the energy spectrum with after careful studies about the estimation of the aperture and the live time.

7.1 Data Set

In this analysis, the data collected with FDs in the BRM and in the LR stations are analyzed with the monocular mode analysis described in Chapter 5 during 3.7 year from January 2008 to September 2011. Some of the data includes cloudy days. As discussed in section 3.4.4, the data for the analysis is selected based on weather at that time recorded as the WEAT code because the WEAT code monitoring covers observation period of the data.

7.1.1 Calculation of Live Time

When FD stations are making event triggers for data acquisitions, there are dead times, ~ 4 ms, to collect data from all telescopes. Since the BRM and LR stations are independently making event triggers, we can calculate the following three different live times.

- Stereo live time
- BRM monocular live time
- LR monocular live time

Fig. 7.1 shows the schematic diagram of the three different types of dead time appearances. There are live times and dead times for the BRM and the LR

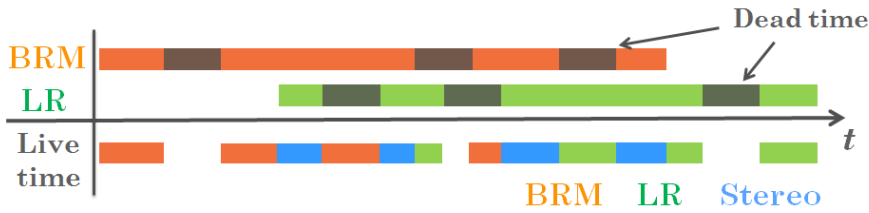


Figure 7.1: The schematic view of calculation of BRM and LR live time. There are 3 types of live time: stereo (blue), BRM monocular (orange), LR monocular (green).

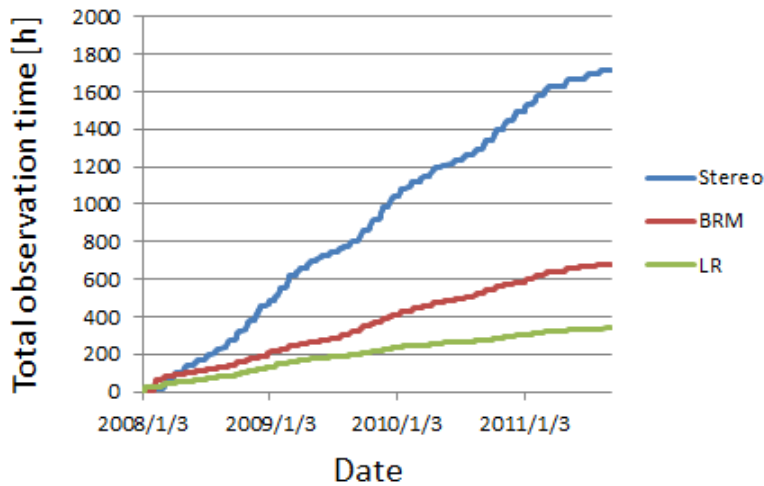


Figure 7.2: The three types of live times with the WEAT code cut. These broken lines indicate the total live time durations in the stereo (blue), the BRM station (orange) and the LR station (green). The growth rates of live times vary with the seasons.

stations, independently. When both BRM and LR stations are operating without dead times to observe showers at the same time, the time durations are accumulated as the stereo live time shown as the blue area in Fig. 7.1. When only a single station observes without dead times, operating time durations are accumulated as a live time of the single station. Even if both stations are operating, when there are dead times in one station, the time durations are calculated as the live time of the other station, not as the stereo live time. Thus, to accumulate as the stereo live time, the BRM and the LR stations need to be operated without dead times at both stations.

Using the method to calculate live times, the three types of live times are estimated without the WEAT code cut.

- Stereo live time : 2307.1 hours
- BRM monocular live time : 985.1 hours
- LR monocular live time : 486.0 hours

After we apply the WEAT code cut with the criteria discussed in section 3.4.4,

- Stereo live time : 1716.7 hours (74%)
- BRM monocular live time : 681.9 hours (69%)
- LR monocular live time : 337.7 hours (70%)

where the values in the parentheses are the percentages compared with live times before WEAT code selections. The about 70% observation time are survived after the WEAT code cuts.

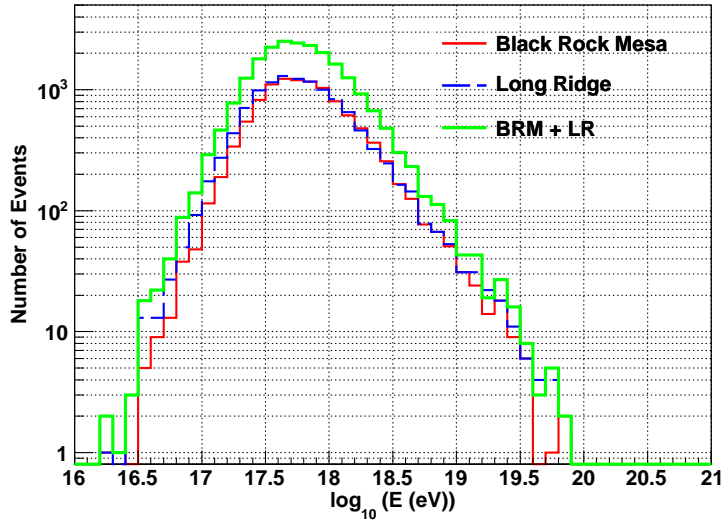
The accumulate observation times are shown in Fig. 7.2. These broken lines indicate the total live time in the stereo (blue), the BRM station (orange) and the LR station (green). All of the growth rates variates depending on the seasons, because the observation time per night in the winter is longer than that in the summer. As the other importance thing, the live time of LR is apparently shorter than that of BRM and the growth rate of LR is also smaller than that of BRM. It is for this reason that when we have started LR remote operations from May 2009, the finish times of LR observation are one hour earlier than that of the BRM stations for the safety operations. Thus, the live time of LR is shorter than that of BRM.

7.1.2 Number Spectrum

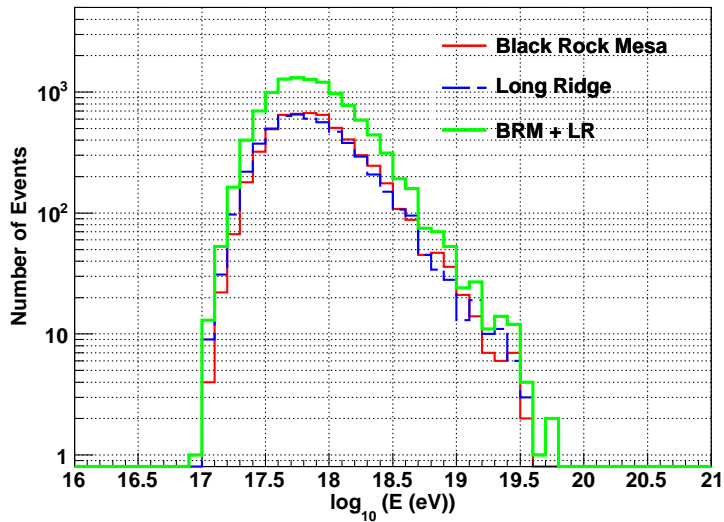
After the event selections based on a weather evaluated as the WEAT code are applied, the selected data measured at the BRM or the LR stations are analyzed in each monocular mode. Number spectra corresponding to the histograms of reconstructed primary energies are shown in Fig. 7.3(a). The red line shows a histogram of energies reconstructed in BRM monocular mode, the blue line shows a histogram of energies reconstructed in LR monocular mode.

At higher energies above 10^{19} eV, most EASs are reconstructed at both the BRM and the LR stations because they have the common detectable area. Thus, if EASs are successfully analyzed by both stations, in order to avoid a double-counting of EASs, we select results reconstructed at a station with the larger number of photo-electrons than the other station in the same way of Monte Carlo simulations.

The three types of the number of reconstructed showers under the standard cuts are shown in Tab. 7.1. From the number of reconstructed EASs and the live times shown in Fig. 7.2, we observe EASs every 10 minute by the roughly



(a) Standard cut



(b) Fiducial volume cut

Figure 7.3: Number spectra under the standard cuts (a) and under the FVC (b). There are three types of reconstructed energy histograms for the BRM station (red), the LR station (blue) and combined them (green).

estimation from the number of showers and the live time in the TA experiment.

Additionally, to avoid the acceptance biases on averaged X_{\max} in the mass composition analysis, we apply the FVC to the observed shower candidates as

item	standard cut	+fiducial volume cut (FVC)
BRM	10929	5711 (62%)
LR	11756	5575 (47%)
Combined	22417	11127 (50%)

Table 7.1: The number of reconstructed EASs under both selection rules.

discussed section 6.2.3. The number of showers after FVC are also shown in Tab.7.1. Thus, the 50% EASs are removed by the FVC in return for the bias-free measurement on averaged X_{\max} . The number spectra after the FVC is shown in Fig. 7.3(b). Comparing the histogram before the FVC with that after the FVC, there are the similar reductions of EASs at all energies, although the reductions are slightly large at low energies.

7.2 Data/MC Comparison

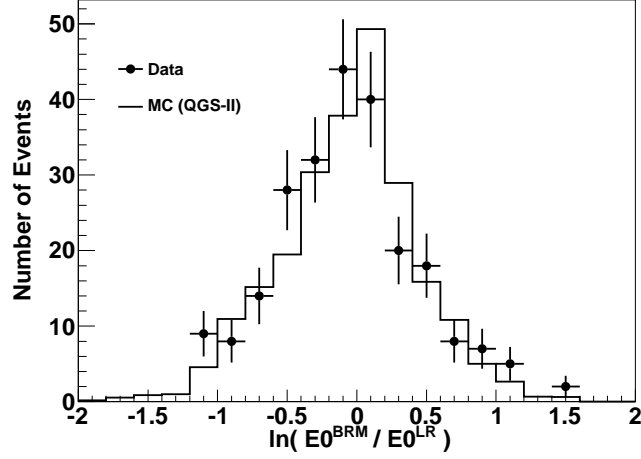
As further enhancement of our reliability in our analysis, the distributions of the several parameters obtained from the reconstructions of the observed data are compared with the expected ones estimated from MC simulations. Moreover, we apply the two types of selection rules which are the standard cut and the FVC, and we compare the observed distributions of the several parameters with the expected ones not only under the standard cut, but also under the FVC.

In our MC simulations, we generate EASs events with the spectral index, $\gamma = -1.0$ with energies from 10^{17} eV to 10^{20} eV as discussed in section 6.1.1. Since observed spectra almost follow a spectral index, $\gamma = -3.1$, and hence we assume that the spectrum index is -3.1 in all energy ranges in the Data/MC comparisons.

Results of Data/MC comparisons are shown in appendix at the end of the thesis. In these figures, the black plots indicates the distributions observed at the BRM or LR station, the red or blue histograms indicates the expected distributions estimated from MC simulations at the BRM or LR station for primary protons and irons, respectively. The distributions of each MC is normalized to the number of observed data. These plots are in reasonable agreements between data and MC simulations not only under the standard cut, but also under the FVC.

7.3 Check of Resolution in Monocular Mode

Air showers reconstructed by both stations are useful to confirm accuracies of a reconstructed energy and X_{\max} . Comparing each detectors installed at the BRM and the LR stations respectively, they are completely identical each others, and hence we consider that both stations have same resolutions on



(a) Energy

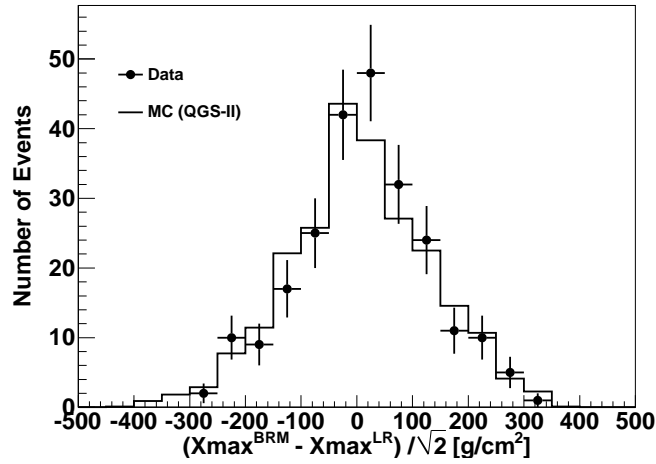
(b) X_{\max}

Figure 7.4: Pull plots of energies (a) and X_{\max} (b). The peak energy of reconstructed EASs including pull plots is $10^{18.6}$ eV.

reconstructed energies and X_{\max} . Therefore, the standard deviation from distributions of the difference between both reconstructed results are given by

$$\sigma_{\text{BRM+LR}} = \sqrt{\sigma_{\text{BRM}}^2 + \sigma_{\text{LR}}^2}. \quad (7.1)$$

Thus, we can estimate resolutions from distributions of a difference of reconstructed results in the BRM and the LR stations, called as “pull plot”. There are 234 events reconstructed by both stations, and pull plots for reconstructed energies and X_{\max} are shown in Fig. 7.4. Since the distance between BRM and

LR is 35 km, only cosmic ray above at least $10^{18.5}$ eV can be reconstructed at both stations. Therefore, a peak energy of EASs reconstructed at both stations including pull plots is $10^{18.6}$ eV.

The gaussian fitted mean and sigma of pull plot are

- Energy (Data) : Mean = -0.08 ± 0.04 , Sigma 0.46 ± 0.05
- Energy (MC) : Mean = -0.03 ± 0.01 , Sigma 0.47 ± 0.01
- X_{\max} (Data) : Mean = 12 ± 8 g/cm² , Sigma 116 ± 7 g/cm²
- X_{\max} (MC) : Mean = 3 ± 1 g/cm² , Sigma 120 ± 1 g/cm²,

respectively. The energies reconstructed at the LR station are 8% higher than ones reconstructed at the BRM station, and 8% is smaller than systematic uncertainties of TA FD. From these result, we evaluated the robust energy and X_{\max} resolutions without MC simulations, which are 40% and 120 g/cm², respectively.

7.4 Mass Composition Analysis

Since MC simulations have been confirmed reasonable agreement with measured data, the averaged X_{\max} values reconstructed at the BRM and LR stations are compared with the expectation ones estimated from MC simulations for primary protons and irons.

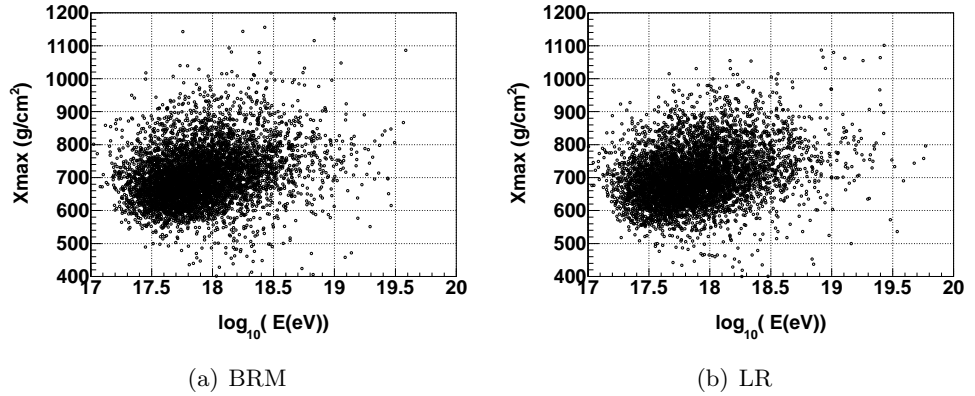


Figure 7.5: Scatter plot of reconstructed energy and X_{\max} applied the fiducial volume cut in BRM and LR monocular analysis.

7.4.1 Mass Composition Results in BRM or LR Station

At first, mass composition measurements under the FVC are shown in this section, and next, ones under the standard cuts are shown in section 7.4.3.

The scatter plots of energy and X_{\max} reconstructed at the BRM and the LR station under the FVC are shown in Fig. 7.5. From the measured data in Fig. 7.5, averages are calculated and compared with the expected lines estimated from MC simulations for primary protons and irons using the QGSJet-II model as a hadron interaction model. The results are shown shown in Fig. 7.6. The plots are the average of X_{\max} , the error bars are mean errors of the averaged X_{\max} , $\sigma/\sqrt{N_{Data}}$ where N_{Data} is the number of events. In Fig. 7.6, the pink and sky blue lines indicates the averaged X_{\max} of thrown MC simulations which are estimated only to use CORSIKA simulations. The red and blue lines indicate the averaged X_{\max} which are calculated in our MC simulations with acceptance biases of limited FOV of FDs.

The mass composition in the energy range of $10^{17.5} \text{ eV} \leq E \leq 10^{18.5} \text{ eV}$ indicated an evidence of the transition from heavy to light compositions. The mass composition above $10^{18.5} \text{ eV}$ was consistent with the pure proton expectation.

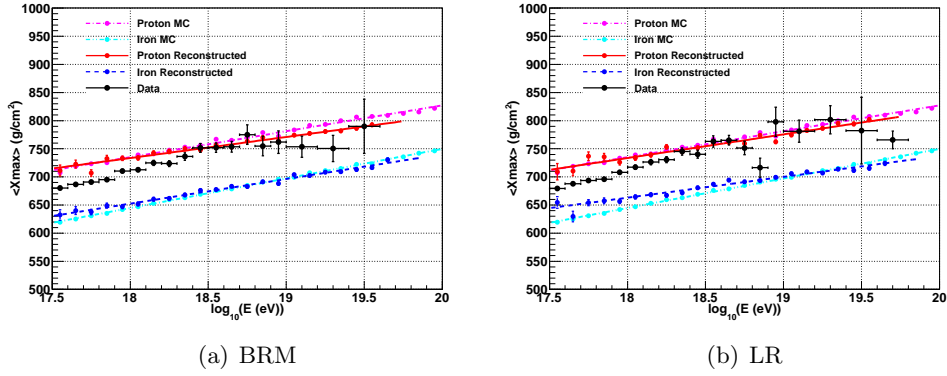


Figure 7.6: The measured and expected of averaged X_{\max} in the monocular analyses at the BRM station (a) and the LR stations (b) under the fiducial volume cuts. The pink and sky blue lines indicates the averaged X_{\max} of thrown MC which are estimated only to use CORSIKA simulations. The red and blue lines indicates the averaged X_{\max} which are calculated in our MC simulations with acceptance biases of limited FOV of FDs. The MC lines are estimated using the QGSJet-II model as a hadron interaction model.

7.4.2 Mass Composition Results in Combined Mode

Next, in order to calculate the averaged X_{\max} with more statistics of EASs, we evaluate the averaged X_{\max} from a combination of observed EASs analyzed at both the BRM and the LR stations. As the same way of MC simulations, we select results reconstructed at a station with the larger number of photoelectrons than the other station.

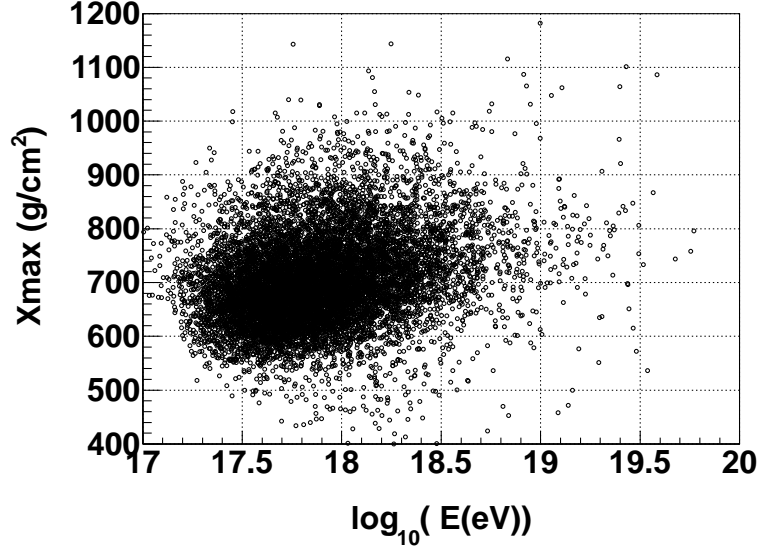


Figure 7.7: Scatter plots of energies and X_{\max} reconstructed at both the BRM and LR stations under the fiducial volume cuts.

With the criteria, a scatter plot of energies and X_{\max} reconstructed at both stations under the FVC is shown in Fig. 7.7, and the combined averaged X_{\max} are shown in Fig. 7.8 with the expected lines estimated from MC simulations with the same criteria as shown in Fig. 6.16. In Fig. 7.8, the plots indicate the averaged X_{\max} , and the pink and sky blue lines indicate the averaged X_{\max} of thrown MC which are estimated only to use CORSIKA simulations. The red and blue lines indicate the averaged X_{\max} which are calculated in our MC simulations with acceptance biases of limited FOV of FDs. The MC lines are estimated using the QGSJet-II model as a hadron interaction model.

These results indicate the same tendency as the BRM and LR monocular analysis results shown in the previous section, which have transitions at low energy around $10^{18.0}$ eV and the proton dominant at high energies above 10^{19} eV.

Moreover, measured averaged X_{\max} values are compared with ones obtained for MC events simulated using a hadron interaction model of QGSJet-II or SIBYLL. The result is shown in Fig. 7.9 with the number of observed EASs. The interpretation for the mass composition is not changed when we adopt the SIBYLL MC simulation. Comparing observed averaged X_{\max} values with the QGSJet-II or the SIBYLL model, measured averaged X_{\max} values are better agreements with expected averaged X_{\max} values for the QGSJet-II model than those of SIBYLL model in high energies above $10^{18.5}$ eV.

To discuss mass composition results using X_{\max} technique, it is important to compare not only averaged X_{\max} , but also distributions of observed X_{\max}

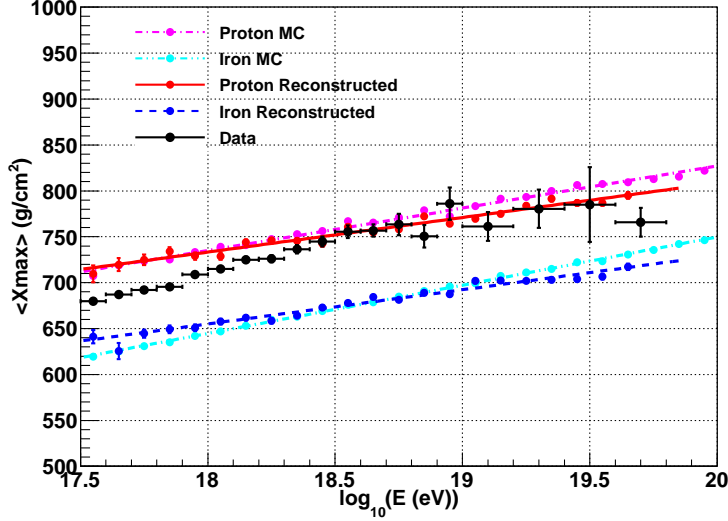


Figure 7.8: The averaged X_{\max} as a combination of both BRM and LR reconstructed events under the fiducial volume cuts. The pink and sky blue lines indicates the averaged X_{\max} of thrown MC estimated by only CORSIKA shower generations. The red and blue lines indicates the averaged X_{\max} with the acceptance bias of each FD station. The MC lines are estimated using the QGSJet-II model as a hadron interaction model.

with expectations estimated from MC simulations for primary protons or irons. We can compare shapes of observed X_{\max} distributions with expected ones including averaged X_{\max} values. Therefore, distribution of X_{\max} are shown in figures from Fig. 7.10 to Fig. 7.14 under several energy ranges. The plots indicate the measured X_{\max} analyzing observed data, and the red and blue histograms of X_{\max} are estimated in MC simulations with primary protons, irons, respectively. The pink histogram of X_{\max} indicates results of mixed composition which are estimated from MC simulations for 50% proton and 50% iron primaries. In results with energies of $10^{17.5} \text{ eV} \leq E < 10^{17.8} \text{ eV}$, the observed distribution of X_{\max} agrees with the mixed one. Until results with energies of $10^{18.4} \text{ eV} \leq E < 10^{18.6} \text{ eV}$, the measured distribution of X_{\max} moves from the mixed one to the proton one. Above $10^{18.6} \text{ eV}$, the observed distribution of X_{\max} is consistent with the expected distribution for proton primaries. Thus, these figures also indicate that there are transitions of dominant components from heavy to light nuclei from $10^{17.5} \text{ eV}$ to $10^{18.5} \text{ eV}$ and proton dominants above $10^{18.5} \text{ eV}$.

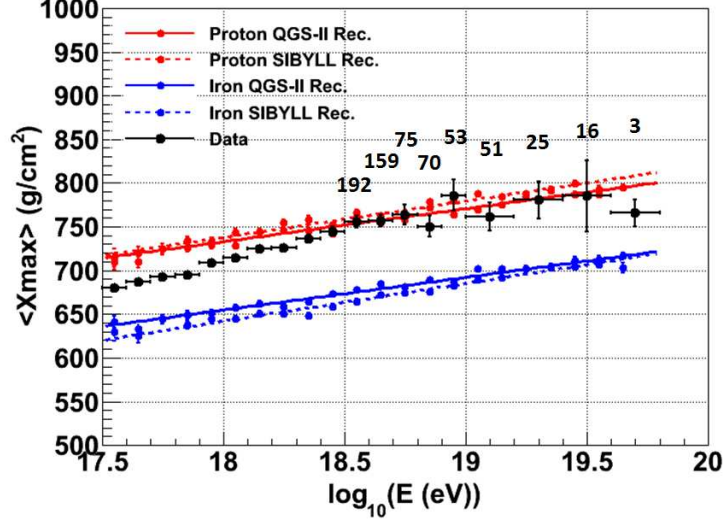


Figure 7.9: The comparison with data and MC line estimated from QGSJet-II model and SIBYLL model under the fiducial volume cuts. The number symbols indicates the number of EASs in each bin.

7.4.3 Compatibility of X_{\max} Distribution on Kolmogorov-Smirnov Test

Here, we apply Kolmogorov-Smirnov test (KS test) to the evaluation of compatibility between the observed X_{\max} distribution and X_{\max} distribution expected by proton, iron or mixed mass composition.

The KS test is a standard method to use to estimate quantitatively whether two distribution functions differ stochastically or not [95]. In the KS test, a statistical value of compatibility is calculated using the difference of cumulative probabilities. Fig. 7.15 shows the cumulative probabilities for observed X_{\max} compared with expected distributions of X_{\max} estimated from MC simulation for primary protons, irons, mixed compositions with energies from $10^{18.4}$ eV to $10^{18.6}$ eV shown in Fig. 7.10(e). In order to evaluate the compatibility, the D value is calculated by

$$D = \max_{-\infty < x < \infty} |S_N(x) - P(x)| \quad (7.2)$$

where $S_N(x)$ and $P(x)$ are the cumulative probabilities of observed X_{\max} distribution and expected distributions estimated from MC simulations, respectively. Hence, the D values are also shown in Fig. 7.15 using the plots with a broken line. In the energy range from $10^{18.4}$ eV to $10^{18.6}$ eV, the observed X_{\max} distribution is compatible with the expected distribution estimated from MC simulations for primary protons. From the D value, the probability P is

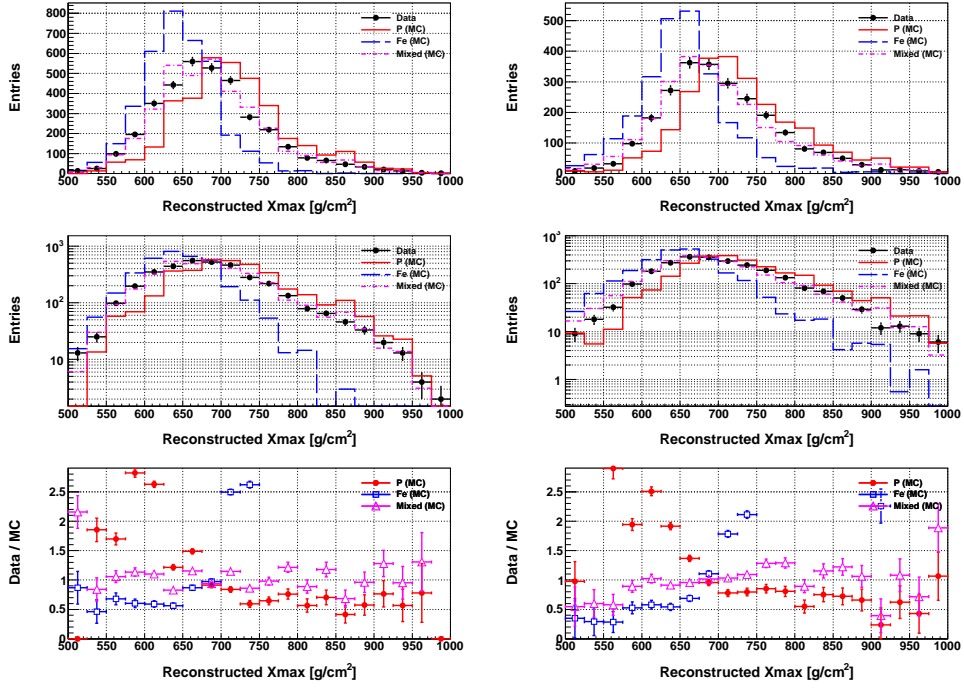
(a) $17.5 \leq \log(E) < 17.8$, 3590 events(b) $17.8 \leq \log(E) < 18.0$, 2482 events

Figure 7.10: X_{\max} distribution in $10^{17.5} \text{ eV} \leq E < 10^{17.8} \text{ eV}$ and $10^{17.8} \text{ eV} \leq E < 10^{18.0} \text{ eV}$ compared with the expected distribution estimated from MC simulation for primary protons (red), irons (blue) or mixed compositions (pink) under the fiducial volume cuts. Three types of the vertical axis indicate the linear scale, the logarithmic scale and its ratio between data and MC simulations.

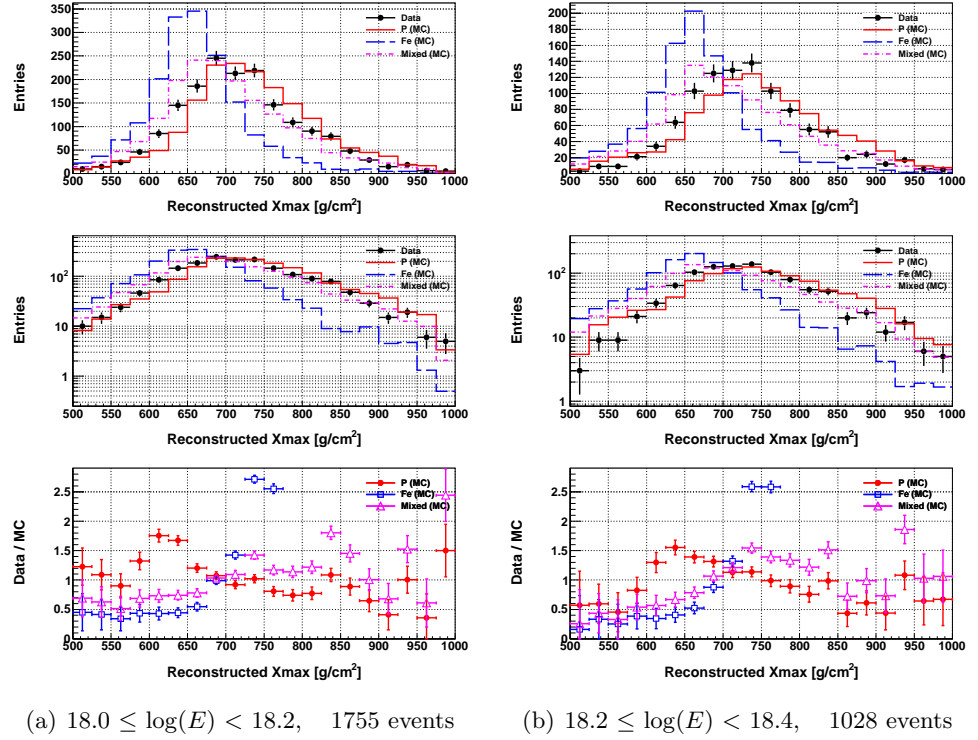


Figure 7.11: X_{\max} distribution in $10^{18.0} \text{ eV} \leq E < 10^{18.2} \text{ eV}$ and $10^{18.2} \text{ eV} \leq E < 10^{18.4} \text{ eV}$ compared with the expected distribution estimated from MC simulation for primary protons (red), irons (blue) or mixed compositions (pink) under the fiducial volume cuts. Three types of the vertical axis indicate the linear scale, the logarithmic scale and its ratio between data and MC simulations.

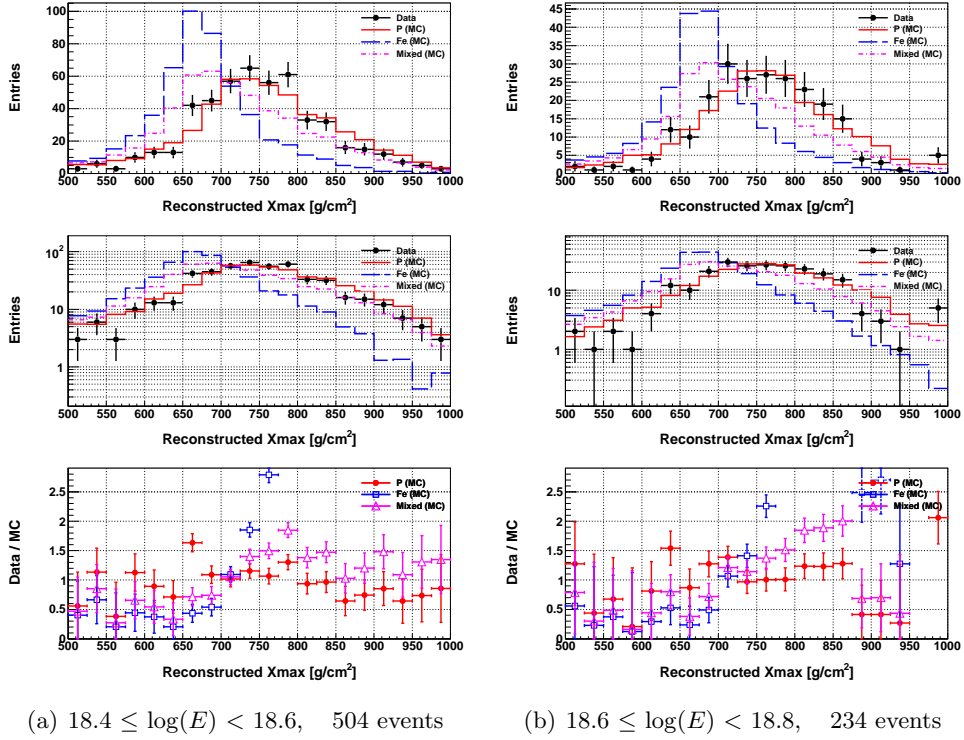


Figure 7.12: X_{\max} distribution in $10^{18.4} \text{ eV} \leq E < 10^{18.6} \text{ eV}$ and $10^{18.6} \text{ eV} \leq E < 10^{18.8} \text{ eV}$ compared with the expected distribution estimated from MC simulation for primary protons (red), irons (blue) or mixed compositions (pink) under the fiducial volume cuts. Three types of the vertical axis indicate the linear scale, the logarithmic scale and its ratio between data and MC simulations.

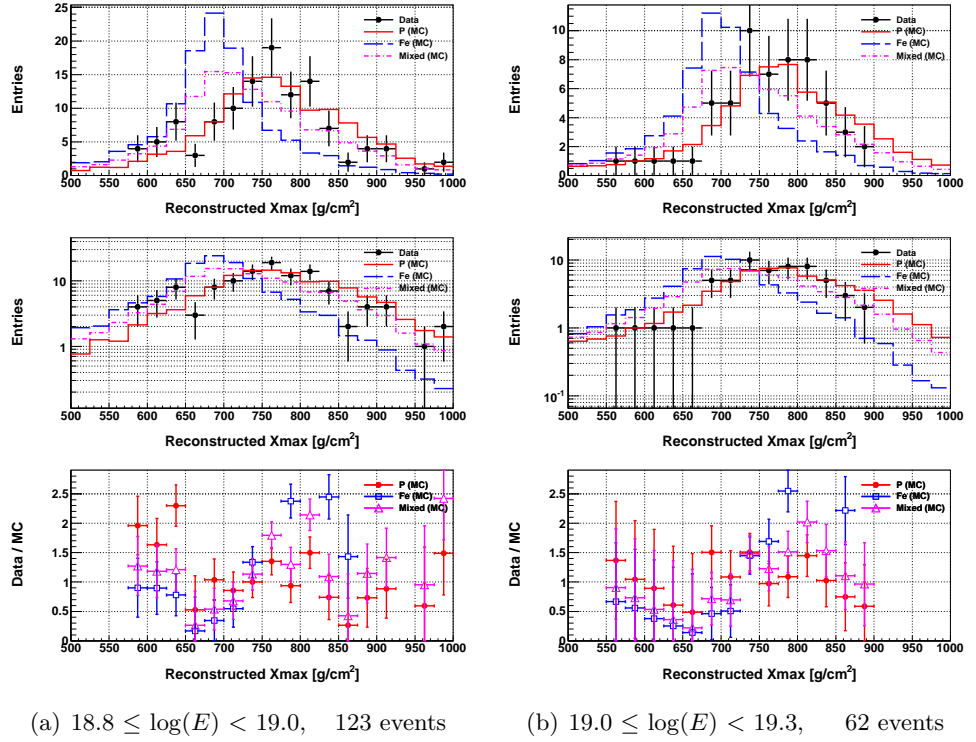


Figure 7.13: X_{\max} distribution in $10^{18.8} \text{ eV} \leq E < 10^{19.0} \text{ eV}$ and $10^{19.0} \text{ eV} \leq E < 10^{19.3} \text{ eV}$ compared with the expected distribution estimated from MC simulation for primary protons (red), irons (blue) or mixed compositions (pink) under the fiducial volume cuts. Three types of the vertical axis indicate the linear scale, the logarithmic scale and its ratio between data and MC simulations.

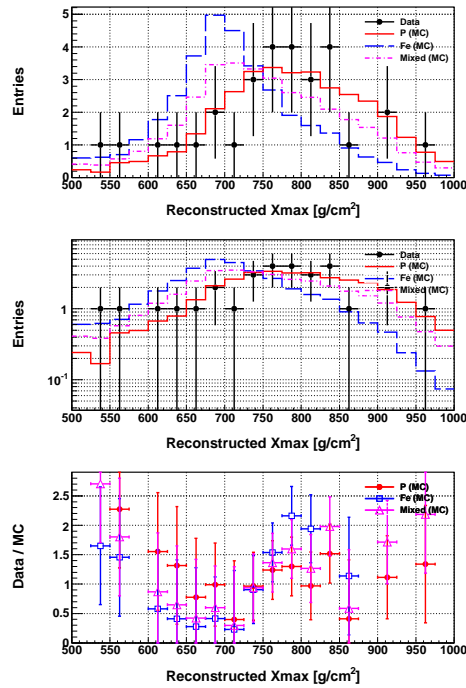
(a) $19.3 \leq \log(E)$, 33 events

Figure 7.14: X_{\max} distribution in $10^{19.3} \text{ eV} \leq E$ compared with the expected distribution estimated from MC simulation for primary protons (red), irons (blue) or mixed compositions (pink) under the fiducial volume cuts. Three types of the vertical axis indicate the linear scale, the logarithmic scale and its ratio between data and MC simulations.

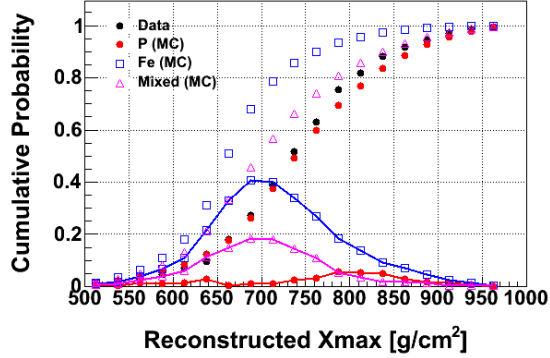


Figure 7.15: The X_{\max} distribution of the observed data and MC simulated by protons and irons with $10^{18.4} \text{ eV} \leq E < 10^{18.6} \text{ eV}$ under the fiducial volume cuts, which is the same data shown in Fig. 7.10(e).

evaluated as follows.

$$P(D > \text{observed}) = Q_{KS} \left(\sqrt{\frac{N_1 N_2}{N_1 + N_2}} D \right) \quad (7.3)$$

where Q_{KS} is the function given by

$$Q_{KS}(\lambda) = 2 \sum_{j=1}^{\infty} (-1)^{j-1} \exp(-2j^2 \lambda^2). \quad (7.4)$$

Fig. 7.16 shows the probabilities calculated from KS tests with each energy bin comparing observed X_{\max} distribution calculated from observed data analysis with expected X_{\max} distribution estimated from MC simulations for primary protons and irons using the QGSJet-II model and the SIBYLL model as a hadron interaction model. At the lowest plot of reconstructed energies at $10^{17.65} \text{ eV}$, the measured X_{\max} distribution was compatible with the expected distribution estimated from MC simulations for mixed composition primaries. In the energy region above $10^{18.5} \text{ eV}$, the measured X_{\max} distribution calculated from observed data analysis was only compatible with primary protons and incompatible with primary irons or the mixed compositions. The result was also consistent with the transition from a heavy dominant composition to a light dominant at the energy of $10^{18.5} \text{ eV}$.

Evaluation of Proton Fraction and Mean Logarithmic Mass

From measurements of averaged X_{\max} , we estimate proton fractions using the two component model, assuming a mixed composition of purely protons and irons. The proton fraction P_{fraction} is calculated with

$$P_{\text{fraction}} = \frac{X_{\max}^{\text{Obs.}} - X_{\max}^{\text{Fe}}}{X_{\max}^{\text{P}} - X_{\max}^{\text{Fe}}}. \quad (7.5)$$

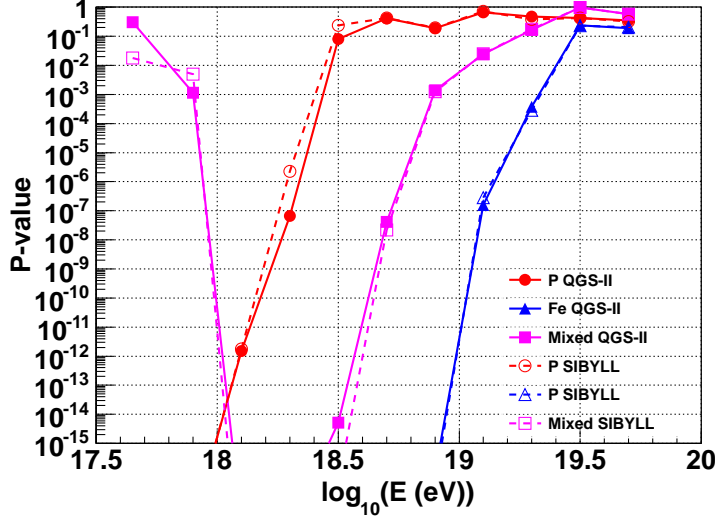


Figure 7.16: The probabilities estimated by KS test using several compositions of QGSJet-II and SIBYLL. Red: proton, Blue: iron, Pink: mixed composition assuming 50% proton and 50% iron primaries.

However, estimations of proton fractions need to correct differences of acceptance biases between primary protons and irons. The acceptance difference corresponds to the difference of apertures shown in Fig. 6.11(c). In low energies less than $10^{18.0}$ eV, the acceptance of primary irons is smaller than that of primary protons, because the averaged X_{\max} for primary irons is smaller than one for primary protons. Here, acceptance differences between primary protons and irons are calculated from apertures shown in Fig. 6.11. A ratio of acceptance difference, R , is calculated from

$$R = \left(\frac{N_{\text{reco.}}^{\text{Fe}} / N_{\text{thrown}}^{\text{Fe}}}{N_{\text{reco.}}^{\text{P}} / N_{\text{thrown}}^{\text{P}}} \right) = \frac{A\Omega^{\text{Fe}}}{A\Omega^{\text{P}}} \quad (7.6)$$

where $N_{\text{reco.}}$ is the number of reconstructed events, N_{thrown} is the number of thrown events. $A\Omega^{\text{P}}$ and $A\Omega^{\text{Fe}}$ indicate the apertures for primary protons and irons, respectively.

Therefore, (7.5) is modified to use R of (7.6),

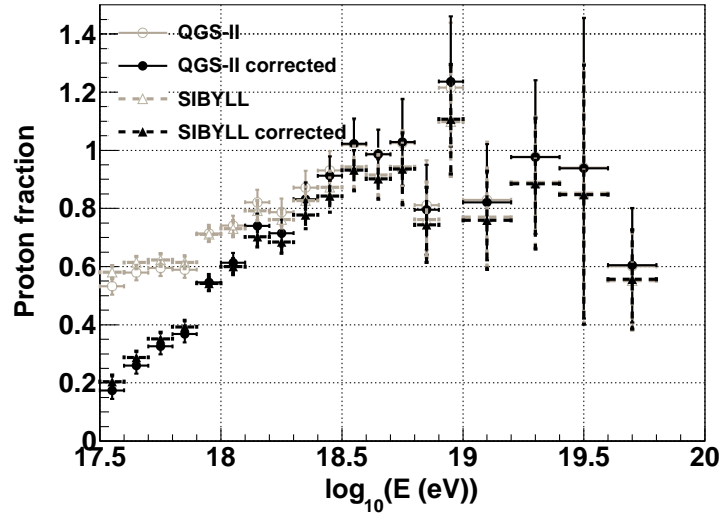
$$P_{\text{fraction}}^{\text{Corr.}} = \frac{(X_{\max}^{\text{Obs.}} - X_{\max}^{\text{Fe}}) \cdot R}{(X_{\max}^{\text{P}} - X_{\max}^{\text{Fe}}) + (R - 1) \cdot X_{\max}^{\text{Obs.}}} \quad (7.7)$$

where $P_{\text{fraction}}^{\text{Corr.}}$ is the proton fraction corrected the acceptance bias.

Moreover the mean of logarithm natural of atomic mass number is evaluated from $P_{\text{fraction}}^{\text{Corr.}}$ assuming the two component model,

$$\langle \ln A \rangle = (1 - P_{\text{fraction}}^{\text{Corr.}}) \times \ln 56. \quad (7.8)$$

Fig. 7.17 shows $P_{\text{fraction}}^{\text{Corr.}}$ and $\langle \ln A \rangle$ calculated from the averaged X_{max} and the expected lines from MC simulations using primary protons and irons.



(a) Proton fraction

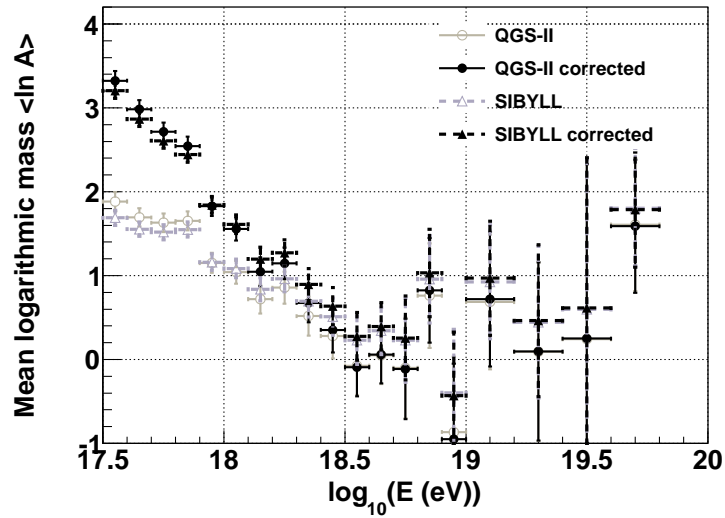
(b) $\langle \ln A \rangle$

Figure 7.17: The proton fraction and the averaged $\langle \ln A \rangle$ measured by the BRM and the LR stations under the fiducial volume cuts.

Mass Composition Results under the Standard Cuts

For the purpose of the cross-checking of mass composition measurements, the FVC is removed in the combined data and MC simulations. Fig. 7.18 shows the averaged X_{\max} for observed and MC events selected with the standard cut only. In Fig. 7.18, the pink and sky blue lines indicates the averaged X_{\max} of thrown MC estimated by only CORSIKA shower generations. The red and blue lines indicates the averaged X_{\max} with the acceptance bias of each FD station. The MC lines are estimated using the QGSJet-II model as the hadron interaction model.

The averaged X_{\max} values only under the standard cuts have the similar tendency with those under the FVC. The averaged X_{\max} values in the energy range of $10^{17.5} \text{ eV} \leq E \leq 10^{18.5} \text{ eV}$ indicate transitions of dominant components from heavy to light nuclei and are consistent with the pure proton expectation above $10^{18.5} \text{ eV}$. These interpretations of the results are the same with those with the FVC shown in Fig. 7.8. Therefore, we demonstrated the systematic shift caused by acceptance biases of limited FOV of FD in MC simulations. Moreover, we confirmed that the interpretation on the mass composition obtained from our observations and analyses does not depend on whether we apply the FVC as bias-free X_{\max} measurements or not.

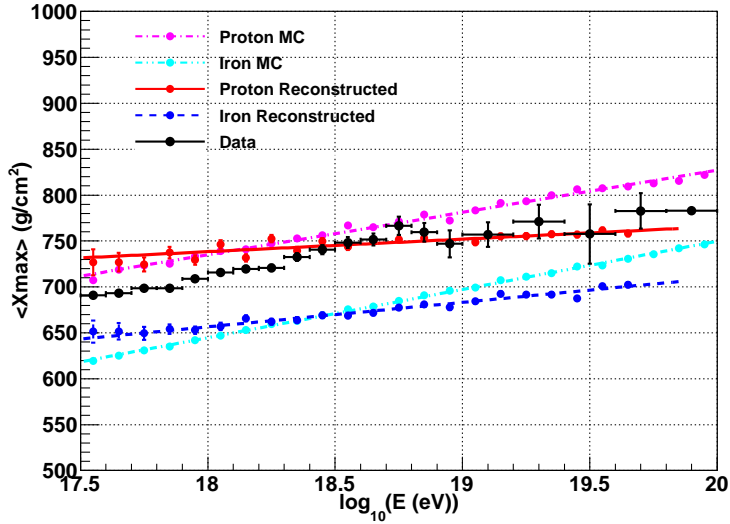


Figure 7.18: The measured and expected of averaged X_{\max} with *only the standard cuts*. The pink and sky blue lines indicates the averaged X_{\max} of thrown MC estimated by only CORSIKA shower generations. The red and blue lines indicates the averaged X_{\max} with the acceptance bias of each FD station. The MC lines are estimated using the QGSJet-II model as the hadron interaction model.

7.5 Energy Spectrum

Next, we obtain the energy spectrum based on the detector aperture, the live time and the number spectrum estimated in section 6.1.

7.5.1 Combined Exposure

Firstly, we use the results from BRM and LR data obtained independent analyses, and we calculated the energy spectra assuming independent observation from the BRM and the LR stations. Secondly, we calculate a combined spectrum. Since the BRM and LR stations with the common sensitive area are independently operated, some of EASs with high energies above $10^{18.5}$ eV are reconstructed at both stations. Thus, we carefully select results of both reconstructed EASs to avoid a double-counting of EASs. As a result, the reconstructed EASs include results reconstructed three types of observation mode: both the BRM and the LR stations mode, monocular mode of only the BRM or LR station. Therefore, considering three types of the apertures and the live times, we estimate the combined exposure, $\omega(E)$. The exposures of the BRM and the LR stations are simply given by

$$\omega(E) = A\Omega(E) \cdot t \quad (7.9)$$

where t indicates the live time and aperture, $A\Omega(E)$, is already estimated in Fig. 6.11. The fluxes measured at the BRM and the LR stations are straightforward to evaluate with the following formula.

$$J(E) = \frac{N(E)}{\omega(E) \cdot \Delta E}. \quad (7.10)$$

However, we consider the three types of the apertures shown in Fig. 6.11(b) and the three types of the live times. Thus, the combined aperture are modified as

$$\omega^{\text{ALL}}(E) = A\Omega^{\text{BRM}}(E) \cdot t^{\text{BRM}} + A\Omega^{\text{LR}}(E) \cdot t^{\text{LR}} + A\Omega^{\text{combined}}(E) \cdot t^{\text{Stereo}} \quad (7.11)$$

where $A\Omega^{\text{BRM}}$, $A\Omega^{\text{LR}}$ and $A\Omega^{\text{Combined}}$ shows the aperture of only the BRM station, only the LR station and the combined aperture, respectively, t^{BRM} , t^{LR} and t^{Stereo} show their live times. Here, we assume pure proton primaries as the mass composition.

The combined flux $J(E)$ is given by (7.11) substituting $\omega^{\text{ALL}}(E)$ for $\omega(E)$. Fig. 7.19 shows BRM, LR and the combined spectra multiplied by E^3 in order to check details of a spectrum structure. The red, blue and green plots indicate the energy spectra measured at the BRM station and the LR stations, and their combination, respectively. The error bars indicate \sqrt{N} with the assumption of the Poisson distribution, where N is the number of EASs in each energy bin.

Since the data in high energies above 10^{19} eV have not enough statistics, the size of binning is changed from $\text{dlog } E = 0.1$ step to $\text{dlog } E = 0.2$, the results are shown in the right figure of Fig. 7.19.

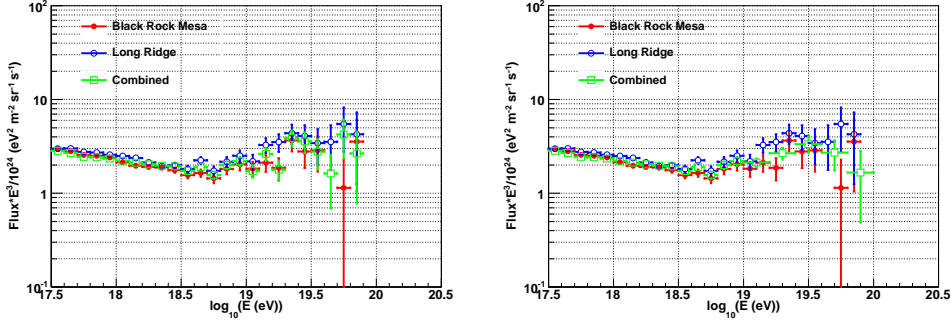


Figure 7.19: Energy Spectra. In the right figure, the size of binning is changed from $d\log E = 0.1$ step to $d\log E = 0.2$.

Energy Spectra considering Mass Composition Measurements

Estimated apertures depend on assumed primary composition, as shown in Fig. 6.11. Once the proton fraction is obtained, the aperture based on the mixed composition, $A\Omega^f$, can be obtained

$$A\Omega^f = A\Omega^p (R + f \cdot (1 - R)) \quad (7.12)$$

where f is the proton fraction, R is difference of acceptance shown in (7.5) [84].

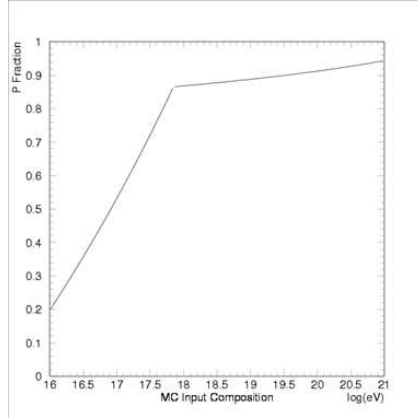


Figure 7.20: The proton fraction measured by HiRes/MIA experiment [84].

Fig. 7.20 shows the proton fraction measured by HiRes/MIA experiment [38]. On the other hand, we have already obtained the proton fraction from the TA monocular analyses for data measured with the BRM and LR stations described in section 7.4, and the results are shown in Fig. 7.17. The apertures for primary protons and irons are already estimated in Fig. 7.17. We calculate

two apertures assuming proton fractions obtained from HiRes/MIA experiment or from TA monocular analyses. Using the estimated apertures, energy spectra are re-calculated as shown in Fig. 7.21. Although obtained fluxes in low

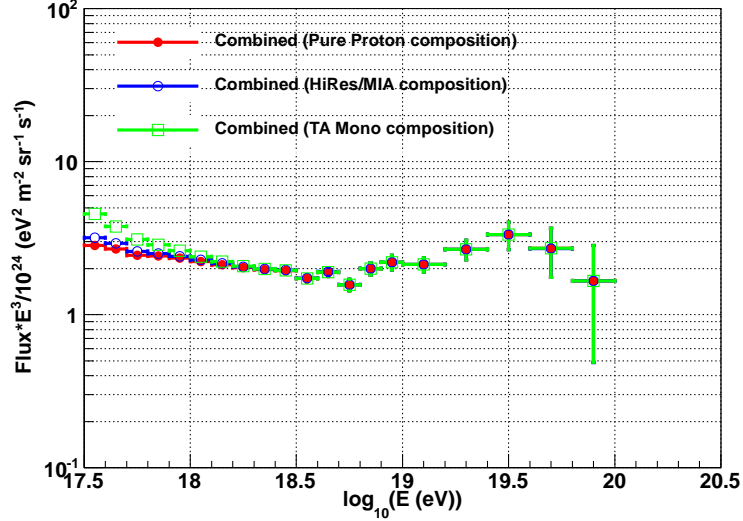


Figure 7.21: TA combined spectra assuming several compositions: pure proton, HiRes/MIA composition and measurement result in TA monocular mode.

energies less than 10^{18} eV are large differences between composition assumptions, the fluxes in high energies above $10^{18.5}$ eV is almost independent on assumptions of the proton fraction.

Fig. 7.22 shows the comparisons of other spectra measured by the TA surface detector and by the FDs at the TA Middle Drum station transported from HiRes experiment. In the Fig. 7.22, the spectrum labeled as BRM+LR under the assumption of the HiRes/MIA proton fraction is shown, because the spectrum of Middle Drum assumes the HiRes/MIA composition. The blue plots show the spectrum analyzing data collected at the BRM and the LR stations, the open squares show the spectrum measured at the Middle Drum station [71], the pink triangles indicate the spectrum measured by TA SD with 27% scaled as the same energies with TA FD energies [72]. These spectra are in good agreement with each other.

7.6 Study of Systematic Uncertainty

In this section, we discuss systematic uncertainties on energies and X_{\max} determined with FD measurements [73].

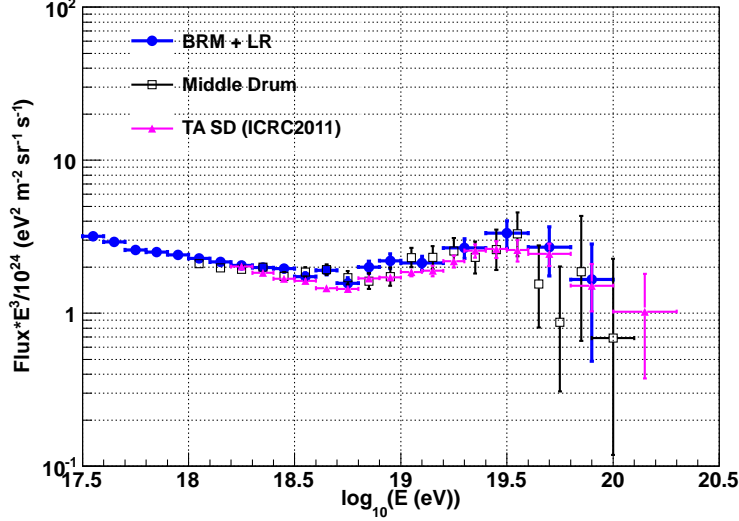


Figure 7.22: Energy spectra in the TA measurement. The blue plots show the spectrum analyzing data collected at the BRM and the LR stations, the open squares show the spectrum measured at the Middle Drum station [71], the pink triangles indicate the spectrum measured by TA SD with 27% scaled as the same energies with TA FD energies [72]

7.6.1 Fluorescence Yields

Firstly, the uncertainty attributed to the fluorescence yields is discussed. Fig. 7.23 shows several measurements of the fluorescence yields as a function of altitude in the US standard atmosphere [60] [61] [92] [93] [94]. In TA FD analysis, we adopt an absolute value of the number of fluorescence photons measured by Kakimoto et al. [61], and also we adopt the relative intensity spectrum measured by FLASH measurements [92]. Comparing total yield measured by Kakimoto et al, (blue triangles) with that measured by Nagano et al. (purple squares) at an altitude of 10 km, the difference to other measurements is 11%, and this is the systematic error attributed to the uncertainties of the fluorescence yields.

The fluorescence yields are independent of longitudinal developments of EASs, Thus, uncertainties on X_{\max} caused by the systematic error attributed to the uncertainties of fluorescence yields can be estimated from the averaged X_{\max} and its energy dependence shown in Fig. 6.2. If the energy are shifted 11%, the shift on the averaged X_{\max} is less than 5 g/cm² in all models. Therefore we estimated 5 g/cm² as X_{\max} systematic uncertainty caused by the fluorescence yield systematic error.

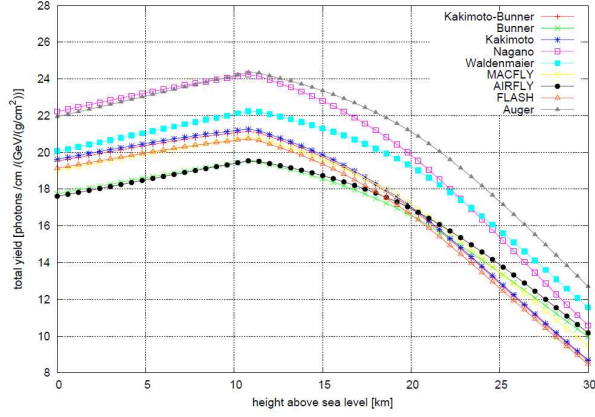


Figure 7.23: The fluorescence yield comparisons between several measurements with US standard atmosphere [60] [61] [92] [93] [94].

7.6.2 Atmospheric parameters

Secondly, we estimate the uncertainty attributed to the uncertainties on atmospheric parameters. In FD analysis, we adopt a typical value of the horizontal attenuation length (29.4 km, $VADO = 0.034$), and as the other atmospheric condition parameters we adopt the monthly average values obtained from radiosonde observations at ELKO. In order to study systematic differences, MC simulations using daily values of the horizontal attenuation length measured by the LIDAR system and also using daily values of parameters measured by radiosondes lunched daily are used as an event generator. The obtained MC events are reconstructed by two different ways. One is the reconstruction process using the typical VAOD and the monthly averaged parameters. The other is the reconstruction process using daily values which are used in the corresponding MC simulations. The distribution of differences on reconstructed energies and on X_{\max} between two analyses for the identical MC events indicate the systematics uncertainties. The systematic uncertainties on energies and on X_{\max} caused by atmospheric parameter uncertainties are $\pm 11.2\%$ and $\pm 12.4 \text{ g/cm}^2$, respectively [108].

7.6.3 Calibrations

Thirdly, we estimate the uncertainty caused by detector calibrations which directly effects the uncertainty of reconstructed energies. The major systematic error caused by the detector calibrations is attributed to the uncertainty on the absolute calibrations using CRAYS. The systematic error on a primary energy estimation is 7.2% attributed to the accuracy of the energy probe in CRAYS for the laser power measurement. Additionally the uncertainty on primary energies

of 3.7% is attributed to systematic gain drifts caused by the transports of the calibrated PMTs to TA experimental site [75].

Gains of PMTs vary caused by aging effects. We monitor the gain drifts on the absolutely calibrated PMTs by the aging effects by YAP as the calibration sources. The results of the gain drift monitoring using YAP pulsars show that no apparent gain drift is observed on any cameras. The standard deviation of drifting gains is less than 3%.

Another source of the systematic error on primary energy estimations is the mirror reflectance uncertainty attributed to the systematic uncertainty on the spectrophotometer and interpolation errors on the time variation curves of the monitored mirror reflectance. The contribution from the mirror reflectance uncertainty is the systematic energy shift of 3% and the fluctuation of less than 2%. The mirror areas also have uncertainties at the edges and the center attributed to the fluctuations on the anodization process, which is estimated to be 2%.

We adopt an average value of the transmittances of the filters on each PMT photo-cathode as the typical transmittance for all filters. The standard deviation for all the measured filters is 1%, and the same amount contributes to the energy uncertainty. The other source is the time variations of the transmittance of the camera windows damaged by dusts and fogs. However, we have not detected any apparent decreases, and it is estimated to be less than 1%.

From the square root of the quadratic sum of the uncertainties mentioned above, the total uncertainty attributed to the uncertainties on the detector calibrations is estimated to be 10%. Also we evaluated contributions from the same sources on the systematic error of X_{\max} , and it is 5 g/cm².

7.6.4 Geometry of Fluorescence Telescopes

As discussed in section 3.4.5, the directions of the telescopes are calibrated with observations and analyses of star tracks on the focal planes. The directions of the telescopes are determined with an accuracy of 0.01 degree, and the accuracy of each PMT direction is 0.1 degree. Using these values, the systematic uncertainties on energies and X_{\max} attributed to the uncertainties on telescope's and PMT's pointing directions are estimated less than 4% and 9 g/cm² with MC simulation studies.

7.6.5 Reconstruction Methods

As shown in Fig. 4.1, the averaged missing energy is difference between primary protons and irons. In our analysis, every estimated primary energy is corrected with averaged missing energy calculated for primary protons. Thus, it causes the systematic error on primary energies of 5%.

Moreover, primary energies reconstructed in the monocular analysis are systematic smaller than the thrown energies caused by geometrical accuracies in the monocular mode. Thus, we correct the systematic shift of reconstructed

energies estimated from MC simulations as shown in Fig. 6.1.2. The correction factor is estimated as 7% at $10^{19.5}$ eV.

As shown in section 7.2 of Data/MC comparisons, the shapes of lateral density distributions are slightly different for observed showers and MC simulated showers based on the NKG function. Thus, we reconstruct the observed data without lateral density distributions, and compare the reconstructed energies without lateral density distributions with energies considering lateral density distribution based on the NKG function. The contribution on the systematic error on energy estimations is 3% with our reconstruction software.

As discussed in section 6.1.2 of accuracies on X_{\max} estimated from MC simulations, there are systematic differences between thrown X_{\max} values and reconstructed ones in the monocular analysis. The averaged systematic bias is 10 g/cm^2 estimated from MC simulations shown in Fig. 6.6. Since the reconstructed X_{\max} values are not corrected in the monocular analysis, hence we use 10 g/cm^2 attributed to systematic uncertainty on X_{\max} .

7.6.6 Total Systematic Uncertainty

Table 7.2 shows the systematic uncertainties attributed to several sources. The total systematic uncertainties on energies and X_{\max} are summarized in this table. As the result, we conclude that the total systematic uncertainty on energy and X_{\max} are 21% and 19 g/cm^2 , respectively. The energy systematic error is almost same as the other experiments (AGASA: 18%, HiRes: 17%, Auger: 22%).

item	Energy	X_{\max}
Fluorescence Yield	11%	5 g/cm^2
Atmosphere	11%	12 g/cm^2
Calibration	10%	5 g/cm^2
Detector Geometry	4%	9 g/cm^2
Reconstruction	10%	10 g/cm^2
Total	21%	19 g/cm^2

Table 7.2: The total systematic uncertainty of energy and X_{\max} .

Chapter 8

Discussion

In this chapter, we summarize the analysis results for the mass composition and the energy spectrum based on the monocular analysis for TA FDs, and we discuss possible interpretations for the results and for UHECR origins.

8.1 Mass Composition Measurement

At first, we discuss interpretations of the mass composition measurement. Fig. 8.1 shows the fitting results of averaged X_{\max} estimated from MC simulations for two primary species and two hadron interaction models and calculated from observed data analysis under the FVC. The left figure and the right figure of Fig. 8.1 are fitted by different types of linear functions using the least square method of a single line fitting (a) and of two lines and a break energy (b), respectively. The point at the highest energy includes only three EASs, and these points are located at adjacent positions. Although a standard deviation calculated from these points was small, the standard deviation is much smaller than those estimated from MC simulations for all primary species and interaction models using enough statistics. In order to avoid the accidental bias attributed to small statistics, we exclude the point at the highest energy from the fittings.

Comparing reduced χ^2 of a single line function, $\chi^2/\text{ndf} = 9.682/16 \simeq 0.61$, with that of a two lines function, $\chi^2/\text{ndf} = 5.434/14 \simeq 0.39$, the fitting result using two lines connecting at a break point are better than that with a single line. When we apply two line fit on the averaged X_{\max} plots, we define the breaking energy, E_B , and elongation rates below/above E_B , D_{10}^{low} and D_{10}^{high} [g/cm²/decade]. Then we obtained $\log(E_B) = 18.6 \pm 0.2$, $D_{10}^{\text{low}} = 74 \pm 5$ and $D_{10}^{\text{high}} = 30 \pm 24$.

On the other hand, the elongation rates for MC results, with the hadron interaction model of QGSJet-II and SIBYLL, are $D_{10}^{\text{P,qgsII}} = 38 \pm 1$ and $D_{10}^{\text{P,sibyll}} = 42 \pm 2$, respectively, for protons. For primary irons, the MC calculated elongation rates are $D_{10}^{\text{Fe,qgsII}} = 37 \pm 1$ and $D_{10}^{\text{Fe,sibyll}} = 43 \pm 2$ for irons. The measured elongation rate below E_B , $D_{10}^{\text{low}} = 74 \pm 5$, is larger than the MC predicted values

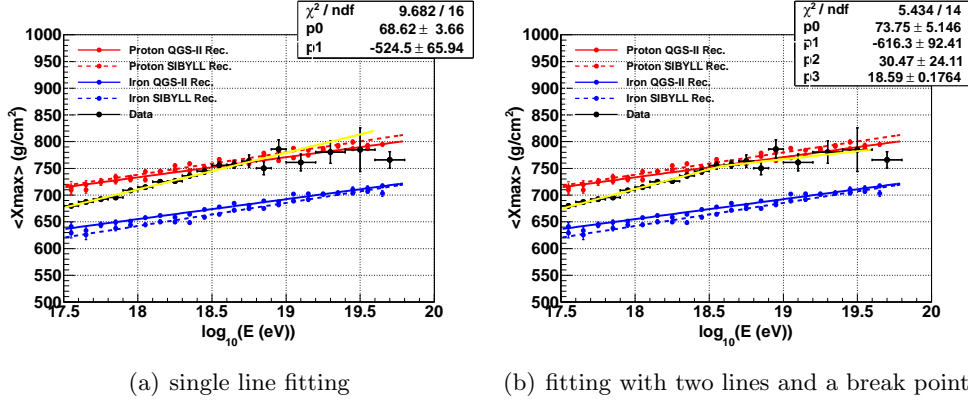


Figure 8.1: The measured averaged X_{\max} fitted by two types of line functions using the least square method.

with assuming a constant composition, regardless of hadron interaction models. Thus, the result strongly suggests the transition of the dominant component from heavy to light nuclei in the energy range from $10^{17.5}$ eV to $10^{18.5}$.

At higher energies above E_B , the measured elongation rate above E_B , $D_{10}^{\text{high}} = 30 \pm 24$, is consistent with expected elongation rates with assuming a constant composition, regardless of the hadron interaction models within the statistical error. Therefore, the result is compatible with a constant composition in the mass composition of UHECRs from $10^{18.6}$ eV to $10^{19.6}$ eV.

8.1.1 Transition of Mass Composition from $10^{17.5}$ eV to $10^{18.5}$ eV

As shown in Fig. 7.9 and Fig. 8.1, the measured averaged X_{\max} shows the clear evidence of the transition from the heavy dominant components to the light dominant components from $10^{17.5}$ eV to $10^{18.5}$ eV. Moreover, distributions of X_{\max} also indicate the same tendency in Fig. 7.10. The observed proton fraction of Fig. 7.17 calculated from averaged X_{\max} values and acceptance biases is 20% at $10^{17.5}$ eV and 90% at $10^{18.5}$ eV.

Compared with the Stereo Fly's Eye and the HiRes/MIA and HiRes measurements shown in Fig. 8.2(a)(b), the observed transition of the mass composition of the TA monocular analysis seems to be consistent with that measured by the Fly's Eye experiment. From the result of the HiRes/MIA experiment, the transition energy of HiRes/MIA is smaller than that of TA monocular analysis. However, the HiRes collaborator claims the observed X_{\max} of Fly's Eye is in agreement well with that of HiRes/MIA considering the systematic shift of 13 g/cm^2 on X_{\max} within their systematic uncertainty [38]. Thus, since a systematic uncertainty of TA monocular analysis is 19 g/cm^2 , the X_{\max} measurement of TA monocular analysis is also consistent with those of the Fly's Eye and HiRes/MIA.

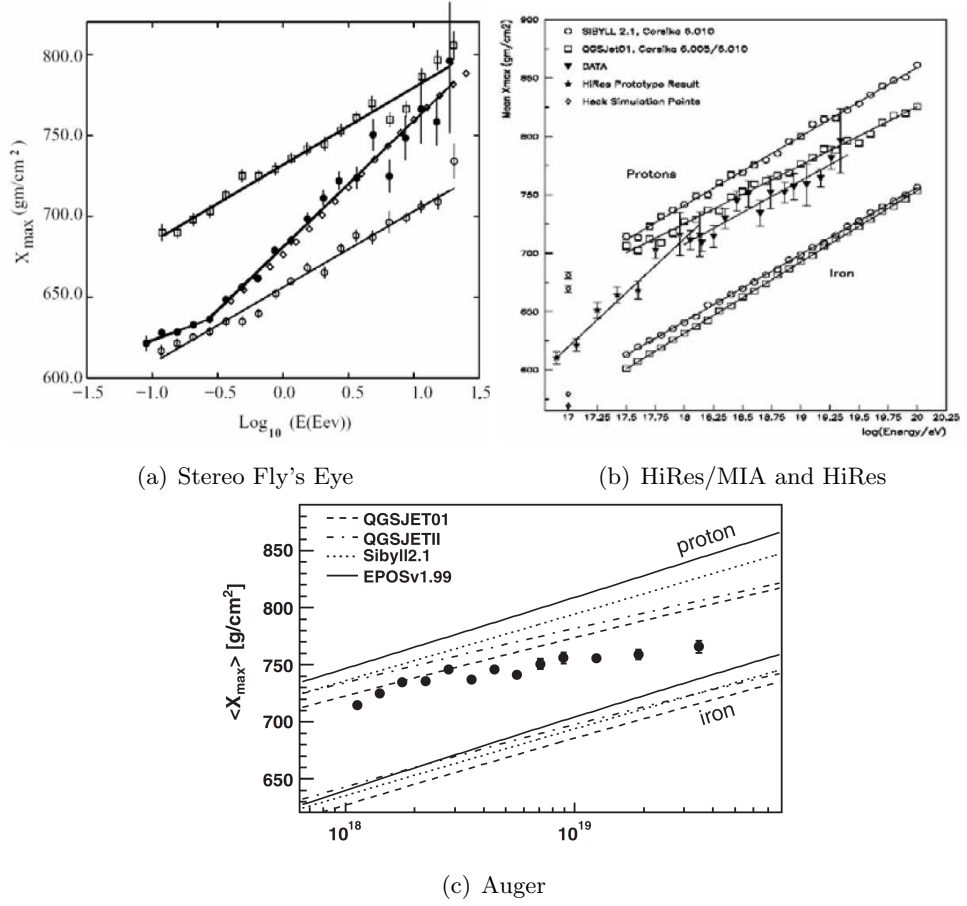


Figure 8.2: The averaged X_{\max} for Stereo Fly's Eyes (a) and HiRes/MIA and HiRes (b) [38] [37]. Auger measured $\langle X_{\max} \rangle$ compared with air shower simulations using different hadronic interaction models [40]. They are the same figures shown in Fig. 2.13 and Fig. 2.15.

As a possible interpretation, we discuss the transition of the mass composition of UHECRs. The result indicates cosmic rays are accelerated on two different types of origins: sources accelerated for iron nuclei around $10^{18.0}$ eV, and source accelerated for protons above $10^{18.0}$ eV.

If we assume rigidity dependent acceleration models such as Fermi accelerations in which maximum acceleration energies are dependent on a charge of nuclei, we can consider iron nuclei are accelerated to $\sim 10^{18.0}$ eV on a origin. Fig. 8.3 shows the observed energy spectra around knee region for several mass compositions. The Tibet group reported heavy elements dominate at the knee and beyond [97]. Additionally, cosmic rays with energies around the knee believe to be accelerated in our local galaxy. Since, we observed iron dominant at $10^{17.5}$ eV, we can consider the maximum acceleration energy reaches to $10^{17.5}$

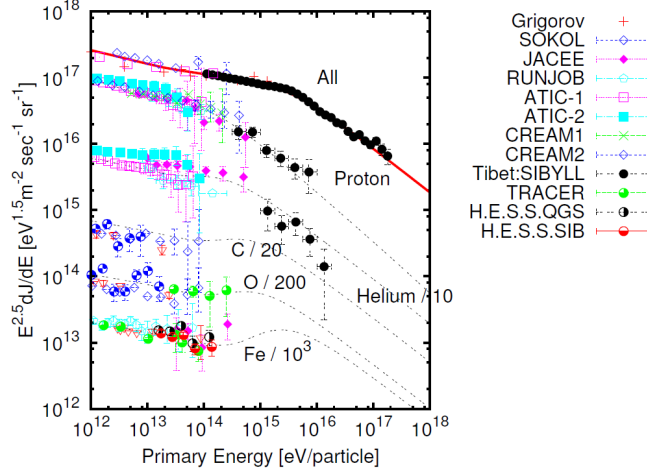


Figure 8.3: Energy spectra of several composition observed by several experiments around the knee region. The dotted lines indicate the expected flux assuming a rigidity dependent acceleration model using the results of the Tibet group [97].

eV for irons in our galaxy. In origins of higher energies, cosmic rays are accelerated above $10^{18.0}$ eV in extra-galactic sources, such as GRB, neutron star, AGN, galactic cluster and so on. Therefore, as a possible interpretation, the observed mass composition indicates a transition of origins of cosmic rays from galactic to extra-galactic sources.

If we assume cosmic rays are accelerated by neutron stars with distances enough short to avoid bending of galactic magnetic fields in our galaxy, a clear anisotropy should be observed around $10^{18.0}$ eV at the direction of astronomical objects. Therefore, it is important to observe an anisotropy of UHECRs in order to conclude origins of UHECRs.

8.1.2 Proton Dominant above $10^{18.5}$ eV

Secondly, as shown in the averaged X_{\max} of Fig. 7.9, the monocular analyses for the mass composition indicate proton dominant above $10^{18.5}$ eV.

Comparing with other measurements, the proton dominant result is also consistent with the HiRes measurement. However, the Auger claims that the mass composition is getting heavier nuclei above $10^{18.5}$ eV, which is shown in Fig. 8.2(c). Thus, there is still the contradiction between TA and Auger measurements. In this thesis, we applied the FVC on X_{\max} measurements to understand our discrepancy. Compared with the mass composition under the standard cut, an interpretation of the mass composition is the identical with the result under the FVC, because acceptance biases are also demonstrated

in the MC predicted lines as same as observed data as shown in comparisons between Fig. 7.8 and Fig. 7.18. Therefore, we confirmed the mass composition measurement by X_{\max} technique is independent of selection rules.

The TA and the Auger collaborators should understand the discrepancy on the mass composition between north hemisphere and south hemisphere. Therefore, we have plans to exchange common calibration sources or analysis softwares as future plans as world-wide international collaborations between the TA and the Auger.

As discussed in section 2.3.2, The top-down modes predict gamma-ray dominant composition above $10^{19.0}$ eV, such as the Z-burst model or annihilations/decays of dark matters. Therefore, we exclude the top-down models, and the result is consistent with bottom-up models instead of top-down models.

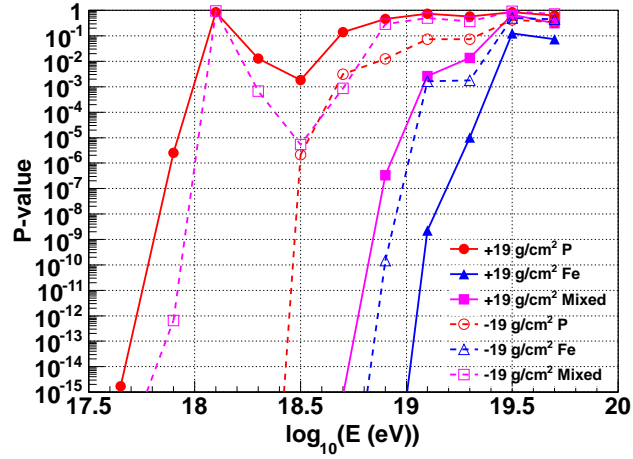


Figure 8.4: The P-values of KS test with the systematic shift on X_{\max} , ± 19 g/cm² under the fiducial volume cut. The solid and dotted lines show results of the systematic shift of $+19$ g/cm² and -19 g/cm², respectively. The red, blue, and pink lines show the result of primary protons, irons and mixed composition, respectively.

Systematic shift on X_{\max}

In order to estimate an effect of the systematic uncertainty on X_{\max} , we apply the systematic shift on observed X_{\max} values. As shown in Tab.7.2, the systematic uncertainty on X_{\max} is evaluated as 19 g/cm² in monocular mode. Thus, X_{\max} values reconstructed from observed data analysis are shifted by ± 19 g/cm², and we calculate P-values, (7.3), on KS test estimated from comparisons between observed X_{\max} distributions and the expected ones for primary protons, irons and mixed composition. This results are shown in Fig.8.4. If we

adopt the maximum systematic shift on X_{\max} , the observed X_{\max} distribution is compatible with that of pure proton model above $10^{18.8}$ eV.

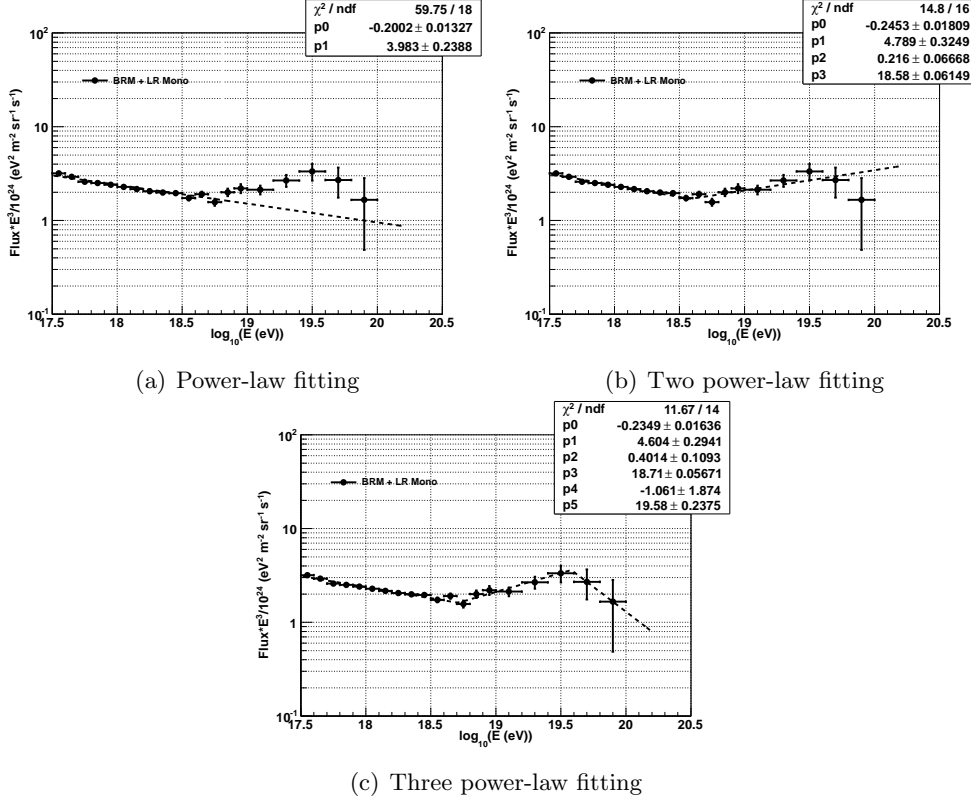


Figure 8.5: The measured energy spectrum fitted by three types of power-law function using the method of least squares.

8.2 Energy Spectrum Measurement

In the TA monocular analysis, we measured the energy spectrum with broad energies from $10^{17.5}$ eV to $10^{20.0}$ eV. Firstly, we discuss systematic uncertainties caused by the assumption of a proton fraction. Fig. 7.21 shows the energy spectra assuming proton fractions of pure proton, HiRes/MIA and TA monocular measurements. The difference is large at low energies less than $10^{18.0}$ eV, but it is negligible at high energies above $10^{18.5}$ eV. Thus, an assumption of the proton fraction impacts only at low energies less than $10^{18.0}$ eV.

Secondly, the measured spectrum in the TA monocular analysis is fitted by three types of power-law formulas shown in Fig. 8.5. The single power-law fitting is excluded by a value of the reduced χ^2 , $\chi^2/\text{ndf} = 59.75/18 \simeq 3.32$. The reduced χ^2 of three power-law fitting, $\chi^2/\text{ndf} = 11.67/14 \simeq 0.83$, is slightly better than one of two power-law fitting, $\chi^2/\text{ndf} = 14.8/16 \simeq 0.93$.

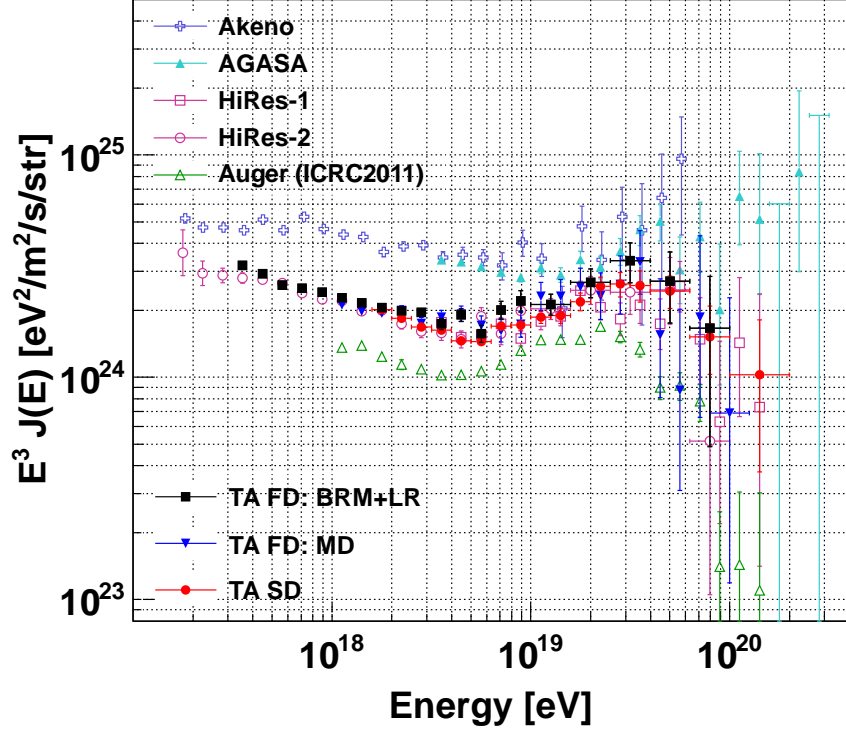


Figure 8.6: The energy spectra compared with several measurements [9] [11] [12] [44] [50] [71] [72].

Next, we compare the measured energy spectrum in the TA monocular analysis with other measurements shown in Fig. 8.6. The TA monocular spectrum is in good agreement with the HiRes measurements at all energy ranges. Moreover, the fitted values are compared with other measurements shown in Fig. 8.7 reported at UHECR 2012 Symposium [98]. The definition of fitting parameters are also described in the same figure. The fitted values in the TA monocular spectrum is consistent with values of the HiRes spectrum. The HiRes collaborators conclude a detection of the GZK suppression caused by photo-pion interactions and e^+e^- pair-creations between UHE protons and CMBR through $\gamma + p \rightarrow p + \pi^0 + \pi^\pm \dots$ and $\gamma + p \rightarrow p + e^+ + e^-$, respectively.

The left figure of Fig. 8.8 shows the propagated spectra for pure proton extra-galactic cosmic ray sources. The injection spectral index is $E^{-2.6}$ for the HiRes data. Since the TA monocular spectrum is in agreement with the HiRes spectrum, the spectrum is also consistent with the GZK cutoff.

At suppression energies shown in Fig. 8.7, E_S , there is a discrepancy beyond the fitted errors between TA SD and Auger. However, the suppression energy of the TA monocular analysis has a large fitted error attributed to low statistics.

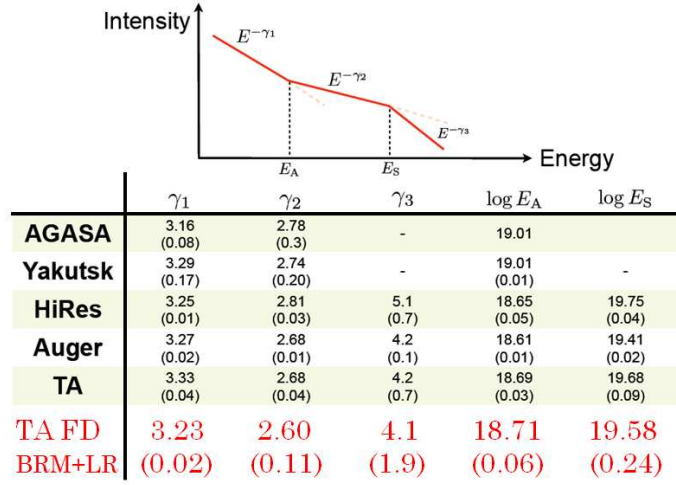


Figure 8.7: The comparison of fitted values measured by AGASA, Yakutsk, HiRes and TA(SD) reported at UHECR2012 Symposium and by BRM and LR monocular mode [98].

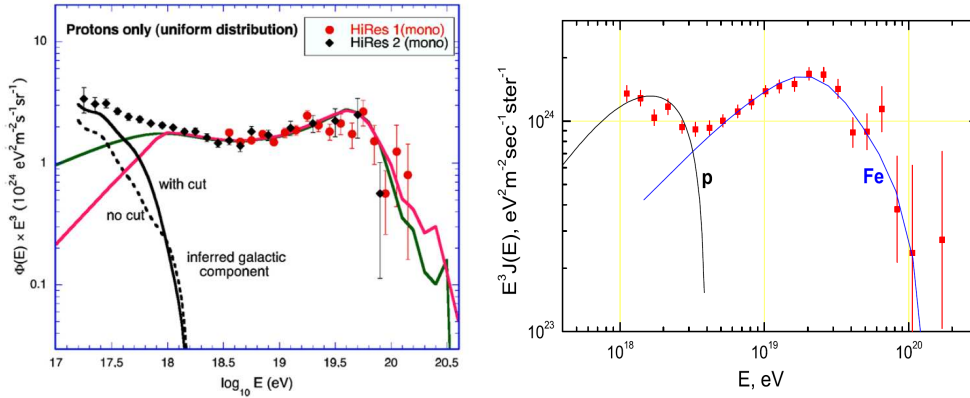


Figure 8.8: Propagated spectra, $f(E) \cdot E^3$, for pure proton extra-galactic cosmic ray sources (left). The injection spectral index is $E^{-2.6}$ for the HiRes data. Two different propagated spectra and the corresponding inferred galactic cosmic ray component are shown, for an injection spectrum either with or without a low energy cut [99]. UHECR spectra to be expected from a two component model (right) [15], which is the same figure shown in Fig. 2.4.

The suppression energy of the TA monocular analysis is consistent with both TA SD and Auger within the fitted error. Therefore, there is not enough statistics for the TA monocular spectrum to distinguish the suppression energies

measured by TA and Auger.

The ankle energy and the spectral indexes around ankle estimated from the TA monocular spectrum are consistent with those of TA SD. When the Auger energies are scaled to fit the ankle energy, the scaled Auger spectrum is also consistent with the TA SD except for the suppression energy as shown in Fig. 8.9. As a result, considering energy scales, the TA monocular spectrum is consistent with all spectra within the error.

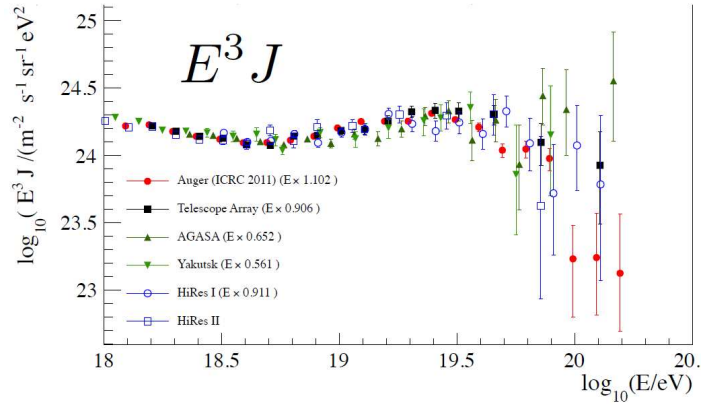


Figure 8.9: The scaled energy spectra measured by AGASA, Yakutsk, HiRes and TA(SD) reported at UHECR2012 Symposium [98]. The TA SD, HiRes and Auger are in agreement well within the systematic uncertainties.

8.3 Combined Interpretation

The clever advantage to observe UHECRs in the TA monocular analysis is measurements of both the energy spectrum and the mass composition with broad energies from $10^{17.5}$ eV to 10^{20} eV.

The structure of the measured energy spectrum is consistent with the interaction between UHE protons and CMBR, and the measured mass composition is proton dominant above $10^{18.5}$ eV. Therefore, we claim the ankle structure of the energy spectrum is generated through e^+e^- pair-creations between UHE protons and CMBR. In contrast, these results are clearly contradictions with the dip transition model from galactic to extra-galactic sources shown in Fig. 2.4.

As a result, since the position of ankle is universal, we can apply the ankle structure as an energy calibrator as shown in Fig. 8.9. Furthermore, the observed energy spectrum and mass composition results are also consistent with expectation estimated from GZK feature. However, since there are low statistics above $10^{19.6}$ eV in the mass composition analysis, and the spectral index of the energy spectrum above the suppression energy has large statistical error,

we can not significantly claim the observation of the GZK cutoff.

If GZK neutrinos which are generated through GZK processes are observed in neutrino detectors, such as the IceCube experiment [102], it is a significant evidence to exist the GZK mechanism. If the mass composition of UHECRs with energies above 10^{20} eV is still protons, we could measure a correlation between arrival directions of UHECRs and large scale structures or known astronomical objects, and observe a recovering from the GZK suppression above 10^{21} eV in next-generation observations.

In order to conclude proton dominant of cosmic rays with energies above $10^{19.6}$ eV, we need more statistics of UHECRs under the FVC. The measured mass composition under the standard cuts with twice statistic also indicates proton dominant above $10^{19.6}$ eV, although the acceptance biases are large. These result is consistent with acceleration models of extra-galactic sources such as GRB, AGN, galactic cluster. However, we can not distinguish these origin models to observe the mass composition and the energy spectrum, and need to observe an anisotropy of UHECRs. If these sources are origins of UHECRs, the correlation between arrival directions and known astronomical objects should be clearly observed by surface detectors to collect more statistics of UHE protons in near future.

8.4 Future Plans

The TA experiment has been started constructing a dense of surface detector array and new fluorescence detectors, called Telescope Array low energy extension (TALE) [100]. The schematic view of TALE is shown in Fig. 8.10.

The TALE consists of 105 SDs same as the TA SD with three types of spacing: 400 m, 600 m and 1200 m, respectively, and 14 FDs with a upper field of view to observe UHECRs from low energies, above $10^{16.5}$ eV, using hybrid techniques. Using collected data, we will measure the mass composition with high resolution due to the hybrid technique, and an anisotropy measurement above $10^{16.5}$ eV by the dense deployed SDs.

Moreover, the TA experiment has started “hybrid triggers” in the end of 2010 at three FD stations [107]. The hybrid trigger has been shown from our MC studies that geometry determination accuracies of monocular FD events are significantly improved using SD information. However, in lower energy region below $10^{18.5}$ eV, trigger efficiency for the TA SD is small compared with that of FD, therefore some showers have no SD information. Then to collect the small SD signals, we have installed an FD driven SD trigger system: this introduces an external triggering scheme to the TA SD using triggering signals from FD. We have already measured the FD and SD data collected by the hybrid trigger more than 1 years. In near future, the mass composition are measured with high accuracies and statistics using the hybrid technique.

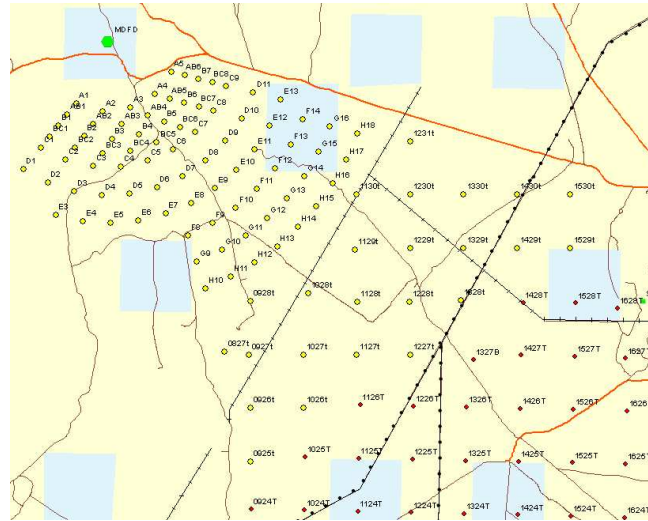


Figure 8.10: The schematic view of the TALE experiment. The yellow circle shows newly constructed dense SDs, the red circle shows the SDs of TA. The green hexagon indicates the TALE FD at the same location of TA MD.

Telescope Array 2

We have started the research and development of Telescope Array 2 (TA-2) as the future plan of TA. The TA-2 will be the world record of UHECR detectors which consists of 10,000 SDs with 2.0 km spacing and covers with $\sim 40,000$ km² effective area. The comparison of effective area of UHECR observations are shown in Fig. 8.11. You see that TA-2 is the largest detector to observe UHECRs.

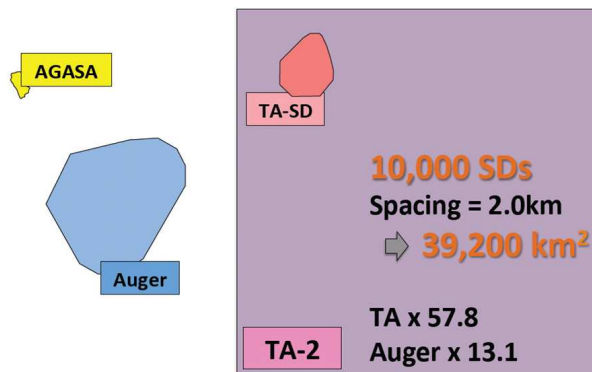


Figure 8.11: The comparison of effective area of UHECR observations: AGASA, Auger, TA SD and TA-2.

In the TA-2, we concentrate on the UHECR detections with energies above $10^{19.5}$ eV. Therefore, we can identify UHECR sources and conclude the UHECR origins using TA-2 measurements.

JEM-EUSO

An other future plan to observe UHECRs is the Extreme Universe Space Observatory on board Japanese Experiment Module (JEM-EUSO) [101]. JEM-EUSO is a new type of observatory that uses the earth's atmosphere as a detector. As shown in Fig.8.12, JEM-EUSO will be installed on the International Space Station (ISS) located on the orbit, and observe UHECRs with energies above $3 \times 10^{19.0}$ eV using a super wide-field telescopes from the space.

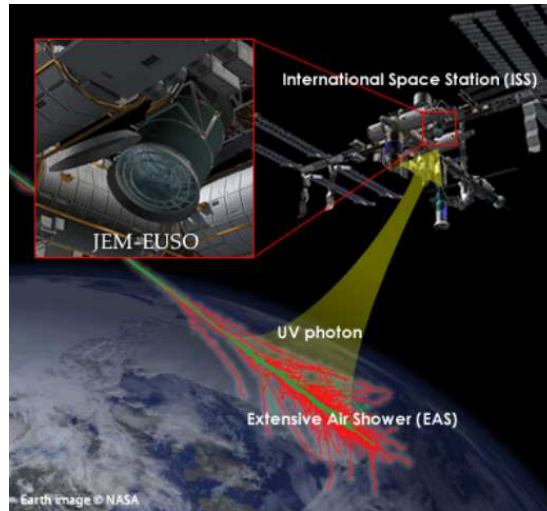


Figure 8.12: Overview of JEM-EUSO project [101].

The JEM EUSO telescopes has a super-wide-field of view $\pm 30^\circ$, with two double side curved Fresnel lenses and records the track of an EAS with a time resolution $2.5 \mu\text{s}$ and a spatial resolution of about 0.75 km, corresponding to 0.1° . The time-segmented images allow a determination of energies and directions of UHECRs. The light receiving section of the JEM EUSO telescope is formed by about 6000 multi-anode PMTs. The number of pixels is about two hundred thousand. The observational aperture of the ground area is a circle with 250 km radius, and its atmospheric volume above it with a 60° field of view is one tera-ton or more.

The remote-sensing JEM-EUSO orbits around the earth every 90 minutes on a board of the ISS at the altitude of 400 km with a huge effective area. Thus, in addition to the significant increase of the overall exposure by about an order of magnitude compared with Auger as of today, the orbiting JEM-EUSO telescope will cover the entire Celestial Sphere. Such advantage is more

pronounced if UHECRs from a single source are observed with angular spread, and more important to open up “particle astronomy” through the investigation of UHECR origins.

Chapter 9

Conclusions

In order to conclude origins of cosmic rays, the Telescope Array experiment has started stable observations in 2008, and it consists of 38 Fluorescence detectors located in three stations and 507 surface detectors with 1.2 km separations covering with 700 km² of effective area. We explained our MC simulations and reconstruction methods of fluorescence detectors, and then evaluated an performance of FD in monocular mode though analyzing simulated shower events. In order to evaluate the energy spectrum and the mass composition of UHECRs, an aperture of FD and an averaged X_{\max} expected for primary protons or irons are estimated from the MC simulations. Moreover, since FDs have the limited field of view and the observed average X_{\max} has the bias, we determined the fiducial volume cut and almost confirmed bias-free of averaged X_{\max} in the MC simulation.

Using the developed reconstruction, we analyzed the data collected at the BRM and LR stations during 3.7 years in monocular mode. As a result, twenty thousand showers are analyzed, and then we confirmed reasonable agreements between observed data distribution of several parameters and the expected one estimated from MC simulations. Moreover, our developed software was compared with *independently developed software* for the cross-checking, and we confirmed consistencies within expected errors.

As further enhancement of our reliability in our analysis, the measured averaged X_{\max} was compared with the expectation value estimated from MC simulations for primary protons or irons using the QGSJet-II hadron interaction model or the SIBYLL one. The measured X_{\max} indicated a transition of dominant components from heavy to light nuclei from $10^{17.5}$ eV to $10^{18.5}$ eV and proton dominant with energies above $10^{18.5}$ eV. The proton fraction and the mean of $\ln A$ were also evaluated from averaged X_{\max} assuming a mixed composition of purely protons and irons. Moreover, the averaged X_{\max} values under fiducial volume cuts was compared with those under only standard cuts, corresponding to *biased* X_{\max} . Since both results were consistent, we confirmed the mass composition is not dependent on the selection rules.

We measured the energy spectrum of UHECRs with a broad energies from

$10^{17.5}$ eV to $10^{20.0}$ eV, and observed spectrum is in good agreement with TA SD and TA MD transported from the HiRes experiment. Finally, we evaluated that systematic uncertainties of energy and X_{\max} are 21% and 19 g/cm², respectively.

Appendix

A.1 Observed EAS Events

We show event displays of the top-three highest observed EASs shown in Fig. 7.7 under the fiducial volume cut (FVC). The left side of each figure shows observed photon signals emitted from EASs for all PMTs of a station. The colors indicate timings entering photons emitted from EASs and sizes of plots show the number of detected photo-electrons on each PMT. The right side of each figure indicates detected signals on PMT cameras. The plots indicate observed signals analyzing data observed at FD stations, and the color histograms show a contribution of fluorescence photons (red) and contamination of direct Čerenkov photons (green), its Rayleigh scattered photons (blue) and its Mie scattered photons (purple).

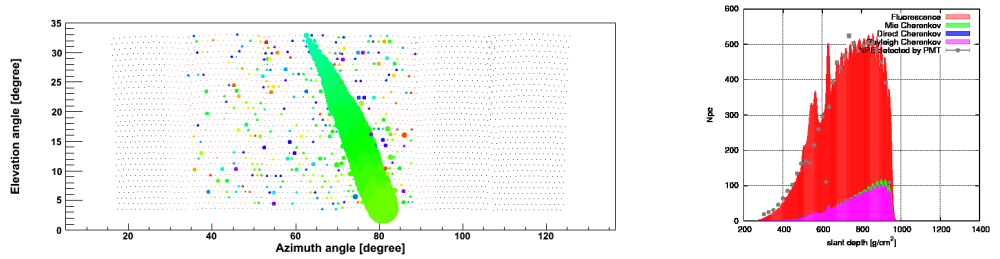


Figure A.1: The observed UHECRs : $E = 10^{19.77}$ eV, $X_{\max} = 796$ g/cm²

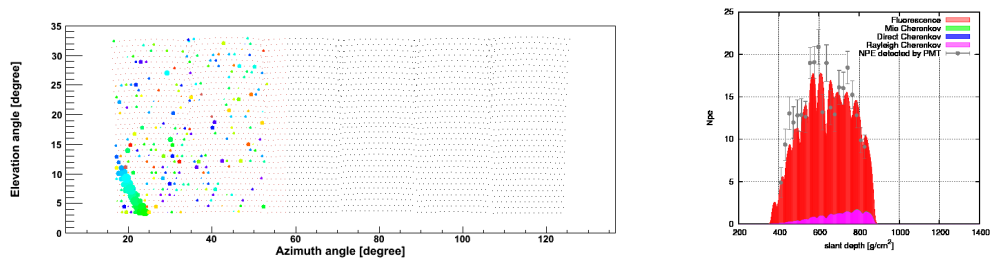


Figure A.2: The observed UHECRs : $E = 10^{19.75}$ eV, $X_{\max} = 758$ g/cm²

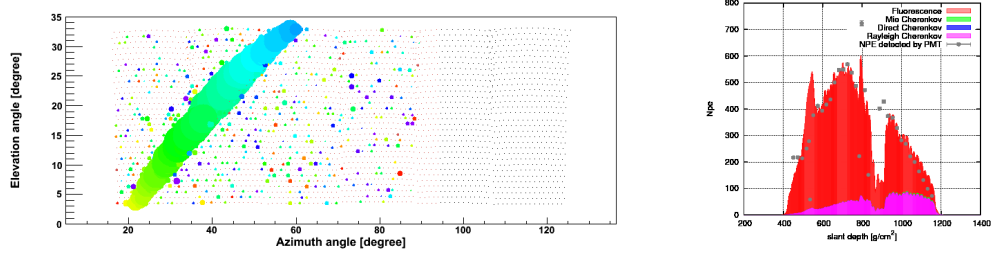


Figure A.3: The observed UHECRs : $E = 10^{19.67}$ eV, $X_{\max} = 743$ g/cm²

A.2 Data/MC comparison

As further enhancement of our reliability in our analysis, distributions of the several parameters obtained from the reconstructions of the observed data are compared with the expected ones estimated from MC simulations. In analyses of this thesis, there are two types of selection rules as discussed in Sec. 6.1.1. One is called as the standard cuts, and The other is called as the *fiducial volume cuts* to achieve a bias-free analysis on X_{\max} measurements. Here, we compare distribution of several parameters of observed UHECR with energies above $10^{17.5}$ eV under both of the selection rules between observed data and MC simulations. Results under the standard cuts are shown in Fig. A.4 to A.17 and under the *fiducial volume cuts* in Fig. A.18 to A.31.

There are discrepancies caused by differences of a mass composition, assumption of a spectral index and a lateral density distribution of EASs assuming the NKG function. At highest energies region above 10^{19} eV, the energy spectrum does not follow the spectral index of -3.1, and then it attributes to discrepancies of far showers. At measurements of cosmic rays with energies less than $10^{18.0}$ eV, which has the largest statistic, we measure transitions of dominant components from heavy to light nuclei with energies from $10^{17.5}$ eV to $10^{18.5}$ eV. Therefore, compositions were mixed in the energy range. Differences of the number of selected PMTs are caused by discrepancies of physics models of lateral density distributions of EASs. The results indicate the lateral density distribution estimated from NKG function used in our analysis software is wider than that obtained from observed data reconstructions. However, the differences are enough small, and we included as systematic uncertainties as discussed in Sec. 7.6. As a result, the distributions estimated from MC simulations are in reasonable agreements with the distributions obtained from reconstructions of observed data.

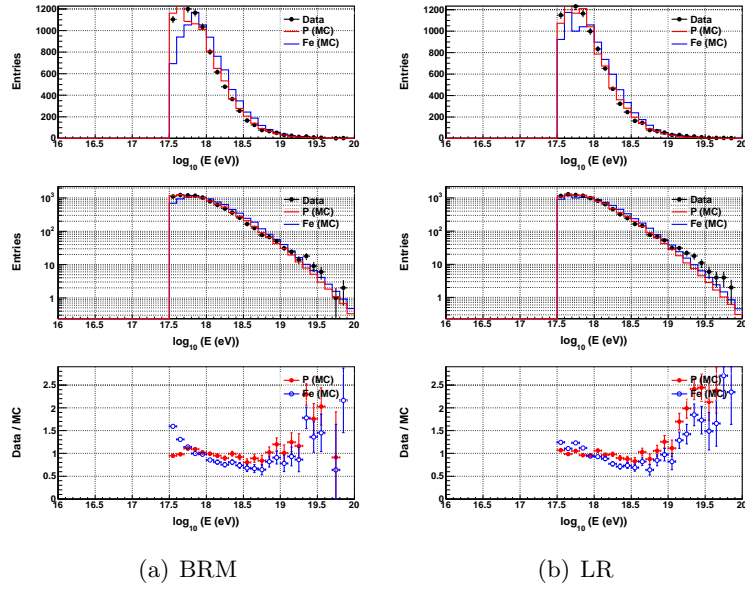


Figure A.4: The distribution of Energy between data and MC simulation under the standard cut. At the highest region, there is slightly difference caused by the assumption of spectrum index, $E^{-3.1}$.

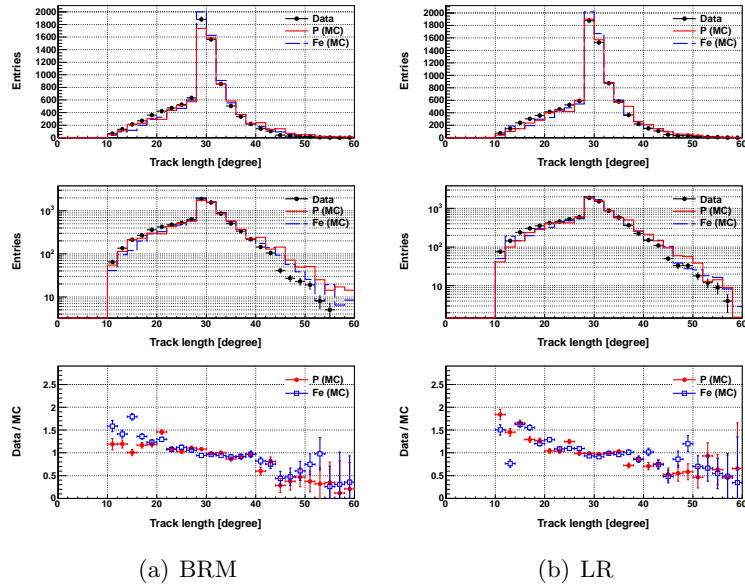


Figure A.5: The distribution of the track length between data and MC simulation under the standard cut.

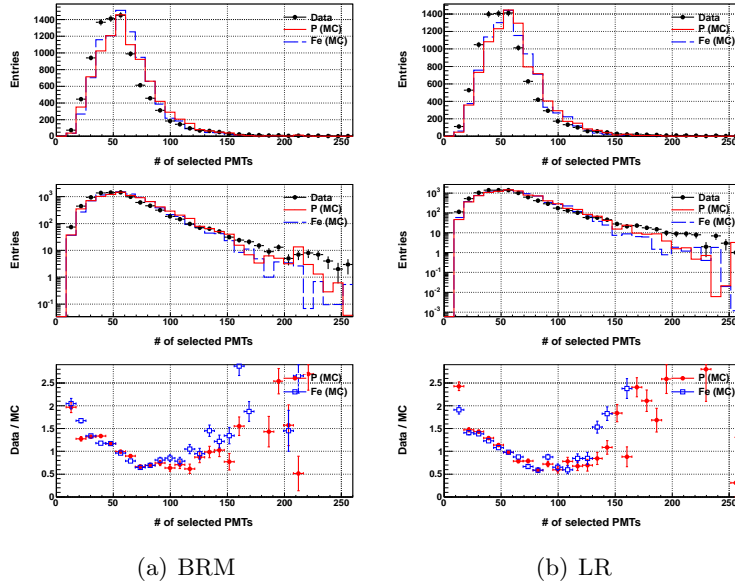


Figure A.6: The distribution of the number of selected PMTs between data and MC simulation under standard cut. The result indicates the difference of physics model of the lateral density distribution of EAS. The observed lateral density distribution is wider than one expected from NKG function used in our software.

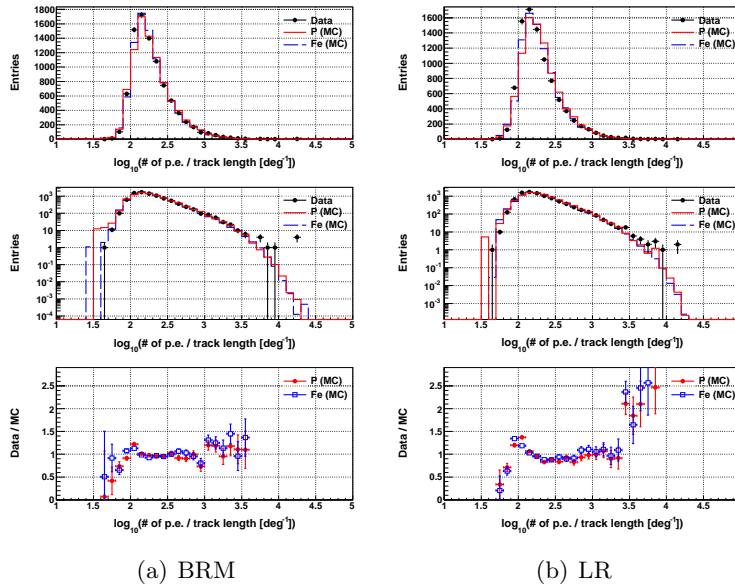


Figure A.7: The distribution of the number of photo-electrons divided by track length between data and MC simulation under the standard cut.

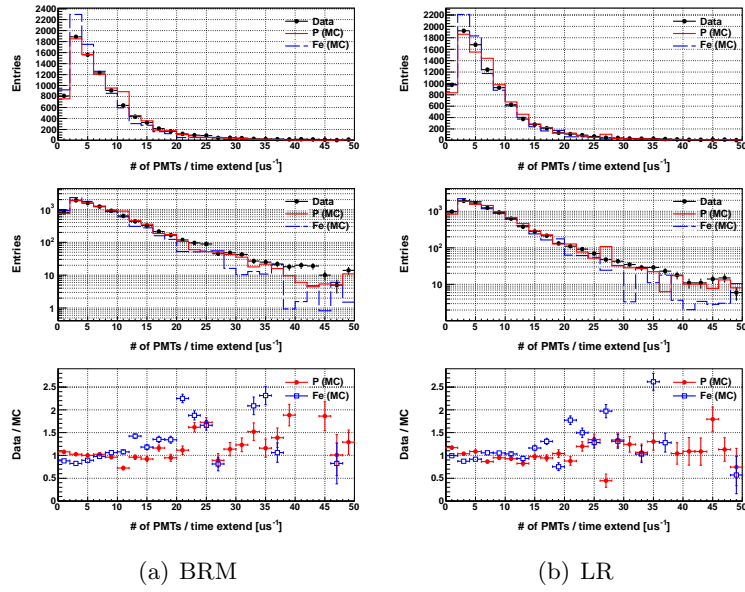


Figure A.8: The distribution of the number of selected PMTs divided by time extent between data and MC simulation under the standard cut.

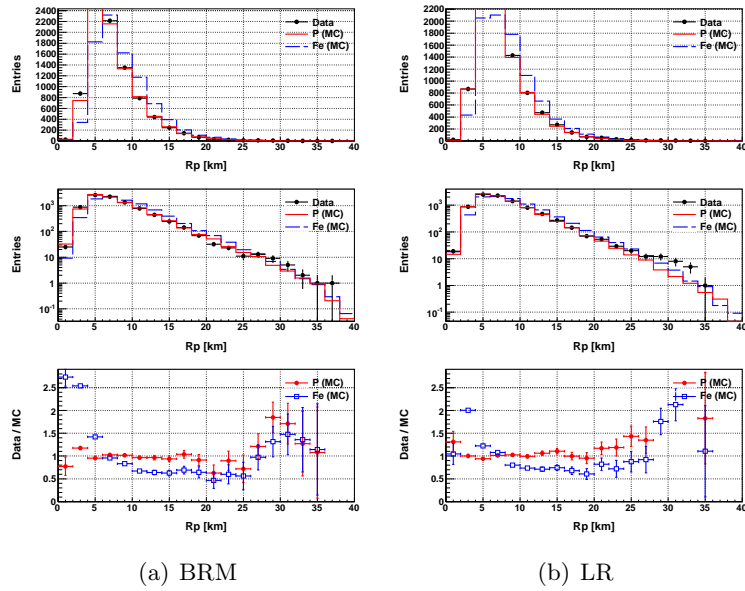


Figure A.9: The distribution of the impact parameter between data and MC simulation applied under the standard cut. At the highest region, there is slightly difference caused by the assumption of spectrum index, $E^{-3.1}$.

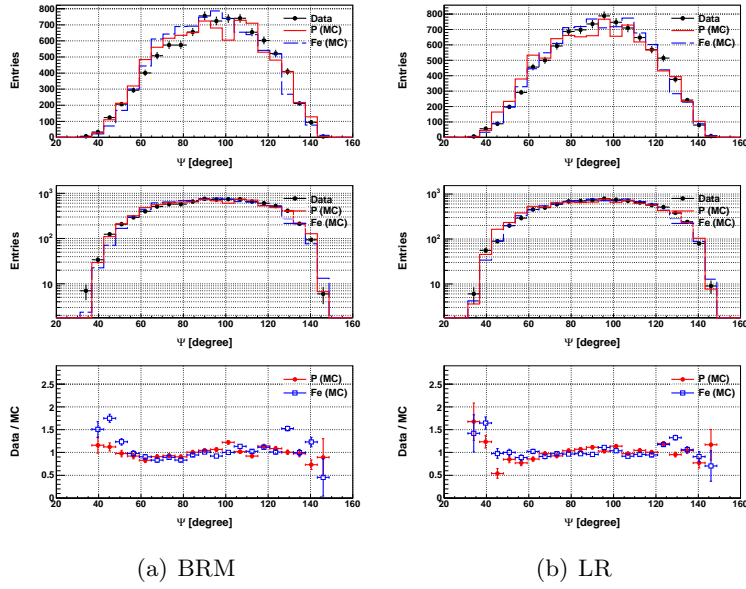


Figure A.10: The distribution of the angle on SDP between data and MC simulation applied under the standard cut.

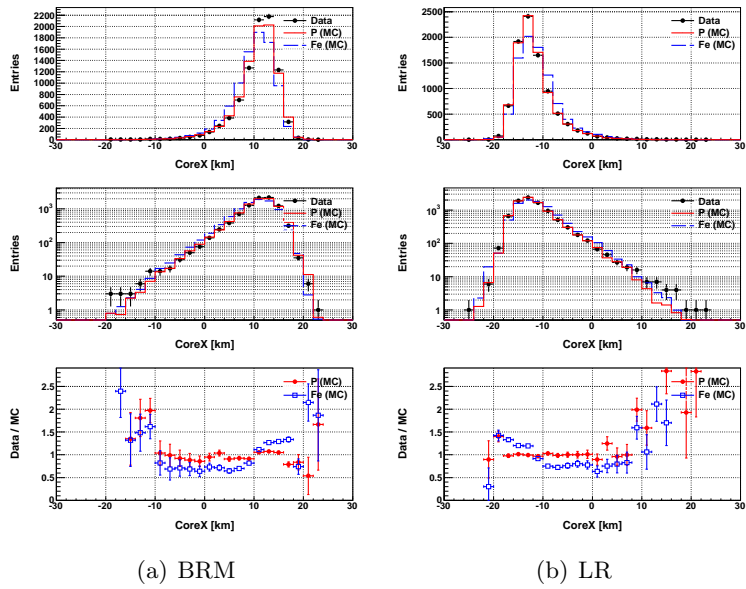


Figure A.11: The distribution of core location of West-East direction between data and MC under the standard cut.

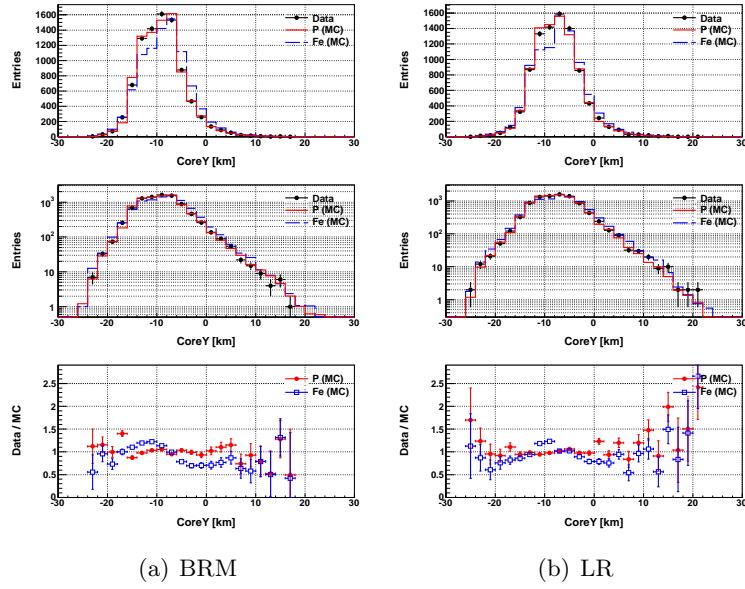


Figure A.12: The distribution of core location of South-North direction between data and MC simulation under the standard cut.

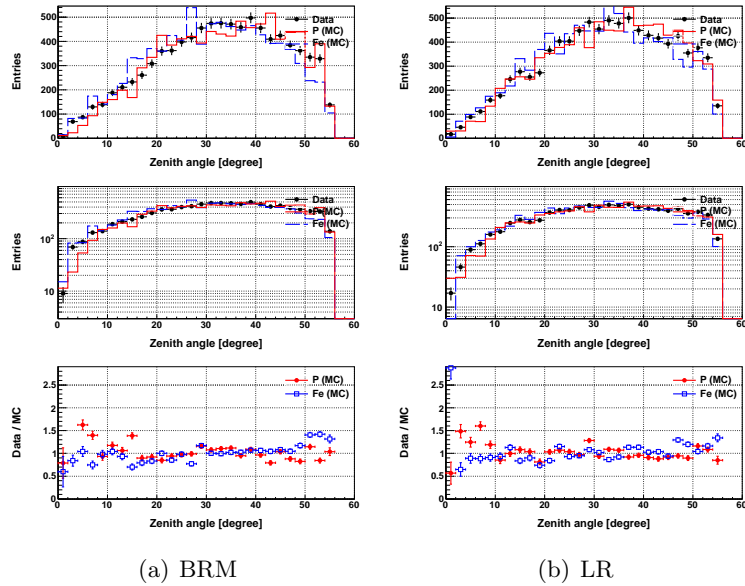


Figure A.13: The distribution of zenith angle between data and MC simulation under the standard cut.

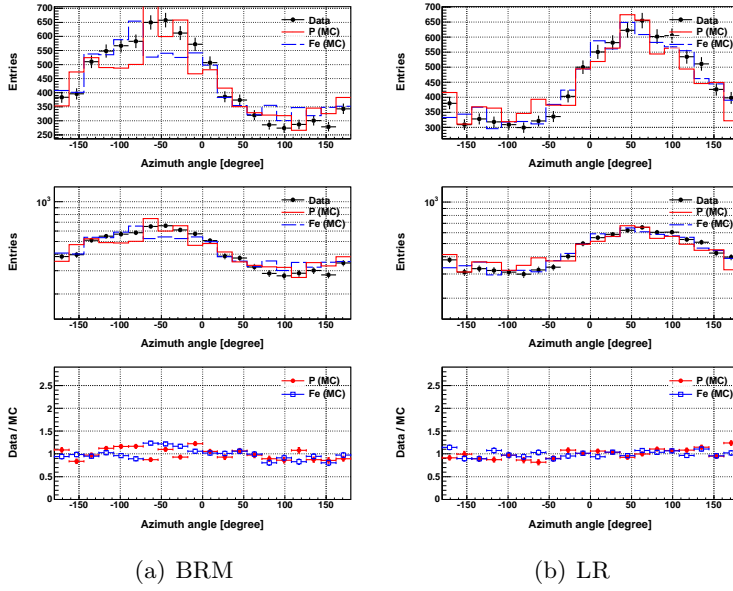


Figure A.14: The distribution of azimuth angle between data and MC simulation under the standard cut.

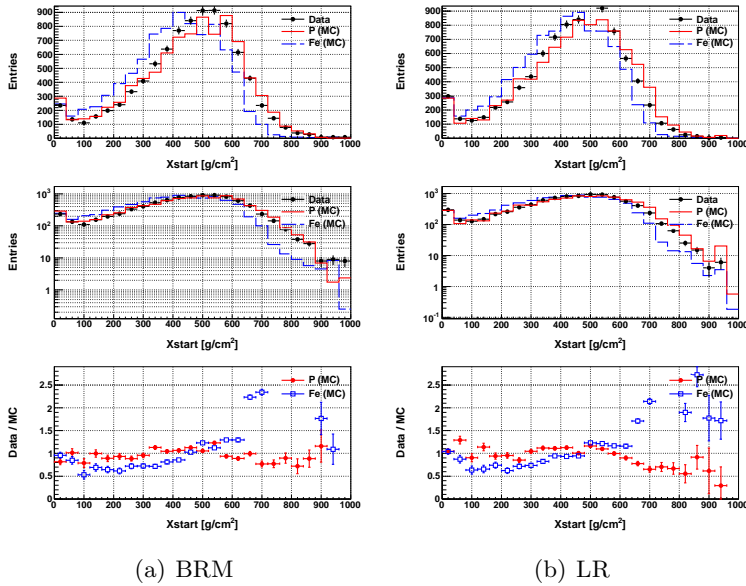


Figure A.15: The distribution of X_{start} between data and MC simulation under the standard cut.

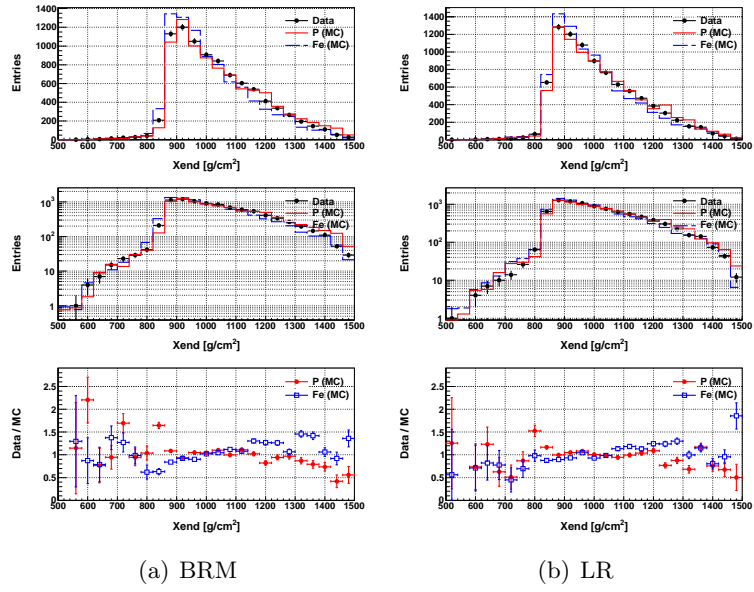


Figure A.16: The distribution of X_{end} between data and MC simulation under the standard cut.

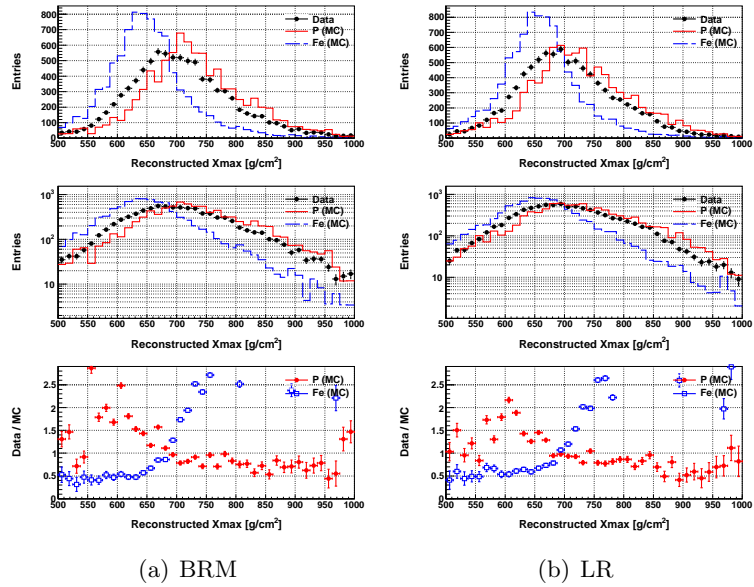


Figure A.17: The distribution of X_{max} between data and MC simulation under the standard cut. Since the discrepancy of difference between protons and irons is large, X_{max} is the most sensitive parameter to evaluate the mass composition of EASs.

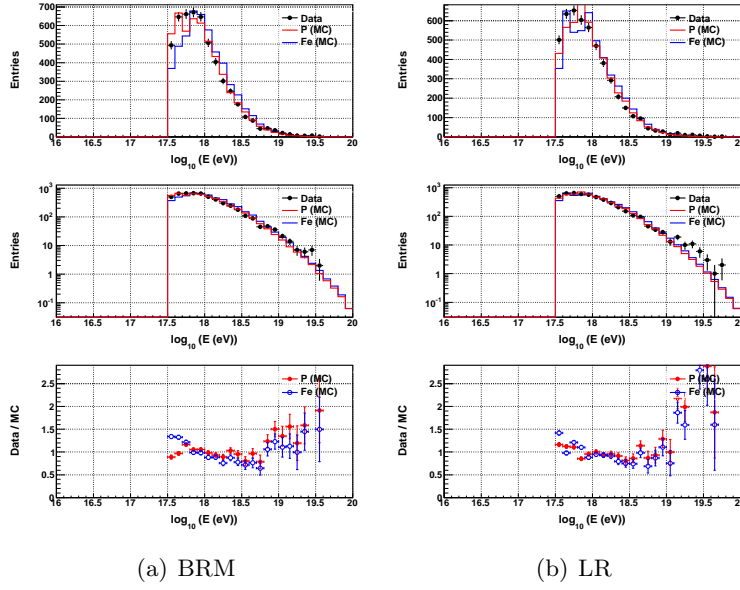


Figure A.18: The distribution of energy between data and MC simulation under the *fiducial volume cut*. At the highest region, there is slightly difference caused by the assumption of spectrum index, $E^{-3.1}$.

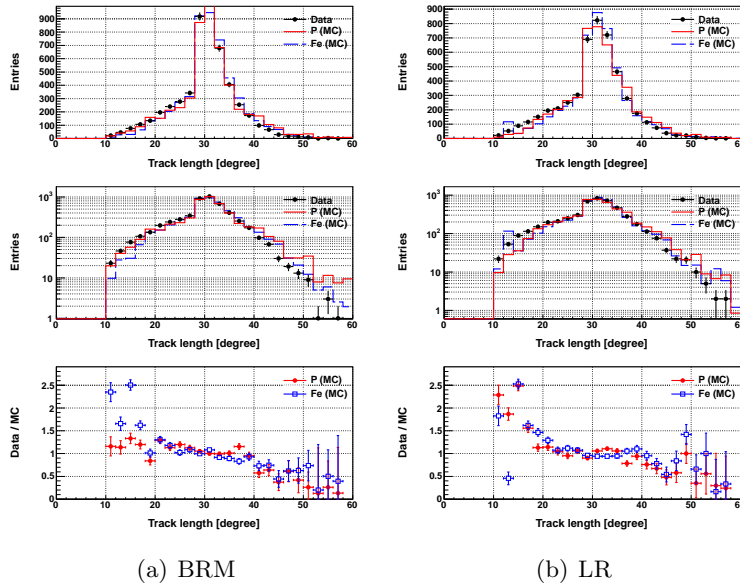


Figure A.19: The distribution of the track length between data and MC simulation under the *fiducial volume cut*.

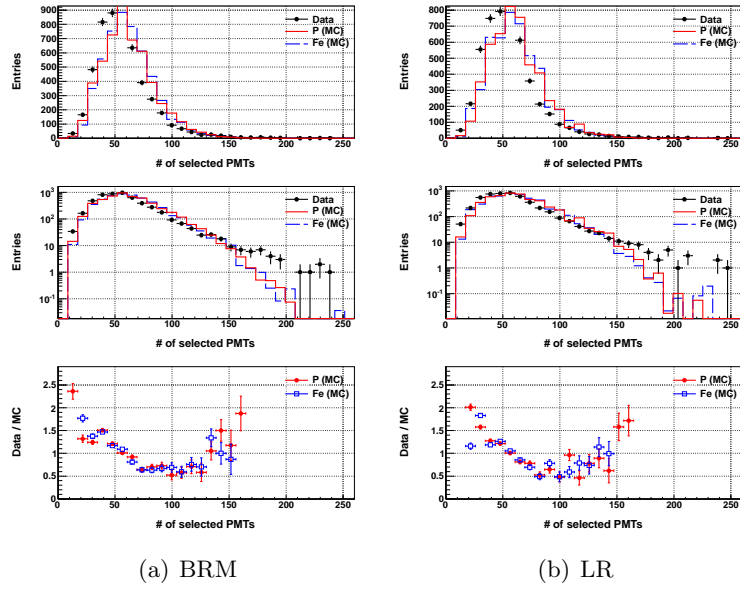


Figure A.20: The distribution of the number of selected PMTs between data and MC simulation under the *fiducial volume cut*. The result indicates the difference of physics model of the lateral density distribution of EAS. The observed lateral density distribution is wider than one expected from NKG function used in our software.

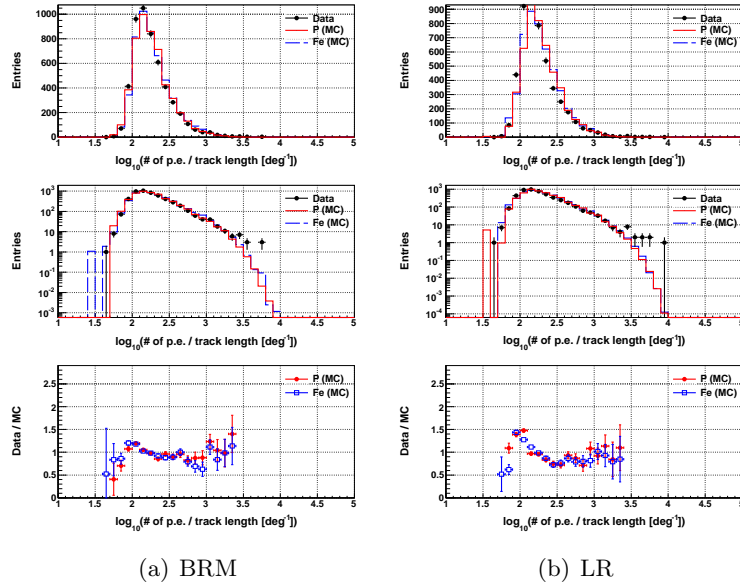


Figure A.21: The distribution of the number of photo-electrons divided by track length between data and MC simulation under the *fiducial volume cut*.

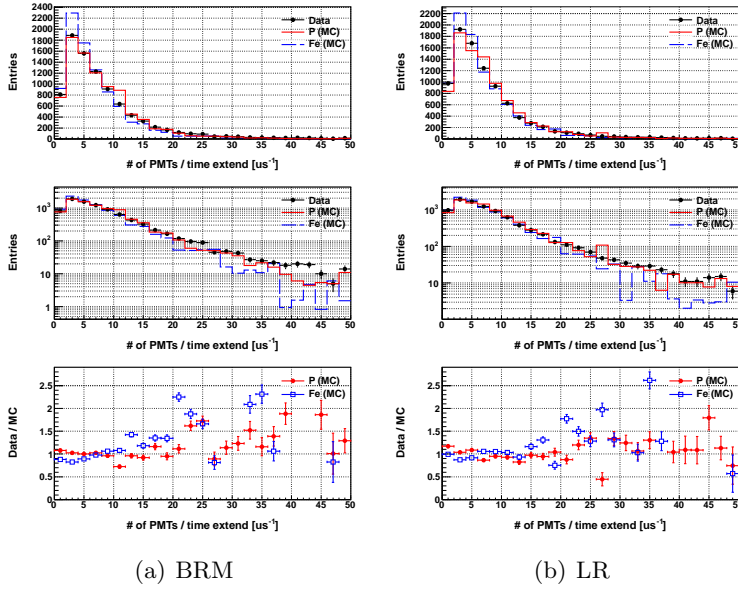


Figure A.22: The distribution of the number of selected PMTs divided by time extent between data and MC simulation under the *fiducial volume cut*.

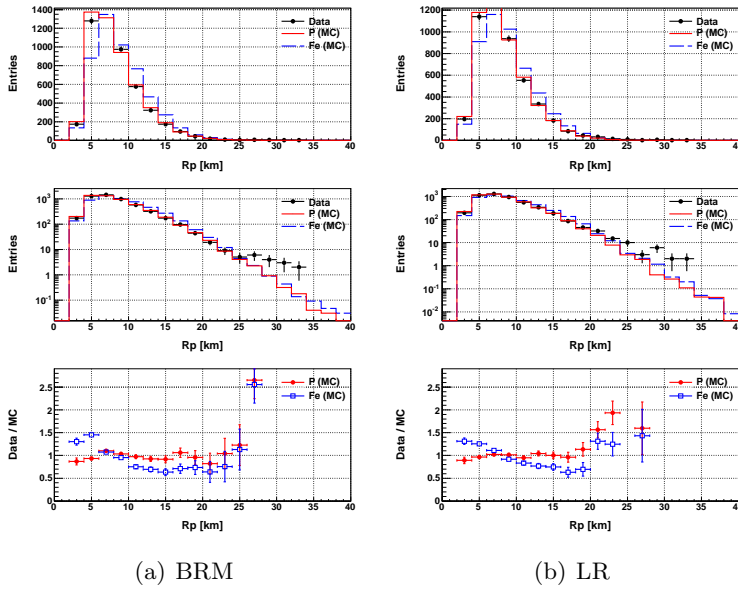


Figure A.23: The distribution of the impact parameters between data and MC simulation under the *fiducial volume cut*. At the highest region, there is slightly difference caused by the assumption of spectrum index, $E^{-3.1}$.

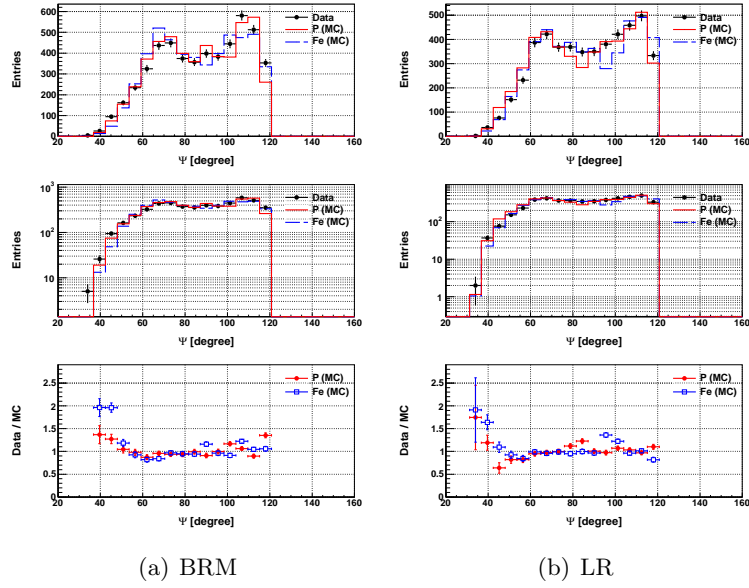


Figure A.24: The distribution of the angle on SDP between data and MC simulation under the *fiducial volume cut*. The angle of $\Psi > 120$ are excluded because of Čerenkov contaminations.

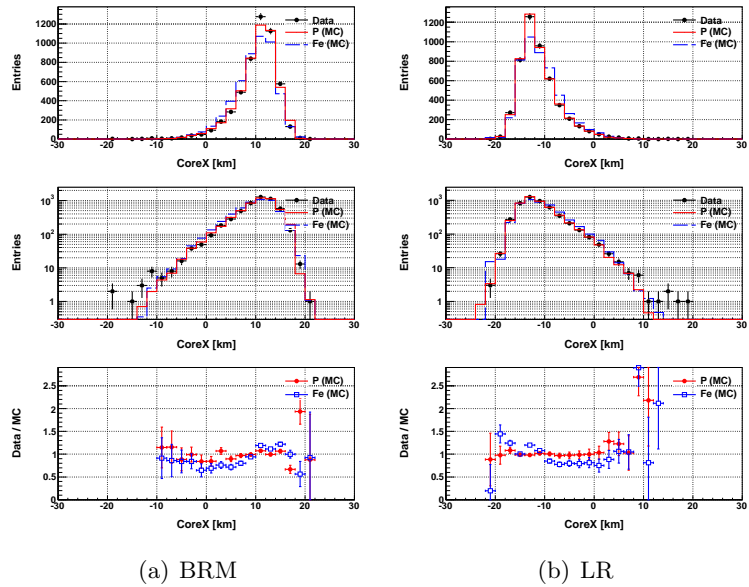


Figure A.25: The distribution of the core location of West-East direction between data and MC simulation under the *fiducial volume cut*.

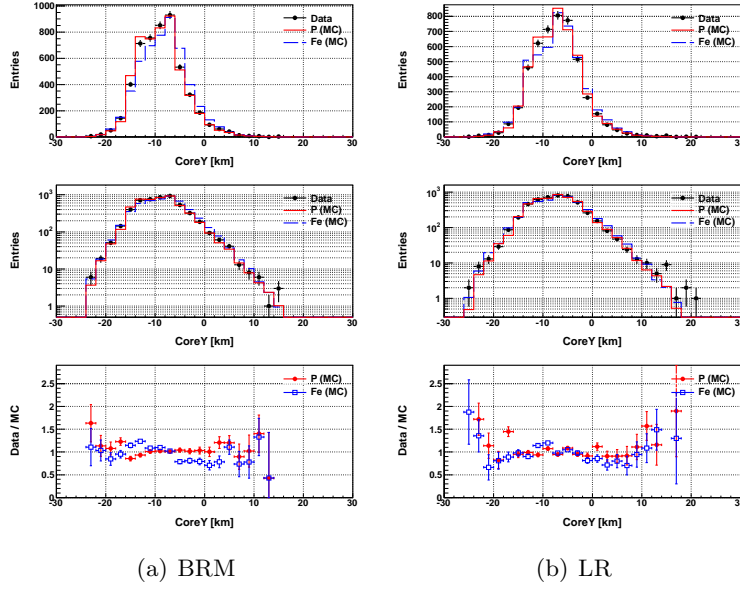


Figure A.26: The distribution of the core location of South-North direction between data and MC simulation under the *fiducial volume cut*.

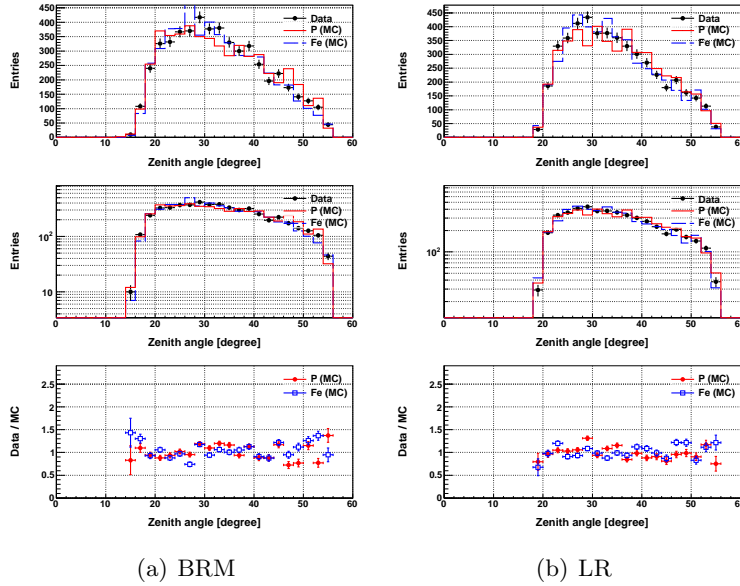


Figure A.27: The distribution of the zenith angle between data and MC simulation under the *fiducial volume cut*. The inclined shower is disappeared under the fiducial volume cut to avoid the acceptance bias of X_{\max} .

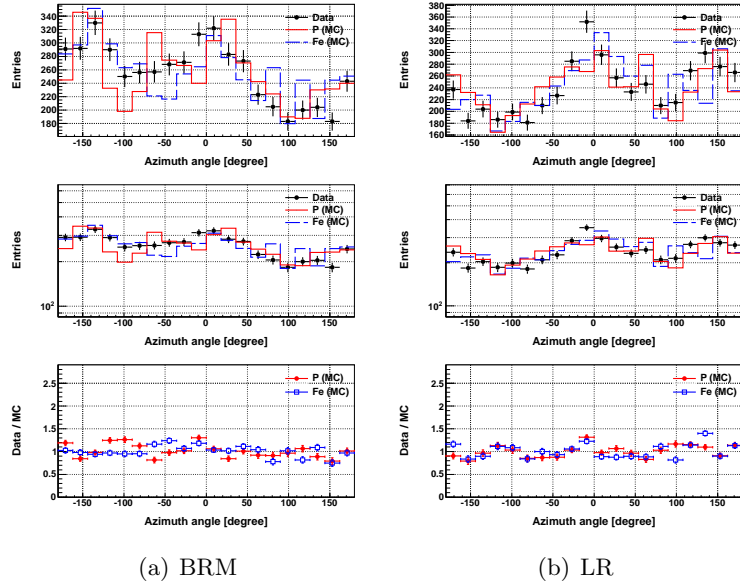


Figure A.28: The distribution of the azimuth angle between data and MC simulation under the *fiducial volume cut*.

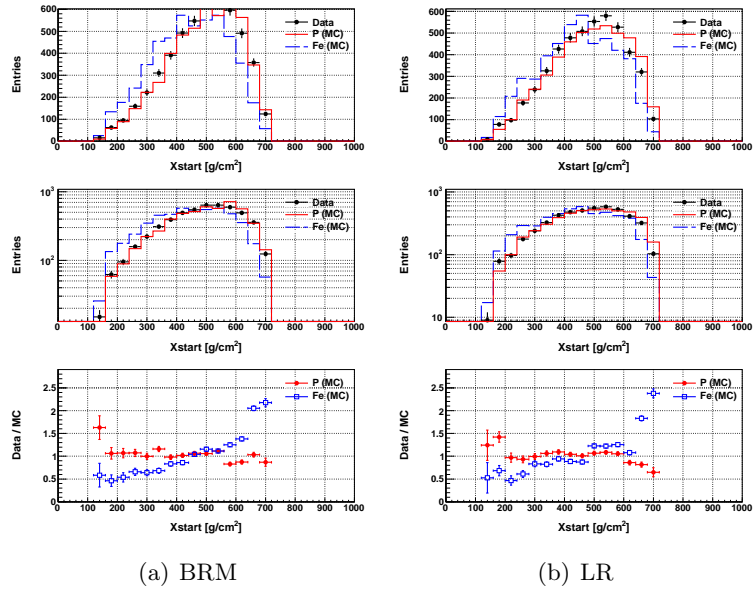


Figure A.29: The distribution of X_{start} between data and MC simulation under the *fiducial volume cut*. We applied the selection rule as $150 \text{ g/cm}^2 < X_{\text{start}} < 700 \text{ g/cm}^2$.

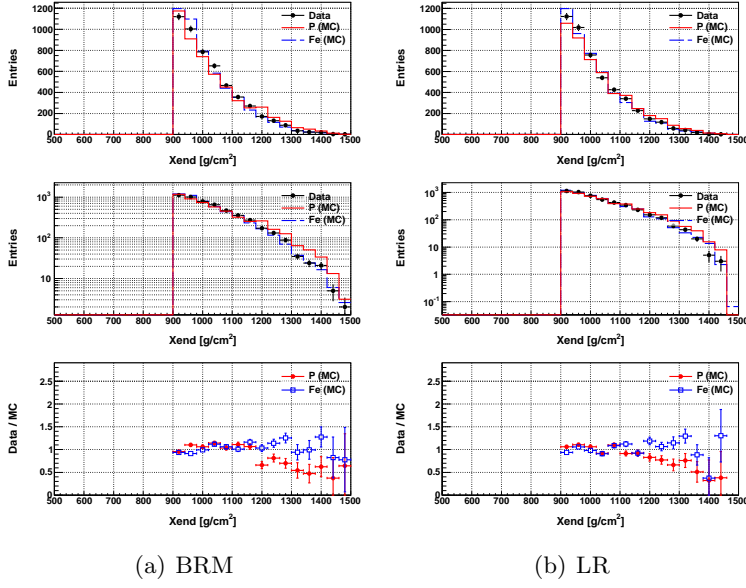


Figure A.30: The distribution of X_{end} between data and MC simulation under the *fiducial volume cut*. We applied the selection rule as $900 \text{ g/cm}^2 < X_{\text{end}}$.

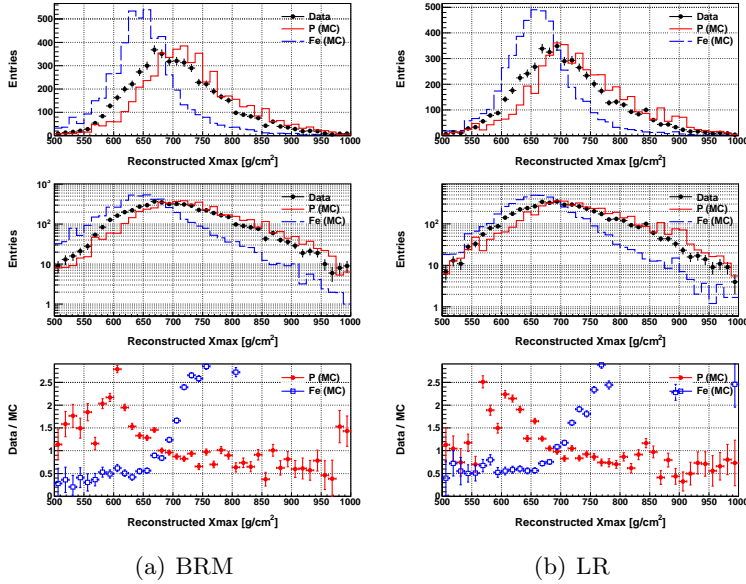


Figure A.31: The distribution of X_{max} between data and MC simulation under the *fiducial volume cut*. Since the discrepancy of difference between protons and irons is large, X_{max} is the most sensitive parameter to evaluate the mass composition of EASs.

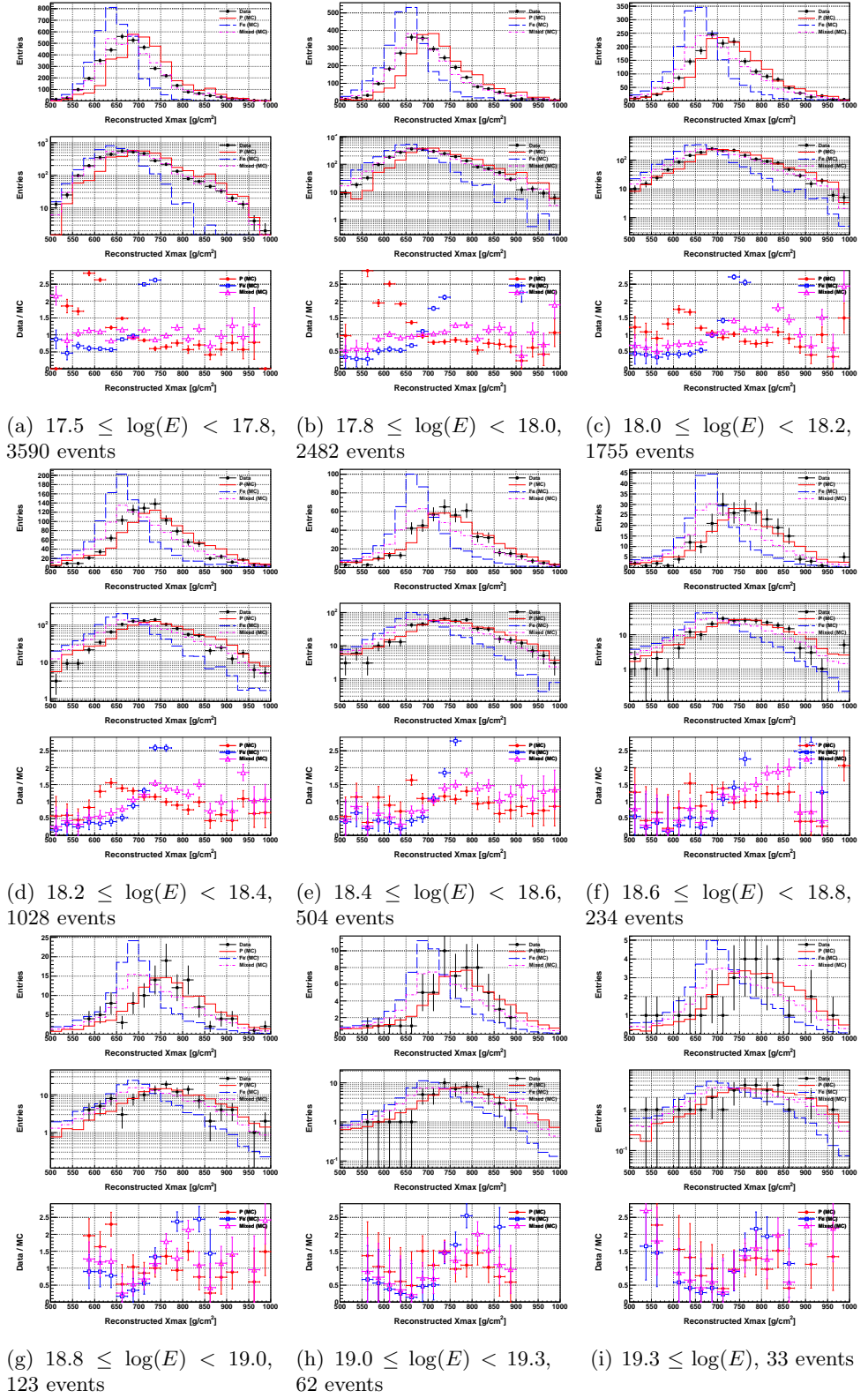


Figure A.32: X_{\max} distribution in several energy ranges compared with the expected distribution estimated from MC simulation for primary protons (red), irons (blue) or mixed compositions (pink) under the fiducial volume cuts. These figures are identical with the figures from Fig. 7.10 to Fig. 7.14.

Bibliography

- [1] V. F. Hess, *Phys. Z.* **13**, 1804 (1912).
- [2] *The Telescope Array Project Design Report* (2000).
- [3] *Pierre Auger Observatory Design Report* (1997).
- [4] M. S. Longair, *High Energy Astrophysics*.
- [5] T. K. Gaisser, *Cosmic Rays and Particle Physics*.
- [6] Minoru Oda, *Cosmic Rays*, 小田稔, 宇宙線
- [7] E. Seo et al., *Astrophys. J.* **378**, 763 (1991).
- [8] N. Grigorov, et al., *Proc. 12th International Cosmic Ray Conference* **5**, 1760 (1971).
- [9] M. Nagano, et al., *J. Phys. G* **18**, 447 (1992).
- [10] T. Antoni, et al., *Astropart. Phys.* **24**, 1 (2005).
- [11] J. Abraham, et al., *Phys. Lett.* **101**, 061101 (2008).
- [12] L. Perrone, et al., *Proc. 30th International Cosmic Ray Conference* **4**, 331 (2007).
- [13] K. Greisen, *Phys. Rev. Lett.* **16**, 748 (1966).
- [14] T. Zatsepin, V.A. Kuzmin, *JETP Lett*, **4**, 178 (1966).
- [15] R. Aloisio et al., *Astropart. Phys.* **34**, 620 (2011).
- [16] L. Drury, *Rep. Prog. Phys.*, **46**, 973 (1983).
- [17] P. O. Lagage and C. J. Cesarsky *Astron. Astrophys.*, **118**, 223 (1983).
- [18] C. Thompson, R. Duncan, *Monthly Notices of the Royal Astron. Society*, **275**, 255 (1995).
- [19] P. Blasi, R. Epstein et al., *Astrophys. J. Lett.*, **533**, L123 (2000).
- [20] A. Hillas, *Annual Review of Astronomy and Astrophysics*, **22**, 425 (1984).

- [21] E. Blodt, P. Ghosh, *Mothly Notices of the Royal Astronomical Society*, **307**, 491 (1999).
- [22] J. Rachen and P. Biermann, *Astron. Astrophys.* **272**, 161 (1993).
- [23] M. J. R. Rees, R. Mészáros, *Astrophys. J.*, **93**, 430 (1994).
- [24] H. Kang, D. Ryu and T. W. Jones, *Astrophys. J.* **456**, 422 (1996).
- [25] V. Kuzmin and I. Tkachev, *Soviet Journal of Experimental and Theoretical Phys. Lett.*, **68**, 271 (1998).
- [26] T. J. Weiler, *Astropart. Phys.*, **3**, 303 (1999).
- [27] H. Sato and T. Tati, *Progr. Theor. Phys.*, **47**, 1788 (1972).
- [28] J. Abraham et al., *Astropart. Phys.*, **29**, 188 (2008).
- [29] The Pierre Auger Collaboration, *Science*, **9**, 938 (2007).
- [30] The Pierre Auger Collaboration, *Astropart. Phys.* **24**, 314 (2010).
- [31] T. Abu-Zayyad et al., ArXiv: 1205.5984v1, (2012).
- [32] D. S. Gorbunov et al., *JETP Lett.*, **80**, 145 (2004). D. S. Gorbunov et al., *JCAP*, 0601, 025 (2006).
- [33] D. Heck et al., *Forschungszentrum Karlsruhe Report FZKA*, 6019 (1998).
- [34] H. M. J. Barbosa et al., *Astropart. Phys.*, **22**, 159 (2004).
- [35] V. Berezhinsky, astro-ph/0801.3028v1, (2008).
- [36] T. Shibata et al., *Nucl. Instr. and Meth. A*, **597**, 61 (2004).
- [37] R.U. Abbasi et al., *Phys. Rev. Lett.*, **104**, 161101 (2010).
- [38] P. Sokolsky, John Belz and the HiRes Collaboration, *29th International Cosmic Ray Conference*, Pune, **00**, 101 (2005).
- [39] Y. Tameda et al., *32th Proc. of International Cosmic Ray Conference*, **HE1.3**, 1268 (2011).
- [40] J. Abraham et al., *Phys. Rev. Lett.*, **104**, 091101 (2010).
- [41] P. F. S. Luis for the Pierre Auger Collaboration, *32th Proc. of International Cosmic Ray Conference*, (2011), ArXiv:1107.4804 (2011).
- [42] D. Garcia-Gómez for the Pierre Auger Collaboration, *32th Proc. of International Cosmic Ray Conference*, (2011), ArXiv:1107.4804 (2011).
- [43] C. Aramo et al., *Astropart. Phys.* **23**, 65 (2004).

- [44] M. Takeda et al., *Phys. Rev. Lett.*, **81(6)**, 1163 (1998)
- [45] S. Yoshida et al., *J. Phys. G: Nucl. Part. Phys.*, **20**, 651 (1994)
- [46] M. Takeda et al., *Astrophys. J.*, **522**, 225 (1999).
- [47] M. Takeda et al., *Astropart. Phys.*, **19**, 447 (2003).
- [48] Y. Uchihori et al., *Astropart. Phys.*, **13**, 151 (2000).
- [49] N. Hayashida et al., *Astropart. Phys.*, **10**, 303 (1999).
- [50] Abbasi R et al., *Phys. Rev. Lett.*, **100(10)**, 101101 (2008).
- [51] Egorova V et al., *Nuclear Phys. B - Proc. Supplements*, 136:3 (2004).
- [52] H. Tokuno et al., *Nucl. Instr. and Meth. A.*, **601**, 364 (2009).
- [53] H. Tokuno et al., *Nucl. Instr. and Meth. A.*, **676**, 54 (2012).
- [54] Y. Tameda et al., *Nucl. Instr. and Meth. A.*, **609**, 227 (2009).
- [55] P. Sreekumar et al., *Astrophys. J.*, **494**, 523 (1998).
- [56] P.W. Gorham et al., *Phys. Rev. Lett.*, **93**, 041101 (2004).
- [57] N.G. Lehtinen, et al., *Phys. Rev. D*, **69**, 013006 (2004).
- [58] The Pierre Auger Collaboration, *Phys. Rev. D*, **79**, 102001 (2009).
- [59] A. M. Hillas, *Astron. Astrophys.*, **22**, 425 (1984).
- [60] A. N. Bunner, *Ph.D. Thesis, Cornell University*, (1967).
- [61] F. Kakimoto et al., *Nucl. Instr. and Meth. A.*, **372**, 527 (1996)
- [62] M.-P. Véron-Cetty, P. Véron, *Astron. Astrophys.*, **455**, 773 (2006).
- [63] Nerling F et al., *Astropart. Phys.*, **24**, 421 (2006).
- [64] P. Bhattacharjee and G. Sigl, *Phys. Rept.*, **327**, 109 (2000).
- [65] M. Kachelriess et al., *Phys. Rev. D*, **68**, 043005 (2003).
- [66] E. Waxman and J.N. Bahcall, *Phys. Rev. D*, **59**, 023002 (1999).
- [67] J. Bellido, for the Pierre Auger Collaboration, ArXiv:0901.3389v1, (2009).
- [68] T.J. Weiler, in *Radio Detection of High Energy Particle*, edited by David Saltzberg and Peter Gorham, *AIP Conf. Proc.*, No. 579, p. 58.
- [69] C.T. Hill and D.N. Schramm, *Phys. Rev. D*, **31**, 564 (1985).
- [70] K. Mannheim, *Astropart. Phys.*, **3**, 295 (1995).

- [71] T. Abu-Zayyad et al., ArXiv: 1205.5141v1, (2012).
- [72] D. Ivanov et al., *32th Proc. of International Cosmic Ray Conference*, **HE1.3**, 1297 (2011).
- [73] Y. Tsunesada et al., *32th Proc. of International Cosmic Ray Conference*, **HE1.3**, 1270 (2011).
- [74] Abu-Zayyad T, Al Seady M. Belov K, et al., *Nucl. Instr. and Meth. A* **450**, 253 (2000).
- [75] S. Kawana et al., *Nucl. Instr. and Meth. A* **681**, 68 (2012).
- [76] S. Machida et al., *29th Proc. of International Cosmic Ray Conference*, (2007)
- [77] T. Tomida et al., *Nucl. Instr. and Meth. A* **654**, 653 (2011).
- [78] R.U. Abbasi et al., *Astropart. Phys.*, **25**, 74 (2006).
- [79] Kobayashi M, Shinkawa T, Sato T et al., *Nucl. Instr. and Meth. A* **337**, 355 (1994).
- [80] M. Chigawa et al., *31th Proc. of International Cosmic Ray Conference*, (2009).
- [81] A. Taketa et al., *31th Proc. of International Cosmic Ray Conference*, 924 (2009).
- [82] T. Abu-Zayyad, T. Nonaka, et al., ArXiv: 1201.4964v2, (2012).
- [83] R. Abbasi, et al, *Astropart. Phys.*, **25**, 74 (2006).
- [84] R.U. Abbasi et al., *Astropart. Phys.*, **27**, 370 (2007).
- [85] A. Ostapchenko *Nuclear Physics B - Proceedings Supplement*,, **151**, 143 (2006).
- [86] N. Kalmykov , S.Ostapchenko, *Nuclear Physics B - Proceedings Supplement*,, **52**, 17 (1997).
- [87] R. Fletcher, T. Gaisser, P. Lipari et al., *Phys. Rev. D*, **50**, 5710 (1994).
- [88] T. Sako, O. Adriani, L. Bonechi et al., *Nucl. Instr. and Meth. A* **587**, 146 (2007).
- [89] Chronological science tables, National Astronomical Observatory of Japan, Maruzen, (2011).
- [90] The Bright Star Catalog, 5th Edition, preliminary. Hoffleit D., and Warren Jr W.H.

- [91] G.I. Thompson et al., Catalog of Stellar Ultra-violet Fluxes, *The Science Research Council*, (1978).
- [92] J.W. Belz et al. *Astropart. Phys.*, **25**, 129 (2006). R. Abbasi et al. *Astropart. Phys.*, **29**, 77 (2008).
- [93] M. Nagano et al. *Astropart. Phys.*, **20**, 293 (2003), M. Nagano et al. *Astropart. Phys.*, **22**, 235 (2004).
- [94] P. Colin et al., *Astropart. Phys.*, **27**, 317 (2007), The MACFLY Collaboration, *Astropart. Phys.*, **30**, 312 (2009).
- [95] W. H. Press, B. P. Flannery, S. A. Teukolsky, W. T. Vetterling, *Numerical Recipes in C*.
- [96] <http://www-frd.fsl.noaa.gov/mab/raob/>
- [97] M. Amenomori et al., *Astrophys. Space Sci. Trans.*, **7**, 15-20, (2011)
- [98] Y. Tsunesada et al., *International Symposium on Future Directions in UHECR Physics*, Feb. 2012,
<http://indico.cern.ch/conferenceDisplay.py?confId=152124>
- [99] D. Allard et al., *Astropart. Phys.*, **27**, 61 (2007).
- [100] G. Thomson et al., *32th Proc. of International Cosmic Ray Conference*, **HE1.4**, 1307 (2011).
- [101] <http://jemeuso.riken.jp/>
T. Ebisuzaki et al., *A.I.P. Conf. Proc. of International Symposium on the Recent Progress of Ultra-High Energy Cosmic Ray Observation*, Aichi, Japan, (2010).
- [102] <http://icecube.wisc.edu/>
- [103] T. Fukuda, *Master Thesis*, Tokyo Institute of Technology, (2009).
- [104] Y. Tameda, *Doctor Thesis*, Tokyo Institute of Technology, (2010).
- [105] D. Ikeda, *Doctor Thesis*, Institute of Cosmic Ray Research, (2010).
- [106] K. Hayashi, *Master Thesis*, Tokyo Institute of Technology, (2011).
- [107] R. Ishimori, *Master Thesis*, Tokyo Institute of Technology, (2011).
- [108] Y. Kobayashi, *Master Thesis*, Tokyo Institute of Technology, (2011).
- [109] T. Fujii, *Graduation Thesis*, Osaka City University, (2008).
- [110] T. Fujii, *Master Thesis*, Osaka City University, (2010).